NATIONAL AERONAUTICS AND SPACE ADMINISTRATION

Technical Report 32-1597

Application of ERTS Images and Image Processing to Regional Geologic Problems and Geologic Mapping in Northern Arizona

A. F. H. Goetz, F. C. Billingsley, A. R. Gillespie,
M. J. Abrams, and R. L. Squires
Jet Propulsion Laboratory

E. M. Shoemaker
California Institute of Technology

I. Lucchitta and D. P. Elston
U.S. Geological Survey, Flagstaff

JET PROPULSION LABORATORY
CALIFORNIA INSTITUTE OF TECHNOLOGY
PASADENA, CALIFORNIA

May 15, 1975

NATIONAL AERONAUTICS AND SPACE ADMINISTRATION

Technical Report 32-1597

Application of ERTS Images and Image Processing to Regional Geologic Problems and Geologic Mapping in Northern Arizona

A. F. H. Goetz, F. C. Billingsley, A. R. Gillespie,
M. J. Abrams, and R. L. Squires
Jet Propulsion Laboratory

E. M. Shoemaker
California Institute of Technology

I. Lucchitta and D. P. Elston
U.S. Geological Survey, Flagstaff

JET PROPULSION LABORATORY
CALIFORNIA INSTITUTE OF TECHNOLOGY
PASADENA, CALIFORNIA

May 15, 1975

Page intentionally left blank

Preface

The work described in this report was performed by the Space Sciences Division of the Jet Propulsion Laboratory.

Dr. Richard L. Squires was a National Research Council resident research associate during the period of this task.

Acknowledgment

The authors thank Helen Paley for her efforts in obtaining and reducing field spectrometer data and for her efforts in ensuring that no ERTS picture was lost.

We thank Ermine van der Wyk for her unstinting efforts in bringing together a comprehensive document out of the contributions from such a diverse group of authors.

Contents

I. Introduction 1

II. Use of ERTS and Other Correlative Data 4
A. F. H. Goetz

A. Spectral Reflectance 5

B. Spectral Mapping 5

C. Spectroradiometry 6

D. Field Reflectance: Comparison With ERTS 7

References 12

III. Computer Image Processing 13
F. C. Billingsley, A. R. Gillespie, and A. F. H. Goetz

A. Rectification 14

1. Geometric Rectification 14

2. Radiometric Rectification 15

B. Cosmetics 17

C. Analysis 17

D. Display 18

References 22

IV. Geologic Investigations 23

A. The Bright Angel, Mesa Butte, and Related Fault Systems of Northern Arizona 23
E. M. Shoemaker, R. L. Squires, and M. J. Abrams

1. Bright Angel Fault System 27

2. Mesa Butte Fault System 27

3. Other Fault Systems 31

4. Relation of Eruptive Centers to Faults 33

5. Precambrian Origin of Faults 35

6. Aeromagnetic and Gravity Anomalies 37

7. Shylock and Chaparral Fault Zones 38

8. Cenozoic History of Displacement 40

B. The Shivwits Plateau 41

I. Lucchitta

1. General Characteristics 41

2. Methods Used 47

3. Applications of Remote-Sensing Data in the Shivwits Plateau Study 47
4. Results 49
C. The Coconino Plateau 73
R. L. Squires and M. J. Abrams
1. Regional Setting 73
2. Previous Mapping 73
3. Stratigraphy 73
4. Structure 76
5. Geologic Mapping 76
6. Modified Geologic Map 76
7. Mapping of Area B 76
8. Conclusions 81
D. The Verde Valley 81
D. P. Elston
1. Geologic Map 81
2. Fault and Lineament Map 81

References 89

V. Applications 97
A. Water on the Shivwits Plateau 97
I. Lucchitta
B. Water on the Coconino Plateau 102
R. L. Squires, E. M. Shoemaker, and M. J. Abrams
C. Water South of Flagstaff 102
D. P. Elston

VI. Evaluation of Computer-Enhanced Image Products 107
A. F. H. Goetz, R. L. Squires, I. Lucchitta, D. P. Elston, and M. J. Abrams
A. Contrast Stretches 107
1. Standard Linear Stretch 108
2. Individual Linear Stretch 109
3. Gaussian Stretch 110
4. Ramp CDF Stretch 112

B. Ratio Images 112
1. Log Ratio Images 114
2. Ratio and Log Ratio Images with Atmospheric Correction 115
C. Difference Pictures 115
D. Combinations of Various Processed Images 116
E. Filtered Images 118
F. Sequential Image Differencing 118
G. Summary 121

VII. Conclusions and Recommendations 123
A. F. H. Goetz
A. General Remarks 123
B. Image Processing 123
C. Spectral Information 123
D. Geologic Results 124
E. Applications 124
F. Recommendations 124
1. Resolution 124
2. Number and Location of Spectral Bands 125
3. Overflight Times 125
4. Radiometric Calibration 125

Appendix A. Image Processing System Considerations and VICAR . . 126
F. C. Billingsley

Appendix B. Digital Processing of ERTS Images 131
A. R. Gillespie and F. C. Billingsley

Appendix C. Computer Program Descriptions 175
A. R. Gillespie

Appendix D. ERTS Image Processing Sequence 181
A. R. Gillespie

Appendix E. Portable Field Reflectance Spectrometer 183
A. F. H. Goetz

Tables

II-1. PFRS spectral reflectivities, ERTS pixel values and their standard deviations, and multiplying factor values for the Coconino Plateau areas shown in Fig. II-4 9

II-2. Values for N_x in NASA picture ERTS E-1014-17373 10
II-3. Ratio contrasts for the six ERTS band ratios 10
II-4. Ratio contrasts for the six ERTS band ratios using PFRS data 11
VI-1. Types and number of observations made on I²S viewer in the Shivwits Plateau region 108
VI-2. Cumulative points for the combination of difference picture transparencies 5-4 (negative), 4-7 (negative), and 4-5 (negative) 109
VI-3. Cumulative points for transparency combinations analyzed . . 110
VI-4. Evaluation of features in a Coconino Plateau standard linear-stretch image 111
VI-5. Coconino Plateau individual linear-stretch image evaluation . . 112
VI-6. Coconino Plateau gaussian-stretch image evaluation 114
VI-7. Coconino Plateau ramp-CDF-stretch image evaluation 114
VI-8. Ranking extending from 1 to 6 of ratio images with and without atmospheric correction in the Coconino Plateau . . . 115

Figures

I-1. Areas studied in ERTS investigation 2
II-1. Relative reflectance of pressed Fiberfrax with respect to MgO 6
II-2. Reflectance of soil derived from the Moenkopi Formation . . 6
II-3. (a) Three laboratory sample spectra of rock chips and soil taken with the DK2-A spectrometer. (b) Average of ten spectra within unit 3 of the Alpha Member of the Kaibab Formation taken using the PFRS 7
II-4. Areas in which ground measurements were taken using the PFRS 8
II-5. Brightness values (DN) along an image line crossing a cloud shadow 10
II-6. Average PFRS spectra of geologic units on the Coconino Plateau outlined in Fig. II-4 11
III-1. Frequency-response restoration through Fourier filtering . . . 16
III-2. Contour map of two-dimensional PDF 18
III-3. Single-channel PDFs 19
III-4. Directional high-pass convolution filtering 20

III-5. Nondirectional high-pass convolution filtering 21

IV-A-1. ERTS-1 picture of Coconino Plateau showing Bright Angel and Mesa Butte fault systems 24

IV-A-2a. Map of faults in northwestern Arizona 25

IV-A-2b. Index to sources of information shown in Fig. IV-A-2a 26

IV-A-3a. Oblique high-altitude aerial photograph of Mesa Butte fault system 28

IV-A-3b. Oblique high-altitude aerial photograph of Bright Angel fault system 29

IV-A-4. Map of part of Bright Angel and Mesa Butte fault systems . . 30

IV-A-5. Principal fault systems of northwestern Arizona 32

IV-A-6. Simplified residual aeromagnetic map of northwestern Arizona 34

IV-A-7. Sub-Paleozoic geologic map of Grand Canyon National Park. 36

IV-A-8a. ERTS-1 picture, showing Shylock and Chaparral fault zones in central Arizona 39

IV-A-8b. Simplified residual aeromagnetic map, showing Shylock and Chaparral fault zones 39

IV-A-9. Distribution of earthquake epicenters in northwestern Arizona for the period 1938 to 1973 42

IV-B-1. General area of the Shivwits Plateau studied in ERTS investigation 45

IV-B-2. Location map of northwestern Arizona 46

IV-B-3. Cross sections across western Grand Canyon region, Arizona 50

IV-B-4. Diagrammatic cross section across western Grand Canyon region, showing stratigraphic units 51

IV-B-5. Map of northwestern Arizona showing scarps of various types, ages and degrees of dissection; flow vectors in lavas; and streams that represent ancient pre-Grand Canyon drainages 53

IV-B-6. Geomorphic elements in the western Grand Canyon region 54

IV-B-7. Map showing segments comprising the Colorado River drainage 55

IV-B-8a. Hunt's hypothesis. Ancestral Colorado Drainage before basin–range faulting 57

IV-B-8b. Hunt's hypothesis. Ancestral Colorado Drainage after effusion of Peach Springs Tuff and basin–range faulting . . . 58

IV-B-8c. Hunt's hypothesis. Ancestral Colorado Drainage shortly before integration into modern course 59

IV-B-9a. Hypothesis of McKee et al. Ancestral Colorado Drainage before major basin–range faulting 60

IV-B-9b. Hypothesis of McKee et al. Ancestral Colorado Drainage after basin–range faulting and effusion of *Peach Springs Tuff* 61

IV-B-9c. Hypothesis of McKee et al. Ancestral Colorado Drainage becoming modern Colorado River through headward erosion, capture, and integration after opening of the Gulf of California 62

IV-B-10a. Lucchitta's hypothesis. Ancestral Colorado Drainage before basin–range faulting 65

IV-B-10b. Lucchitta's hypothesis. Ancestral Colorado Drainage after basin–range faulting and effusion of Peach Springs Tuff . . . 66

IV-B-10c. Lucchitta's hypothesis. Ancestral Colorado Drainage becoming modern Colorado River through headward erosion, capture, and integration after opening of the Gulf of California 67

IV-B-11. Tectonic map of the Shivwits Plateau, Arizona 68

IV-B-12. Northeast-trending features in northwestern Arizona and in southeastern Nevada 72

IV-C-1. ERTS picture of the Coconino Plateau, showing outline of mapped areas A and B and high-altitude and U. S. Forest Service photographic coverage 74

IV-C-2. Stratigraphic column of rock units on the Coconino Plateau 75

IV-C-3. Geologic map of part of the Coconino Plateau 77

IV-C-4. Simplified geologic map of the Coconino Plateau, showing distribution of geologic units 78

IV-C-5. (a) Fault map derived from ERTS images. (b) Fault map derived from field observations 79

IV-C-6. (a) Geologic Map of Arizona showing Area B. (b) Geologic map made in the laboratory using unenhanced and computer-enhanced ERTS images. (c) Same as (b), except that extra strippling was used to distinguish unit from that in (d). (d) Part of the simplified geologic map covering Area B 80

IV-D-1. Geologic map of north-central Arizona from Geologic Map of Arizona 82

IV-D-2a. Geologic map of north-central Arizona from published and unpublished information on ERTS-1 images 83

IV-D-2b. Geologic map of north-central Arizona shown in Fig. IV-D-2a superimposed on background of an ERTS-1 image 84

IV-D-2c. Explanation for Figs. IV-D-2a, b and IV-D-3a, b 85

IV-D-3a. Fault and lineament map of north-central Arizona 87

IV-D-3b. Fault and lineament map or north-central Arizona shown in Fig. IV-D-3a superimposed on background of an ERTS-1 image 88

V-A-1. Diagrammatic stratigraphic section of the Grand Canyon region, showing lithologies and locations of main spring and seep lines 98

V-A-2. ERTS-1 picture of the western Grand Canyon region, centered on the Shivwits Plateau, showing the Shivwits and Uinkaret lavas flowing north-northwest in the direction of strike 100

V-A-3. Diagrammatic composite sections of the Shivwits Plateau, showing sequence of events in late Cenozoic time 101

V-B-1. Existing wells on the Coconino Plateau 103

V-B-2. Stratigraphic column of mapped rock units 104

V-B-3. Simplified geologic map of the Globe Ranch area, Coconino County, Arizona, showing test hole locations 105

VI-1. Gaussian contrast-stretch print (band 7, negative), showing superior display of structure within areas of vegetation on the Coconino and Kaibab Plateaus 113

VI-2. (a) Individual stretch, color additive composite of the Verde Valley region. (b) Color ratio composite of the same area (4:5, 5:6, 6:7) 116

VI-3. Log ratio color composite of the negative transparencies of bands 4:5, 4:7, and 7:4 printed as green, red, and white, respectively 117

VI-4. NASA picture ERTS E-1014-17375-5 processed to enhance high spatial-frequency detail 119

VI-5a. Difference pictures showing temporal changes in the Coconino Plateau. Misregistration is attributed to parallax 121

VI-5b. Difference pictures showing temporal changes in the Coconino Plateau. Misregistration is evident in areas of high relief 122

A-1. Image processing system 130
B-1. Nearest neighbor and bilinear interpretation resampling techniques 132
B-2. Resampling by convolution 133
B-3a. Difference pictures showing temporal changes in the Coconino Plateau 133
B-3b. Difference pictures showing temporal changes in the Coconino Plateau 134
B-4. Image degradation during resampling when the resampling site is midway between original samples 135
B-5. Displacements that will map control points from their found locations in the input picture to their desired locations in the geometrically corrected output picture . . . 137
B-6. Image degradation during resampling 139
B-7. Sampling intervals and field of view of the ERTS MSS 140
B-8. Restoration of correct frequency response 140
B-9. Measured frequency response of MSS band 4 140
B-10. Frequency-response correction 141
B-11a. Skewing of image caused by the Earth's rotation 142
B-11b. ERTS and Earth geometry 142
B-12. Effect of spacecraft roll on MSS viewing geometry 145
B-13. Parallax in adjacent ERTS images 146
B-14. (a) Digital topographic map. (b) Irradiance map 146
B-15. In-flight sensor calibration for NASA picture ERTS E-1111-04340, MSS band 4, sensor 1 only 147
B-16. Residual radiometric striping in NASA picture ERTS E-1072-18001 148
B-17. Hysteresis 149
B-18. Removal of radiometric striping using "notch" filters 150
B-19. Use of "decision spaces" to describe classes of materials. . . 151
B-20. Comparison pictures of Verde Valley 155
B-21. Mojave Desert viewed by MSS in four bands on December 14, 1972 156
B-22. Relative radiances of four surface materials viewed by ERTS in the Mojave Desert 157
B-23. Simple decision boundaries 157
B-24. Parallelepiped decision boundaries 158

B-25. Classification vs enhancement for part of the Coconino Plateau 160
B-26. Classification vs enhancement for part of the Verde Valley . . 161
B-27. Hydrothermal alteration detection in the Goldfield, Nevada, test area 162
B-28. Contrast stretches 164
B-29. Box filtering to enhance structural features 165
B-30. Increased pixel density by resampling image 166
B-31. Chromaticity PDF 167
B-32. Construction of pictures representing hue, saturation, and intensity 169
B-33. Color and contrast enhancement 172
E-1. Portable field reflectance spectrometer in operating position 183
E-2. Exploded view of optical head 185
E-3. Composite circular variable filter wheel 186
E-4. Functional block diagram of the portable field reflectance spectrometer 187
E-5. (a) Raw spectrum of an andesite sample. (b) Spectral reflectance spectrum of an andeside sample 188

Plate

I. Geologic map of part of the Shivwits Plateau, Mojave County, Arizona. 43

Abstract

The purpose of this study was to apply the techniques of computer image processing to ERTS images as an aid to the solution of some regional geologic problems of significant interest.

ERTS-1 images were applied to studies in the Shivwits Plateau, Coconino Plateau, and north-central Arizona regions. Unprocessed ERTS images revealed a wealth of new structural information and enabled a broad regional study to be made of the tectonic history of the southwestern Colorado Plateau.

Spectral information from ERTS-1 was shown to be compatible with ground spectral reflectance measurements made with a portable field instrument developed during this investigation, provided that allowance was made for atmospheric effects.

Computer image processing yielded lithologic boundary information within the Coconino Plateau region not obtainable from unprocessed images. Various enhancement techniques were compared in the three areas of study, and some simple rules were developed to guide the processing of images in unknown areas.

A new hypothesis was developed for the history of the Colorado River. An ancestral and relatively old Upper Colorado Drainage followed approximately its present course as far as the western side of the Kaibab Uplift, where it diverged from the present course by following a strike valley trending north-northwest. This drainage was captured relatively recently by a much younger Lower Colorado Drainage, which developed by headward erosion after the opening of the Gulf of California.

A byproduct of the regional studies in each of the three areas was the identification of areas favorable for the localization of shallow and deep ground waters. On the Shivwits Plateau water trapped in the axis of the old strike valley underlying the Shivwits lavas is a potential source. On the Coconino Plateau sandstone lenses, underlain by clays, within the otherwise permeable Kaibab Limestone are potential perched aquifers. These can be identified on computer-enhanced images. Lineaments detected first on ERTS-1 frames and later verified on aerial photographs were used south of Flagstaff, Arizona, to identify maximum fracturing along the Oak Creek fault in the Woody Mountain well field; a site for a new deep well has been selected and is being drilled by the city of Flagstaff.

I. Introduction

The Earth Resources Technology Satellite (ERTS), launched on July 23, 1972, began a new era in synoptic, small-scale photoreconnaissance. The primary purpose of this investigation was to use an interdisciplinary approach in applying the new technologies of repetitive orbital multi-spectral photography and computer image processing to several specific local and regional geologic problems. The investigation had dual objectives:

(1) To test the applicability of processed Earth orbital images in geologic mapping.

(2) To apply the orbital image data to the solution of geologic problems of outstanding scientific interest.

Field areas, located in northwestern and north-central Arizona, included areas that previously had been intensively mapped, which were used as ground truth sites, and large adjoining areas that were virtually unmapped. ERTS images were used to map these latter areas at both small and intermediate scales. Corresponding problems of image utilization were:

(1) Mapping individual geologic units based on spectral reflectivity.

(2) Defining structures such as faults and joint patterns.

(3) Discovering and mapping subtle geomorphic features such as abandoned drainage systems.

The main advantages in using ERTS images rather than conventional aerial photographs for this work were the regional coverage and the nearly orthographic view gained from recording at satellite altitude.

The focal geologic problem of this investigation was the nature and late Cenozoic history of part of the boundary between the Colorado Plateau and the Basin and Range provinces. During this investigation, the structure of a portion of this part of the boundary was mapped and showed its structural history to be recorded in middle to late Tertiary and Quaternary sedimentary deposits and volcanic rocks. Significant evidence regarding the development of the Basin and Range province is contained in the evolution of the Colorado River drainage system. The record of this geomorphic evolution is preserved in a series of ancient disrupted drainage channels, partly filled with sediments and volcanic rocks, and in other more widespread fluviatile and lacustrine deposits and lava flows. These deposits were the object of special study, in an effort to solve the history of the Colorado River and its principal tributaries in the vicinity of the Grand Canyon.

Although not originally proposed, during this investigation a study was made of the potential ground-water supplies and the applicability of ERTS images as an aid to their locations (see Section V).

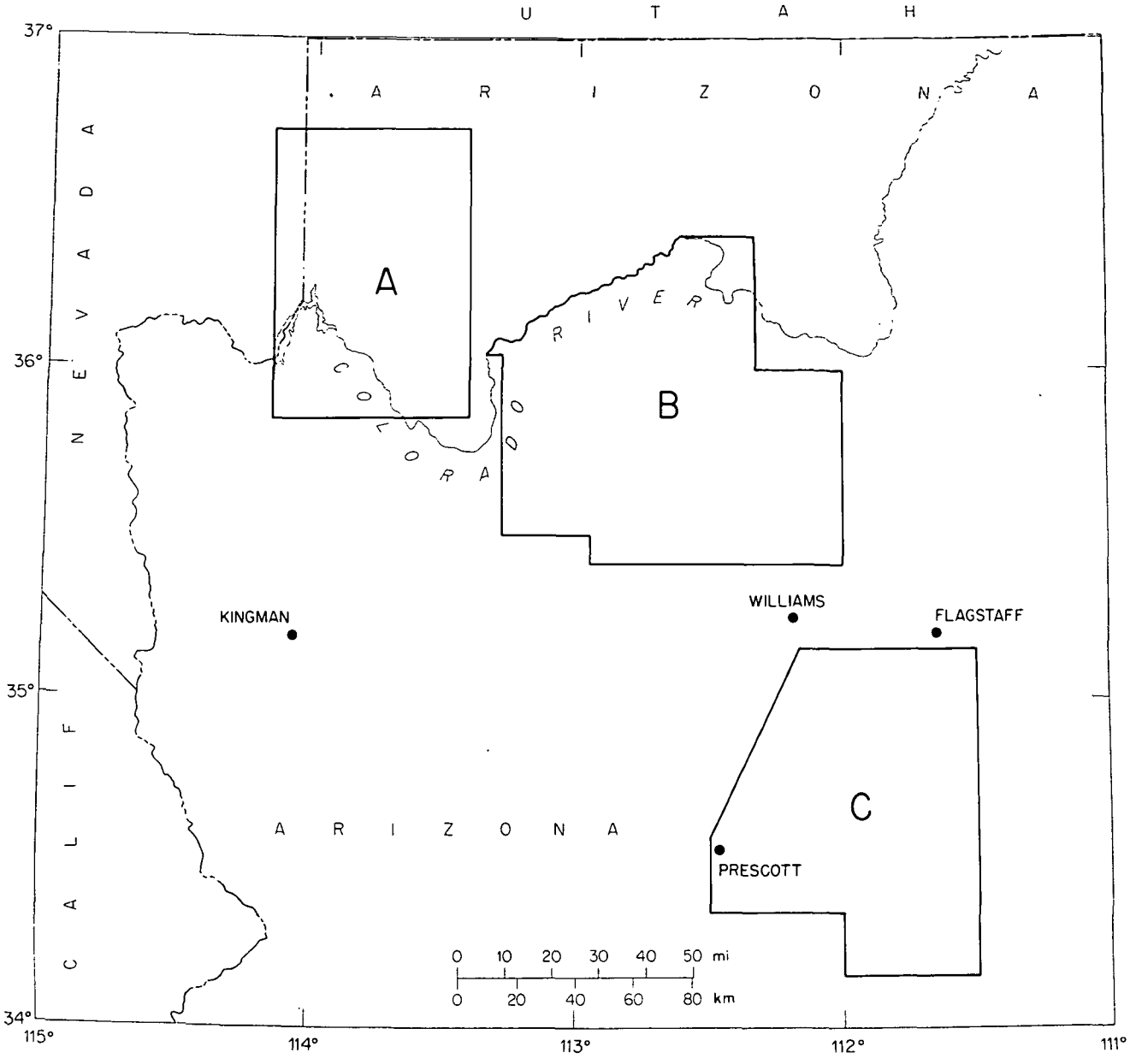

Fig. I-1. Areas studied in ERTS investigation

Three areas (see Fig. I-1) in north-central and northwestern Arizona were studied. Area A was mapped in detail by I. Lucchitta (see Section IV-B). This area was of major interest because it includes:

(1) An exceptionally clear transition from the Colorado Plateau to the Basin and Range province.

(2) An easterly basin of the basin-range type, well dissected by the Colorado River, which furnishes an excellent insight into the three-dimensional geometry of a typical interior basin deposit, the early history of the Colorado River, and the structural history of the margin of the Colorado Plateau.

(3) The westernmost part of the Grand Canyon, an area critical to the understanding of the history of the Colorado River and of the pre-Colorado drainage system.

Area B was mapped by R. Squires and M. Abrams under the direction of E. M. Shoemaker (see Section IV-C). This area was chosen because the Cataract Creek Basin is a critical area in which the geomorphic evolution of the boundary of the Basin and Range province with the Colorado Plateau can be studied, and it has never been studied in detail. The area was especially suited to mapping by small-scale, multi-spectral images because:

(1) Different rock types are distinctively colored: gray Paleozoic limestone, remnants of red Mesozoic sandstone and shale and black Cenozoic basalt.

(2) Outcrops are of reasonable size for mapping by low-resolution images, and the stratigraphic and structural relationships are relatively simple.

Area C, centered on the Verde Valley, was studied by D. P. Elston (see Section IV-D). This area was chosen for its wide variety of igneous, metamorphic, and sedimentary rocks which range in age from very young to very old (Pleistocene to Precambrian). Environments of formation for the igneous rocks include plutonic, hypabyssal, and volcanic, and for sedimentary rocks marine and continental. The area embraces parts of two major structural provinces: the structurally simple Colorado Plateaus province, and the more complicated terrain that is transitional into the Basin and Range province. The area is comparatively well known geologically, and geologic maps at scales of 1:24,000, 1:48,000, and 1:62,500 cover much of the area. The objective at this test site was to determine the multi-spectral characteristics of a wide variety of rock types and to apply analyzed remote-sensing data to the interpretation of stratigraphy and structure in simple to complex geologic terrains.

The approach used to solve problems at the test sites centered about surface geologic mapping aided by conventional and high-altitude aerial photographs and computer-enhanced ERTS multi-spectral images. Computer enhancement of the ERTS images and attempts at quantitative lithologic identification were carried out by A. Goetz, F. Billingsley, and A. Gillespie.

Field spectrometry was used in two of the areas (B and C) to establish the relationship between surface reflectivity and ERTS-image picture element values.

II. Use of ERTS and Other Correlative Data

A. F. H. Goetz

Basic data used in the ERTS investigation were provided by means of the ERTS multi-spectral scanner (MSS), which consists of 24 detectors, six in each of four spectral bands. These bands are designated by the numbers 4, 5, 6, and 7 and span the approximate spectral ranges of 0.5 to 0.6, 0.6 to 0.7, 0.7 to 0.8, and 0.8 to 1.1 μm. The Earth's surface is scanned by a mirror, perpendicular to the spacecraft's orbital path, and the image is formed six lines at a time. At the end of each second mirror sweep, calibration data are obtained from a gray wedge and standard lamp. The signal from the detectors is digitized and compressed for transmission to ground stations.

The instantaneous signal produced by any detector, K_X, is represented by:

$$K_X = \frac{1}{\pi} \int_{\lambda_1}^{\lambda_2} \rho(\lambda)\, \Phi(\lambda)\, H(\lambda)\, \tau(\lambda)\, I(\lambda)\, d\lambda + \int_{\lambda_1}^{\lambda_2} N(\lambda)\, d\lambda \qquad (1)$$

where

X = detector sensitive to radiation within the wavelength region between λ_1 and λ_2

λ = wavelength

ρ = bidirectional surface reflectance

Φ = surface photometric function

H = solar irradiance at the surface

τ = atmospheric transmittance

I = instrument factor combining detector response and transmission of the MSS optical system

N = path radiance

The second term in Eq. (1) represents the path radiance or contribution of sunlight scattered by the atmosphere in the instrument's line of sight. The key parameter in distinguishing rock types in ERTS pictures is the spectral reflectance $\rho(\lambda)$. Generally, in a good frame all other parameters remain almost constant within an image.

A. Spectral Reflectance

Reflectance of minerals and rocks in the visible and near-infrared spectral regions is controlled by electronic and lattice vibrations (Refs. II-1 and II-2). The electronic transitions, most important in producing absorptions in the spectral region under 1 μm, are of two types: (1) those due to transitions in anion electronic energy levels, which can be modified by interaction with crystal fields, and (2) those due to interchange of electrons among ions, known as charge transfer. Charge transfer is more energetic and causes absorption in the ultraviolet part of the spectrum.

Compared with electronic transitions, vibrational processes produce relatively sharp bands usually less than 0.1 μm wide. Vibrational processes do not cause discernible absorptions in the spectral region of ERTS. Between 1 and 2.5 μm, overtones and combinations of normal modes of anion groups such as OH^{-1}, CO_3^{-2}, and SO_4^{-2} produce absorption. No fundamental modes produce absorptions under 2.5 μm.

The major influences on the spectrum, in the visible and near-infrared regions, are electronic processes involving the transition metal ions, notably iron. The combination of ferric and ferrous absorptions is responsible for the colors in most of the rocks in the field. For example, the green of olivine is not caused by any specific chromophoric group, but rather by strong ferrous bands in the ultraviolet and near 1 μm, with absorption wings extending into the visible region (see Ref. II-1).

The red color in soils is generally caused by a combination of hematite and goethite. The absorption at short wavelengths, causing the red color, is due to the presence of a charge transfer, or conduction band in Fe^{3+}. The absorption edge, between about 0.5 and 0.6 μm, is subdued by the presence of impurities and imperfections in the crystal lattices, resulting in a general falloff in reflectivity toward shorter wavelengths (Ref. II-3).

B. Spectral Mapping

Discrimination among rock units is based on their relative reflectivity in each of the four ERTS spectral bands. The difficulty in making accurate lithologic identifications, using spectral reflectance only, is compounded by several factors:

(1) In almost all environments, materials exposed at the surface have been weathered to some degree. Because absorption and reflection of light occur in the upper microns of the surface, the spacecraft observer has a definite disadvantage with respect to the ground observer who can break off a fresh sample for identification.

(2) The spectral reflectivity of rock materials is strongly affected by the abundance and oxidation state of iron, as previously mentioned. The ground observer makes compositional conclusions on the basis of texture and mineral type, independent of the average abundance of iron. Geologic units, in some cases, also can be identified on the basis of grain size, patterns of surface weathering, or fossil evidence, indicators not resolvable from spacecraft altitudes.

(3) Vegetation cover contributes significantly to the apparent average reflectance detected by the spacecraft, especially within bands 6 and 7 where the reflectance of vegetation exceeds by a factor of 2 or more that of most rock and soil materials. Allowances can be made for vegetation if the cover is not complete. However, if the cover exceeds about 50% of the surface area, separation only among grossly different rock types is possible. Difficulties arise when the vegetation cover is not uniform. Variations in vegetation density masquerade as surface composition anomalies. Although such vegetation-cover inhomogeneities may reflect soil composition variation, so much a priori information is necessary for interpretation that it negates the advantages of remote ERTS mapping of unknown areas.

These problems, however, do not preclude remote geologic mapping, but do require some adjustments. In many cases, the geologic unit mapped on the ground does not coincide with the "telegeologic" or "remote-sensing" unit mapped from ERTS. The result is invariably an outcrop map rather than a true geologic map.

Units with grossly different albedos such as basalts and acidic igneous rocks are rarely confused on any single band in an ERTS image, but units with intermediate albedos cannot be identified without resorting to multispectral information; only in rare cases is it possible to identify a rock type directly. Rowan et al. (Ref. II-4) have identified minerals associated with hydrothermal alteration by means of computer image-enhancement methods. These methods (see Section III) allow the separation of areas into telegeologic units based on spectral information. In most cases, however, absolute identification is impossible without sampling key areas on the ground.

A major objective of this study was to determine to what extent it is possible to map individual geologic units

based on spectral reflectivity. The method used was to make laboratory and field spectral-reflectivity measurements and compare them with the ERTS spectral data as discussed below. When this was not possible because of accessibility constraints, such as on the Shivwits Plateau, comparisons were made between field and ERTS products that had been computer processed to provide the best contrast among units.

The problems of scale between laboratory and spacecraft measurements, atmospheric absorption, and atmospheric scattering are manifest. Although it is not possible to eliminate the effects of observing through the Earth's atmosphere, several techniques that minimize the disturbance are available and are discussed below.

C. Spectroradiometry

Measurements of spectral reflectance in the 0.4- to 2.5-μm region were made in situ by means of a portable field reflectance spectrometer (PFRS; see Appendix E) and in the laboratory using a Beckman DK2-A hemispherical reflectance spectrometer. The objective was to bridge the gap in scale among the different instruments (ERTS, PFRS, and DK2-A) that have fields of view of approximately 6000 m^2, 200 cm^2, and 1.5 cm^2, respectively. The difficulty in comparing a DK2-A spectrum and ERTS values in four bands is obvious. All natural surfaces at the scale of ERTS are heterogeneous in nature, particularly when vegetation is considered. On the other hand, it should be possible to obtain a statistically significant sample within an ERTS picture element by making traverses involving discrete sampling with the PFRS.

Spectral-reflectance measurements with the DK2-A use MgO as a reference standard. Field measurements were made using Fiberfrax, a white ceramic wool, as a standard (Ref. II-5). This material has the advantage that the surface can be renewed after contamination by peeling the surface layer and pressing the new surface flat.

Figure II-1 shows the reflectance of pressed Fiberfrax with respect to MgO. This curve differs somewhat from that shown by Watson (Ref. II-5) in that the reflectance rises more rapidly toward longer wavelengths in the 0.5- to 0.9-μm region and the average reflectance is 1 to 3% higher. Fiberfrax reflectance values beyond 0.9 μm are not given in Ref. II-5.

Figure II-2 gives a comparison between the average field spectrum of ten areas sampled within the Moenkopi Formation, at a feature called Abrams Sag, and the laboratory spectrum of one sample of the red clay soil.

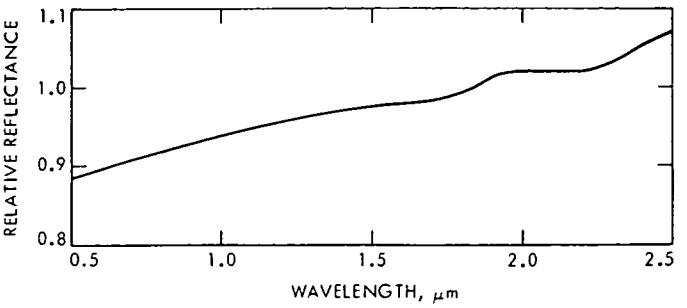

Fig. II-1. Relative reflectance of pressed Fiberfrax with respect to MgO

The field spectrum has been corrected to the MgO standard.

The match between the spectra is surprisingly good. However, the slope of the curves in the visible region, an important factor when spectral band ratios are considered, is significantly different. The latter can be attributed to the contribution of vegetation, mostly short dry grasses, in the field spectra and to the increased relative abundance of darker soil over that measured in the one laboratory sample.

Figure II-3 demonstrates the difficulty of matching laboratory and field spectra because of the heterogeneity of the surface. The unit is number 3 within the Alpha Member of the Kaibab Formation and consists of shale, siltstone, gypsum, interbedded limestone, and fine-grained calcareous sandstone (see Section IV-C). The three laboratory spectra shown in Fig. II-3a are of soil and rock chips taken at different locations within the unit. Figure II-3b is the average of 10 spectra taken with the PFRS. The average reflectance falls below that measured for laboratory samples, probably because of the predomi-

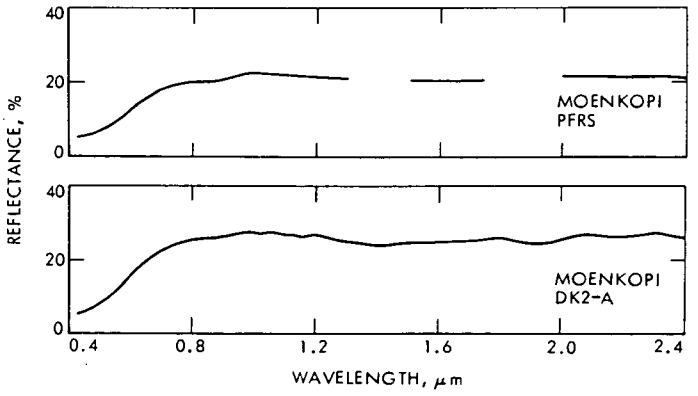

Fig. II-2. Reflectance of soil derived from the Moenkopi Formation, for an average of ten areas using the PFRS, and for one area as measured with the DK2-A spectrometer in the laboratory

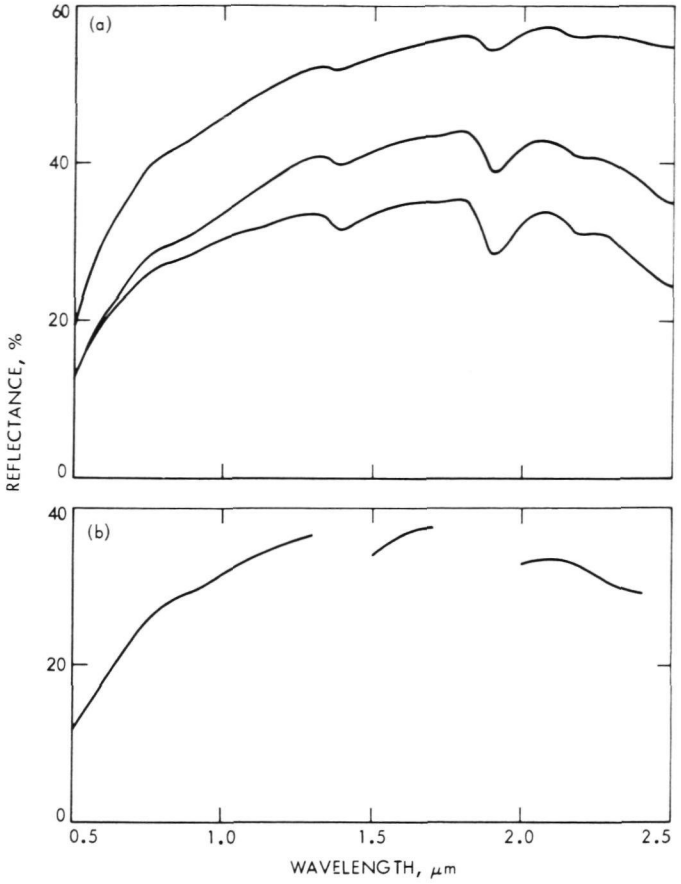

Fig. II-3. (a) Three laboratory sample spectra of rock chips and soil taken with the DK2-A spectrometer. (b) Average of ten spectra within unit 3 of the Alpha Member of the Kaibab Formation taken using the PFRS

nance of soil and dry vegetation which cannot be introduced into the DK2-A.

As might be anticipated, therefore, field measurements are more realistic in determining the spectral reflectance of the Earth's surface, as seen by ERTS, than are measurements made in the laboratory.

D. Field Reflectance: Comparison With ERTS

The Coconino Plateau was chosen for a comparison study between ERTS and PFRS reflectance values because of the large size of relatively homogeneous units and because of the lack of large vegetation species, which would be difficult to include in a ground spectral survey.

The August 24, 1974, ERTS-1 picture shown in Fig. II-4 was used for comparison with PFRS field surveys made in May 1974. The expected seasonal differences in surface reflectance caused by variations in vegetation and soil moisture probably were not significant factors because both periods were preceded by extensive dry spells, and in May 1974 much of the spring grass cover had already turned brown, thus simulating the vegetation cover expected in late summer. The areas of study are outlined by black boxes in Fig. II-4 and are numbered according to the corresponding unit within the Alpha Member of the Kaibab Formation.

Approximately 20 field spectra were taken in each of the areas. Because each spectrum is reduced to spectral reflectivity with respect to a Fiberfrax standard, the measurements are almost free of bias introduced by sun angle or atmospheric conditions. On the other hand, the ERTS picture element values and their standard deviations over an area are dependent on sun angle and the distribution of topographic slopes. High sun angles yield data with smaller variations in reflected intensity within a given area.

Table II-1 shows the average PFRS reflectance values plus ERTS brightness values ranging from 0 to 255 and their measured standard deviations. The values are comparable only in a relative sense, assuming that both instrument systems are linear. A more direct comparison can be made by considering Eq. (1). The variable of interest is the surface reflectance $\rho(\lambda)$. The parameters solar irradiance, atmospheric transmittance, and the instrument factor can be considered to be constant in a small area of an ERTS picture. Φ is a function of position, and the variation in Φ due to topographic relief is the dominant factor contributing to the spread in pixel values within a test area. The constant parameters can be grouped into a single multiplicative factor M_X shown in Table II-1.

$$M_X = \frac{K_X - N_X}{P_X} \tag{2}$$

where K_X is the average value for a small area in band X; N_X is the atmosperic path radiance value, the derivation of which is discussed below; and P_X is the field reflectance value within an ERTS band X (Ref. II-6). Values for N_X are given in Table II-2. M_X can be used to convert any area in an ERTS frame to spectral reflectance as long as the mean slope is close to zero.

As shown in Table II-1, the values for M_X are relatively consistent, with a standard deviation of approximately 6% of the mean. However, the variations in M among different units in band 4 are nearly twice as large. This variation has not yet been explained satisfactorily, although atmospheric effects, particularly the path

Fig. II-4. Areas in which ground measurements were taken using the PFRS

Table II-1. PFRS spectral reflectivities (P_X), ERTS pixel values (K_X) and their standard deviations, and multiplying factor (M_X) values for the Coconino Plateau areas shown in Fig. II-4

Unit	P_4	K_4	σK_4	M_4	P_5	K_5	σK_5	M_5	P_6	K_6	σK_6	M_6	P_7	K_7	σK_7	M_7
Pkα2	19.2	96.6	4.3	3.78	25.3	122.7	6.8	4.34	29.7	127.1	7.2	3.94	33.8	118.9	5.4	3.34
Pkα3	16.2	82.0	2.6	3.58	22.5	104.6	4.5	4.07	27.2	113.4	4.5	3.80	31.4	112.0	4.5	3.38
Pkα4	18.2	89.6	4.0	3.60	24.2	114.5	6.3	4.19	25.5	120.3	6.1	4.33	28.5	114.1	5.9	3.79
Pkα5	12.8	76.0	3.2	4.06	17.9	96.8	6.3	4.68	23.8	98.8	8.0	3.73	25.9	100.2	9.5	3.64
Pkα6	18.0	86.1	5.3	3.45	23.9	107.2	7.0	3.94	27.2	108.2	5.8	3.61	29.6	101.4	7.3	3.22
Moenkopi	14.1	93.0	8.6	4.89	23.2	119.0	7.8	4.57	27.2	118.8	6.5	4.00	29.9	111.9	6.4	3.54
Basalt	14.2	77.3	3.2	3.75	19.4	87.9	5.4	3.86	21.8	90.1	5.5	3.67	23.5	84.5	5.3	3.34
$\bar{m}$				3.87				4.24				3.87				3.46
$\sigma/\bar{m}$				0.13				0.07				0.06				0.06

radiance, exert their greatest influence on band 4. The major contributing factor is the apparent excessively low PFRS value for Moenkopi Formation material. Without this value $\sigma/\bar{m}$ for band 4 would be 0.06.

The atmospheric path radiance is represented by the second integral in Eq. (1) and must be removed before an accurate comparison among ERTS and PFRS spectral values can be made. Rogers (Ref. II-7) describes a method using simultaneous ground measurements to determine the path radiance. If no in situ measurements are made during an ERTS overflight, other methods must be used to determine the scattering component. The most obvious method is to scan each spectral band for the lowest radiance value and subtract it from the entire frame. The lowest values are most often found in cloud shadows. Figure II-5 depicts a cross section through a cloud shadow taken from an ERTS computer-compatible tape (CCT) listing. DN values on an 8-bit scale are plotted against sample number along one line. As expected, it can be seen that band 4 shows the largest and band 7 the smallest residual signal. However, not all of the signal received from the shadow is due to path radiance. Measurements of reflected radiation of the surface of Red Lake Playa, Arizona, made with the PFRS during passage of a fair-weather cumulus cloud, about 1 km in diameter, showed that in band 4 the reflected sky and scattered cloud radiation in the shadow amounted to about 25% of the unshadowed value. Therefore, it cannot be assumed that the atmospheric-scattering term is the cloud shadow value.

An approximate model can be constructed to determine both the reflected skylight and the atmospheric-scattering terms. Let

$$K_{XA} = A + N_X \text{ (outside shadow)}$$
$$K_{XB} = B + N_X \text{ (inside shadow)} \quad (3)$$

where K_{XA} and K_{XB} are the spacecraft-measured values of brightness outside and inside a cloud shadow in band X, A and B are the respective contributions from the surface, and N_X is the path radiance term. Assuming that the reflectivities of the adjacent shadowed and unshadowed regions are equal and that the radiance from the shadowed and unshadowed areas differ by some multiplication value, i.e.,

$$A = c_X B \quad (4)$$

where c_X represents the relative contribution from the reflected skylight in band X, Eq. (3) gives

$$N_X = \frac{K_{XA} - c_X K_{XB}}{1 - c_X} \quad (5)$$

Assuming a uniform N and c over the region of interest in an ERTS picture and using varying values of K_{XA} and K_{XB} for different cloud shadows, c can be determined by regression analysis. Relatively consistent values of N have been obtained using a minimum of seven separate cloud shadows in two separate areas: Goldfield, Nevada (ERTS E-1072-18001), and the Coconino Plateau (ERTS E-1014-17373). The values for N_X in ERTS E-1014-17373 are given in Table II-2.

This simple model appears to break down for band 7 because it is possible to find lower DN values for bodies of water than in cloud shadows. Those values are as low as 6 in NASA picture ERTS E-1014-17375. This value was used

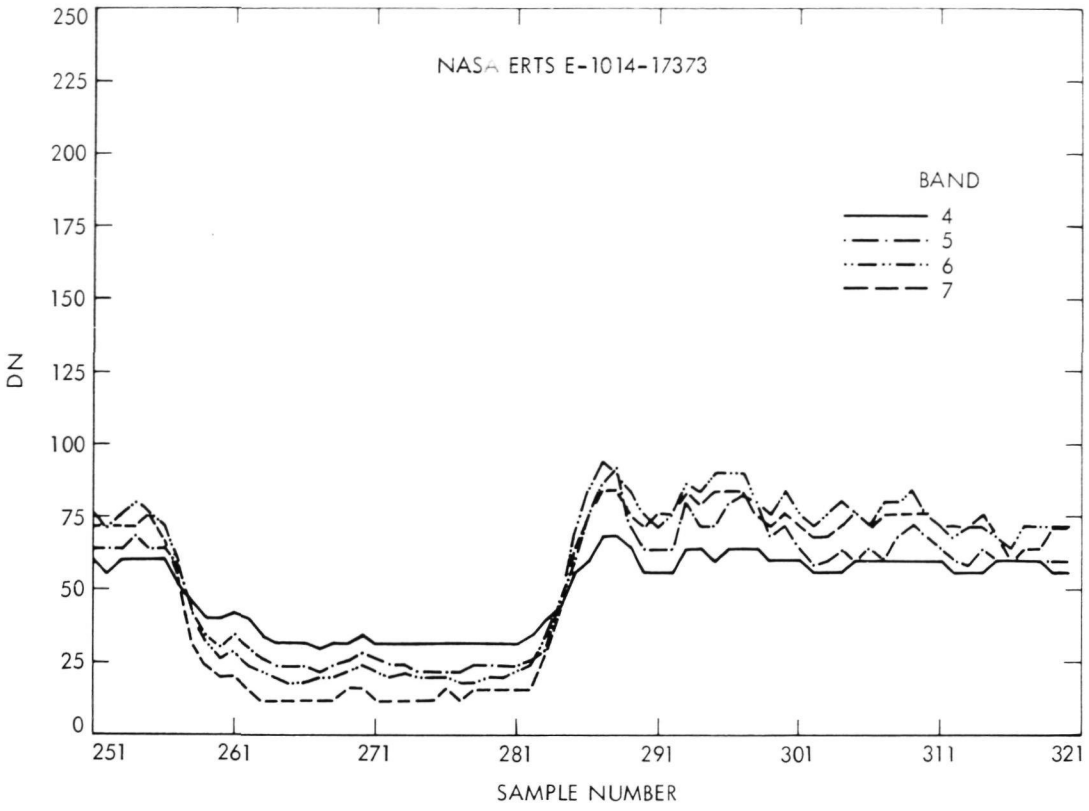

Fig. II-5. Brightness values (DN) along an image line crossing a cloud shadow

Table II-2. Values for N_X in NASA picture ERTS E-1014-17373

Band	$N_X(DN)$	c_X
4	24	0.24
5	13	0.16
6	10	0.10
7	14	0.00

in calculating M_7 in Table II-1. In spite of the over-simplicity of the model, this exercise does emphasize the fact that taking the lowest DN values in cloud shadows to be the atmospheric contribution is not necessarily correct.

It has been shown that a reasonable correlation exists among ERTS brightness values and in situ spectroscopic measurements. If this correlation is sufficiently good, then it should be possible to determine which combination of ERTS bands will produce the best discrimination among geologic units of interest.

As discussed in Sections III and IV, color images formed from band ratio combinations seem to provide the best contrast among geologic units, particularly in areas where the albedo contrast is low. Empirical studies were made of numerous combinations of computer-processed images, as

Table II-3. Ratio contrasts for the six ERTS band ratios

Unit	Ratio					
	4:5	4:6	4:7	5:6	5:7	6:7
Pkα2	0.786	0.760	0.812	0.967	1.033	1.069
Pkα3	0.784	0.723	0.732	0.922	0.934	1.012
Pkα4	0.783	0.745	0.785	0.951	1.003	1.054
Pkα5	0.785	0.769	0.759	0.979	0.967	0.987
Pkα6	0.803	0.796	0.796	0.991	1.057	1.067
Moenkopi	0.782	0.783	0.831	1.002	1.063	1.061
Basalt	0.879	0.857	0.914	0.975	1.040	1.067
$\overline{x}$	0.800	0.776	0.804	0.970	1.013	1.045
$\sigma/\overline{x}$	0.044	0.055	0.073	0.027	0.048	0.031

discussed in Section VI. For the Coconino Plateau the ratios 4:5, 4:7, and 5:7 often appear superior in separating units of interest.

Eschewing statistical rigor, a quantitative measure of contrast among geologic units can be determined by calculating the standard deviations of the ratio values for all units of interest. In order to compare contrast among different ratio pairs the quantity $\sigma/\bar{x}$, the standard deviation divided by the mean, is a more appropriate quantity. Tables II-3 and II-4 list the ERTS image values and the PFRS values, respectively, along with the values for $\sigma/\bar{x}$. The PFRS spectra used in calculating the values in Table II-4 are shown in Fig. II-6. The three ratios (4:6, 4:7, 5:7) that contain the greatest apparent contrast among units in the ERTS scene were also predicted by PFRS measurements. The only major disagreement is the relative merit of 5:6. A possible explanation is that in the calculation of the PFRS average reflectance within an ERTS band, band 5 falls within the first segment and band 6 within the second segment of the filter wheel (see Appendix E). The overlap error ranges between 0 and 3% in reflectance, enough to cause an artificially high 5:6 ratio contrast.

As mentioned previously, in practice the ratio image 4:5 is found to be useful, even though it ranks fourth in Table II-3, because vegetation is most easily distinguished in this ratio image. If vegetation values had been introduced into Tables II-3 and II-4, the relative rank of 4:5 would have risen.

It seems, therefore, that field spectroscopic data can be used to predict which band ratios can be used most profitably in separating targets of interest from the background. This result has bearing on the selection of optimum bands for geologic mapping in future satellite systems. A statistically rigorous treatment of these data and the contrast selection method will be subjects of a future study.

Table II-4. Ratio contrasts for the six ERTS band ratios using PFRS data

Unit	Ratio					
	4:5	4:6	4:7	5:6	5:7	6:7
Pkα2	0.759	0.646	0.568	0.852	0.749	0.879
Pkα3	0.720	0.579	0.516	0.804	0.717	0.892
Pkα4	0.752	0.714	0.639	0.949	0.849	0.895
Pkα5	0.715	0.538	0.494	0.752	0.691	0.919
Pkα6	0.753	0.662	0.608	0.879	0.807	0.919
Moenkopi	0.608	0.518	0.472	0.853	0.776	0.910
Basalt	0.732	0.651	0.604	0.890	0.826	0.928
$\bar{x}$	0.719	0.615	0.557	0.854	0.774	0.906
$\sigma/\bar{x}$	0.073	0.117	0.115	0.074	0.075	0.020

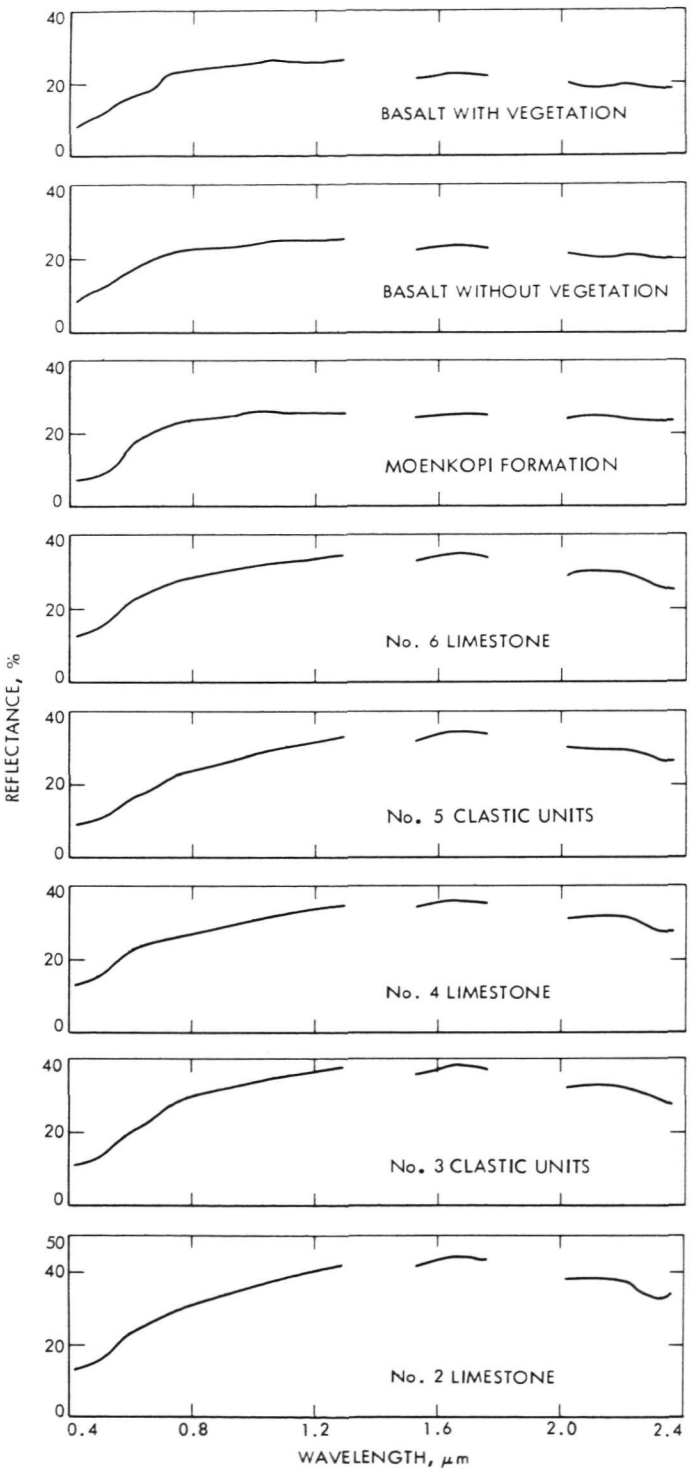

Fig. II-6. Average PFRS spectra of geologic units on the Coconino Plateau outlined in Fig. II-4

References

II-1. Hunt, G. R., and Salisbury, J. W., "Visible and Near-Infrared Spectra of Minerals and Rocks: I. Silicate Minerals," *Modern Geology*, Vol. I, pp. 283–300, 1970.

II-2. White, W. B., and Keeter, K. L., "Selection Rules and Assignments for the Spectra of Ferrous Iron in Pyroxenes," *American Mineralogists*, Vol. 52, pp. 1508–1514, 1967.

II-3. Hunt, G. R., Salisbury, J. W., and Lenhoff, C. J., "Visible and Near-Infrared Spectra of Minerals and Rocks: III. Oxides and Hydroxides," *Modern Geology*, Vol. 2, pp. 195–205, 1971.

II-4. Rowan, C., Wetlaufer, P. H., Goetz, A. F. H., Billingsley, F. C., and Stewart, J. H., "Discrimination of Rock Types and Altered Areas in Nevada by the Use of ERTS Images," *U. S. Geol. Survey Prof. Paper 883*, 1974.

II-5. Watson, R. D., "Spectral and Bidirectional Reflectance of Pressed vs. Unpressed Fiberfrax," *Applied Optics*, Vol. 10, p. 1685, 1971.

II-6. Norwood, V. T., Fernelia, L. R., and Tadler, G. A., *Final Report, Vol. I. Multispectral Scanner System for ERTS*, Hughes Aircraft HS324-5214, 1972.

II-7. Rogers, R. H., and Peacock, K., "A Technique for Correcting ERTS Data for Solar and Atmospheric Effects." *Symposium on Significant Results Obtained from Earth Resources Technology Satellite-1*, NASA SP-327, pp. 1115–1122, Washington, D. C., 1973.

III. Computer Image Processing

F. C. Billingsley, A. R. Gillespie, and A. F. H. Goetz

A main objective of the ERTS investigation was to study methods for extraction and display of the most significant data from the ERTS images and apply them to the geologic mapping problem. To convert a picture into an analytic tool for research requires the use of "image processing," the generic name of a set of procedures designed to prepare an image for effective human viewing and interpretation, to improve the fidelity of an image to the imaged scene, and to extract statistical or other information from an image.

Whitaker (Ref. III-1) used film methods in one of the earliest attempts to discriminate rock units in lunar pictures on the basis of spectral reflectivity. In the apparently uniform regolith of Mare Imbrium, two basaltic lava flows were distinguished in a black and white composite produced by masking blue and infrared telescopic photographs. Using a similar approach, Billingsley et al. (Ref. III-2) manipulated digitized multi-band telescopic photographs in the computer, and Goetz et al. (Ref. III-3) devised a method for analyzing Apollo orbital multi-band pictures. Yost et al. (Ref. III-4) practiced an extension of these techniques using a three-band photographic ratio method. During the same period, Vincent and Thompson (Ref. III-5) ratioed aircraft scanner images taken in the near-infrared spectral region to discriminate among terrestrial lava flows.

Although image enhancement methods are possible using the ERTS film products (Ref. III-6), Rowan et al. (Ref. III-7) found that, in order to extract the maximum information from an ERTS multi-spectral scanner (MSS) image, it was necessary to employ computer image processing with digital data, which can be taken from film by scanning densitometry or taken directly from MSS computer-compatible tapes (CCTs).

A digital image is a sampled scalar field representing scene radiance. Local scene radiance, as measured by the sensing instrument, is encoded as an integer or digital number (DN).

The MSS encodes the log of the scene radiance in 6 binary bits of information, which is expanded to a 7-bit linear scale before CCT recording. Seven bits encompass 128 gray levels or DN. At the Image Processing Laboratory (IPL) at JPL the data are additionally scaled to occupy 8 bits, or 256 gray levels. The digital image is stored, as it is acquired, as a series of digital numbers on tape or on a magnetic disk rather than as an actual image. The representation of the image as a scalar field is physically accomplished only during production of a film display.

Digital image processing consists of applying an algorithm or function to each stored DN and accumulating a new image from the processed data, as expressed by Eq. (1), which applies a convolution filter to an image.

$$DN'_{ij} = \sum_{n=-N}^{N} \sum_{m=-M}^{M} W_{nm} DN_{i+n,j+m} \quad (1)$$

where n and m are integers, W is a weight matrix, DN_{ij} is the input DN at positions i and j in the sampled field, and DN_{ij}' is the DN in the filtered picture.

As another example of a simple digital process, the image can be rescaled so that the contrast is increased. Assume that the brightness range in the scene is from $DN = 10$ to $DN = 110$ and that this range is to be expanded to fill all gray levels of the dynamic range of the playback device. The linear transformation

$$DN'_{ij} = 2.55\ DN_{ij} - 25.5 \quad (2)$$

causes $DN = 10$ to be mapped to $DN' = 0$ (= black), and $DN = 110$ to be mapped to $DN' = 255$ (= white). This and other contrast manipulations are called "stretches."

Digital images are converted to pictures for human interpretation by using the encoded radiance (DN) to modulate a light source that scans a photographic film. The exposed picture, when developed, superficially resembles a normal photographic image. However, in a normal photographic image, scene detail is represented by continuous changes in the number density of grains in the emulsion. In a photographic representation of a digital image, scene detail is represented by changes in average brightness of small areas in the emulsion (picture elements, or pixels). Brightness of the pixels is controlled by the DN in the digital image.

Alternatively, a digital image can be displayed as a computer listing, actually printing the DN values in a matrix. However, because a single ERTS MSS frame (all four bands) is composed of more than 30,000,000 numbers, requiring 17,000 sheets of printout for display, this approach has limited value.

Digital image processing techniques consist of four procedures:

(1) *Rectification*, or compensation for geometric and radiometric distortions introduced by the imaging instrument, and for elimination of systematic or coherent noise.

(2) *Cosmetics*, or removal of random noise or imperfections in data.

(3) *Analysis*, which includes data extraction and image comparison.

(4) *Display*, or enhancement for visual interpretation.

These procedures are discussed in more detail in the subsequent parts of this section and in Appendix B.

A. Rectification

1. Geometric Rectification

The purpose of geometric rectification is to compensate for geometric distortions introduced by the imaging instrument. The most significant distortion encountered in ERTS images is caused by rotation of the Earth during the 25 s required to scan a scene. The trace of each scan line on the Earth is carried by Earth's rotation due east, so that the trace of the entire frame is skewed to approximate a parallelogram. The skew of the parallelogram is a function of geographic latitude, but is typically about 3°. This distortion in the raw images is corrected by displacing each scan horizontally and adjusting the aspect ratio, or the ratio between vertical and horizontal pixel spacing, to ensure the correct shape of the image.

Geometric rectification also is required to compensate for the motion of the Earth during each scan as opposed to each frame, variations in spacecraft attitude, and scale normalization, all of which are systematic distortions and relatively simple to correct for if properly identified. However, images acquired during attitude-correction maneuvers may have local geometric distortions that are difficult to identify. In that case, local distortion must be identified by comparing locations of features in the image with the same features in another correct image, or map.

Once identified, geometric distortions are removed by using a "resampling" process. During resampling, the location of each pixel of the geometrically correct output picture is computed in the distorted input picture. The DN of that output pixel is interpolated from the DN of the pixels adjacent to the specified location in the input picture.

Another type of geometric distortion is introduced by degradation of high spatial-frequency response in the imaging instrument. Any imaging instrument with a finite sensing element or optical system will lessen the sharpness of features.

Typically, the image of an impulse (e.g., a star) has a nominally gaussian intensity distribution called the "point-spread function" (PSF). A sampled scene can be considered to be composed of an array of impulses; the image of that scene is considered to be constructed by the superposition of an array of gaussian intensity distribu-

tions, which is equivalent to the convolution of the scene and the PSF. The imaging system acts as a low-pass filter whose spatial-frequency response is displayed by the Fourier transformation (FT) of its point-spread function. The PSF can be measured in practice by constructing the FT of an impulse or other sharp feature discernible in an image.

To achieve the correct frequency response, a convolution filter whose FT is the reciprocal of that of the PSF can be theoretically constructed. This actually is unreasonable because as the FT of the PSF goes to zero at high frequencies, the FT of the filter goes to infinity. Therefore, the FT of the filter is modified so that its amplitude drops to zero at the Nyquist frequency (Ref. III-8). This filter can be applied in the frequency domain or in the spatial domain. The result of compensating for frequency-response degradation in this way is shown in Fig. III-1. Because random-impulse type noise may have the same amplitude at all frequencies (the FT of an impulse in a discretized system is constant at all frequencies out to the Nyquist frequency) and because the amplitude of the signal, like that of the PSF, decreases as frequency increases, the signal-to-noise ratio is lowest at high frequencies. The filter increases the amplitude most at high frequencies; thus, the noise is also increased. This effect can be suppressed by dropping the amplitude of the FT of the filter at high frequencies, although there is a tradeoff between image restoration and noise suppression that must be considered separately (see Appendix B).

Before digitally comparing images taken at different times or through different instruments, it is often necessary to force the scene geometry to conform. When camera and scene positions and orientation defining image geometry are used to create a geometric function that will map into cartographic format, the process is called "projection." Because ERTS MSS data already are in an approximately cartographic format, projection is not necessary. However, registration is important if ERTS pictures taken of the same scene at different times are to be compared. This is especially true with features in the "sidelap" region, which is the part of the scene imaged in consecutive revolutions (orbits), with the orbit traces about 150 km apart. (Distance and amount of sidelap vary with latitude.) Obviously, parallax is a major cause of local image misregistration in such pictures. Because parallax is scene-dependent, scene topography must be accurately modeled to compensate for it. This is difficult and has not been achieved successfully, at least on a satisfactory production basis. Thus, registration must be achieved by identifying pixel displacements necessary to cause local scene coincidence for several identifiable features over an image pair, which may be done automatically using cross-correlation techniques. However, if both images contain coherent noise (six-line striping), the program tends to register the noise rather than the scene detail. The actual geometric transformation is accomplished by "resampling," as discussed above and in Appendix A.

2. Radiometric Rectification

Radiometric rectification is a process that compensates for nonlinearities in the response of the MSS to scene radiance. An absolute calibration of image DN to scene radiance cannot be achieved, as more complete knowledge is required of the sensing instrument's response than is possible with the existing MSS design. Relative calibration is provided by an illuminated gray scale that is scanned periodically during image acquisition. Only 6 out of about 500 bytes of calibration information are actually available to the users of CCTs, and these are arranged in three pairs as a precaution against bit errors. One pair is extracted close to the saturated part of the gray scale, and may not be reliable (see Ref. III-9).

These calibration data are used by Goddard Space Flight Center (GSFC) to define a linear instrument response, and data are corrected to scene radiance using that equation. Thus,

$$DN' = aDN + b \tag{3}$$

The assumption of linearity is not justified, as indicated by the problem of striping. Although an attempt was made to fit a second-order polynomial to the calibration data, insufficient points were available to make the fit meaningful. Subsequent decalibration using the second-order polynomial did not completely remove the striping. Residual noise can be attributed to truncation during successive computer processes, or it can be introduced after data are acquired (e.g., during transmission).

Absolute calibration of ERTS images using ground spectra is possible if homogeneous regions, on the scale of 10 pixels, of different reflectivities can be occupied during overflight. A transfer function relating DN to ground radiance can be specified, and the image can thus be rectified to compensate for the instrument and also atmospheric effects. However, the difficulty of both finding and occupying homogeneous sites within a study area close to the time of overflight is sufficient to preclude widespread use of this technique (see Appendix E). Although successful radiometric rectification causes artifacts such as striping to disappear, complete removal of striping is generally not possible. In severe cases,

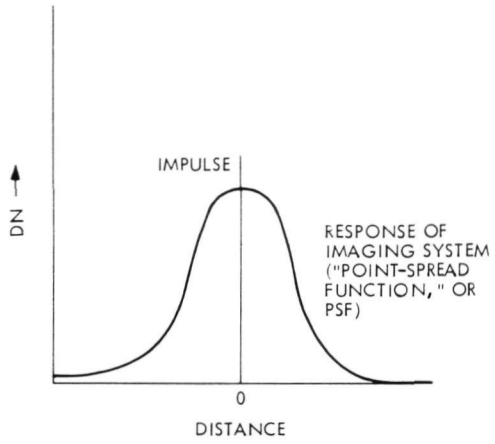

THE RESPONSE OF MOST IMAGING SYSTEMS TO AN IMPULSE RESEMBLES A GAUSSIAN DISTRIBUTION

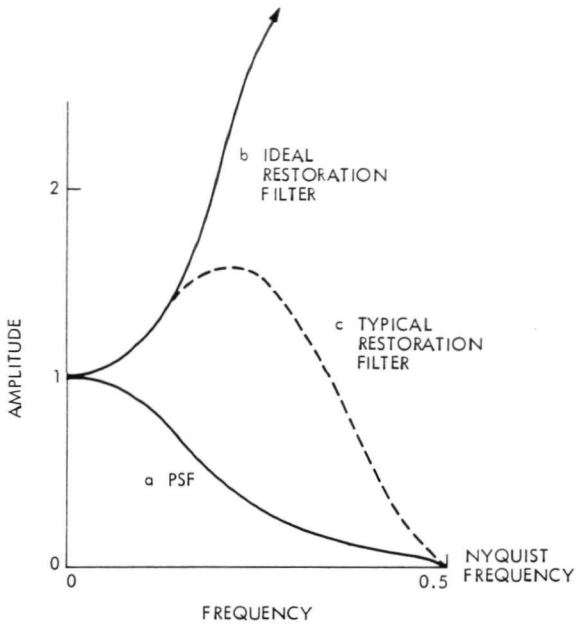

FOURIER TRANSFORM OF THE PSF (a), INDICATING RESPONSE OF IMAGING SYSTEM AT DIFFERENT SPATIAL FREQUENCIES, AND FILTERS DESIGNED TO COMPENSATE FOR IT (b, c)

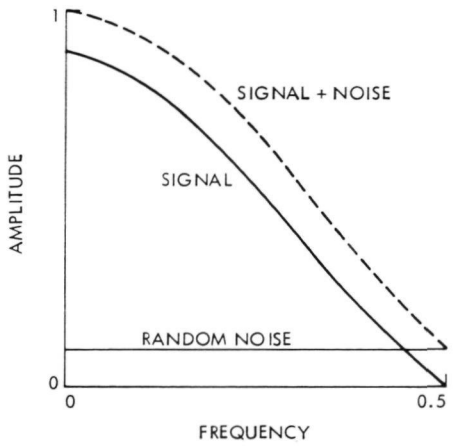

FOURIER TRANSFORMATION OF AN IMAGE (ONLY ONE DIMENSION IS DEPICTED)

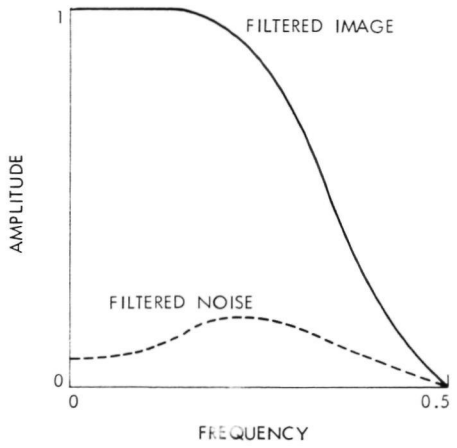

FOURIER TRANSFORMATION OF AN IMAGE AFTER FILTERING TO RESTORE FREQUENCY RESPONSE. RANDOM NOISE SPECTRUM AFTER FILTERING RESEMBLES THE FILTER SPECTRUM

Fig. III-1. Frequency-response restoration through Fourier filtering. Note the increased resolution and noise after filtering

cosmetic procedures can be used to remove unwanted noise.

B. Cosmetics

Cosmetics procedures are designed to remove unwanted noise or image defects and systematic noise of uncertain origin or exceptional severity. In ERTS data, cosmetic routines are most frequently used to remove striping and to compensate for dropped lines.

Several approaches can be used to remove striping. It is possible to compute a histogram (DN frequency distribution or probability-density function, PDF) for each of the six sensors contributing data to each image. By assuming that a reference sensor is selected, the histograms of the other sensors can be modified to cause the means and standard deviations to match using a linear equation to "stretch" the suspect data:

$$DN'(k,l)_{ij} = a(k,l)\ DN(k,l)_{ij} + b(k,l) \qquad (4)$$

where k is a sensor, l is an image channel, i is a sample, and j is a line. However, this approach is not totally successful, presumably because the offending sensor light-transfer characteristic is nonlinear.

It is possible to force empirically five sensor histograms to resemble a sixth (or six histograms to resemble their average) nonlinearly. This is accomplished by redistributing DNs in such a way as to enforce the criterion for all n, $0 \leq n \leq 255$:

$$\sum_{DN=0}^{n} f_k(DN) = \sum_{DN=0}^{n} f_{STD}(DN) \qquad (5)$$

where f is frequency; the subscript k is a sensor, $1 \leq k \leq 6$; and the subscript STD refers to the reference histogram. This technique also yields unsatisfactory results, possibly because some striping may be scene-dependent; that is, the sensor transfer function may be a function of the recent history of the sensor.

Spatial filtering also can be used to remove striping. Because striping is correlated with certain sensors, it is repeated in the image every six lines; thus, striping is coherent. A power spectrum of an image with striping reveals high amplitudes at frequencies of 1/6, 1/3, and 1/2 cycles per pixel vertically. This coherent noise can be removed by a convolution filter in the spatial domain or by identifying and removing noise spikes in the FT and retransforming the clean transform to produce a smooth image (see Ref. III-10).

Alternatively, a simple high-pass convolution filter applied line by line can be used to display only deviations from a local sensor mean. This technique, although effective, simple, and inexpensive, destroys image radiometry and is thus unsatisfactory for some purposes.

Computer algorithms can also be constructed to recognize and interpolate across bit errors, or to identify lines that are missing or that cannot be read from tape. Missing or dropped lines are especially damaging if different channels of otherwise registered data are to be compared digitally.

C. Analysis

Analytic programs and procedures increase the information (as contrasted to data) contained in an image or reveal information that was implicit only in the original image. This new information is obtained by application of mathematical formulas or by correlation of image information with data derived from another source.

Four basic approaches are used in image analysis:

(1) *Extraction of statistical information from an image.* Local means, standard deviations, or PDFs can be extracted from an image and displayed on a line printer. Similarly, the local covariance between different spectral bands can be computed, or correlations between image brightness and topography or any other mappable variable can be computed.

(2) *Representation of statistical measures as an image.* Any statistical quantity can be scaled to fit the dynamic range of a digital image, and thus displayed. For example, the variance of a local area consisting of a pixel and its eight nearest neighbors can be computed and scaled for output in an image comprising the variance of local areas centered about each pixel. Similar measures of image "texture" have been demonstrated to increase accuracy of bayesian classifiers when used as an additional channel of input (Ref. III-11).

(3) *Multi-image processing techniques.* One way of increasing information obtainable from an image is to use more than one spectral channel of input, or to monitor a scene over a period of time. Simple procedures include image differencing, which is a useful procedure for temporal comparisons, and ratioing, which is useful for spectral comparisons.

Rotation of the multi-spectral vector can be used to increase feature discriminability within an image (Figs. III-2 and III-3), and can be used to reduce the

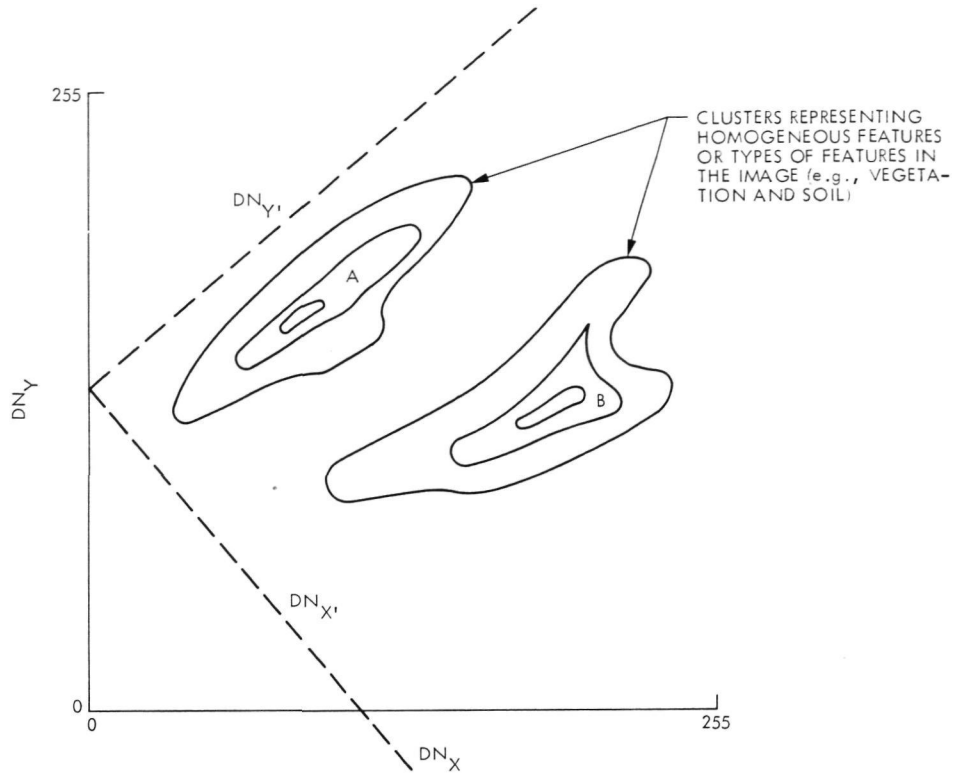

Fig. III-2. Contour map of two-dimensional PDF depicting frequency of occurrence of DN couplets in image channels x and y

number of channels required to adequately describe a scene (see Fig. III-3). The new axis is chosen to maximize the separation of information clusters projected onto it.

Ratioing (see Section VI) is an important tool for selective enhancement of spectral differences and removal of topographic information from the scene. There are six possible unique ratios of the four ERTS spectral bands. For presentation, three ratios are chosen, correctly stretched, and combined into a color image. By this method, in our experience, up to a five-fold increase in apparent scene contrast is possible because the topographic information clutter has been removed. The best color ratio composite displays the maximum separation among spectral reflectivity units. The human interpreter can then clarify the units based on a number of parameters such as spatial context, which are not available to computer classification routines. This method seems to be superior to direct computer classification, as discussed in Section VI.

(4) *Classification.* Classification is a process designed to construct thematic maps from multi-channel images, based on the observation that DN *n*tuplets from a thematically homogeneous area tend to congregate in clusters in an *n*-space where the axes depict the intensity, or DN, of the various channels. The clusters shown in Fig. III-2 are an example of this in a two-dimensional space. If the clusters that comprise an image can be identified, then the proximity of a given DN *n*tuplet to the various cluster centers can be measured. The boundary surfaces among clusters are based on statistical decisions. Much information has been published in the area of classification techniques (Refs. III-11 through III-13). Classification procedures usually require the analyst to define homogeneous areas in the image. These training areas are used to construct the spectral clusters to which each DN *n*tuplet in the image is compared. The output picture indicates, pixel by pixel, to which cluster the local DN *n*tuplet belongs.

D. Display

Display procedures are designed to present to the human viewer as much information as possible in a convenient useful format. Although many techniques are available, the one considered most basic is contrast modification, or "stretching." This procedure reassigns

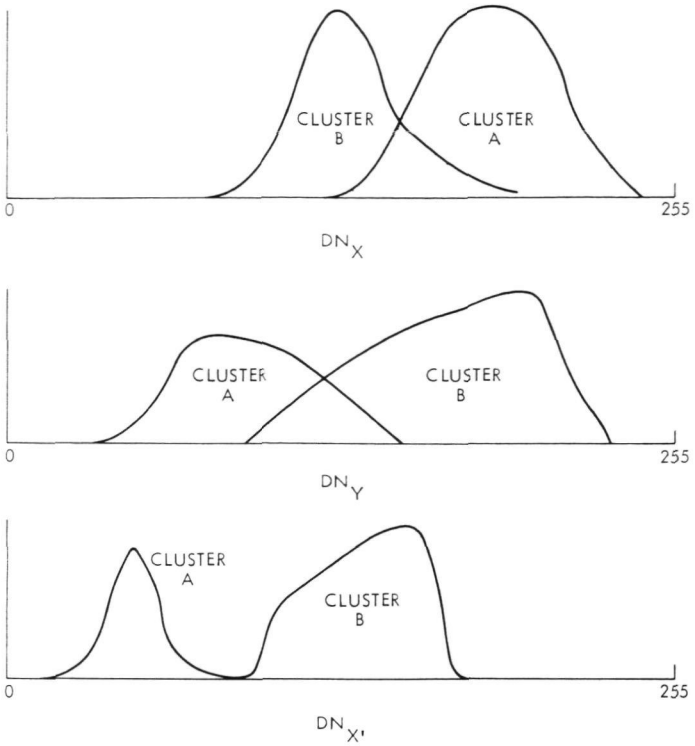

Fig. III-3. Single-channel PDFs. Note that x ′ has better separation than either original channel. The single-channel PDF is the projection of the two-dimensional distribution onto a single axis

input DN to new gray levels according to one of several schemes, with the goal of utilizing the entire dynamic range of the display device to convey only those portions of the image dynamic range which actually contain data (see Eq. 2). Many linear and nonlinear stretches are available. For instance, if the analyst recognizes that the most interesting or significant information in an image is contained in dark regions, he might wish to increase its contrast at the expense of contrast in brighter, less important, regions. He would apply either a square root or log "stretch" to accomplish this.

Usually a linear stretch is necessary to pack the data into the dynamic range of the display. In the examples used previously, the output of a decimal log stretch would fall from $DN = 0$,(log 1), to $DN = 2.41$,(log 255). Thus the stretch actually used could be:

$$DN' = \frac{255}{\log(255)} \log(DN) \tag{6}$$

which maps 1 to 0 and 255 to 255.

Spatial filtering, already discussed in the context of image rectification, also is a significant part of image display. Typically, an analyst may wish to enhance local contrast so that differences from the local average brightness are displayed. This is accomplished by a filter which, in effect, subtracts the local average DN from the local DN (high-pass filter). Figures III-4 and 5 show the effects of filters of different sizes; the larger the filter, the larger the area for which the local average DN is computed and the less severe the filter.

Color is an important display tool. The human eye easily discriminates many more hues than gray levels. Thus, a single color image is capable of conveying more information than a single black and white picture or the set of three black and white transparencies from which the color picture is made.

Color images, as well as single black and white images, can be modified for optimum display. The simplest technique is to stretch the three input pictures individually before the creation of the color picture. Alternatively, it is possible to decompose the image triplet into color coordinates (hue, saturation, and intensity) or into standard Internationale de l'Éclairage (CIE) chromaticity coordinates (x, y, and intensity). Contrast modification is performed on the new images, which are subsequently processed to form into the blue, green, and red images required for color construction. A more detailed discussion of the individual routines developed for rectification, analysis, and display is presented in Appendix C.

UNFILTERED PICTURE

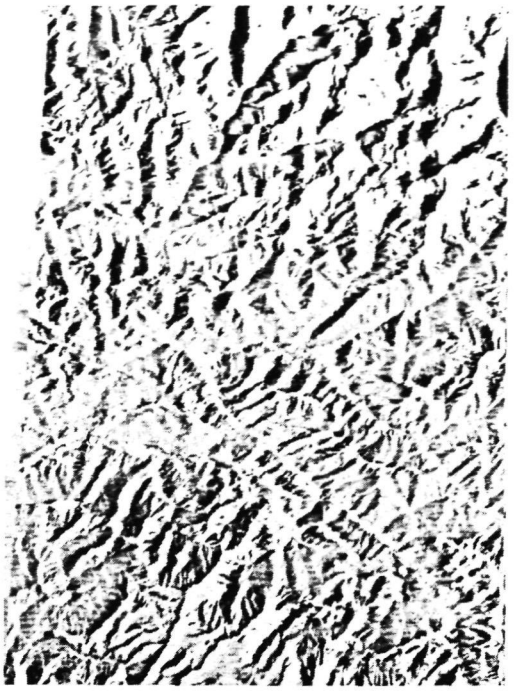

PICTURE FILTERED USING 1-LINE-BY-31-SAMPLE FILTER KERNEL

PICTURE FILTERED USING 31-LINE-BY-1-SAMPLE

PICTURE FILTERED USING 1-LINE-BY-101-SAMPLE FILTER KERNEL. THE LARGER THE FILTER KERNEL, THE SMALLER IS THE INCREASE IN AMPLITUDE AT HIGH SPATIAL FREQUENCIES

Fig. III-4. Directional high-pass convolution filtering

PICTURE FILTERED USING 7-BY-7-SAMPLE KERNEL

PICTURE FILTERED USING 15-BY-15-SAMPLE KERNEL

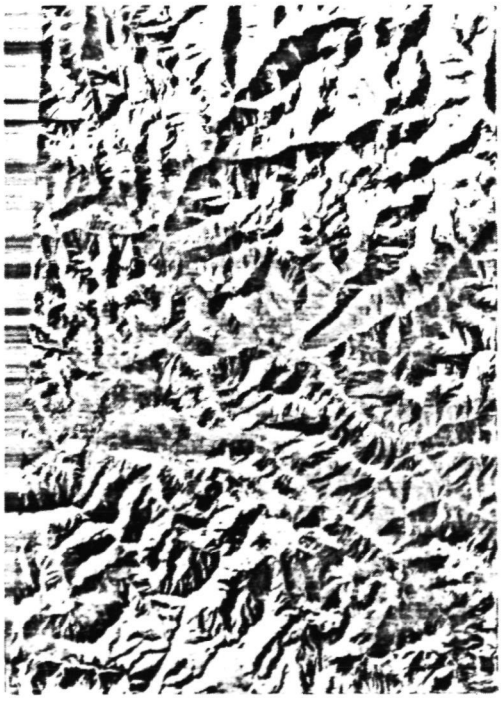

PICTURE FILTERED USING 31-BY-31-SAMPLE KERNEL

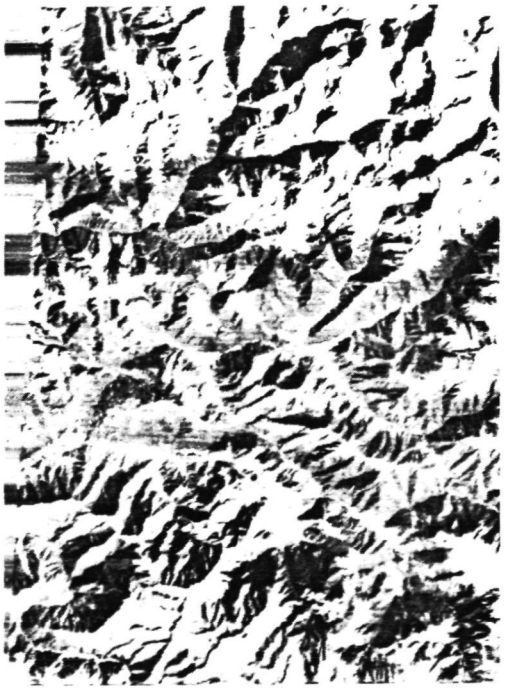

PICTURE FILTERED USING 101-BY-101-SAMPLE KERNEL

Fig. III-5. Nondirectional high-pass convolution filtering

References

III-1. Whitaker, E. A., "Colors and the Meso-structure of the Maria," in *Ranger VII, Part II. Experimenters' Analyses and Interpretations*, Technical Report 32-700, pp. 29–39, Jet Propulsion Laboratory, Pasadena, Calif., 1965.

III-2. Billingsley, F. C., Goetz, A. F. H., and Lindsley, J. N., "Color Differentiation by Computer Image Processing," *Photographic Science and Engineering*, Vol. 14, p. 28, 1970.

III-3. Goetz, A. F. H., Billingsley, F. C., Yost, E., and McCord, T. B., "Apollo 12 Multi-spectral Photography Experiment," in *Proceedings of the Second Lunar Science Conference, Supp. 2, Geochem. Cosmochim. Acta*, Vol. 3, p. 2301, 1971.

III-4. Yost, E., Anderson, R., and Goetz, A. F. H., "Isoluminous Additive Color Method for the Detection of Small Spectral Reflectivity Differences," *Photographic Science and Engineering*, Vol. 17, pp. 177–182, 1973.

III-5. Vincent, R. K., and Thompson, F. J., "Rock-Type Discrimination From Ratioed Infrared Scanner Images of Pisgah Crater, California," *Science*, Vol. 175, p. 986, 1972.

III-6. Liggett, M. A., Childs, J. F., and Ehrenspeck, H. E., *A Reconnaissance Space Sensing Investigation of Crustal Structure for a Strip From the Eastern Sierra Nevada to the Colorado Plateau*, ERTS Final Report, Cyprus Mines Corp., 1974.

III-7. Rowan, L. C., Wetlaufer, P. H., Goetz, A. F. H., Billingsley, F. C., and Stewart, J. H., "Discrimination of Hydrothermally Altered Areas and of Rock Types Using Computer Enhanced ERTS Images, South-central Nevada," *U. S. Geol. Survey Prof. Paper*, in press.

III-8. Nathan, R., *Digital Video Data Handling*, Technical Report 32-877, Jet Propulsion Laboratory, Pasadena, Calif., 1966.

III-9. *Earth Resources Technology Satellite Data Users Handbook*, Appendix G, NASA Goddard Space Flight Center, Greenbelt, Md., 1972.

III-10. Billingsley, F. C., and Goetz, A. F. H., "Computer Techniques Used for Some Enhancements of ERTS Images," *Symposium on Significant Results Obtained From Earth Resources Technology Satellite-1*, NASA SP-327, pp. 1159–1167, Washington, D. C., March 1973.

III-11. Haralick, R. M., and Shanmugam, K. S., "Combined Spectral and Spatial Processing of ERTS Images," *Symposium on Significant Results Obtained From Earth Resources Technology Satellite-1*, NASA SP-327, pp. 1219–1228, Washington, D. C., March 1973.

III-12. Landgrebe, D. A., *Systems Approach to the Use of Remote Sensing*, LARS Information Note 041571, Laboratory for the Application of Remote Sensing, Purdue University, Lafayette, Ind., 1971.

III-13. Duda, R. O., and Hart, P. E., *Pattern Classification on Scene Analysis*, Wiley, 1973.

IV. Geologic Investigations

A. The Bright Angel, Mesa Butte, and Related Fault Systems of Northern Arizona[1]

E. M. Shoemaker, R. L. Squires, and M. J. Abrams

Among the structural features of northern Arizona, the Bright Angel fault is perhaps one of the best known. Thousands of tourists hike along part of the Bright Angel fault each year as they descend from the south rim of the Grand Canyon into the inner gorge along the Bright Angel trail, or from the north rim along the Kaibab trail. It is not known how many of these visitors are aware that a fault has controlled the route of easiest descent and the course of Bright Angel Canyon, through which the Kaibab trail passes. It is clear, however, that the easy access into the Grand Canyon provided by these trails has led to close inspection of the fault by many geologists.

The Bright Angel fault was first described by F. L. Ransome (Ref. IV-A-1), who recognized that displacement on the fault had occurred during at least two widely separated periods of time: one Precambrian and one post-Paleozoic. The first map to portray the fault was a reconnaissance map of northern Arizona and New Mexico by N. H. Darton (Ref. IV-A-2), who also briefly described the fault and noted the two episodes of displacement. In 1914, a part of the fault lying within the Bright Angel quadrangle south of the Colorado River was mapped in detail by L. F. Noble (Ref. IV-A-3); although he contributed some important observations about the fault (see Refs. IV-A-4 and IV-A-5), the map was never published. In 1929, McKee described the Bright Angel fault in a short paper (Ref. IV-A-6).

The problem of multiple episodes of faulting on the Bright Angel and related faults attracted the attention of Maxson and Campbell (Ref. IV-A-7) as they worked on the ancient crystalline rocks of the Grand Canyon. Much later, Maxson published a detailed map of the Bright Angel quadrangle and described a complex history of displacement on the Bright Angel fault and on intersecting faults (Ref. IV-A-8). Most recently, Sears (Ref. IV-A-9), who has reinterpreted the history of displacement, remapped the Bright Angel fault where it cuts exposed Precambrian rocks.

The present writers became interested in the Bright Angel fault during a regional geologic investigation of the hydrographic basin of Cataract Creek, the principal drainage of the Coconino Plateau, which forms the south rim of the Grand Canyon. Starting from the southern boundary of the Bright Angel quadrangle, we traced the Bright Angel fault 30 km to the southwest. At this point the fault dies out, but other parallel faults continue to the

[1] Publication authorized by the Director, U.S. Geological Survey.

Fig. IV-A-1. ERTS-1 picture of Coconino Plateau showing Bright Angel and Mesa Butte fault systems (NASA picture ERTS E-1104-17382-5, Nov. 4, 1972)

southwest at least another 20 km. In this investigation we employed ERTS pictures taken from an altitude of 907 km. While studying these pictures, we noted a remarkably long zone or system of faults of which the Bright Angel fault is a member. From the center of the Cataract Creek region the fault system can be traced northeastward for at least 270 km. A parallel system of faults that lies about 50 km southeast of the Bright Angel system can also be recognized in the ERTS pictures (see Fig. IV-A-1). Some of the principal Cenozoic eruptive centers on the Coconino Plateau appear to be localized along these two fault systems.

At this stage in our investigation the evidence suggested that the two fault systems, which are observed primarily in Phanerozoic rocks, might be related to major ancient structures in the underlying Precambrian crystalline complex. To test this hypothesis we compiled a map of the faults in northwestern Arizona (Fig. IV-A-2) and compared this map with a residual aeromagnetic map of Arizona published by Sauck and Sumner (Ref. IV-A-10). About 60% of the fault map is based on published and unpublished maps. The remainder is based on new detailed and reconnaissance field mapping by us and by I. Lucchitta, using ERTS pictures and aerial photographs.

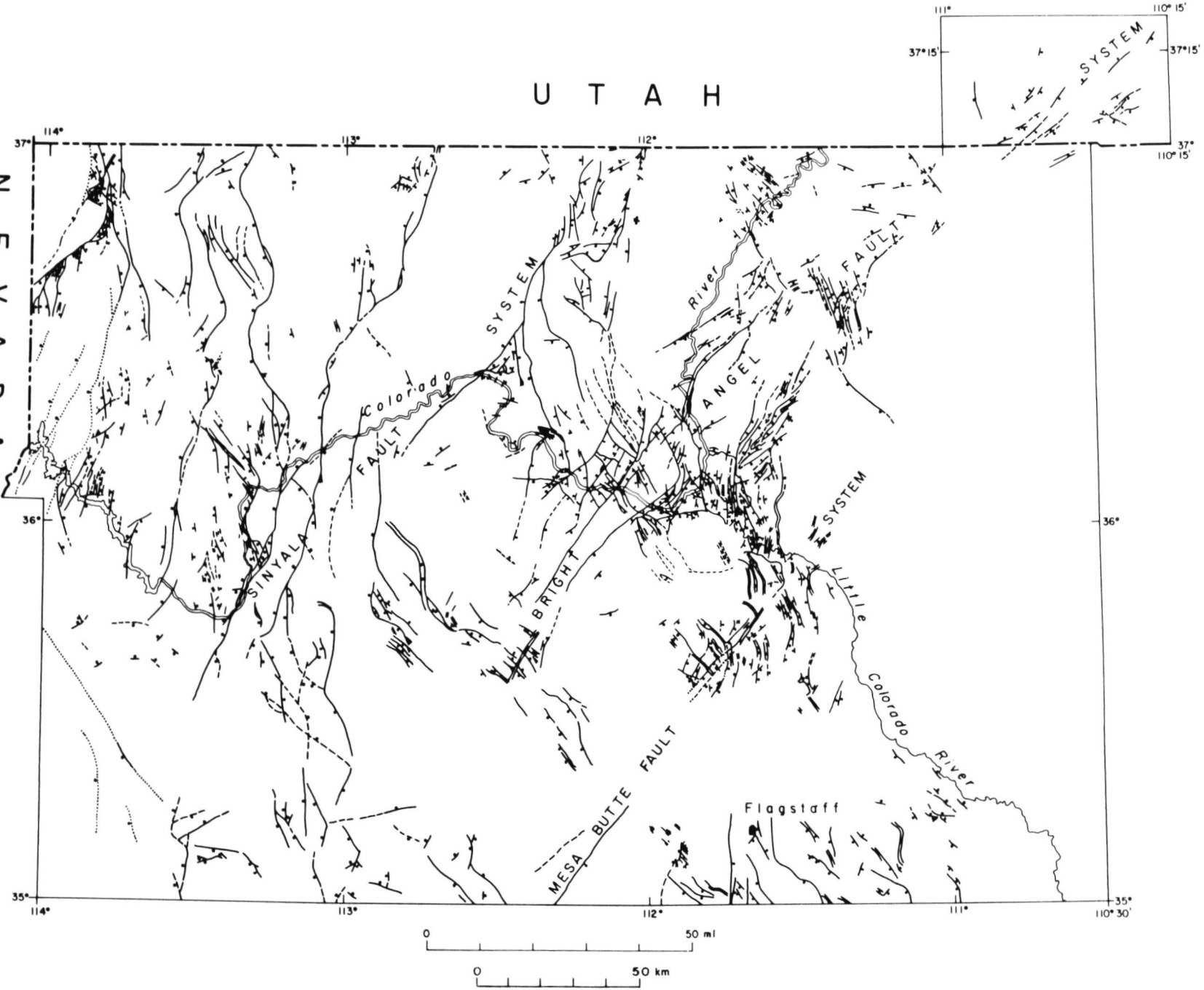

Fig. IV-A-2a. Map of faults in northwestern Arizona. Most faults shown are normal faults. Bar and dot on downthrown side of faults

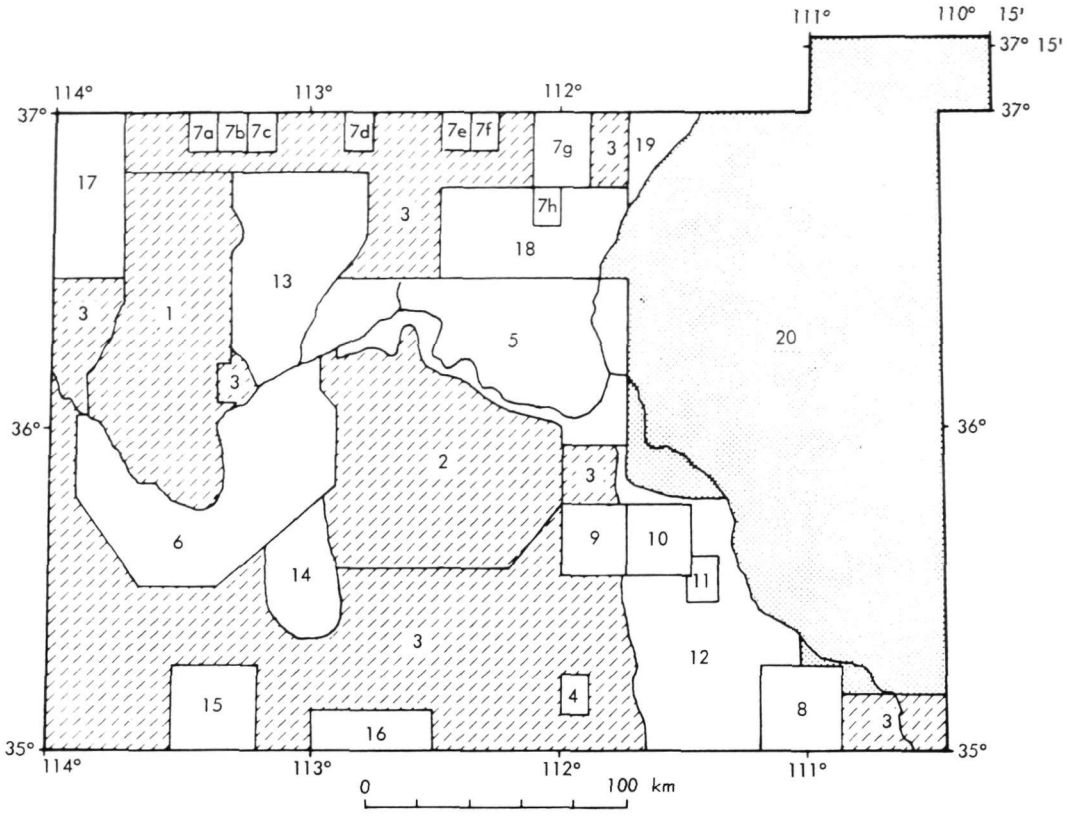

MAPPING UTILIZING ERTS-1 PICTURES

1. LUCCHITTA, I. (SEE REF. IV-A-48)
2. ABRAMS, M. J., AND SQUIRES, R. L., UNPUBLISHED MAP
3. SHOEMAKER, E. M., SQUIRES, R. L., AND ABRAMS, M. J., UNPUBLISHED RECONNAISSANCE

OTHER SOURCES OF DATA

4. HOLM, E. A., UNPUBLISHED MAP
5. MAXSON (SEE REFS. IV-A-59 AND IV-A-60)
6. TWENTER (SEE REF. IV-A-19)
7a. POMEROY (SEE REF. IV-A-61)
7b. MARSHALL (SEE REF. IV-A-62)
7c. MARSHALL (SEE REF. IV-A-63)
7d. PILLMORE (SEE REF. IV-A-64)
7e. MORRIS (SEE REF. IV-A-65)
7f. McQUEEN (SEE REF. IV-A-66)
7g. WELLS (SEE REF. IV-A-67)
7h. MARSHALL (SEE REF. IV-A-68)
8. SHOEMAKER (SEE REF. IV-A-69)
9. BROCK, M. R., HAYNES, D. D., POMERENE, J. B., PROSTKA, H. J., RINEHART, C. D., UNPUBLISHED MAP
10. ULRICH, G. E., AND BAILEY, N. G., UNPUBLISHED MAP
11. BABENROTH AND STRAHLER (SEE REF. IV-A-13)
12. COOLEY, M. E., UNPUBLISHED MAP
13. KOONS (SEE REF. IV-A-18)
14. BLISSENBACH (SEE REF. IV-A-30)
15. FUIS (SEE REF. IV-A-49)
16. KRIEGER (SEE REFS. IV-A-16 AND IV-A-70)
17. MOORE (SEE REF. IV-A-71)
18. HUNTOON (SEE REF. IV-A-72)
19. PHOENIX (SEE REF. IV-A-73)
20. COOLEY et. al. (SEE REF. IV-A-17)

Fig. IV-A-2b. Index to sources of information shown in Fig. IV-A-2a

Comparison of the pattern of faults with the aeromagnetic map revealed many features of interest. The subsequent paragraphs concern mainly the Bright Angel fault system and the parallel system of faults to the southeast, referred to here as the Mesa Butte fault system. Other fault systems are described briefly.

1. Bright Angel Fault System

The Bright Angel fault system extends as a continuous zone of northeast-trending normal faults from Cataract Creek on the southwest to the Echo Cliffs on the northeast. Beyond the Echo Cliffs, the system may be traced northeastward to the Monument upwarp in Utah as a more diffuse continuous zone of normal faults.

South of the Grand Canyon, the Bright Angel system comprises several distinct faults, each of which is tens of kilometers long. The Bright Angel and Vishnu faults are the principal members of the system (Figs. IV-A-3 and IV-A-4). Here the faults cross the Coconino Plateau, which is capped by Kaibab Limestone of Permian age. Maximum displacement of the exposed Permian rocks on each of the larger faults is about 100 m. On most faults, displacement is down to the southeast. The downthrown side generally exhibits reverse drag; narrow prisms of beds belonging to the Moenkopi Formation of Triassic age are preserved in a few places on the hanging wall. Stripping away of the easily eroded Moenkopi from much of the rest of the plateau has left relatively prominent fault-line scarps, formed by the upthrown resistant beds of Kaibab Limestone.

A curious feature of the Bright Angel fault system, which is well illustrated on the Coconino Plateau, is the tendency of individual faults to die out as they approach northwest-trending monoclines (Fig. IV-A-4). Two small monoclines lie athwart the Bright Angel fault system on the plateau. None of the individual faults in the system cross either of these monoclines.

The Bright Angel fault is one of the longest members of the entire fault system. It can be traced for a total distance of 65 km. At its northern end, the fault swings around from a northeasterly to a northerly strike and then dies out as it approaches the East Kaibab monocline (Fig. IV-A-4). A series of en echelon faults continues farther to the northeast along the main trend of the Bright Angel fault.

Displacement of Permian beds on the Bright Angel fault is down to the southeast, both on the Coconino Plateau and on the Kaibab Plateau. Where it crosses the Grand Canyon, however, a complex set of relationships may be observed along the fault in older beds, particularly the Precambrian rocks. The net displacement of beds belonging to the Grand Canyon Supergroup, of late Precambrian age, is up on the southeast. Their displacement is due primarily to one or more episodes of reverse faulting in late Precambrian time (Refs. IV-A-8 and IV-A-9).

Northeast of the East Kaibab monocline, along the projected trend of the main part of the Bright Angel fault, the narrow Eminence Break graben can be traced across the Marble Platform (FIg. IV-A-4), a stripped surface capped by the Kaibab Limestone. Beds southeast of the graben lie at a higher elevation than the beds northwest of the graben. Thus, the displacement is greater on the fault bounding the graben on the southeast side. A prominent northwest-facing fault-line scarp, the Eminence Break, is developed along the southeast-bounding fault. This fault is 40 km long and has a maximum displacement of about 100 m. It dies out to the northeast at the Echo Cliffs monocline. The fault bounding the northwest side of the graben is only 30 km long and dies out before reaching the Echo Cliffs monocline. To the southwest, toward the East Kaibab monocline, the graben bends to the south and dies out precisely at the lower axis of the monoclinal flexure. A few shorter faults that are parallel or subparallel with the main part of the Eminence Break graben occur on nearby parts of the Marble Platform.

A zone of en echelon graben continues for a distance of 12 km northeast of the Echo Cliffs along the projected trend of the Eminence Break graben. Beyond this point, the Bright Angel fault system becomes a broad diffuse zone of relatively short faults (see Fig. IV-A-2). In general, faults become more and more widely spaced to the northeast, and the northeastern limit of the system is not well defined. The system extends at least as far as the Monument upwarp, Utah. One branch of the system may be represented by a set of faults that extends to the Comb monocline, just north of the San Juan River in Utah. The easternmost fault of this set is described in Ref. IV-A-11. Between the Echo Cliffs and Comb Ridge, the displacement of faults in the Bright Angel system is generally less than 100 m, and none exceeds 30 km in length. At the surface the faults displace Triassic and Jurassic rocks and, in the vicinity of Monument Valley, Permian rocks.

2. Mesa Butte Fault System

The Mesa Butte fault system, as now recognized, extends from Chino Valley, near Paulden, Arizona, on the southwest, to Shadow Mountain on the northeast. The known length of the fault system is about 150 km, but detailed mapping of Precambrian terrain west and southwest of Prescott, Arizona, may extend the system

Fig. IV-A-3a. Oblique high-altitude aerial photograph of Mesa Butte fault system, looking southwest across Coconino Plateau: (1) Mesa Butte, (2) Cedar Ranch fault, (3) Mesa Butte fault, (4) Red Mountain, (5) Slave Mountain, (6) source of Tappan Wash flow, (7) Kendrick Peak, (8) Sitgreaves Mountain, (9) Bill Williams Mountain (U. S. Geological Survey high-altitude photograph)

many tens of kilometers farther to the southwest. About midway along its known length, the fault system is concealed beneath Quaternary lava flows of the San Francisco volcanic field. The recognized faults in the system are thus grouped into a northeastern segment and a southwestern segment.

The Mesa Butte fault is the principal member of the northeastern segment of the fault system. It was first noted by Johnson (Ref. IV-A-12) and was mapped and named by Babenroth and Strahler (Ref. IV-A-13). Mesa Butte, an elongate basaltic cinder cone, was formed by fissure eruption along the fault (see Fig. IV-A-3a). Southwest of Mesa Butte, the fault is covered by Pleistocene lava flows that lap against the base of the fault scarp. The position of the fault and its displacement can be estimated with some precision, however, for a distance of about 10 km southwest of Mesa Butte. Farther to the southwest the

Fig. IV-A-3b. Oblique high-altitude aerial photograph of Bright Angel fault system, looking southwest across Coconino Plateau: (1) Howard Hill, (2) Mt. Floyd (U. S. Geological Survey high-altitude photograph)

fault scarp is completely concealed beneath younger lava flows and basaltic cinder cones (Fig. IV-A-4). Northeast of Mesa Butte, the fault emerges from beneath the lavas and becomes the northwest-bounding fault of the spectacular long, narrow Mesa Butte graben (see Fig. IV-A-3a). The graben is 300 to 400 m wide, 15 km long, and forms a trench 100 to 200 m deep in the surface of the Coconino Plateau. Formations exposed in the walls of the trench are the Coconino Sandstone, Toroweap Formation, and Kaibab Limestone, all of Permian age. The Mesa Butte fault can be recognized at the surface for a distance of about 35 km; maximum observed displacement is about 100 m.

A branch fault, the Cedar Ranch fault, joins the Mesa Butte fault near Mesa Butte. It can be traced southwestward about 15 km, where it disappears beneath younger lavas. The Cedar Ranch fault is covered by lava that laps

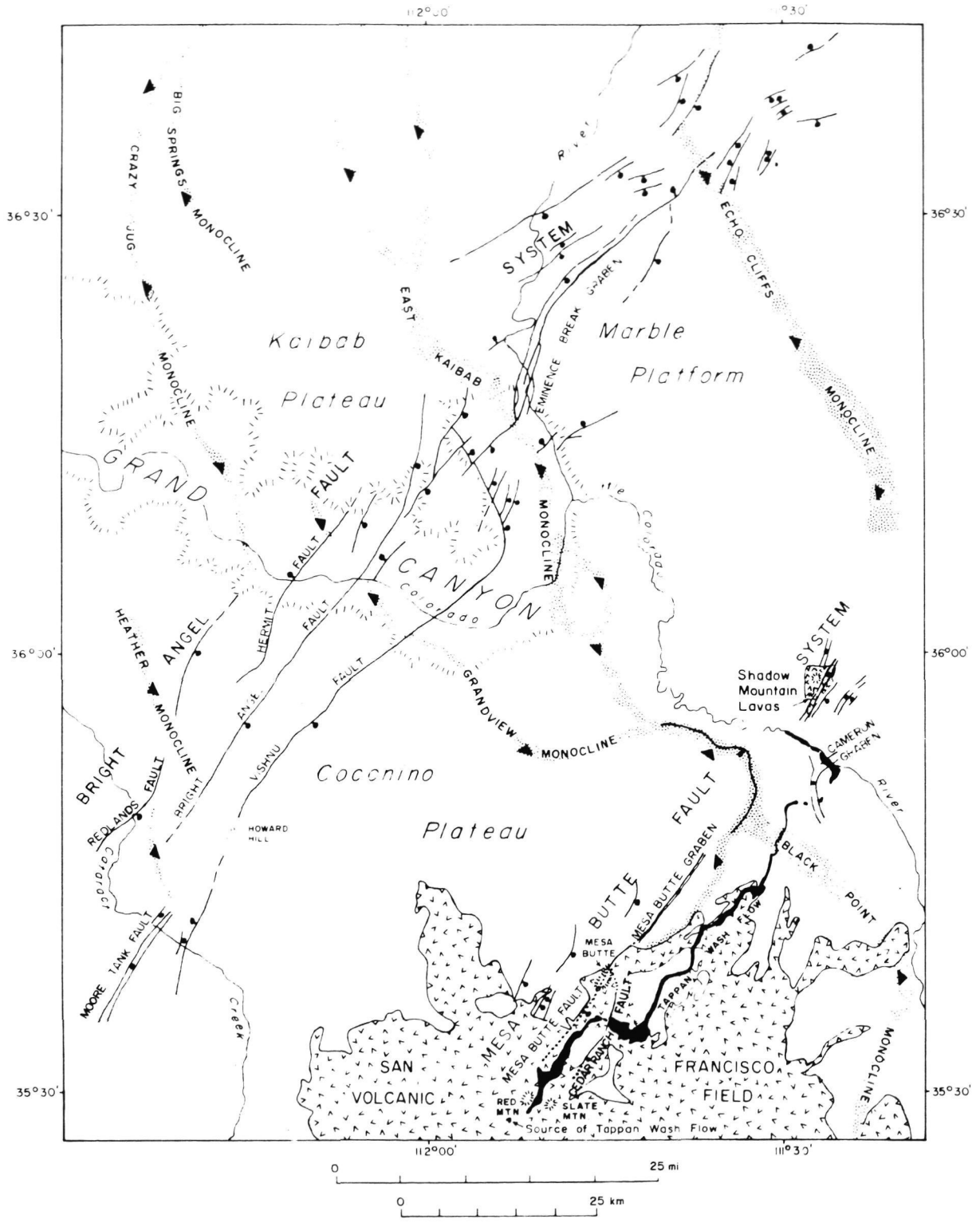

Fig. IV-A-4. Map of part of Bright Angel and Mesa Butte fault systems, showing relation of faults to monoclines and Cenozoic volcanic rocks. Bar and dot on downthrown side of faults; triangles indicate dip direction of steep limb of monocline

against the fault scarp, but locally the lava is offset by faulting. As along the Mesa Butte fault, displacement is down to the southeast.

Northeast of the Mesa Butte graben and directly in line with it is the sharply flexed, locally faulted southern salient of the Grandview monocline (Fig. IV-A-4). Farther to the northeast the monocline swings around to the west and veers away from the Mesa Butte fault system. About 30 km beyond the Mesa Butte graben, a cluster of small northeast-trending faults near Shadow Mountain marks the northeastern limit of exposed faults in the Mesa Butte system. However, a series of monoclines along the northwestern edge of Black Mesa and a segment of the Comb monocline along the southern margin of the Monument upwarp, near Kayenta, Arizona, may be controlled by the northeastern extension of the ancestral Mesa Butte fault in the Precambrian rocks.

Faults belonging to the southwestern segment of the Mesa Butte fault system were mapped along Hell Canyon in the Paulden quadrangle and described by Krieger (Ref. IV-A-14). The principal fault in this segment was traced by Krieger 8 km northeastward from the Paulden quadrangle across the Tonto Rim, where it cuts Pennsylvanian and Permian rocks, and is shown on the geologic map of Arizona (Ref. IV-A-15). The continuation of this fault through the southern part of the San Francisco volcanic field can be recognized in ERTS-1 pictures (see Fig. IV-A-1) and traced an additional 22 km. The total recognized length of the fault is 38 km. Displacement is down on the southeast; maximum displacement of the exposed rocks is about 150 m. The fault disappears northeastward in a field of lava flows of Pleistocene age. Whether the displacement dies out or the fault is covered by younger lavas is not known, as the relations have not been studied in detail in the field.

Directly in line with the 38-km-long fault, 12 km southwest of its last recognized exposure in Hell Canyon, rocks correlated by Krieger (Ref. IV-A-14) with the Texas Gulch Formation of Precambrian age are in contact with the Mazatzal Quartzite of Precambrian age, the Tapeats Sandstone of Cambrian age, and the Martin Limestone of Devonian age, along closely spaced northeast-trending faults. As mapped by Krieger (Ref. IV-A-14), the displacement that brought the Mazatzal Quartzite in contact with the Texas Gulch Formation (?) at this locality is Precambrian (pre-Tapeats). The latter displacement of Cambrian and Devonian beds may have been controlled by a Precambrian fault zone. It appears possible that the ancestral Mesa Butte fault is partly exposed in the Precambrian rocks at this place.

Still farther to the southwest, on the trend of the Mesa Butte fault system, rocks mapped as the Yavapai Series of Precambrian age are in contact with Precambrian granitoid rocks northwest of Granite Mountain (Ref. IV-A-15). This contact may be the southwestward continuation of the ancestral Mesa Butte fault. Work in the field is needed to test this hypothesis.

3. Other Fault Systems

In addition to the Bright Angel and Mesa Butte fault systems, other swarms or systems of faults can be recognized from the pattern of faulting shown in Fig. IV-A-2. One of these, the Sinyala system, which comprises a swarm of northeast-trending faults, is roughly parallel with the Bright Angel and Mesa Butte systems. Other systems trend northwest and approximately north (Fig. IV-A-5). Each system is a relatively broad lane or zone of faults in which the individual faults tend to be parallel or subparallel with the overall trend of the lane. Where the lanes intersect, faults belonging to two or more systems are present. At these intersections, some individual faults follow the direction of one system for part of their length and then turn abruptly and follow the direction of another system.

The Sinyala fault system consists, in large part, of a set of en echelon faults. It is named for a fault 50 km long that crosses the Colorado River midway along the length of the system (see Fig. IV-A-2) and trends parallel with the total system. Although this fault is very long, its displacement is generally less than a few meters. Some other faults in the Sinyala system with much larger displacements are segments of long faults that follow one system for a distance and then turn and follow another. The faults are observed in rocks ranging in age from Precambrian to Permian.

Four northwest-trending systems of faults are recognized in northern Arizona (see Figs. IV-A-2 and IV-A-5): the Chino Valley system, the Cataract Creek system, the Kaibab system, and the Mormon Ridges system (Fig. IV-A-5). The Chino Valley system of faults is observed primarily in Paleozoic rocks, but a set of fault scarps 20 km long is developed in alluvium in the northwestern Chino Valley along the Big Chino fault of Krieger (Refs. IV-A-14 and IV-A-16).

The Cataract Creek system consists chiefly of a newly mapped swarm of faults that cut Permian, Triassic, and Tertiary rocks in the southern and western parts of the Cataract Creek basin. Faults belonging to this system extend into the Shivwits Plateau on the northwest and

Fig. IV-A-5. Principal fault systems of northwestern Arizona

across the southern part of the San Francisco volcanic field on the southeast.

The Kaibab system is a relatively broad lane of northwest-trending faults that extends from the southern Kaibab Plateau across the Grand Canyon onto the northern Coconino Plateau. Rocks ranging in age from Precambrian to Permian are cut by this system. As in the case of the northeast-trending faults of the Bright Angel system, many faults in the Kaibab system can be shown to have had a long history of displacement that began in Precambrian time.

The Mormon Ridges system is observed principally in Mesozoic rocks. It is named for ridges on the Kaibito Plateau formed along a closely spaced set of faults in the Navajo Sandstone of Triassic (?) and Jurassic age (Ref. IV-A-17).

Two swarms of faults trending approximately north are present in the fault pattern of northern Arizona. They are referred to here as the Toroweap system and the Oak Creek Canyon system. Both systems cut rocks ranging in age from Cambrian to Tertiary. The Toroweap system includes a north-trending segment of the Toroweap fault (Refs. IV-A-18 and IV-A-19), a parallel segment of the Hurricane fault (Ref. IV-A-19), and a roughly north-trending segment of the Aubrey fault (Ref. IV-A-20), each of which has a displacement of several hundred meters. Some smaller faults are also present in the system.

The Oak Creek Canyon system extends north from Oak Creek Canyon, through Flagstaff, Arizona, to the Coconino Plateau. Just north of Flagstaff, the Oak Creek Canyon system is concealed by Quaternary and Pliocene (?) volcanic rocks of the San Francisco volcanic field; the large stratovolcano of San Francisco Mountain lies astride the system.

Northwest of the Sinyala system, faults are somewhat more uniformly distributed than in the region to the east and south (see Fig. IV-A-2). Major faults are present near this corner of the state, and northeast-, north-, and northwest-trending sets of faults are represented in this area, but the faults are not grouped as clearly into discrete lanes as they are in the adjacent region.

4. Relation of Eruptive Centers to Faults

Inspection of the distribution of volcanoes in the San Francisco volcanic field reveals that about half of the silicic to intermediate volcanoes (described in Ref. IV-A-21) lie along the Mesa Butte fault system. This relationship is easily recognized in ERTS-1 pictures (see Fig. IV-A-1); these volcanoes form the most prominent peaks in the region. Closer study shows that Sitgreaves Mountain lies precisely on the projected trend of the Mesa Butte fault (Fig. IV-A-6). Bill Williams Mountain lies a few kilometers northwest of this line, and Kendrick Peak lies a few kilometers southeast of the line, close to the projected trend of the Cedar Ranch fault. Slate Mountain, a relatively small silicic volcanic center, lies on the trend of the Cedar Ranch fault (see Figs. IV-A-3b and IV-A-4). The remaining silicic volcanoes in the San Francisco field occur either on the Oak Creek Canyon system of faults or on the Cataract Creek system.

Several hundred basaltic cinder cones are present in the San Francisco volcanic field, but only a few of these are related in an obvious way to the major fault systems. Red Mountain, one of the largest cinder cones, lies on the line of the Mesa Butte fault (see Figs. IV-A-3a and IV-A-4). Mesa Butte, formed by fissure eruption along the fault, is one of the northernmost eruptive centers in the San Francisco field. Well separated from the rest of the volcanic field, Shadow Mountain lies 45 km farther to the northeast along the Mesa Butte fault system (Figs. IV-A-4 and IV-A-6). It is, however, a basaltic eruptive center of the San Francisco type (Ref. IV-A-22).

Beyond Shadow Mountain lie the monchiquite diatremes and dikes at Tuba Butte and Wildcat Peak (see Fig. IV-A-6). These isolated volcanic centers are far removed from most other diatremes and alkalic basalts of the Navajo country (Refs. IV-A-23 and IV-A-24), but are close to the projected trend of the Mesa Butte fault system.

Eruptive centers are more widely spaced along the Bright Angel fault system. In the vicinity of Monument Valley, Utah, a broad swarm of minette dikes and two kimberlite pipes occur near the extreme northeastern end of the Bright Angel fault system. Navajo Mountain, a prominent structural dome in Utah, just north of the Arizona state line, occurs on the margin of the relatively diffuse part of the fault system. For many years the Navajo Mountain dome was thought to have been formed over a laccolith or stock (Refs. IV-A-23, IV-A-25 through IV-A-27), but without any definite evidence. The dome is distant from the known laccolithic mountain groups of the Colorado Plateau. A small syenite porphyry intrusion near the summit of the dome was reported by Condie in 1964 (Ref. IV-A-28).

Near the southwestern end of the Bright Angel fault system, Howard Hill, a small structural dome that resembles the Navajo Mountain dome in shape but not in size, lies just beyond the end of the Vishnu fault (Figs. IV-

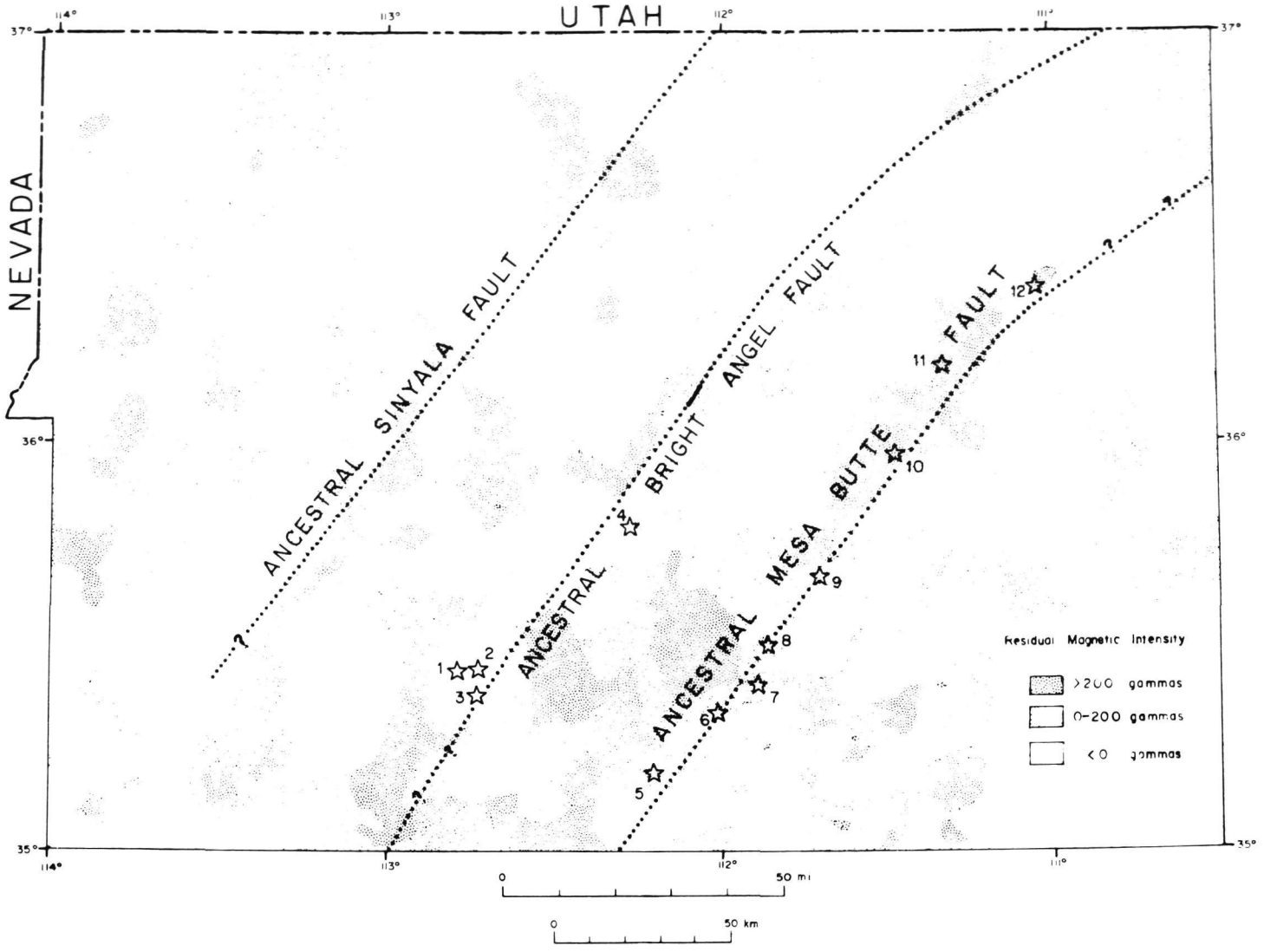

Fig. IV-A-6. Simplified residual aeromagnetic map of northwestern Arizona, showing ancestral Sinyala, Bright Angel, and Mesa Butte fault systems and related eruptive centers. Residual aeromagnetic intensity after Sauck and Sumner (see Ref. IV-A-10). Eruptive centers along faults are denoted by stars: (1) Trinity Mountain, (2) Round Mountain, (3) Mt. Floyd, (4) Howard Hill, (5) Bill Williams Mountain, (6) Sitgreaves Mountain, (7) Kendrick Peak, (8) Slate Mountain, (9) Mesa Butte, (10) Shadow Mountain, (11) Tuba Butte, (12) Wildcat Peak

A-3b and IV-A-4). This dome may be located over a small stock. Still farther to the southwest, Trinity Mountain, Round Mountain, and Mt. Floyd, the principal eruptive centers of the Mt. Floyd volcanic field, occur on the trend of the Bright Angel fault system. Mt. Floyd itself lies almost precisely on the projection of the Bright Angel fault (Figs. IV-A-3b and IV-A-6).

5. Precambrian Origin of Faults

The distribution of eruptive centers along the Bright Angel and Mesa Butte fault systems and the relatively great length of these systems suggest that the faults observed in Phanerozoic rocks may be related to more profound, deep-seated structures in the crust. Where the Bright Angel and Kaibab fault systems cross the Grand Canyon, the relation of the faults to the deeper-lying Precambrian rocks is exposed. Here the principal displacement of Paleozoic beds along both systems of faults was controlled by more ancient faults in the underlying Precambrian rocks.

Walcott (Ref. IV-A-29) was the first to demonstrate that displacement of Phanerozoic rocks in the Grand Canyon had occurred along a Precambrian fault. He found that the northwest-trending Butte fault, which occurs along the East Kaibab monocline and which had reverse movement in Tertiary time, had much larger displacement, but of the opposite sense, in Precambrian time. Ford and Breed (Ref. IV-A-30) estimate as much as 1.5 km of normal displacement on the Butte fault after deposition of the Grand Canyon Supergroup and before deposition of the Tapeats Sandstone of Cambrian age.

Noble (Ref. IV-A-4) recognized many other post-Paleozoic faults that occur along Precambrian lines of displacement. He found that both northwest-trending and northeast-trending faults are controlled by Precambrian structure. On these faults, Phanerozoic displacement is generally smaller and in the opposite sense from that which occurred in late Precambrian time. The northwest-trending Muav fault (Fig. IV-A-7) was shown by Noble to have had a minimum normal displacement of almost 2 km in Precambrian time. A faulted monocline with much smaller throw is developed in the Paleozoic rocks over the Muav fault.

Maxson and Campbell (Ref. IV-A-7) found that the crystalline rocks of the Grand Canyon had been displaced by faults before deposition of the Grand Canyon Supergroup. These faults trend in two different directions:

(1) North 15° to 30° east, parallel with the schistosity of the crystalline metamorphic complex (Vishnu Schist).

(2) North 20° to 30° west, parallel with a direction of master joints, which also were formed before deposition of the Grand Canyon Supergroup.

Some of these faults are overlain by unbroken Precambrian strata; other faults of the same network that displace overlying strata presumably were active in post-Vishnu Schist pre-Grand Canyon Supergroup time (Ref. IV-A-8).

The Bright Angel fault belongs to the second category. Maxson (Ref. IV-A-8) inferred six episodes of displacement on the Bright Angel fault:

(1) Displacement of crystalline metamorphic rocks of early Precambrian age before intrusion of the Zoroaster Granite. Foliated migmatites in the metamorphic complex have been dated at 1695 ±15 m. y. and the Zoroaster Granite at 1725 ±15 m. y., thus pointing to a major episode of Precambrian deformation at about 1700 m. y. (Ref. IV-A-31).

(2) Post-Zoroaster displacement of the crystalline complex before deposition of the Grand Canyon Supergroup.

(3) Displacement after deposition of the Dox Sandstone of Precambrian age and before intrusion of diabase. Diabase intrusions in the Grand Canyon have been dated at 1150 to 1200 m. y. by L. T. Silver (personal communication).

(4) Reverse faulting after deposition of the Grand Canyon Supergroup.

(5) A second episode of reverse displacement before deposition of the Tapeats Sandstone of Cambrian age.

(6) Normal and strike-slip displacement during the Laramide Revolution.

Sears (Ref. IV-A-9) infers a minimum of seven episodes of displacement on the Bright Angel fault:

(1) Displacement of 60 m, up on the southeast, during deposition of the Shinumo Quartzite of Precambrian age.

(2) Post-Dox Sandstone, pre-diabase displacement.

(3) Local displacement during intrusion of diabase.

(4) Post-diabase reverse displacement of 200 m.

(5) Local post-Grand Canyon Supergroup scissors displacement.

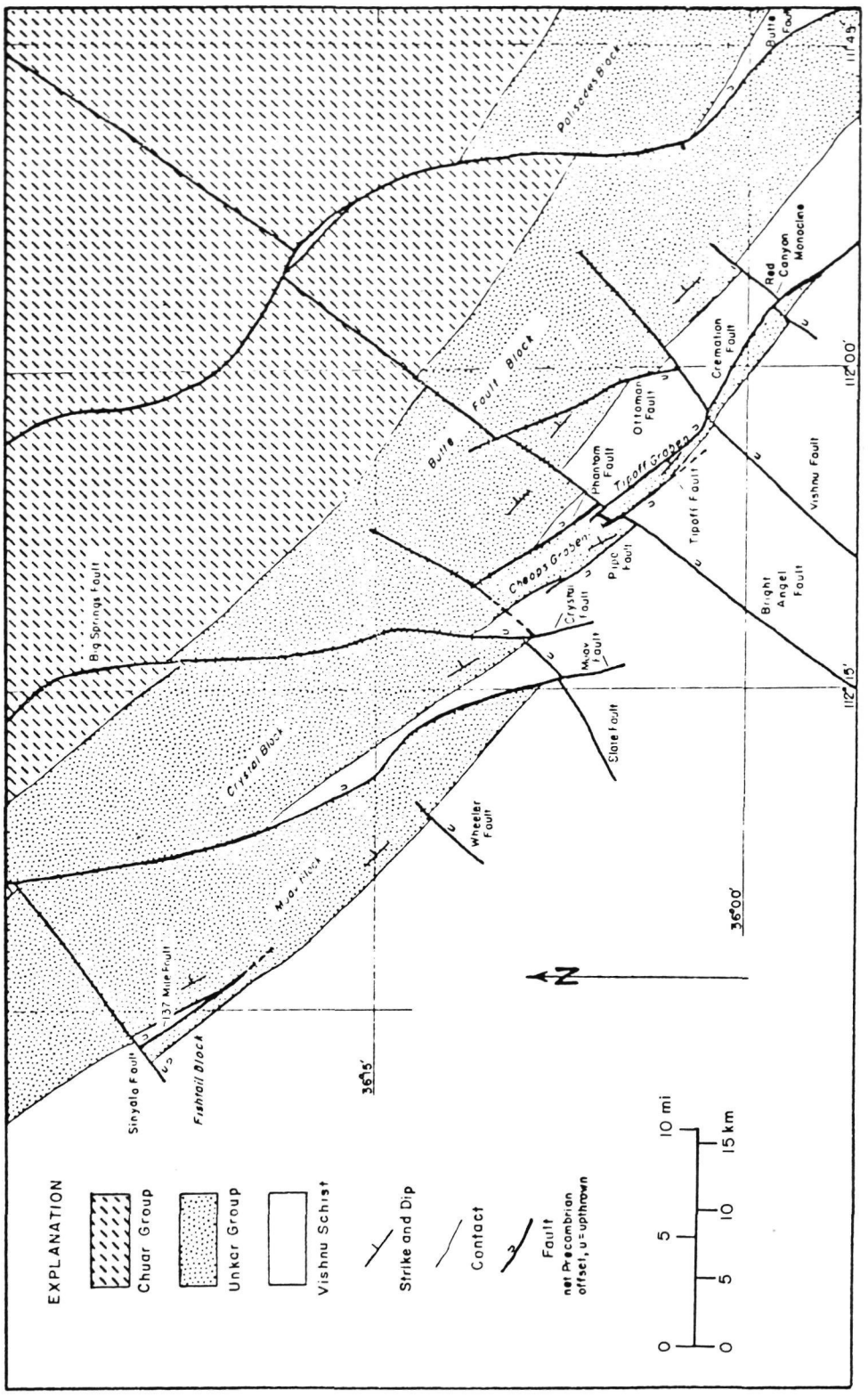

Fig. IV-A-7. Sub-Paleozoic geologic map of Grand Canyon National Park, from Sears (Ref. IV-A-9)

(6) Reverse displacement after deposition of Redwall Limestone of Mississippian age and before deposition of the lowermost beds of the Supai Formation, which are of Pennsylvanian age.

(7) Post-Paleozoic normal displacement.

It appears that at least seven and possibly as many as nine distinct episodes of displacement can be documented at various places along the Bright Angel fault. Most of this displacement occurred during the Precambrian period. Maxson believed that there had been a significant strike-slip component of displacement in post-Paleozoic time, but Sears has strongly challenged this interpretation.

The decipherable network of faults cutting the Grand Canyon Supergroup, which were active in Precambrian time, has been carefully re-examined by Sears (Ref. IV-A-9). His synthesis of this network is shown in Fig. IV-A-7. The more ancient northwest and northeast directions of faulting in the crystalline rocks are closely reflected in the late Precambrian pattern of displacement. This pattern is reflected, in turn, by Phanerozoic displacement along the Bright Angel and Kaibab fault systems. Most of the faults that were active in late Precambrian time were reactivated in the Phanerozoic.

The early history of displacement on the Mesa Butte fault system is much less well known. An episode of Precambrian displacement is documented in the Paulden quadrangle (Ref. IV-A-14). Northeast of the Mesa Butte graben, minor displacement on the Grandview monocline in Permian time may be indicated by slump blocks in the Toroweap Formation of Permian age (Ref. IV-A-32).

6. Aeromagnetic and Gravity Anomalies

Exposures of Precambrian rocks in northern Arizona are relatively limited, and it is desirable to determine the relationship of fault displacements in the Phanerozoic to Precambrian structures over a broader area than the Grand Canyon. Aeromagnetic and gravity data provide powerful tools to examine Precambrian structure, especially in northwestern Arizona, where Phanerozoic rocks are generally less than 2 km thick and, except for Cenozoic volcanic rocks, weakly magnetic. Local magnetic anomalies of limited extent and with steep gradients, associated chiefly with Cenozoic volcanic rocks in the San Francisco volcanic field, are readily distinguished from relatively broad anomalies with low gradients related to the Precambrian rocks. A residual aeromagnetic map of Arizona by Sauck and Sumner (Ref. IV-A-10) and a Bouguer gravity anomaly map of the state by West and Sumner (Ref. IV-A-33) reveal prominent structural trends in the Precambrian that are parallel with the observed system of faults.

Comparison of the principal faults in the Bright Angel, Mesa Butte, and Sinyala fault systems with the residual aeromagnetic map reveals a close correspondence between the positions of these faults and the margins of a series of large northeast-trending magnetic anomalies. This correspondence has emboldened us to infer the traces of the concealed ancestral Bright Angel, Mesa Butte, and Sinyala faults shown in Fig. IV-A-6. Large displacement of the crystalline Precambrian rocks is postulated to have occurred on these faults in order to account for aligned linear margins of the anomalies. Significant displacement of the crystalline rocks along the Bright Angel fault is suggested by the observations of Noble (Ref. IV-A-4).

The ancestral Bright Angel fault is exposed in the Grand Canyon for a distance of 14 km, but the ancestral Mesa Butte fault is not exposed in the area shown in Fig. IV-A-6. Precambrian displacement on the Sinyala fault system has not been demonstrated on the outcrop; the ancestral Sinyala fault is inferred on the basis of the fault pattern in observed Phanerozoic rocks and on the relationship of the observed faults to the magnetic anomalies.

Perhaps the most noteworthy feature of the aeromagnetic map of Arizona is a northeast-trending belt of large positive magnetic anomalies, 400 km long, which extends from the vicinity of Congress to the northern border of the state. The amplitude of these anomalies ranges from about 300 to 700 gammas. Over most of its length in northern Arizona, the magnetic anomaly belt corresponds to a belt of positive gravity anomalies with amplitudes of 10 to 30 milligals; the gravity anomaly belt, however, is less well defined. The Mesa Butte fault system lies along the southeastern margin of the magnetic anomaly belt, and the Mesa Butte fault follows some of the steepest anomaly gradients on this margin. The monoclines along the northeastern projection of the Mesa Butte fault system also follow the margin of the anomaly belt. This relationship suggests that the ancestral Mesa Butte fault continues northeastward beneath these monoclines (see Fig. IV-A-6).

Another large northeast-trending positive magnetic anomaly is bounded on the southeast by the Bright Angel fault. This anomaly, about 75 km long and 15 km wide, has a maximum amplitude of about 700 gammas. Where the anomaly is most pronounced, it corresponds to a well defined positive gravity anomaly with an amplitude of 5 to 10 milligals. Where it crosses the Grand Canyon, the

magnetic anomaly coincides approximately with a belt of amphibolite, migmatite, and schist referred to by Maxson (Ref. IV-A-8) as the "Brahma Schist."

Maxson interpreted the Brahma Schist to be a sequence of metavolcanic and metasedimentary rocks overlying dominantly metasedimentary rocks of the Vishnu Schist. According to Maxson, the Brahma Schist is folded down into the Vishnu terrain in a large isoclinal syncline. Subsequent work has not supported this interpretation, however. The rocks called "Brahma Schist" by Maxson appear to be part of the Vishnu Schist sequence (Ref. IV-A-34); the name "Brahma Schist" has been abandoned. The positive magnetic and gravity anomalies along the prevailing strike of Maxson's Brahma Schist, on the other hand, indicate that the rocks in this part of the Vishnu terrain have higher mean magnetic susceptibility and higher mean density than adjacent parts of the Vishnu Schist, at least northwest of the Bright Angel fault. Probably these physical properties can be attributed to a greater than average abundance of amphibolite in this block of Vishnu terrain. By analogy, we suggest that the large positive magnetic anomalies associated with positive gravity anomalies adjacent to the Mesa Butte fault system are also related to belts of mafic metavolcanic rocks in the crystalline Precambrian complex.

Other large positive magnetic anomalies are bounded by inferred extensions of the ancestral Bright Angel fault (see Fig. IV-A-6), but these anomalies are more widely spaced than those along the Mesa Butte fault system. Some, but not all, of the positive magnetic anomalies along the Bright Angel system are associated with positive gravity anomalies.

The ancestral Sinyala fault has been drawn along the margins of a series of positive magnetic anomalies of relatively limited extent which are grouped into two broad aeromagnetic highs (Fig. IV-A-6). The northeast trend of individual anomalies in these groups is not as pronounced along the Bright Angel and Mesa Butte fault systems. The positive magnetic anomalies along the Sinyala system correspond only roughly with positive gravity anomalies.

Faults belonging to the northwest- and north-trending fault systems also follow linear margins of aeromagnetic anomalies, although these trends are not as obvious as the northeast trend on the aeromagnetic map. A good example is a north-trending magnetic anomaly boundary that coincides with the north-striking Oak Creek Canyon fault. We conclude that the northwest- and north-trending fault systems are also controlled by faults with large displacement in the Precambrian crystalline basement.

7. Shylock and Chaparral Fault Zones

The ancestral Bright Angel and Mesa Butte faults may be related in origin to the Shylock and Chaparral fault zones in the central Arizona mountain belt, which were described by Anderson (Ref. IV-A-35). Here Precambrian rocks are exposed over a wide area; the detailed structure of the Precambrian rocks has been worked out by Anderson and his colleagues (see Refs. IV-A-14, IV-A-35 through IV-A-40). The Shylock and Chaparral fault zones are easily recognized in ERTS-1 pictures (see Fig. IV-A-8a), and the Shylock has been traced south of the area mapped by Anderson on the basis of the ERTS-1 data (extension shown by dashed lines in Fig. IV-A-8b).

The Shylock fault zone is a north-trending belt of roughly parallel interlacing faults cutting Precambrian rocks, which ranges in width from about 1 to 3 km. As interpreted by Anderson (Ref. IV-A-35), the zone represents a major transcurrent fault with a minimum right-lateral displacement of 8 km. Estimates of this displacement are based on the offset of slices of quartz diorite in the fault zone. The total horizontal displacement may be much greater than 8 km.

A large contrast in the magnetic properties of the Precambrian rocks on opposite sides of the Shylock fault zone, indicated by aeromagnetic data (see Fig. IV-A-8b), suggests the displacement may be as great as several tens of kilometers. Positive magnetic anomalies on the west side of the fault are related, in a general way, to metavolcanic rocks of the Big Bug Group of Precambrian age. The anomalies do not correspond closely to mapped geologic units, however. A broad magnetic low on the east side of the fault corresponds, at least in part, to a cluster of plutonic rocks. In contrast to the relations observed along the Bright Angel and Mesa Butte fault systems, the positive magnetic anomalies along the Shylock zone are gravity lows, and the magnetic low coincides with a broad positive gravity anomaly with an amplitude of 25 milligals. The plutonic rocks east of the Shylock fault zone are evidently less strongly magnetized, but have higher density than the metavolcanic rocks of the Big Bug Group.

In the Mingus Mountain quadrangle, along the southern border of the Black Hills, the Shylock fault zone is locally overlain by unbroken Tapeats Sandstone of Cambrian age (see Ref. IV-A-37). The large transcurrent displacement occurred before the Cambrian period and after emplacement of the quartz diorite pluton that is offset by the fault. The quartz diorite has been dated at 1760 ±15 m.y. (Ref.

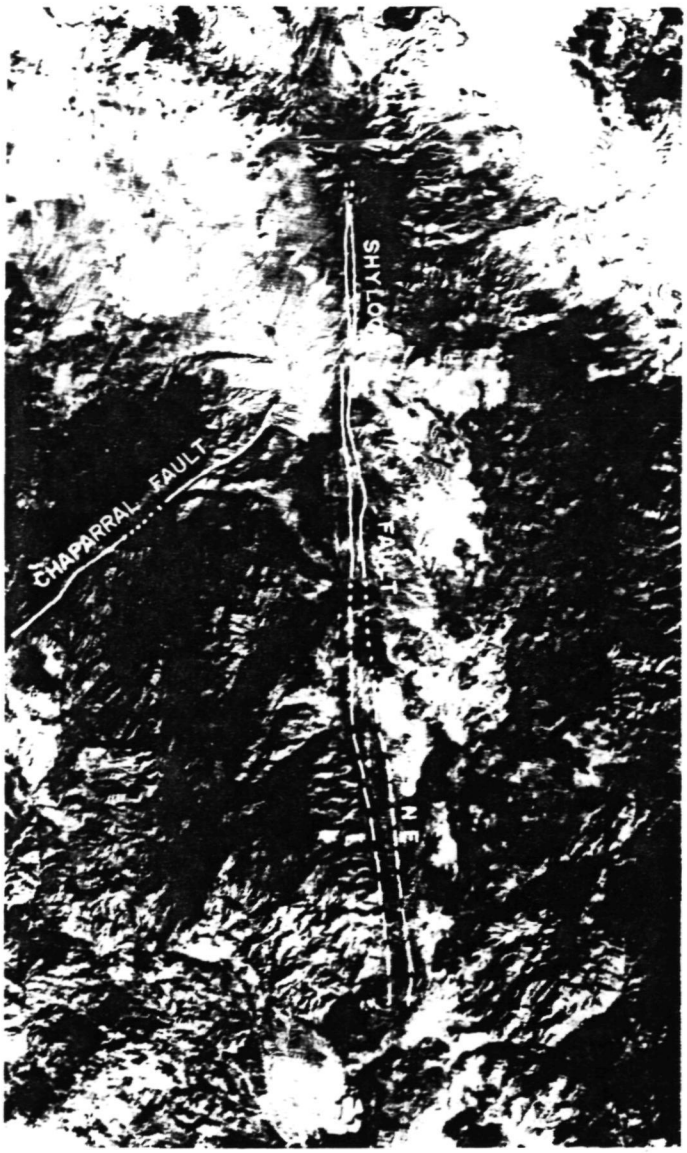

Fig. IV-A-8a. ERTS-1 picture, showing Shylock and Chaparral fault zones in central Arizona (NASA picture ERTS E-1104-17384-6, Nov. 4, 1972)

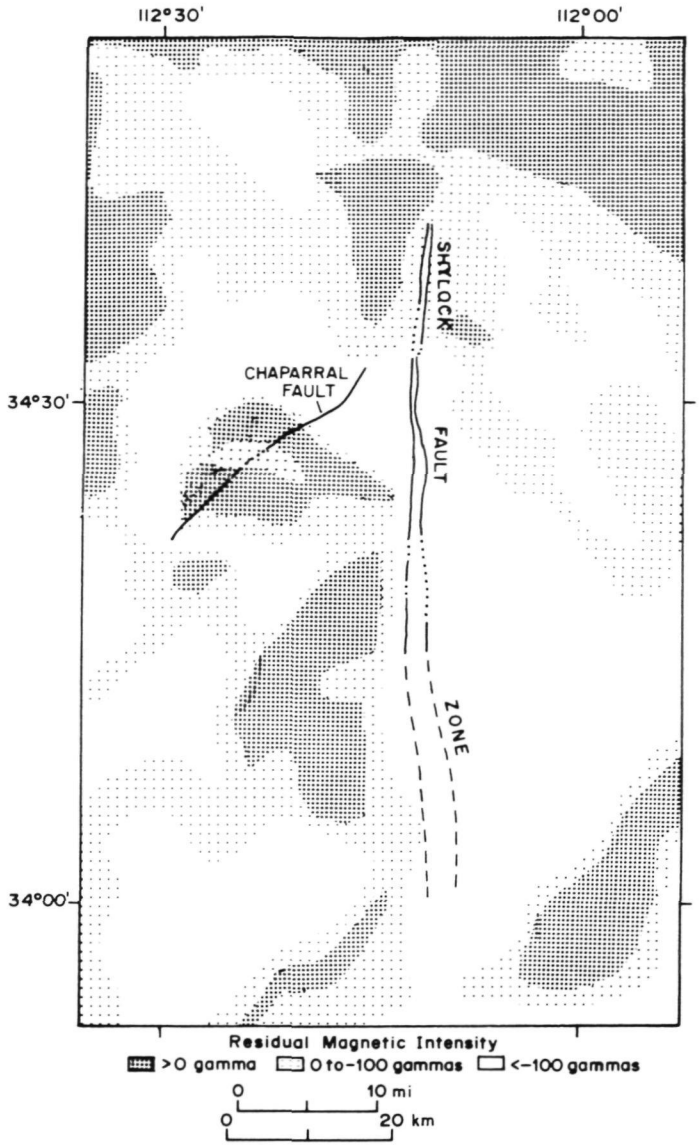

Fig. IV-A-8b. Simplified residual aeromagnetic map, showing Shylock and Chaparral fault zones. Traces of Shylock and Chaparral fault zones based on data from Anderson et al. (Ref. IV-A-39) and on ERTS-1 pictures. Residual aeromagnetic intensity from Sauck and Sumner (Ref. IV-A-10)

IV-A-39). It is possible that the transcurrent displacement along the Shylock zone is related in time to faulting of the Vishnu terrain, which occurred before deposition of the Grand Canyon Supergroup.

Near the Black Hills, the Coyote fault, which branches north–northwest from the Shylock fault zone, displaces Paleozoic and Tertiary rocks (Ref. IV-A-37). North of the Black Hills, directly in line with the main Shylock zone, the Orchard fault also displaces Paleozoic and Tertiary rocks. At least two episodes of normal displacement have occurred on both faults (Ref. IV-A-41). The old transcurrent fault zone has clearly controlled the pattern of Phanerozoic normal displacement.

The Chaparral fault zone is a northeast-trending zone of distributive shear, up to 1 km wide, which cuts Precambrian rocks (Refs. IV-A-14 and IV-A-35). Detailed structural features within the zone indicate right-lateral slip (Ref. IV-A-14). Anderson (Ref. IV-A-35), to account for separation of intrusive rocks common to both sides of the fault zone, suggests that appreciable right-lateral displacement has occurred. The Chaparral fault zone

trends toward the Shylock zone but does not offset it. It appears likely that the Chaparral joins the Shylock tangentially, but the critical area is concealed by Phanerozoic deposits.

We suggest that the northeast- and north-trending fault systems of northern Arizona are controlled by ancestral transcurrent faults in the Precambrian basement similar to the Shylock and Chaparral fault zones. The 1700- to 1800-m.y.-old Precambrian terrain, represented by the Vishnu Schist in northern Arizona and the Yavapai Series (Ref. IV-A-39) in central Arizona and by associated plutonic rocks, probably was riven by right-lateral faults before deposition of the Grand Canyon Supergroup. Displacement on the ancestral Bright Angel and Mesa Butte faults may have been comparable to that on the Shylock fault zone. Major displacement probably occurred on a few main faults that divide the crust into blocks tens of kilometers across. Minor shearing occurred within these blocks, especially along their margins. Both the major and minor faults controlled later, dominantly vertical displacement in late Precambrian and Phanerozoic time.

Whether the ancestral northwest-trending faults are transcurrent faults or whether they are related tectonically to the northeast- and north-trending ancestral transcurrent faults is a problem that awaits further investigation. Evidence should be sought in the central Arizona mountain belt.

8. Cenozoic History of Displacement

Cenozoic deformation in northern Arizona occurred in two widely separated periods. Folding on a monocline parallel with the northern end of the East Kaibab monocline took place after deposition of Upper Cretaceous strata and before deposition of beds now assigned to the Paleocene period (Ref. IV-A-42). The principal folding of some monoclines on the eastern side of the Colorado Plateau occurred near the end of the Eocene period (Ref. IV-A-43). Presumably, the monoclinal folding and broad regional warping of strata in northern Arizona took place during this episode of compressive deformation that lasted from latest Cretaceous to late Eocene time, which commonly has been referred to as the "Laramide Revolution." Some reverse faulting along monoclines probably occurred during this early period of deformation. Subsequently, Paleozoic and Mesozoic strata were deeply eroded and, in central Arizona, stripped entirely away. By mid-Tertiary time a widespread, relatively mature erosion surface had developed (Ref. IV-A-44), which is locally preserved beneath mid-Tertiary sediments and Oligocene and Miocene volcanic rocks (Ref. IV-A-45). Where the history of displacement on faults can be documented by stratigraphic evidence, most or all Cenozoic normal displacement has occurred after emplacement of these mid-Tertiary sediments and volcanics.

In northern Arizona large displacement took place on normal faults in Miocene time and has continued to the present. Displacement on the Grand Wash fault occurred mainly after emplacement of the 17- to 18-m.y.-old Peach Springs Tuff (Ref. IV-A-46), but before deposition of the Muddy Creek Formation of the late Miocene and Pliocene (?) age (Refs. IV-A-47 and IV-A-48). Some normal displacement along the Cottonwood Cliffs occurred before emplacement of the Peach Springs Tuff (Ref. IV-A-49). On faults farther to the east, most displacement postdates middle to late Miocene lavas but predates Pleistocene volcanic rocks. Faulting has continued into the Quaternary, however, as shown by relatively fresh fault scarps in alluvium in Chino Valley and near Cameron, Arizona (Ref. IV-A-50), by minor offset of Pleistocene lava flows, and by the present seismicity of the region.

The Cenozoic history of displacement on the Mesa Butte fault system is fairly well known. On the southwestern segment of the system, most displacement postdates old basaltic lavas in the southern San Francisco volcanic field and predates lavas and sediments now assigned by Krieger et al. (Ref. IV-A-45) to the Perkinsville Formation of Pliocene and Pleistocene age. In some places older units of the Perkinsville are displaced and younger units are not. Old basaltic lavas in the southern part of the San Francisco volcanic field have been dated by McKee and McKee (Ref. IV-A-51) at 11.1 ±0.5 m. y. and 14.4. ±0.6 m. y. from a locality near Sycamore Canyon. Damon et al. (Ref. IV-A-52) have dated a basalt from another locality near Sycamore Canyon at 8.68 ±0.98 m. y. These localities are 15 to 25 km east of the prominent fault scarp, where old basalts are displaced.

On the northeastern segment of the Mesa Butte fault system, most displacement occurred before the extrusion of lavas that follow the base of fault scarps and conceal the faults. Mesa Butte and the lava flows from this vent are clearly later than most of the displacement on the Mesa Butte fault system. Locally these flows are offset, however, both on the Mesa Butte fault and on the Cedar Ranch fault. On the basis of many dated basaltic lavas in nearby parts of the San Francisco volcanic field, normal displacement on the fault systems near Mesa Butte appears to have occurred between about 4.0 and 0.5 m.y. ago (Ref. IV-A-52).

The youngest lavas displaced by faults of the Mesa Butte system are a flow from the Shadow Mountain vent,

dated at 0.62 ±0.23 m.y. (Ref. IV-A-52), and the Tappan Wash flow, dated at 0.510 ±0.079 m.y. (Ref. IV-A-52). The Shadow Mountain lava is displaced about 13 m by a graben that cuts the flow (Ref. IV-A-22). The Tappan Wash flow has been traced by M. Malin and E. M. Shoemaker from a vent southwest of Red Mountain, on the trend of the Mesa Butte fault (Fig. IV-A-4), to previously recognized outcrops in Tappan Wash and along the Little Colorado River. Where it crosses the Cedar Ranch fault, it appears to be displaced several meters. Along the little Colorado River (Fig. IV-A-4), the Tappan Wash flow is displaced about 20 m by the Cameron graben (Ref. IV-A-53). According to that reference, the graben is younger than the flow. A channel was cut into the flow by the Little Colorado River, filled with alluvium, and then abandoned, all before development of the graben (Ref. IV-A-53).

Evidence of the time of displacement on the Bright Angel fault system is indirect. The principal displacement on some faults of the Cataract Creek system, which intersects the Bright Angel system near Cataract Creek, occurred after deposition of mid-Tertiary sediments and extrusion of basalt flows in the nearby Mt. Floyd vocanic field. Basalt flows at Long Point, on the northern edge of this field, have been dated by McKee and McKee (Ref. IV-A-51) at 7.4 ±0.4 m.y. and 14.0 ±0.6 m.y. A well integrated dendritic drainage system in the Cataract Creek basin appears to be antecedent to the Bright Angel fault (see Fig. IV-A-3b). However, the prisms of Moenkopi Formation preserved along several faults in the system show that displacement began before the Moenkopi Formation was stripped from most of the Coconino Plateau. Several faults in the system have controlled the development of side canyons in the Grand Canyon (e.g., Fig. IV-A-3b). Probably the drainage system is anteposed (Ref. IV-A-54) to the fault system.

Several lines of evidence (e.g., Ref. IV-A-55) indicate that normal faulting in northern Arizona has continued into the Holocene period. Indeed, the fault systems are seismically active. Three moderately strong earthquakes (intensity VI to VIII on the Modified Mercalli Scale) occurred in 1906, 1910, and 1912 near or north of Flagstaff (Refs. IV-A-56 through IV-A-58). Newspaper accounts suggest that the epicenters of the 1910 and 1912 earthquakes may have been near the intersection of the Mesa Butte, Oak Creek Canyon, and Kaibab fault systems. In Ref. IV-A-57, 17 earthquakes of intensity IV or greater are reported in northwestern Arizona during the period 1850 to 1966. Except for a few of these earthquakes, however, the epicenters are not known with sufficient precision for comparison with the fault systems.

As of January 11, 1974, 27 earthquakes in northwestern Arizona (see Fig. IV-A-9), for which the epicenters have been estimated to 0.1° latitude and longitude or better, were on record in the hypocenter data file of the National Oceanic and Atmospheric Administration. Only locations determined with five or more seismographic stations are included. The actual error in location of several of the epicenters plotted in Fig. IV-A-9 probably is greater than 0.1°. All focal depths are shallow, probably in the crust. The epicenter locations of relatively minor earthquakes that occurred after 1969 are probably most reliable.

All but one of the epicenters shown in Fig. IV-A-9 lie either within the previously defined fault systems, on the projection of these systems, or along a major fault. The earthquake plotted as No. 2 followed earthquake No. 1 by less than 2 h. It is likely that the distance between the epicenters of these two earthquakes is less than indicated in Fig. IV-A-1; one or both of the epicenters may be significantly in error. Another pair of events (10a and 10b) is separated by 10 min and by about 20 km on the map; a third pair (14 and 15), along the Grand Wash fault, is separated by 2.5 min and 20 km.

The Toroweap, Sinyala, Bright Angel, Mesa Butte, Kaibab, and Oak Creek Canyon fault systems are demonstrably active. A magnitude 5.1 earthquake seems to have occurred along or near the Eminence Break graben in 1945. Five epicenters shown near the western border of the map are along or near the surface trace of the Grand Wash fault.

B. The Shivwits Plateau[1] (Geologic Map in Plate I)

I. Lucchitta

1. General Characteristics

The Shivwits Plateau (Fig. IV-B-1), located in northwestern Arizona, is the westernmost part of the Colorado Plateau province. It measures about 50 km in an east–west direction and about 140 km in a north–south direction (see Fig. IV-B-2 . The western boundary is at the Grand Wash Cliffs, the southern at the Grand Canyon, the eastern at the Hurricane Cliffs, and the northern at St. George Basin in Utah. Most of the plateau is composed of gently rolling terrain dissected less than 100 m and dotted by isolated lava-capped buttes. In this area, the vegetation is grassland and piñon-juniper forest, regolith is abundant, and geologic exposures are relatively poor. By contrast, a band about 15 km wide at the south and southwest edges of the

[1] Publication authorized by the Director, U. S. Geological Survey.

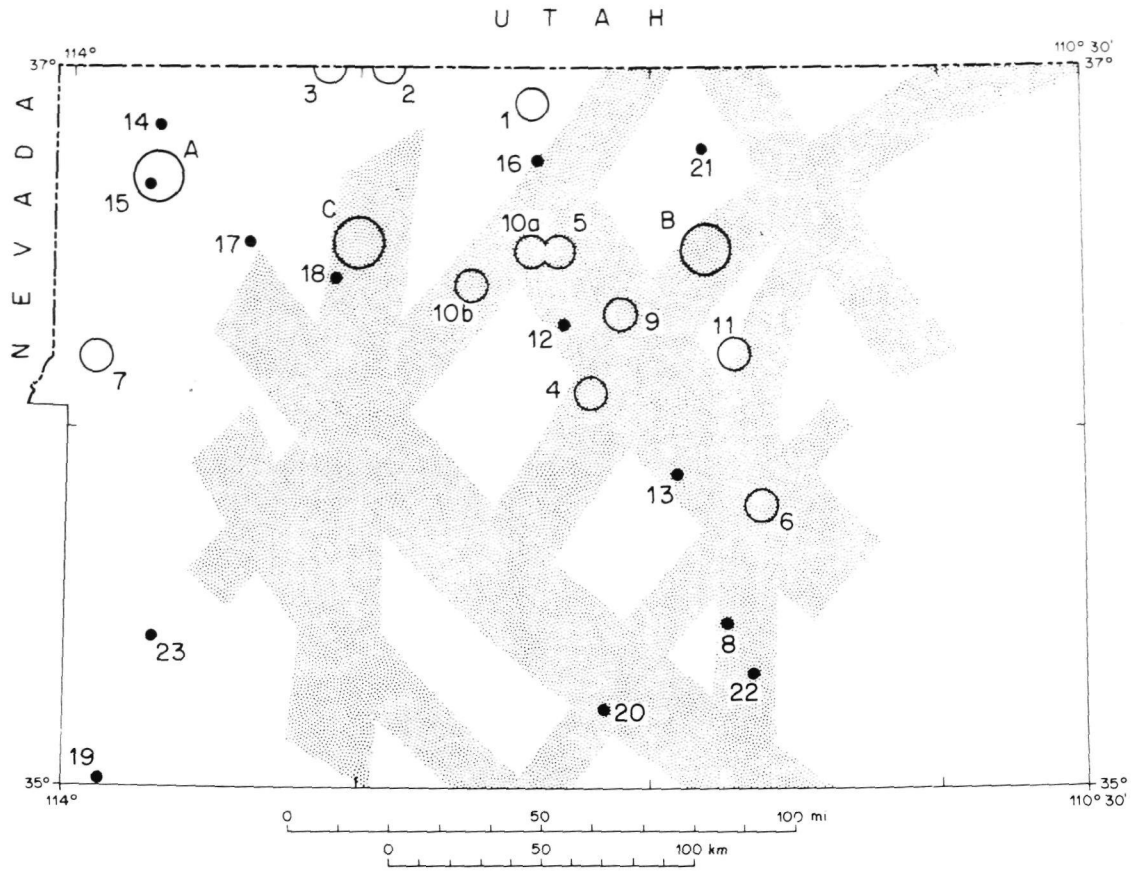

Map number	Date	GMT	Magnitude	Map number	Date	GMT	Magnitude
A	Aug 17, 1938	09:08:06		11	Sept. 4, 1967	23:27:45	
B	Jan. 7, 1945	22:25:32	5.1	12	Nov. 24, 1970	16:47:56	3.0
C	Nov. 2, 1949	02:29:36	4.7	13	Dec. 3, 1970	03:47:25	2.8
1	Feb. 15, 1962	07:12:43	4.5	14	Dec. 16, 1970	13:44:19	2.6
2	Feb. 15, 1962	09:06:45		15	Dec. 16, 1970	13:46:47	2.2
3	Aug. 28, 1964	06:50:47		16	Mar. 27, 1971	04:39:12	2.6
4	June 7, 1965	14:28:01		17	May 1, 1971	03:11:20	2.9
5	Sept. 3, 1966	07:53:20		18	May 6, 1971	16:57:18	2.2
6	Oct. 3, 1966	16:03:51		19	May 23, 1971	21:31:52	3.0
7	Dec. 1, 1966	09:20:41	3.7	20	Nov. 4, 1971	02:18:59	3.7
8	Mar. 28, 1967	03:48:59		21	Dec. 15, 1971	12:58:15	3.0
9	July 20, 1967	13:51:10		22	Apr. 20, 1972	13:28:16	3.7
10a	Aug. 7, 1967	16:24:49		23	Apr. 12, 1973	10:57:48	
10b	Aug. 7, 1967	16:40:32					

Fig. IV-A-9. Distribution of earthquake epicenters in northwestern Arizona for the period 1938 to 1973. Epicenters shown with large circles generally are least accurately known; those shown with solid dots generally are most accurately known. Principal fault systems are shown with stipple

DEPARTMENT OF THE INTERIOR
UNITED STATES GEOLOGICAL SURVEY

Prepared In Cooperation With The
JET PROPULSION LABORATORY, CALIFORNIA INSTITUTE OF TECHNOLOGY
FOR THE NATIONAL AERONAUTICS AND SPACE ADMINISTRATION

PLATE 1

CORRELATION OF MAP UNITS

Qal	Holocene and Pleistocene	QUATERNARY	CENOZOIC
UNCONFORMITY			
	Pleistocene(?)		
Tg	Pliocene	TERTIARY	
UNCONFORMITY			
6my K-Ar			
UNCONFORMITY			
7.5my K-Ar	Miocene		
UNCONFORMITY			
	Pliocene and Miocene		
UNCONFORMITY			
	Lower Triassic	TRIASSIC	MESOZOIC
UNCONFORMITY			
Pkα	Leonardian	PERMIAN	PALEOZOIC
	Wolfcampian		
	Virgilian	PENNSYLVANIAN	
UNCONFORMITY			

INDEX MAP

Contact — Dashed where approximately located

Monocline — Dashed where approximately located. Showing trace of anticlinal axis

Monocline — Dashed where approximately located. Showing traces of anticlinal (A) and synclinal (S) bends

Fault — Bar and ball on downthrown side; long dash where approximately located, short dash where located photogeologically, dotted where concealed

Strike and dip of beds

Volcanic center

Ancient gravel-filled stream channel

PALEOZOIC AND PRECAMBRIAN

45' 30' 113° 15'

DESCRIPTION OF MAP UNITS

Qal — ALLUVIUM AND COLLUVIUM (Quaternary). Blocks, gravel, sand, clay; unconsolidated.

LANDSLIDE DEPOSITS (Pleistocene?). Consist chiefly of tilted slump blocks. Form irregular, hummocky terrain. Occur primarily at edges of mesas formed by lavas capping Moenkopi rocks.

Tg — GRAVEL DEPOSITS (Tertiary?). Unconsolidated to poorly consolidated gravels comprising variously local and far-travelled lithologies. Typically exposed in channels beneath lava caps or forming inverted valleys. Generally *considerably above present erosion surface.*

YOUNGER BASALTIC FLOWS (Pliocene and Miocene). Exposed chiefly in one large flow-shaped remnant in center of mapped area, *and as remnants capping mesas and buttes in central part of* area. Height of remnants above present erosional surface varies from a few tens to several hundreds of meters and is a function of the underlying lithology. Unit has no relation to present topography. Lowermost flow from caprock of isolated butte probably belonging to this unit has yielded *a K-Ar age of 6.5 m.y.*

OLDER BASALTIC FLOWS (Pliocene and Miocene). Form Dellenbaugh Platform in southern part of Shivwits Plateau. Unit includes younger constructional volcanic features superimposed on the older flows. Height of flows above present erosional surface ranges from a few hundred to a few thousand meters (canyons). Unit rests on erosion surface about 50 m higher than that underneath Unit Tbv. Unit has no relation to present

KAIBAB FORMATION, BETA MEMBER (Leonardian). Massive to thick bedded, cherty limestone, gray to gray-brown, locally very fossiliferous. Forms bold cliff. Locally weathers into rounded turret-like forms. Transitional into Toroweap Formation below.

TOROWEAP AND COCONINO FORMATIONS, UNDIFFERENTIATED (Leonardian). Toroweap: composed of three members, in ascending order gamma, beta and alpha. Gamma and alpha are thin, slope-forming, yellowish to reddish, consist of dolomite, gypsum, sandstone, siltstone and breccia, and have been deformed by solution-collapse. The beta member is a massive cliff-former composed of fossiliferous light-gray limestone and chert. In the Shivwits Plateau area, this unit forms the most conspicuous cliff in the upper part of the Grand Canyon.
Coconino: yellowish-white, brown-weathering, cross-bedded, fine-grained sandstone and siltstone. Forms inconspicuous cliff at top of Hermit Shale.

KAIBAB, TOROWEAP AND COCONINO FORMATIONS, UNDIFFERENTIATED (Leonardian). Same units as described above, but grouped where cliff exposures prevent showing individual units on map.

HERMIT AND SUPAI FORMATIONS, UNDIFFERENTIATED (Hermit: Leonardian; Supai: Wolfcampian). Hermit: brick-red, slope-forming, thin-bedded siltstone, fine-grained sandstone and shale. Supai: interbedded reddish sandstone and shale, forming cliffs and ledges. Sandstone beds are medium- to thick-bedded. Cross-*bedding common. Contact between Hermit and Supai is interfingering.* Contact between Supai and Pakoon and Calville below is gradational and interfingering. For mapping purposes, contact placed at base of cliff that forms rim of Esplanade. Over most of Shivwits Plateau, this coincides with base of reddish to buff sandstones.

topography. Lowermost flow of unit has yielded a K-Ar age of 7.5 m.y.

BASALTIC FLOWS, UNDIFFERENTIATED (Pliocene? and Miocene?). Form isolated remnants several hundred meters above present erosional surface. Generally correlative with other basaltic units of area, but exact correlation is not known.

MUDDY CREEK FORMATION (Pliocene and Miocene). Interior-basin deposit. Includes fanglomerate, sandstone, siltstone, limestone, gypsum.

MOENKOPI FORMATION (Lower Triassic). Siltstone, shale, gypsum, conglomerate and limestone, reddish to reddish-brown, with greenish-white interbeds. Gypsum especially abundant in northern part of area. Complete section not exposed.

Pkα

KAIBAB FORMATION, ALPHA MEMBER (Leonardian). Slope-forming, tan, gray, pink and dirty-white silty thin-bedded limestone, cherty limestone, siltstone, shale and gypsum. Shale and gypsum increase northward. In southern part of area, unit consists chiefly of thin-bedded cherty silty limestone.

As one goes westward, these sandstones grade laterally into calcareous beds of the Pakoon and Calville Formations, and the contact is placed at the base of the continuous red bed sequence, typically above rim of Esplanade.

PAKOON AND CALVILLE FORMATIONS, UNDIFFERENTIATED (Pakoon: Wolfcampian; Calville: Wolfcampian and Virgilian). Pakoon Formation: gray to buff limestone, dolomitic limestone and sandstone, thin- to medium-bedded, locally cross-bedded. Forms ledgy slope. Thickens westward from featheredge in central Shivwits Plateau. Trasitional with Calville below and Supai above. Calville Formation: gray to pink limestone, siltstone, shale and sandstone. Typically forms ledgy slope. Beds of cross-bedded sandstone present locally. Upper part of unit becomes sandy eastward and grades laterally into Supai Formation. Lower contact is an erosional unconformity on top of Redwall Limestone. For mapping purposes, contact placed at top of conspicuous Redwall cliff.

LOWER PALEOZOIC AND PRECAMBRIAN ROCKS, UNDIFFERENTIATED (Precambrian through Osagian). Includes, in ascending order, Precambrian igneous and metamorphic rocks; Cambrian Tapeats Sandstone, Bright Angel Shale and Muav Limestone; Devonian Temple Butte Limestone; and Mississippian Redwall Limestone, as well as several disconformities and unconformities. Although typically distinctive, these formations have been grouped in this map because they crop out low in the walls of the Grand Canyon and thus are not visible from *the Shivwits Plateau. Unit forms precipitous cliff-ledge walls* of the inner Grand Canyon.

GEOLOGIC MAP OF PART OF THE SHIVWITS PLATEAU, MOHAVE COUNTY, ARIZONA

1975

Geology by Ivo Lucchitta and Richard Ivanic, 1973 and 1974

Prepared on behalf of the Jet Propulsion Laboratory, under NASA Contract NAS7-100

Plate I. Geologic map of part of the Shivwits Plateau, Mohave County, Arizona

Shivwits and bordering the canyon of the Colorado River is composed of extremely rugged and precipitous canyon country where vegetation is scanty, geologic exposures are excellent, and access is difficult to nonexistent.

The eastern and western geologic boundaries of the Shivwits Plateau are at the Hurricane and the Grand Wash faults, respectively. Both trend approximately north, are high-angle dip-slip and downthrown to the west, have strike lengths measured in hundreds of kilometers and displacements measured in hundreds to thousands of meters. Immediately west of the Grand Wash fault are the deep structural basins, block-faulted ranges, and tilted blocks characteristic of the Basin and Range province.

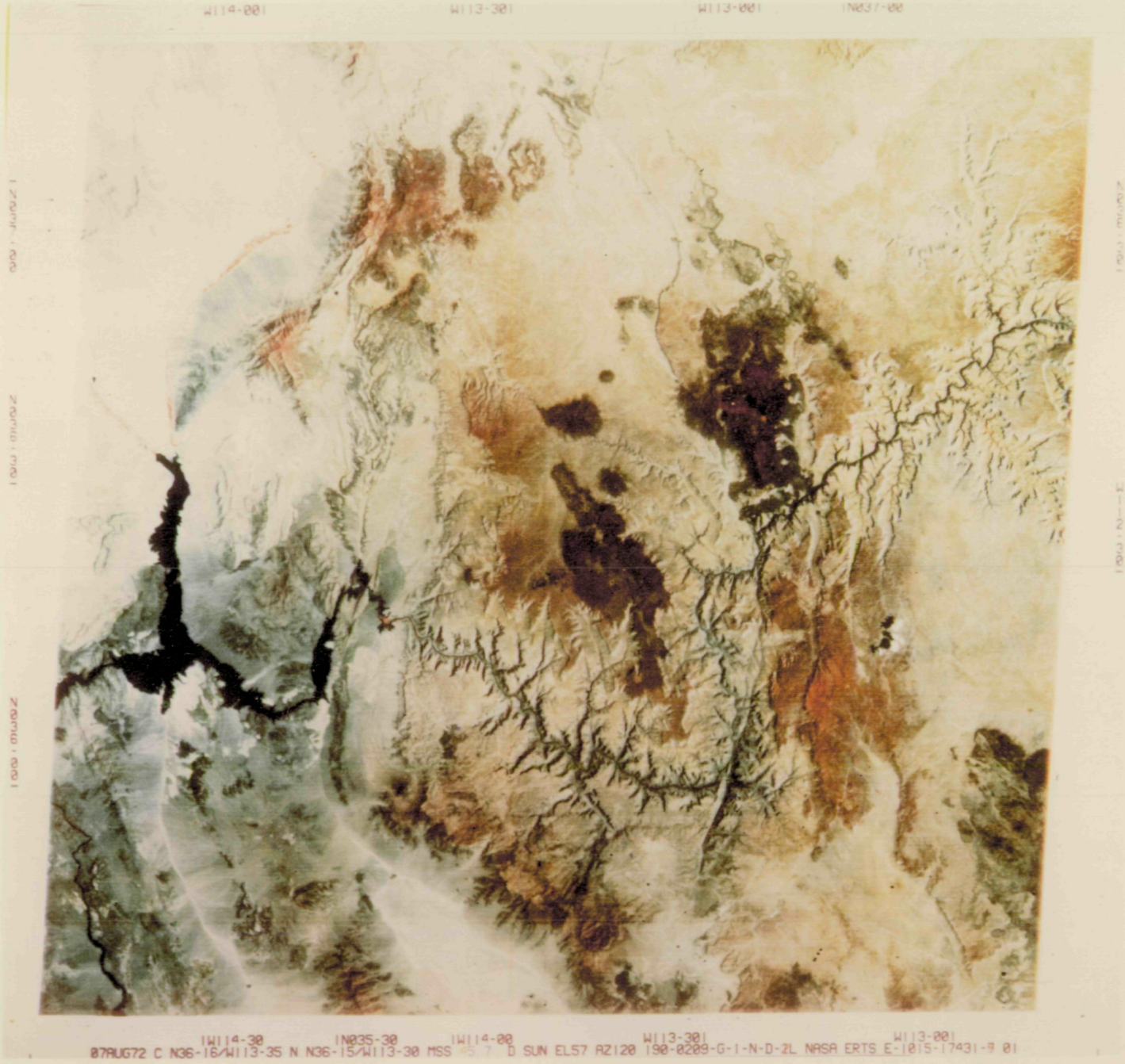

Fig. IV-B-1. General area of the Shivwits Plateau studied in ERTS investigation (NASA picture ERTS E-1015-17431, Aug. 7, 1972)

Preceding page blank

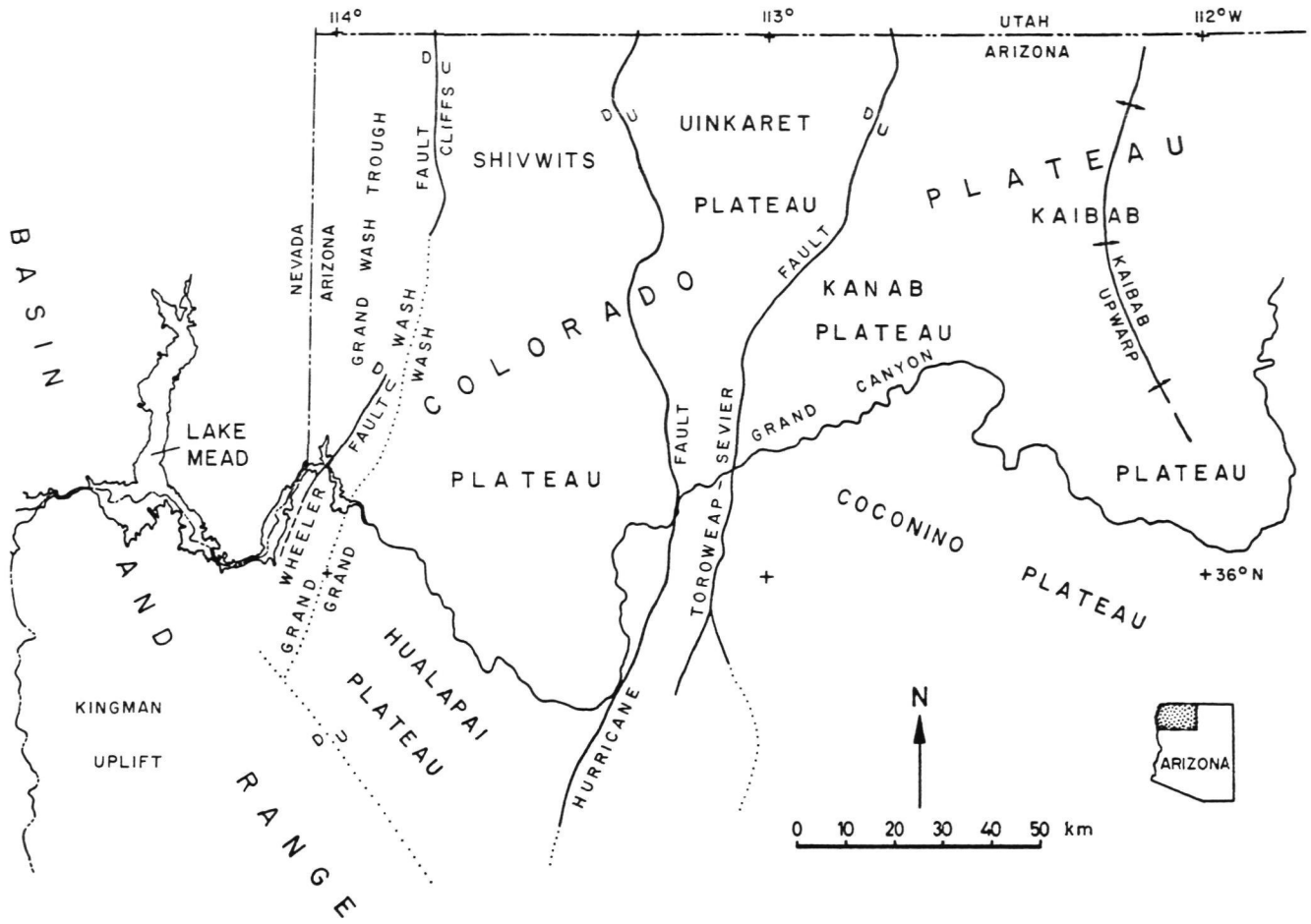

Fig. IV-B-2. Location map of northwestern Arizona. The western Grand Canyon region is west of the Toroweap-Sevier fault

Between the Hurricane and Grand Wash faults are many minor faults, most of which strike in the quadrant from northwest to northeast. All of these faults are high-angle and dip-slip.

The Shivwits Plateau block is underlain by nearly horizontal strata dipping gently north–northeast. Near the western margin of the plateau, the dip steepens to as much as 4° to 5°. These strata can be divided into two main groups on the basis of erosional characteristics: The Paleozoic rocks are, for the most part, resistant to erosion and form the rugged steep-walled canyons and cliffs characteristic of the Grand Canyon. The Mesozoic strata, by contrast, are much less resistant to erosion and consist of relatively thin and hard layers interbedded with thick, much softer layers. These rocks form the open, rolling landscape punctuated with cuesta scarps that characterizes most of northwestern Arizona. This landscape, especially the valleys at the foot of the cuesta scarps, has had a major influence on the pre-Colorado River and early Colorado drainage systems.

Lavas of late Cenozoic age are widely distributed on the Shivwits Plateau. Many are present as erosional remnants a few hundred meters above the current erosional level. Others form extensive sheets that have protected and preserved the ancient valleys down which they flowed. Some overlie, and have protected from erosion, ancient gravels containing clasts of quartzite and crystalline rocks that predate establishment of the modern Colorado River. Consequently, these lavas are important in deciphering the geomorphic history of northwestern Arizona.

The Shivwits Plateau is the northernmost of the three areas that comprise this ERTS investigation. Located at a sharp transition between the Colorado Plateaus and the Basin and Range provinces, and directly north of the

mouth of the Grand Canyon, the Shivwits is ideally situated to study:

(1) Geomorphic development of an area underlain by nearly horizontal. strata under semi-arid conditions.

(2) History of the Colorado River.

(3) Structural style of the western margin of the Colorado Plateau.

(4) Tectonic relation between the Colorado Plateau and the adjacent Basin and Range province.

These are the chief geologic problems to which this study is addressed. The major problem of applied geology has been to understand the factors affecting distribution of shallow water resources in the Shivwits Plateau (see Section V-A).

2. Methods Used

Field mapping was performed primarily on topographic maps at a scale of 1:24,000 (7-1/2 min) supplemented where topographic coverage was not available by color photographs from high-altitude aircraft. The 1:24,000 scale was used because it is that of the only good topographic coverage available, because it results in a good geologic map and thus good calibration for the ERTS data, and because it permits accurate mapping of critical areas. Owing to the large area to be covered in a short time and to the inaccessibility of much of the terrain, most of the mapping was performed by means of suitably spaced ground traverses, with the area between traverses covered by photogeologic mapping anchored by the traverses. Areas of unusual significance or complexity were mapped in detail. This approach was especially necessary and useful in the rugged canyon country at the southern end of the Shivwits Plateau, where traverses typically were made to prominent vantage points from which large areas could be seen and mapped.

ERTS tapes of the Shivwits Plateau area were computer-enhanced at the JPL Image Processing Laboratory (see Section VI of this Report). One product of the enhancement process consists of black and white positive or negative transparencies, each representing the scene modified by a specific enhancement process (stretches of various types, ratios between spectral bands, etc.). These transparencies were studied on the International Imaging Systems (I^2S) viewer, a device that consists of four projectors, each with a blue, green, and red filter, which superimpose the images on a single ground-glass screen. By using various transparencies and changing the color associated with each, specific enhancement procedures that emphasize or subdue any element or class of elements in a given scene can be studied.

The number of transparencies, taken four at a time, with three filter possibilities plus white for each of the four, results in a large number of possible combinations. To simplify and accelerate analysis and to systematize results, three transparencies at a time were viewed. Seventeen discrete, well known structural and stratigraphic features were selected as test points, and each combination of transparencies and colors was tested as to how it portrayed and emphasized each test point. The combinations then were rated as good, fair, or poor and were tabulated.

3. Applications of Remote-Sensing Data[2] in the Shivwits Plateau Study

a. Types and scales of images used. The ERTS images used most frequently in the field were 1:1,000,000-scale paper prints, which included black-and-white prints of spectral bands 5, 6, and 7 and prints of the false-color infrared composite. Also used was a paper print of a false-color enhanced image at a scale of about 1:440,000 and consisting of the green/IR 1 ratio with stretch and atmospheric correction.

All aerial photographs were taken in regular color by high-altitude reconnaissance aircraft. Two different series of photographs, in part overlapping, were used: one at a scale of about 1:114,000, the other about 1:104,000. In the laboratory, 23- by 23-cm (9- by 9-in.) positive transparencies were used; in the field, contact prints on paper base.

b. Uses and limitations of ERTS data as applied to field mapping on the Shivwits Plateau. Owing to the large discrepancy between the scale of the ERTS pictures and that at which field mapping was performed, ERTS images were not used directly for mapping. Although high-altitude aircraft photographs are much more suitable for this purpose, ERTS images were consulted constantly to guide and to direct the mapping and to put it in regional context. The large-scale field data and the small-scale ERTS data usually were combined in a feedback loop that permitted constant generation and testing hypotheses. Field information generally raised questions on the regional significance and validity of the observations made. ERTS data provided answers to these questions and guided further fieldwork to critical areas where detailed mapping could test hypotheses of regional significance.

[2]For purposes of this study, remote-sensing data signify high-altitude aircraft images as well as various types of ERTS data.

Many results were obtained by using ERTS images on the Shivwits Plateau. Some of the most significant results which could not have been derived without the ERTS images are:

(1) Determination of the structural grain of the area.

(2) Comparison of this grain with that of the adjacent Basin and Range province.

(3) Detection of anomalies in the structural pattern.

(4) Mapping of major faults.

(5) Determination of relation between map outcrop patterns of the lavas in northwestern Arizona and the paleogeography existing in lava time.

(6) Determination of significance of cuesta scarps in the development of landscape.

(7) Subdivision of scarps into old erosional ones and younger ones generated by fault movements.

(8) Detection of an anomalous belt of no volcanic centers on the Shivwits and adjacent plateaus, and association of this belt with a belt of anomalous faults, with two great bends in the Hurricane fault, and with transcurrent faults in the Basin and Range province.

(9) Understanding of relations between orientation, age, and degree of dissection of scarps.

(10) Concentration of shallow ground water where faults cut lava filling old valleys.

Direct use of ERTS images could have been made if the Shivwits Plateau had been mapped at a smaller scale, for example the 1:250,000 scale of 2° sheets. The low distortion of the ERTS images makes them almost correct planimetrically, and their scale is more suitable for small-scale mapping than that of commonly available aerial photography. ERTS pictures can be enlarged to scales of 1:250,000 with retention of good resolution and sharpness, and on the basis of experience on the Shivwits Plateau, we recommend using ERTS pictures enlarged to 1:250,000 as an excellent map base for 2° work.

c. Experimental photogeologic maps made on ERTS bases. One of the obvious uses of ERTS pictures is to produce photogeologic maps of large areas in a relatively short time. This would be most useful in areas that have been mapped little or not at all, for example in many developing countries, but only if the maps portray reality reasonably closely.

ERTS-1 pictures show much tonal and color detail, but this detail does not necessarily correspond to geologic features because other factors such as vegetation and slope are superimposed on the signatures of the geologic units. Consequently, the same geologic unit may have different photographic expressions, and different units may appear identical. To complicate matters even further, most of the small "textural" features that give geologic units their characteristic appearance on conventional aerial photographs are well below the resolution limit on ERTS pictures. For example, it is barely possible to see on ERTS pictures that the walls of the Grand Canyon are comprised of stratified rocks, let alone to discriminate and identify individual stratigraphic units. Clearly, one cannot map each detail of tone or color and expect the resulting units to have genuine geologic significance.

To test the level of detail necessary to yield an accurate and realistic map, we prepared several photogeologic maps on a black-and-white paper base at a scale of 1:1,000,000. This base was selected because it represents the most difficult case possible. The use of a larger scale and color should make it easier to discriminate and identify units. The photo covers northwestern Arizona, including the Shivwits Plateau, as well as adjacent parts of the Basin and Range province. Enough geologic mapping exists for this area to provide adequate calibration for the photomaps. The geology includes subhorizontal sedimentary rocks; tilted and deformed sedimentary, metamorphic, and igneous rocks; basin fill; and lava flows.

One map prepared shows all available detail. This map has a large number of units, is cluttered and hard to read, and has poor correspondence between photogeologic and geologic units.

Another map shows basin fill, homogeneous basement, foliated basement, layered sedimentary rocks, and lava flows. It is easy to read, and has a good correspondence to the geology of the area. A map showing this level of detail would be a valuable contribution in areas of unknown geology.

A third map shows the same units as the second map with additional subdivisions wherever this could be done reliably and significantly. The map is easy to read and corresponds well to the geology. However, this type of map can be produced only if exposures are good, if there are distinctive geologic units, or if there is ground control to calibrate photogeologic units.

A fourth map shows lineaments. In preparing this map, it soon became clear that it is easy to produce a busy and impressive map by plotting each lineament. But these lineaments indiscriminately include faults, fractures,

foliation, bedding, dikes, topographic features, and vegetation lines. Furthermore, they span the range from objective to imaginary. A map of this type at best shows the preferred directions of fracturing for an area, or points out concentrations of fractures. At worst, it is confusing and misleading. A significant improvement can be achieved by subdividing into concordant and crosscutting lineaments, which are more likely to be faults than are the concordant ones. Questionable lineaments should either not be mapped, or should be clearly identified as such.

In conclusion, ERTS-based photogeologic maps are likely to be accurate and useful if the photogeologic units are kept simple, and if photo-lineaments are mapped only where objective and are subdivided into concordant and crosscutting. Even minor ground control improves accuracy and commonly permits more detailed mapping.

Geologic results derived from the study of the Shivwits Plateau in the ERTS-1 investigation are discussed in the following paragraphs.

4. Results

Physiographically and geologically, the Shivwits Plateau is typical of the western Grand Canyon region, of which it forms a major part. Consequently, most of the geologic results derived from the Shivwits can be extended to the western Grand Canyon region.

The western Grand Canyon region (see Fig. IV-B-2) is an area of tablelands, scarps, and canyons. This region contrasts strongly with the Basin and Range topography and structure to the west and south, and provides a classic example of landscape development in nearly horizontal sedimentary rocks under semi-arid conditions. The region also contains critical data on the development of drainage in northwestern Arizona, including part of the Colorado River and its canyon. Summarized below are the chief results pertaining to these geologic characteristics.

a. Physiographic development. The physiographic development of the western Grand Canyon area has been controlled by the following factors:

(1) Uplift southwest of the present margin of the Colorado Plateau.

(2) Gentle northeast dip of the strata.

(3) Interlayering of hard and soft strata.

(4) Faulting.

(5) Emplacement of lavas.

(6) Incision by the Colorado River and its tributaries.

The landscape that has resulted from these factors is composed of features that can be grouped in five classes:

(1) Beveled surfaces, typically developed in rocks of uniform resistance to erosion such as massive crystallines (Precambrian basement) or the lower Paleozoic carbonate sequence.

(2) Stripped surfaces, commonly developed on a particularly resistant stratum at the base of a less resistant sequence.

(3) Scarps, either erosional or tectonic.

(4) Aggradation surfaces, most notably represented by lava flows.

(5) Canyons.

The process by which the present landscape evolved began with uplift of a large area southwest of the present margin of the Colorado Plateau. Although this area borders the Colorado Plateau across much of central Arizona, the part under discussion here centers on Kingman, Arizona, and is therefore referred to in this report as the "Kingman Uplift" (see Figs. IV-B-2 and IV-B-3a; also see Refs. IV-B-1 through IV-B-4). The Kingman Uplift is old, as evidenced by the complete removal of all Mesozoic and Paleozoic rocks, and may be as old as Cretaceous (Ref. IV-B-5). Structural uplift has been great, as indicated even now, after general subsidence of the area, by the high topographic elevation of the Precambrian basement.

The Kingman Uplift resulted in deep erosion, which stripped the sedimentary cover from the Precambrian crystalline rocks. The erosion produced pediment-like surfaces truncating rocks of equal resistance to erosion, as well as scarps facing southwest, formed wherever a hard sedimentary stratum capped a relatively soft thick layer (Fig. IV-B-4). The rise of the Kingman Uplift probably also resulted in formation of the gentle northeast dip that prevails throughout northwestern Arizona. This dip, which ranges from as much as 4° at the southwest border of the Colorado Plateau in this area to about 1° in the interior, has enabled the erosional scarps formed on the flanks of the Kingman Uplift to retreat northeast, down the structural slope, at a rate that is high compared with the overall lowering of the region by erosion. A low dip is ideal for the retreat and preservation of scarps. High dips tend to lock scarps into a nearly fixed location. Conversely, scarps developed in flat-lying strata are attacked by erosion from all sides and degenerate into mesas and buttes.

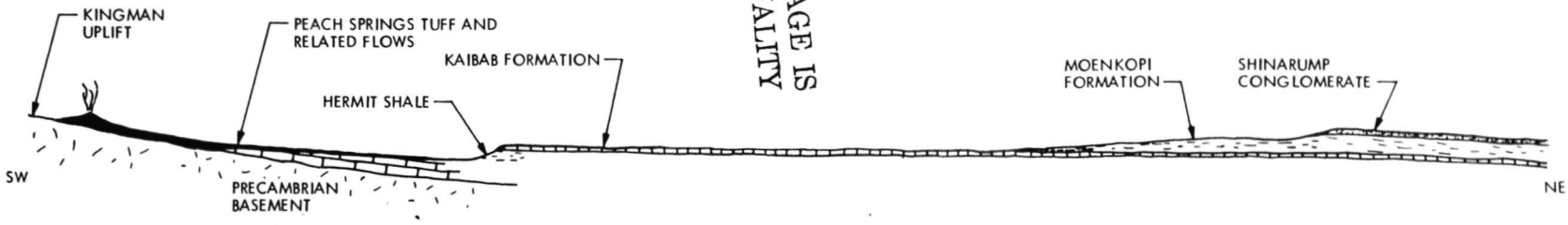

(a) INTERPRETIVE COMPOSITE CROSS SECTION BEFORE MAJOR MOVEMENT ON GRAND WASH AND HURRICANE FAULTS

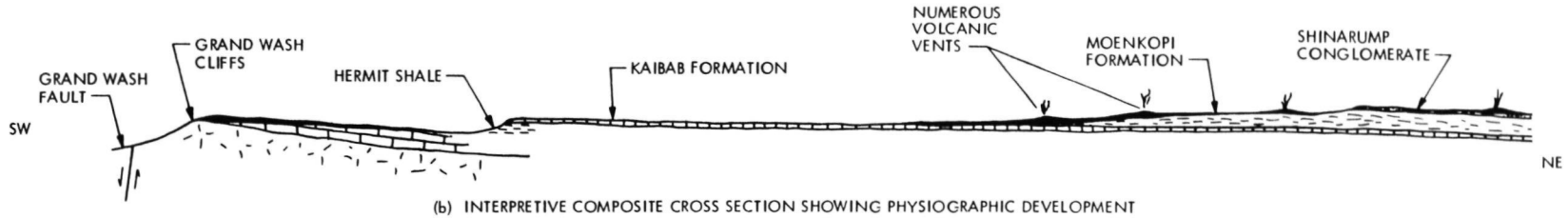

(b) INTERPRETIVE COMPOSITE CROSS SECTION SHOWING PHYSIOGRAPHIC DEVELOPMENT

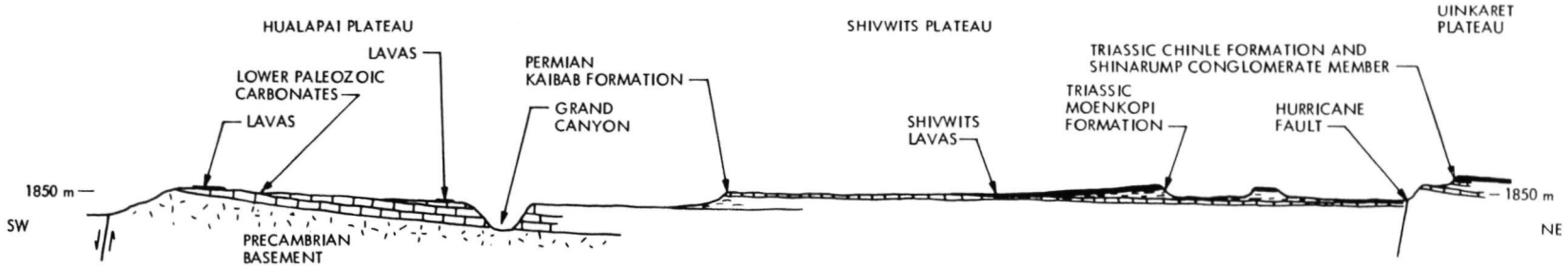

(c) COMPOSITE CROSS SECTION SHOWING PRESENT RELATIONS

Fig. IV-B-3. Cross sections across western Grand Canyon region, Arizona. Not shown to true scale. Width of view is approximately 100 km (a) Before major movement on Grand Wash and Hurricane faults. (b) After movement on Grand Wash fault, but before major movement on Hurricane fault and before Canyon cutting. (c) Present

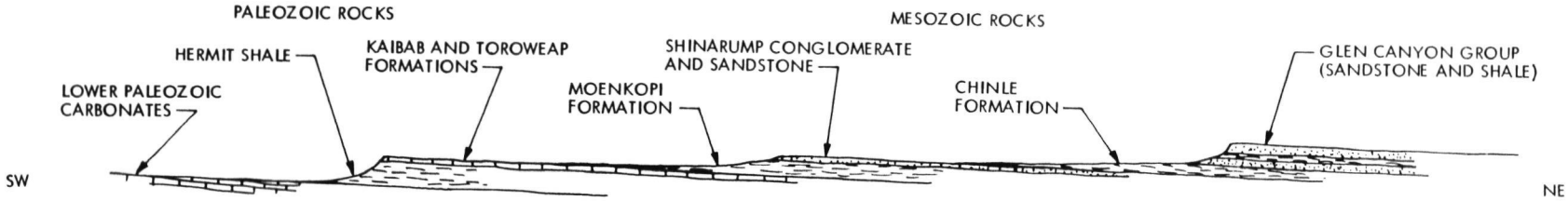

Fig. IV-B-4. Diagrammatic cross section across western Grand Canyon region, showing stratigraphic units significant in the geomorphic development of the area. Not shown to true scale

The principal scarp makers in the western Grand Canyon area have been the Paleozoic Kaibab and Toroweap Limestone over the Hermit Shale, the Mesozoic Shinarump Conglomerate and Sandstone over the Moenkopi Shale and Siltstone, and the Mesozoic sandstone of the Glen Canyon group over the Chinle Shale (Fig. IV-B-5). These, and other similar scarps higher in the section and now located in Utah, form the "Great Staircase" of Dutton (see Ref. IV-B-6).

The old erosional scarps that are still retreating away from the Kingman Uplift are highly embayed (see Fig. IV-B-6). An example is the southwest-facing part of the Upper Grand Wash Cliffs scarp, which is composed of the Kaibab and Toroweap Limestone and Coconino Sandstone over the Hermit Shale. This scarp can be traced southeastward, more or less along strike, through the Aubrey Cliffs, the Sedona area, and finally into the Mogollon Rim of east-central Arizona, indicating that all of these features may be part of an ancient erosional scarp retreating down the structural slope from a belt of uplift composed of the Kingman Uplift and the central Arizona Highlands (see Fig. IV-B-5).

Scarps younger than those mentioned are produced generally by faulting and are relatively little embayed. The youngest scarps, produced by the most recent movements, are embayed very little. Examples are, respectively, the west-facing part of the Upper Grand Wash Cliffs, and the Hurricane Cliffs (see Fig. IV-B-5). Evidently, faulting served as a trigger event that generated new scarps. The orientation of these scarps reflects that of the associated faults, and not regional strike. However, given sufficient time and a favorable orientation to regional dip, these scarps eventually also will retreat down-dip and substantially modify the pre-existing landscape. In the western Grand Canyon region, they have not yet done so.

The erosional lowering of the western Grand Canyon region has been relatively high on soft Mesozoic shale and relatively low on limestone, conglomerate, and sandstone. The Kaibab Limestone especially has been a barrier to erosion so that it now underlies a stripped surface covering much of northwestern Arizona. In many cases, this surface persists over structural highs as well as lows (see Fig. IV-B-6), producing the remarkable coincidence of structural and geomorphic forms characteristic of the southwestern part of the Colorado Plateau. The difference between the rate of erosion in the Kaibab Limestone and that in overlying rocks seems to be at least one order of magnitude. Lesser, but still considerable, disparities exist between the rates of erosion of the various Mesozoic scarp makers and the associated shale units. Consequently, it is unrealistic to calculate a rate of erosion based on a specific unit, and then apply this rate to the whole section. The Kaibab Limestone represents a major erosional discontinuity. Above it, erosion has been fast and has produced the open, subdued landscape typical of most of the southwestern Colorado Plateau. Below it, erosion has operated slowly owing to the greater resistance of the rocks and has produced the sharp, angular landscape of cliffs and canyons exemplified by the Grand Canyon.

On the Shivwits Plateau, which is the westernmost part of the western Grand Canyon region (see Fig. IV-B-2), most of the area (i.e., the part not dissected by canyons) has been lowered no more than 250 m in the last 6 m.y.,[3] the probable age of lavas covering an old erosion surface developed in the Moenkopi Formation. This represents a rate of about 40 m per 1 m.y., probably one of the highest rates for the Mesozoic section. In the same time interval, the Shinarump scarp has retreated northeastward several tens of kilometers. Consequently, the rate of retreat of this scarp, and probably of other scarps higher in the section, has been at least one to two orders of magnitude greater than the overall lowering of the region. The main activity recorded by a time-lapse camera operating on a geologic time scale would be the down-dip, near-horizontal retreat of erosional scarps. Certain aspects of the role of scarps in shaping the landscape of the western Grand Canyon are discussed in Refs. IV-B-6, and IV-B-8 through IV-B-10.

Lavas were emplaced in several parts of the western Grand Canyon region in Miocene and later time. The emplacement occurred in multiple episodes, the most recent commonly in the Holocene epoch. Many of the lavas flowed preferentially north–northwestward along strike valleys, or cuesta troughs, remnants of which are now preserved beneath the lavas. In several instances, the lavas have protected the old valley floors from erosion, resulting in reversal of topography. A conspicuous example of this is the Dellenbaugh Platform at the southern end of the Shivwits Plateau (see Figs. IV-B-3 and IV-B-5).

Many of the lavas in the western Ground Canyon region are concentrated in strike valleys at the foot of the Shinarump scarp. It is likely that this scarp, during its northeastward retreat down the structural slope, has had a major effect on drainage in the area, to which it has imparted a subsequent northwest to north–northwest grain. Evidence for this drainage system is found in lavas

[3] We now have a K-Ar date of 6.0 ±0.3 m.y. for younger (lower) lavas and 7.5 ±0.3 m.y. for older (higher) lavas (see Ref. IV-B-7).

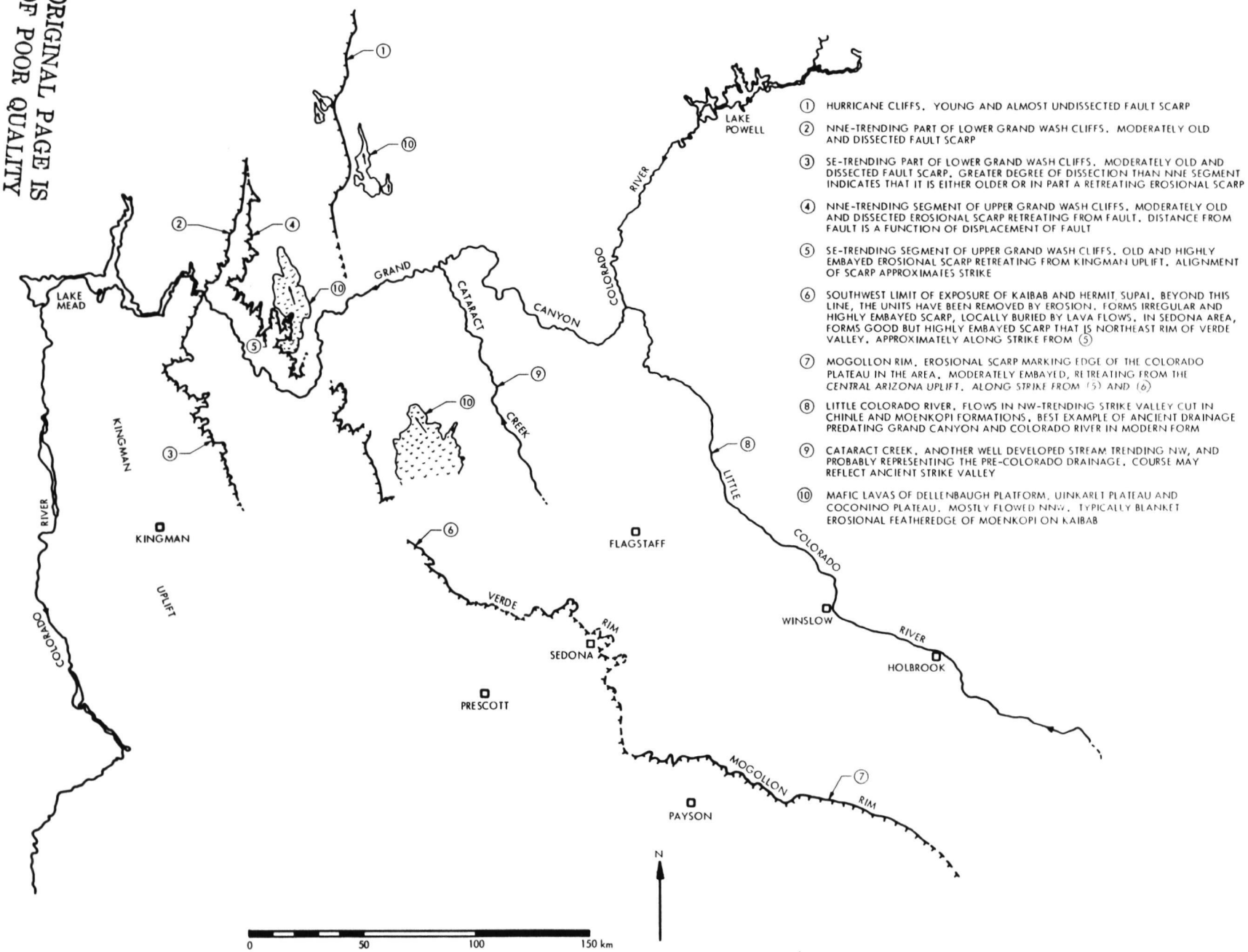

Fig. IV-B-5. Map of northwestern Arizona showing scarps of various types, ages, and degrees of dissection; flow vectors in lavas; and streams that represent ancient pre-Grand Canyon drainages

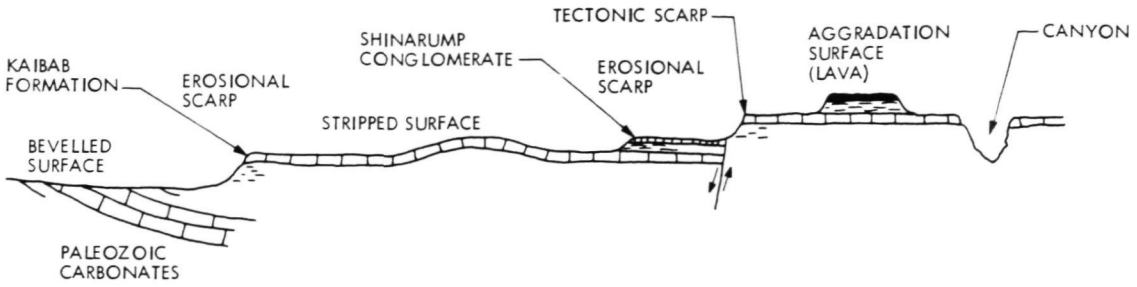

Fig. IV-B-6. Geomorphic elements in the western Grand Canyon region. The Kaibab Limestone is a dominant geomorphic element that persists even on structural highs

of the Shivwits, Uinkaret, and Coconino Plateaus, as well as in the course of the Little Colorado River and of Cataract Creek (see Fig. IV-B-5). Both of these streams are well established, much longer and better developed than other tributaries to the Grand Canyon, and probably older than the Grand Canyon as a whole.

Lavas on the Dellenbaugh Platform, which may be as young as 6 m.y.,[4] are bounded on three sides by the Grand Canyon, yet rest on a surface of low relief covered by locally derived regolith. Moreover, they overlie and are overlain by abundant and unmistakable Shinarump-type gravel, which can have happened only if the lavas flowed in a valley flanked on its northeastern side by a Shinarump scarp that shed its debris into the valley both before and after emplacement of the lavas. The position of this scarp is now in part occupied by the Colorado River and some of its tributaries. These factors suggest that, in lava time, no deeply incised Colorado River drainage existed in the vicinity of the Dellenbaugh Platform.

Conclusions

(1) Erosional scarps, developed where hard strata overlie soft strata, were formed initially by erosion resulting from arching of the Kingman Uplift southwest of the Colorado Plateau and have been retreating northeastward, down dip, since their formation.

(2) The primary physiographic process in the western Grand Canyon region has been the retreat of erosional scarps down dip.

(3) The dip of a structural slope is critical for the retreat and preservation of scarps. If the dip is too steep (greater than about 10°), scarps cannot retreat far. If the dip is too shallow (less than about 1°), scarps are attacked by erosion from all sides and decay into mesas and buttes.

(4) New scarps, formed by faulting, retreat down the structural slope if their orientation to the regional dip is appropriate, in time appreciably modifying the older landscape. On the Shivwits Plateau, they are too young to have done this.

(5) In the western Grand Canyon region, the degree of embayment of scarps formed by resistant layers with similar dips is roughly proportional to their age.

(6) The rate of scarp retreat has been between one and two orders of magnitude greater than the rate of overall lowering of the region.

(7) Scarps, and the cuesta troughs at their bases, have had a major effect on the drainage of the region, to which they have imparted a northwest to north-northwest grain.

b. History of the Colorado River. The Colorado River is a complex drainage system composed of various parts with different and, in some cases, partly independent histories (see Refs. IV-B-1 through IV-B-3, IV-B-11 through IV-B-13). Most notably, three segments must be considered (Fig. IV-B-7):

(1) East and upstream from the Kaibab upwarp, henceforth referred to as the ancestral Upper Colorado Drainage.

(2) West and downstream of the Grand Wash Cliffs, which mark the western edge of the Colorado Plateau. This segment is much younger than the Upper Colorado Drainage and is referred to as the ancestral Lower Colorado Drainage.

(3) The Grand Canyon section, the most magnificent and best known part of the river, but also the most enigmatic because erosion has removed most of the deposits critical to deciphering the river's history in the section.

Data on the Upper Colorado Drainage are summarized in Ref. IV-B-12 by Hunt, who states that some of this

[4] The oldest lava on the Dellenbaugh Platform has yielded a K-Ar age of 7.5 m.y. (see Footnote 3).

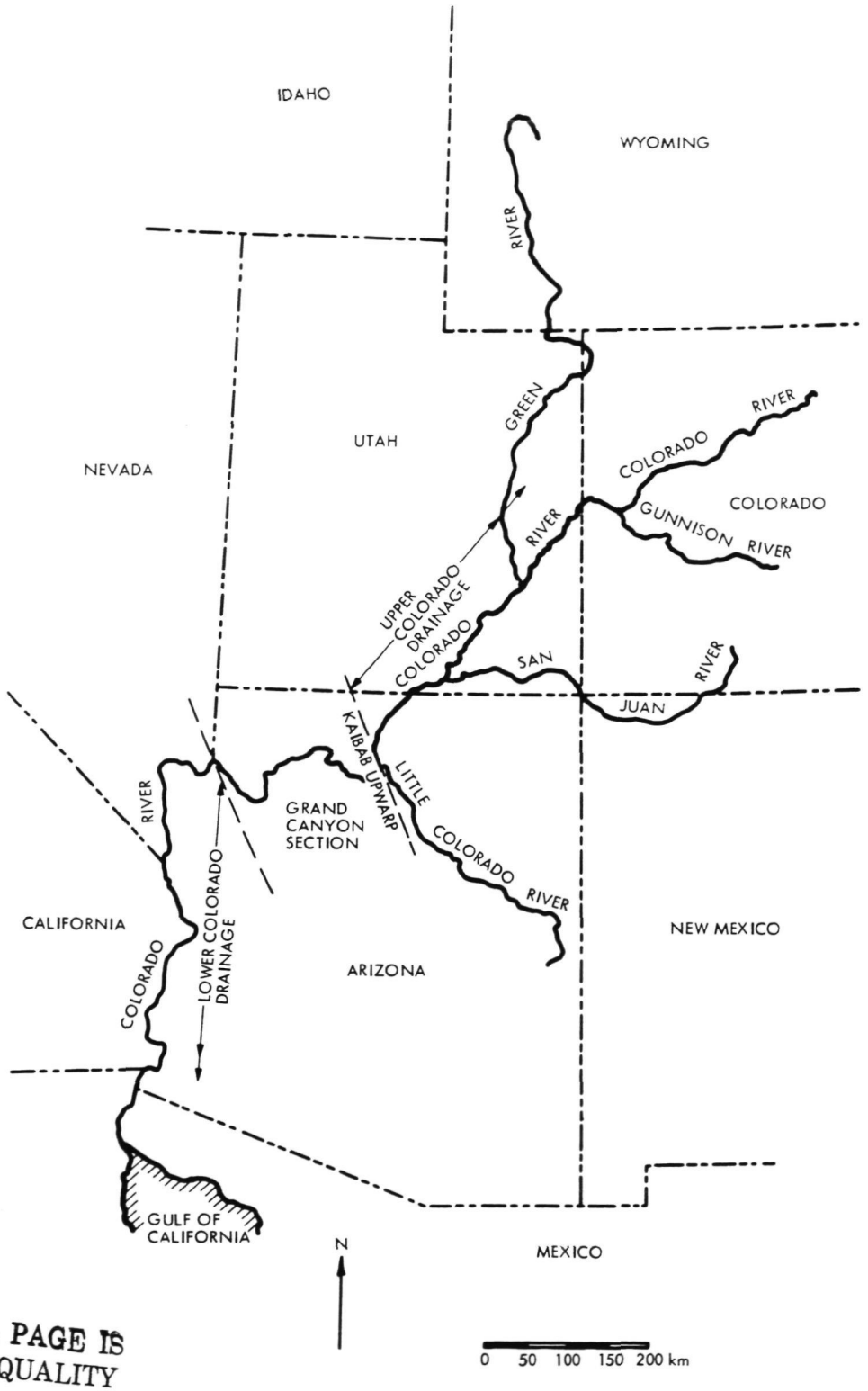

Fig. IV-B-7. Map showing segments comprising the Colorado River drainage

drainage system existed by Oligocene time, and most by Miocene time. Evidence for the Lower Colorado Drainage is summarized in Ref. IV-B-2 by Lucchitta, who states that this part of the river probably originated between 5 and 10 m.y. ago, or in late Miocene to early Pliocene time. These ages raise the following questions:

(1) Where did the ancestral Upper Colorado drain when the ancestral Lower Colorado apparently did not exist?

(2) When, where, and how did the two river systems become integrated into the modern Colorado River?

Earlier workers were not concerned with these problems as such because to them the Colorado was one integrated drainage system from its beginning, which was placed in early Tertiary time by pioneering geologists, and in the late Tertiary, typically Miocene or later, by most subsequent geologists. These later geologists recognized the significance of interior-basin deposits (Muddy Creek Formation) of Miocene to Pliocene age lying across the present path of the Colorado River in western Arizona and southern Nevada (see Ref. IV-B-14), and therefore assumed that the entire river postdated these deposits.

The more modern view that the Colorado River is composed of segments differing in age and mode of origin was proposed by Hunt (Ref. IV-B-11) and later simplified and clarified by McKee et al. (Ref. IV-B-13). Within this framework, two main alternative hypotheses emerged, that of Hunt (Refs. IV-B-11 and IV-B-12) and that typified by McKee et al. (Ref. IV-B-13).

Hunt's hypothesis is that the Colorado River originated relatively early (middle Miocene and earlier) through integration of older drainages of different ages and origins; that its course is partly antecedent and partly superposed; that this course paralleled the present one at the regional scale, but diverged from it considerably in detail; and that, because of the local divergence, certain segments of the modern course (e.g., western Grand Canyon) are younger than the river as a whole (see Fig. IV-B-8a, 8b, 8c). Hunt recognizes that a throughflowing drainage in the Lake Mead area is precluded by the interior-basin deposits, but he applies this limitation only to the river as it flows through the western Grand Canyon and the Lake Mead area, which in his view are recent modifications of the old course. This old course bypassed the Lake Mead area by flowing to the south of it, in the general vicinity of Kingman, Arizona. This drainage system was disrupted and ponded by a welded tuff of westerly derivation, the Peach Springs Tuff of Young (see Ref. IV-B-3) about 18 m.y. ago and then by basin–range faulting west of the Grand Wash fault. The result was a lake located generally in the western Grand Canyon region. Subsequently, large-scale subterranean piping through cavernous Paleozoic limestone resulted in westward discharge from this lake through springs located near the present mouth of the Grand Canyon. These springs filled another lake in which was deposited the Hualapai Limestone, according to Hunt (Ref. IV-B-12) younger than the Muddy Creek Formation and the youngest pre-Colorado-River deposit in the area. When flow in the Upper Colorado Drainage increased, the lakes overflowed, the overflow cut the western Grand Canyon, and the Colorado River was at last established as an integrated drainage in its present course.

The hypothesis of McKee et al. (see Ref. IV-B-13) is based on a relatively recent development of the present Colorado River as an integrated stream (see Fig. IV-B-9a, 9b, 9c). These authors accept the antiquity of the ancestral Upper Colorado Drainage. They also accept that interior-basin deposition was a widespread occurrence in the southern Basin and Range province in Miocene time, so that no Colorado River existed there until after 10.6 m.y. ago (latest Miocene to early Pliocene). This is the youngest date available on the Muddy Creek Formation, which is present at the mouth of the Grand Canyon and widespread in the Lake Mead area. The ancestral Upper Colorado Drainage followed approximately its present course as far west as the Kaibab upwarp, and then swung southeastward along what is now the valley of the Little Colorado River. Ultimately, it followed the course of the present Rio Grande to the Gulf of Mexico. The ancestral Lower Colorado Drainage developed by integration of interior basins and pre-existing drainage systems, and by headward erosion through the Grand Canyon section. Eventually, it cut through the Kaibab upwarp and captured the Upper Colorado Drainage.

Both of these hypotheses accept the existence of an ancestral Upper Colorado Drainage in Miocene or even Oligocene time. This drainage system may have consisted of the ancestral Colorado River itself or of streams such as the San Juan River which are now tributaries to the Colorado. In any case, the ancient drainage system can be traced almost to the present confluence of the Colorado and Little Colorado Rivers. Data that provide a critical test of the two hypotheses have become available in recent years. These data indicate that neither hypothesis can be accepted in its entirety because of conflicts with known facts. The arguments pertaining to the Lower Colorado Drainage have been advanced by Lucchitta (see Refs. IV-B-1 and IV-B-2) and by Young and Brennan (see Ref. IV-B-4); those for the Upper Colorado Drainage are summarized by Lucchitta (Ref. IV-B-15 and IV-16) and by

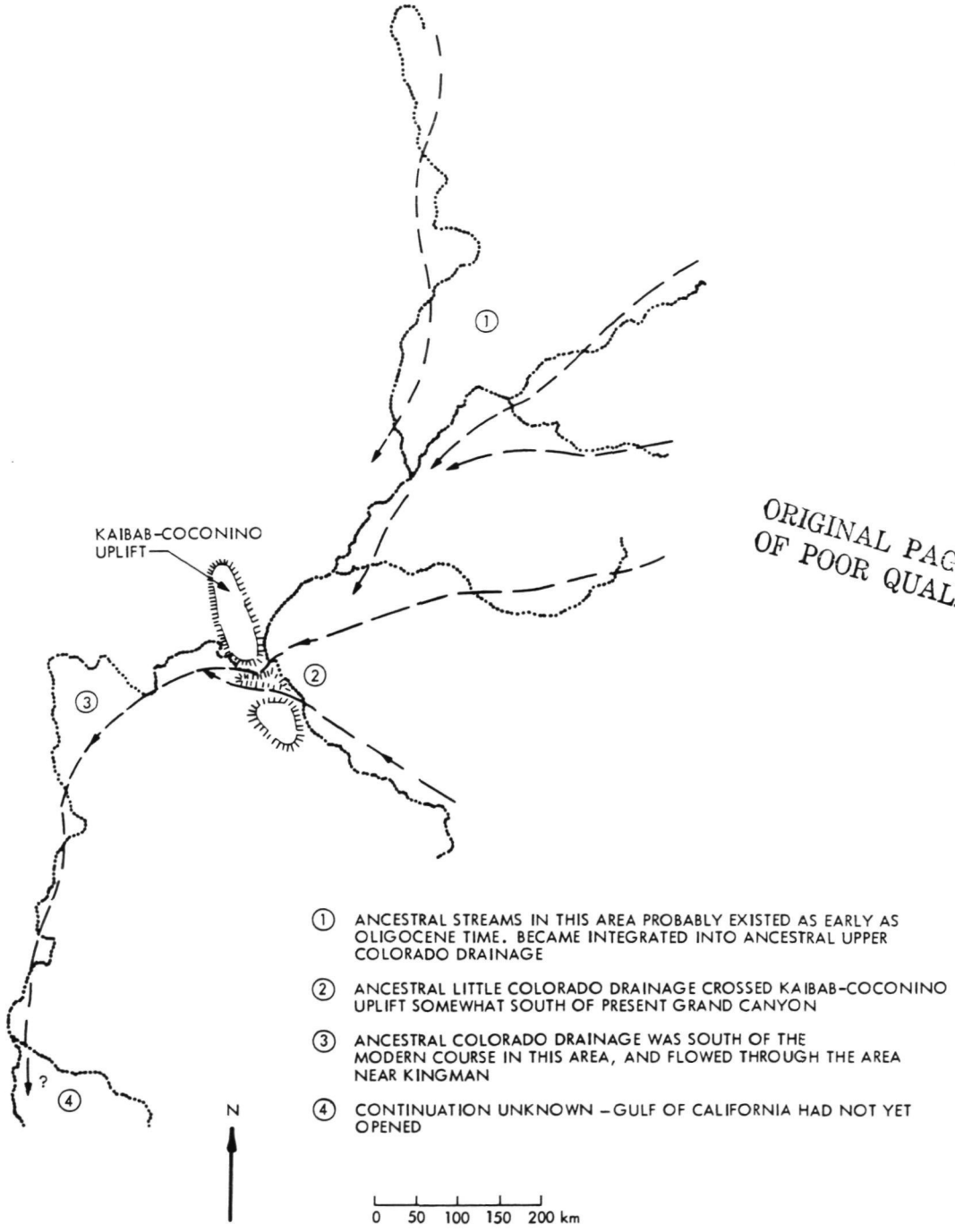

Fig. IV-B-8a. Hunt's hypothesis. Ancestral Colorado Drainage before basin–range faulting (i.e., before about 18 m.y.b.p.)

Lucchitta and Young (Ref. IV-B-17) and will not be repeated here in detail because they are not directly involved in the Shivwits Plateau study. In essence, geomorphic, stratigraphic, and structural data from the Basin and Range area and from the western edge of the plateau indicate that Hunt's idea of an ancient continuation of the Upper Colorado Drainage westward from the Colorado Plateau is untenable. Similarly, several lines of evidence from the Little Colorado River valley in northeastern Arizona indicate that an ancient continuation

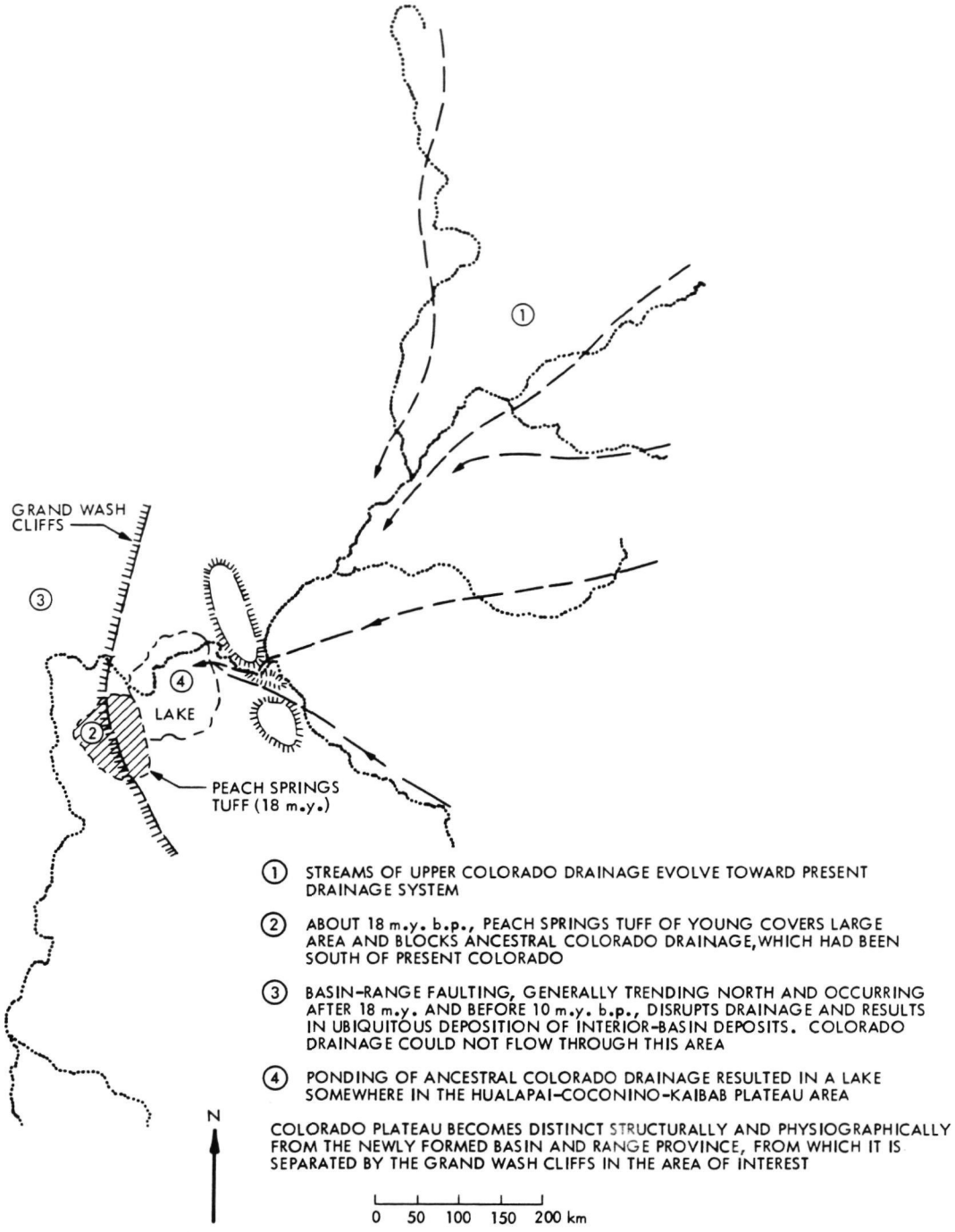

Fig. IV-B-8b. Hunt's hypothesis. Ancestral Colorado Drainage after effusion of Peach Springs Tuff and basin–range faulting (after 18 m.y., before 10 m.y.b.p.)

of the Upper Colorado Drainage southeastward along that valley, as postulated by McKee et al., is improbable. Because there are no other possibilities, it is appropriate to revert to the Grand Canyon section to find the continuation of the Upper Colorado Drainage and to establish how and when the Upper and the Lower Colorado Drainages were united.

Lavas ranging in age from 14 m.y. (Ref. IV-B-18) to less than 5 m.y. (Ref. IV-B-19) are common throughout

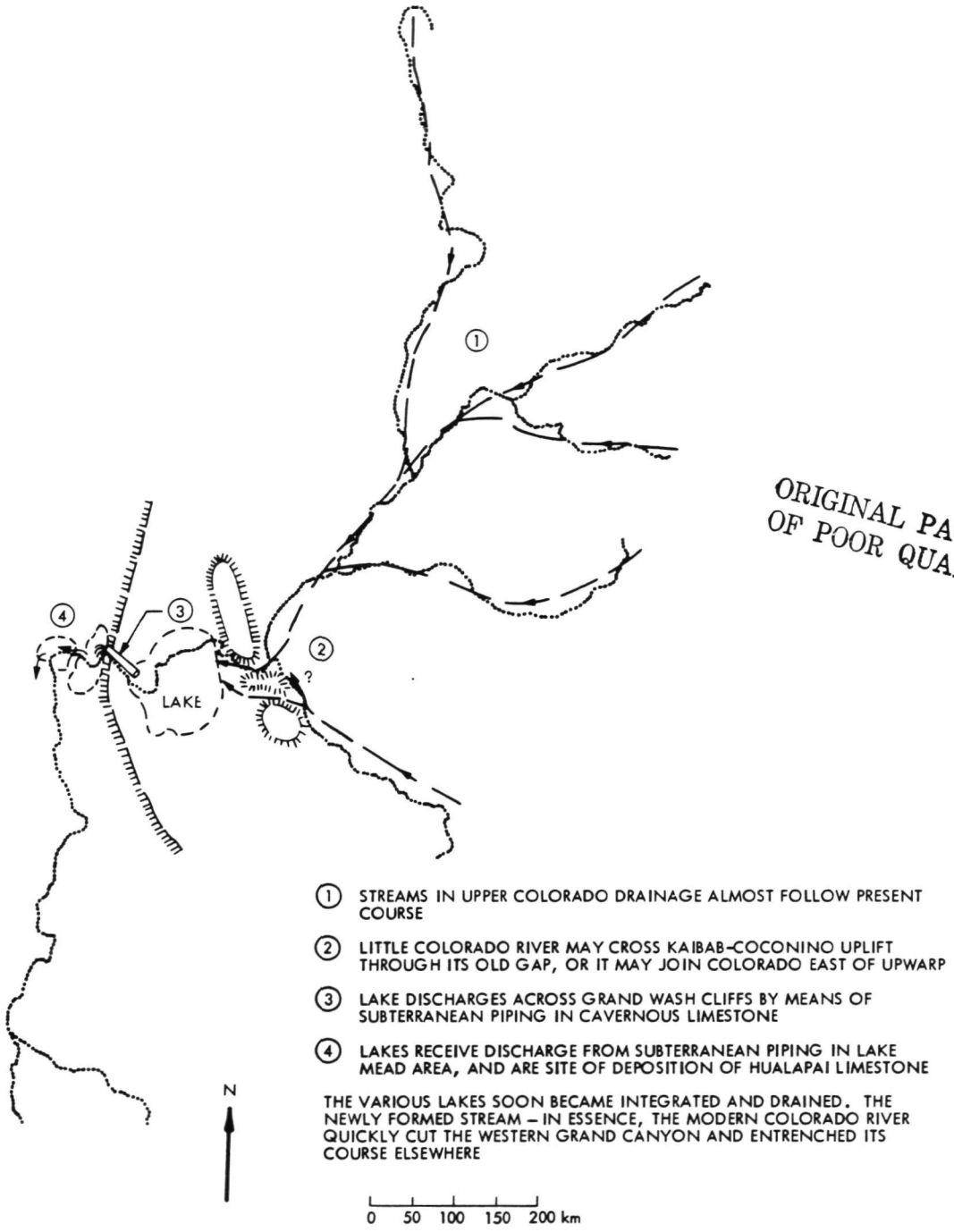

Fig. IV-B-8c. Hunt's hypothesis. Ancestral Colorado Drainage shortly before integration into modern course

northwestern Arizona. Most of these lavas rest on the Moenkopi Formation of Triassic age; some rest on the lower part of the overlying Chinle Formation. Evidently, a Moenkopi and Chinle landscape existed on the Coconino Plateau and, significantly, on the Kaibab upwarp south of the Grand Canyon from middle Miocene to early Pliocene time. The Grand Canyon crosses the Kaibab Plateau in a great bend strongly suggestive of an arcuate strike valley, or "racetrack," as would be developed in the Chinle or Moenkopi Formation across the upwarp. The Grand

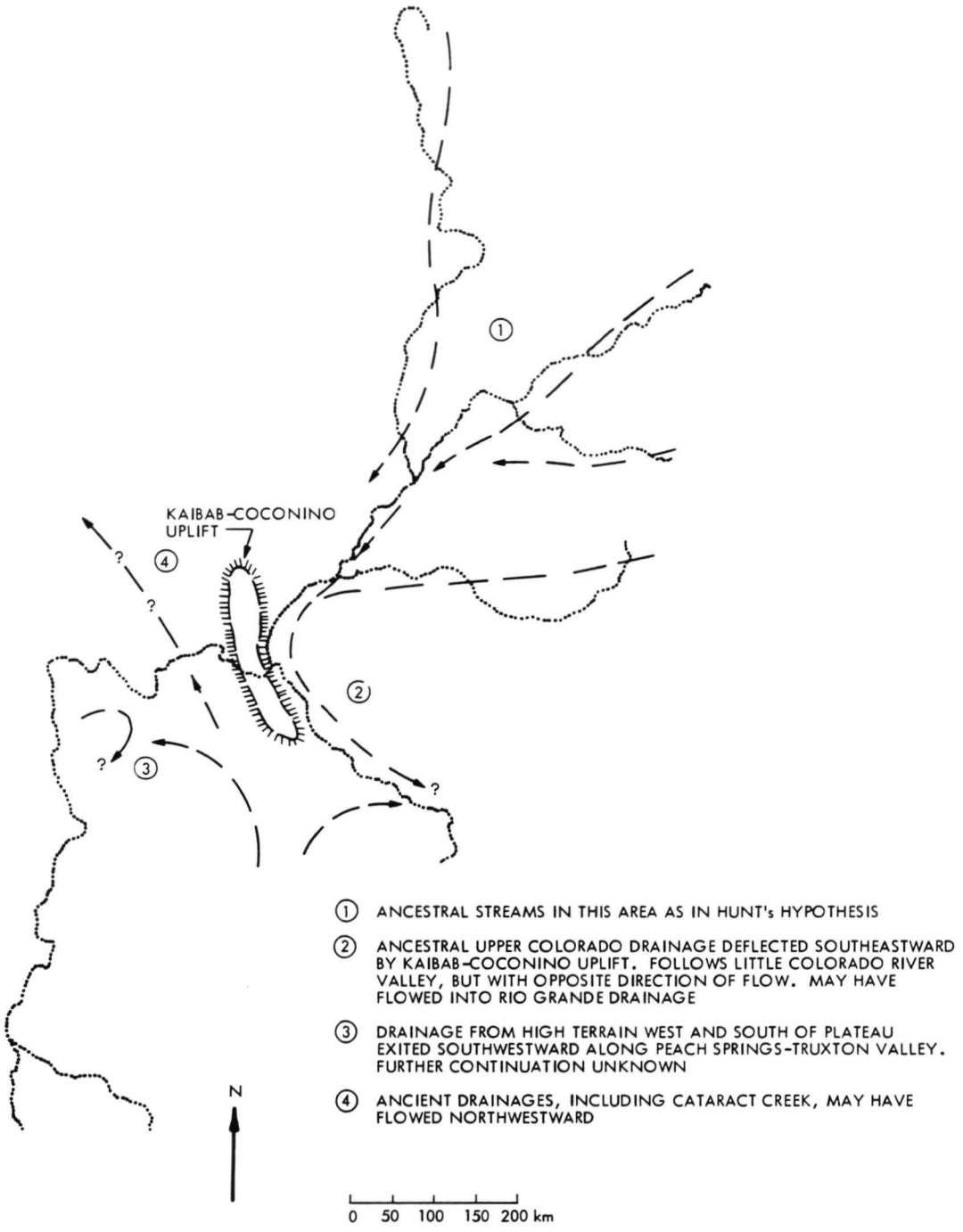

Fig. IV-B-9a. Hypothesis of McKee et al. Ancestral Colorado Drainage before major basin–range faulting (approximately >18 m.y.b.p.)

Canyon also coincides approximately with a subdued structural trough bordered on the south by the north-facing slopes of the Grandview monocline and the Supai anticline and on the north by the south-plunging strata of the Kaibab upwarp. This trough would tend to localize drainages across the upwarp in approximately the position of the Grand Canyon.

The present high topographic elevation of the Kaibab Plateau with respect to surrounding areas is due to the

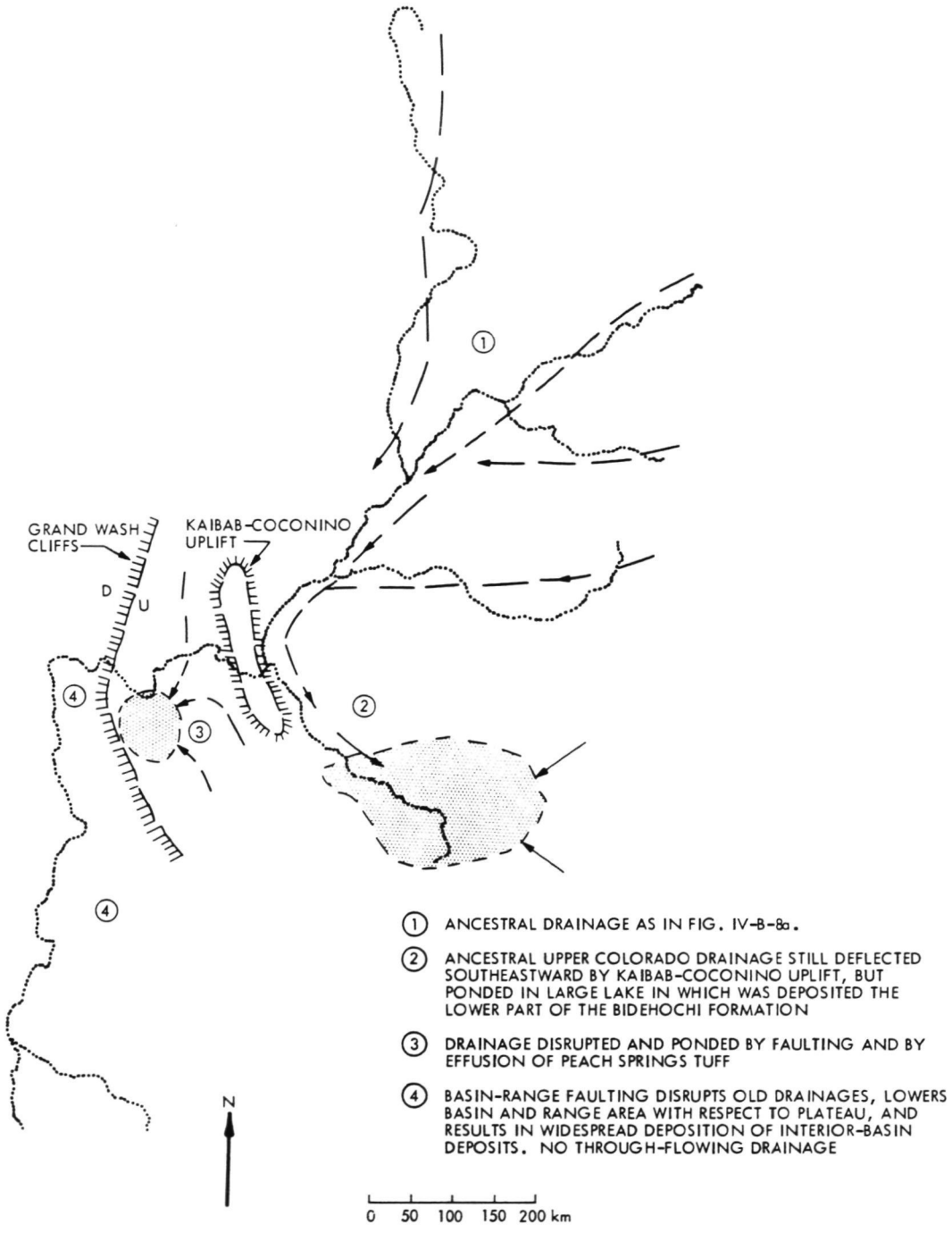

Fig. IV-B-9b. Hypothesis of McKee et al. Ancestral Colorado Drainage after basin–range faulting and effusion of Peach Springs Tuff (approximately 18 m.y. to 10 m.y.b.p.)

high resistance to erosion of the Kaibab Limestone that caps it. While this rock, and consequently the plateau, were being eroded very little, surrounding areas were greatly lowered through removal of softer rocks, thus progressively increasing the topographic relief of the plateau. By following this process back through time, it is apparent that the Kaibab Plateau may have been little, if at all, higher than its surroundings at earlier times, thus

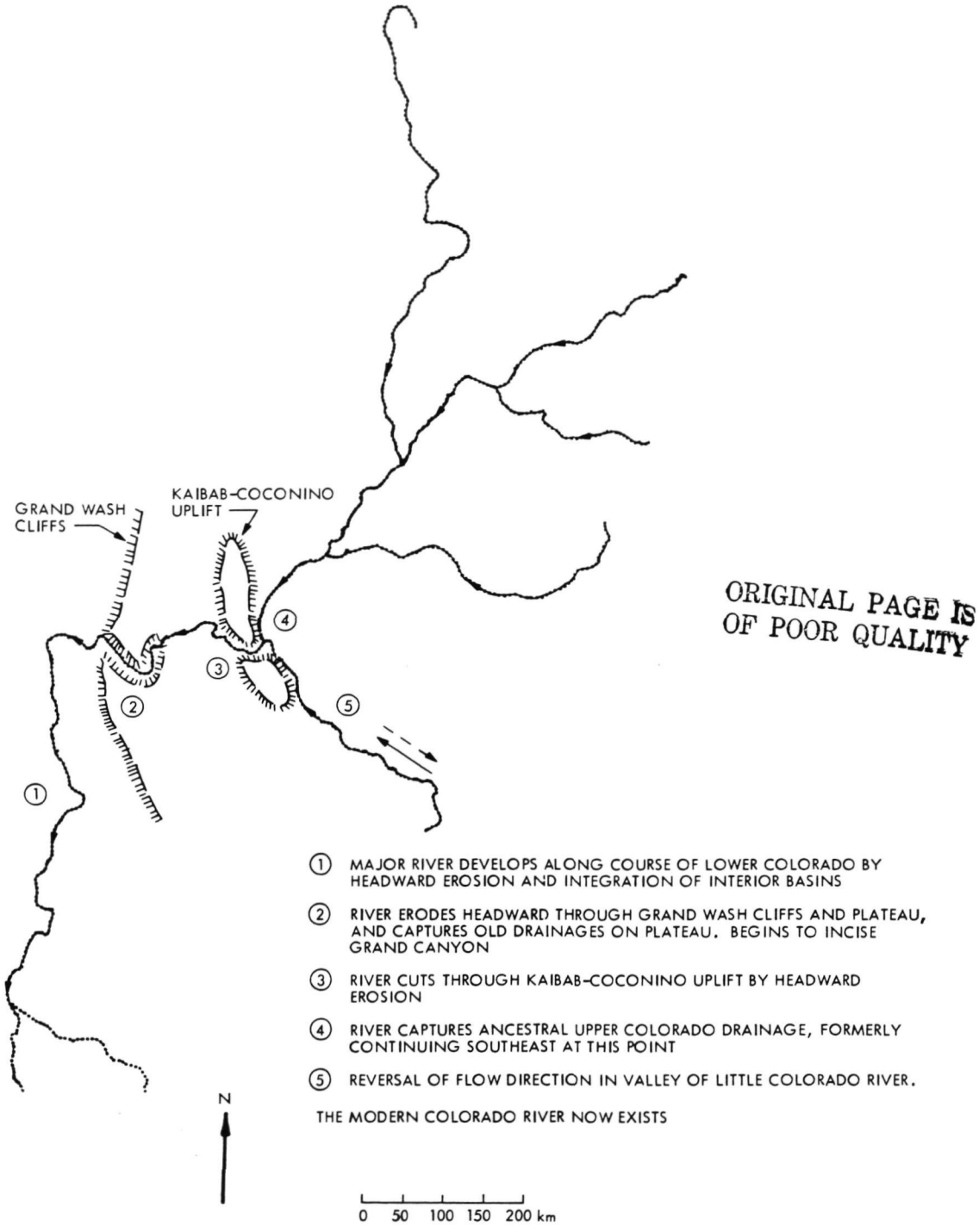

Fig. IV-B-9c. Hypothesis of McKee et al. Ancestral Colorado Drainage becoming modern Colorado River through headward erosion, capture, and integration after opening of the Gulf of California

providing no serious barrier to the westward continuation of the Upper Colorado Drainage. One may therefore postulate that the Upper Colorado Drainage crossed the Kaibab and continued into the area of the Coconino and Kanab Plateaus early in its history. The question still to be answered is: Where did the drainage continue from there?

The area west of the Colorado Plateau and south of Lake Mead was topographically high before basin–range faulting (probably since late Cretaceous time) and deeply eroded (see Refs. IV-B-1 through IV-B-4), as evidenced by the complete removal of Paleozoic and Mesozoic rocks. Cenozoic volcanic and sedimentary rocks rest directly on Precambrian basement. Stratigraphic evidence (channels, gravels, erosion surfaces, and volcanic flows) indicates that drainage was from this topographic high to the north and northeast (the area of the Colorado Plateau, which was then topographically low; see Refs. IV-B-1 through IV-B-4).

Arkosic gravels of southerly provenance are widely exposed along the southern margin of the Colorado Plateau in central Arizona. There, the "rim gravels" indicate that, before basin–range faulting, the area of the Colorado Plateau was lower than its surroundings in much of Arizona. Consequently, drainage was everywhere northeast or north onto the plateau. This drainage direction is roughly at right angles to that of the present Colorado River system.

The various streams that deposited the rim gravels must have been tributary to a master stream. Because no evidence has been found for other master streams in the area, this stream probably was the Upper Colorado Drainage.

Gravels composed of well rounded quartzite pebbles, and subordinate granite, gneiss, and volcanic rocks, locally in a matrix of coarse arkose sand, were discovered and studied on the Shivwits Plateau during this investigation. These gravels rest on Moenkopi rocks and are overlain by lavas that are 6 m.y. old[5] (Refs. IV-B-20 and IV-B-21). The clasts are similar in size and degree of rounding to rim gravels of southerly provenance widely distributed on the western Coconino Plateau and the eastern Hualapai Plateau, but contain fewer crystalline clasts because of longer transport from the source area. The gravels differ in size and composition from pebbles of the Shinarump member of the Chinle Formation, which also are widely present as lag deposits on the Shivwits Plateau. The Claron Conglomerate, now exposed many tens of kilometers to the north, in southern Utah, contains similar quartzites, but no crystalline igneous rocks were found in the outcrops examined. When the Shivwits gravels were deposited the Claron probably outcropped considerably south of where it does now, but still north of the gravels. Drainage at that time was primarily to the north and northwest (see Refs. IV-B-15 and IV-B-16), so that it is not likely that Claron pebbles would have been incorporated in the Shivwits gravels. A source for the gravels directly from the west is not likely because none of the quartzites common in the gravels outcrop in that direction. The most likely source for the gravels is to the south, in the vicinity of Prescott, Arizona (see Fig. IV-B-5), as suggested by Koons (Ref. IV-B-21) for the gravels in the eastern Hualapai Reservation. A southerly derivation for the Hualapai gravels is also inferred by Young (see Ref. IV-B-3). McKee and McKee (see Ref. IV-B-18) suggest a southerly derivation, from central Arizona, for the gravels in the Coconino Plateau. Probably the Shivwits gravels were deposited by the same drainage system responsible for the gravels of the Hualapai and Coconino Plateau. In any case, the gravels had to be deposited by a drainage system flowing north–northwest directly across the present Grand Canyon and also the ancestral Colorado drainage postulated by Hunt. Therefore, neither could have existed at the time these gravels were deposited.

The Shivwits gravels effectively preclude a continuation west or southwest from the Coconino Plateau for the Upper Colorado Drainage. A continuation to the south is not possible because regional drainage is approximately from south to north in that area. Consequently, the only possible direction is generally to the north. This direction is also that of the overall drainage pattern in northwestern Arizona. Practically all tributaries to the Grand Canyon are short and poorly developed and represent a relatively recent modification to an older landscape in which streams flowed northwest to north–northwest along strike valleys. Evidence for these older streams is preserved in Cataract Creek and the Little Colorado River, both long, mature, well established streams that almost certainly predate cutting of the Grand Canyon.

The hypotheses of both Hunt and McKee et al. are partially correct. Hunt probably is correct in proposing that the ancestral Upper Colorado Drainage crossed the Kaibab upwarp in Miocene time or earlier, but the prolongation of the drainage westward through the western Grand Canyon region into what is now the Basin and Range province is not in accord with the recently discovered gravels and the general northerly directions of ancient drainages in those areas. McKee et al. are correct in inferring that the Lower Colorado Drainage developed

[5] See footnote 3.

in the Basin and Range province no earlier than 10.6 m.y. ago, but they are probably wrong in restricting the ancestral Upper Colorado Drainage to the east side of the Kaibab upwarp and prolonging it southeastward along the valley of the Little Colorado River. The new interpretation presented below combines elements of both hypotheses as well as new information (see Figs. IV-B-10a, 10b, 10c).

In Miocene time (see Fig. IV-B-10c), or even earlier, a stream (or system of streams) originating in Colorado and following approximately the present course of the Colorado, or that of the San Juan River, entered Arizona from the northeast. This, the Upper Colorado Drainage, crossed the Kaibab upwarp (then with much less relief than it has now) following a belt of weak rock and a structural low across the upwarp. Once west of the upwarp, the river is postulated to have continued northwestward along a broad and open strike valley, probably cut in the soft Moenkopi or Chinle Formations. This was the master stream of the region. The ancient Little Colorado River, Cataract Creek, and the various north- and northeast-flowing streams were tributary to it. No Lower Colorado Drainage existed during this time. The further continuation of the Upper Colorado Drainage is not known at present, as all likely areas in Utah and Nevada have been deformed intensely by basin–range faulting and are covered by thick sequences of volcanic rocks.

During or shortly after the opening of the Gulf of California, 4 to 6 m.y. ago, a stream began to develop in the Basin and Range province approximately along the present Lower Colorado River (see Fig. IV-B-10c). This stream eroded headward following structural lows and belts of weak rock, and integrated the interior drainages that had been formed by the basin–range faulting. The place at which the stream incised the lower Grand Wash Cliffs (see Fig. IV-B-10), then as impressive a barrier as now, was determined by a high scarp, facing southwest, located directly east of the Grand Wash Cliffs, at the westernmost edge of the Colorado Plateau. This scarp, and the strike valley at its foot, concentrated runoff from a substantial area to the south, and added to the waters of the Lower Colorado. The river then followed the southeast trend of the strike valley, which it deeply entrenched, until it intersected the north-trending Hurricane fault. The belt of weak rock associated with this fault deflected the river into a northerly course, which it followed for about 40 km. Somewhere between this point and the Kaibab uplift, the river captured the Upper Colorado Drainage. This capture was possible because the Lower Colorado Drainage had the shorter course to the sea, and therefore the steeper gradient and greater erosive power. At this time, the Colorado River came into being as an integrated stream in its present course.

c. Structural style and history. The western part of the Colorado Plateau is composed of structural blocks elongated in a northerly direction, dipping gently to the northeast, and separated by major faults trending approximately north. From west to east, these major faults are the Grand Wash, the Hurricane, and the Toroweap-Sevier. All are high-angle dip-slip and downthrown to the west. Strike lengths are measured in tens to hundreds of kilometers, displacements in hundreds to thousands of meters. The faults are composed of segments trending alternately north–northwest and north–northeast (Ref. IV-B-20). This pattern is repeated down to the outcrop scale and is reflected most conspicuously by the Hurricane fault. Displacements on the Hurricane and Toroweap faults decrease to the south, that of the Grand Wash fault to the north.

Although some authors suggest that earliest movements on the faults may be as early as the Laramide period (see Ref. IV-B-23 for the Hurricane fault) or post-Eocene and pre-Miocene (?) (see Ref. IV-B-24 for the Hurricane fault), most agree that movement began in Miocene time (Refs. IV-B-10, IV-B-20, and IV-B-25) and continued into the late Tertiary or, in the case of the Hurricane fault, the Holocene (see Ref. IV-B-20). These ages are based on the relations of faults to sedimentary deposits and lavas in northernmost Arizona and southern Utah. Along much of its length, the Grand Wash fault has not moved since the upper 300 m of Muddy Creek Formation were deposited, i.e., about 10.6 m.y. ago (see Refs. IV-B-1, IV-B-2, and IV-B-26). Main movement occurred after eruption of the Peach Springs Tuff of Young, dated at 18.3 m.y. (see Ref. IV-B-3). Near the northern border of Arizona, however, the Grand Wash fault has displaced lavas 6 m.y. old (see Ref. IV-B-26). Along the central part of the Grand Wash fault system, recent movements, displacing deposits of Quaternary age (see Ref. IV-B-1), have occurred along the Wheeler fault (see Fig. IV-B-2) and not along the main break.

Folds of tectonic origin are not common in northwestern Arizona. The most prominent is the Kaibab upwarp, an anticlinal uplift trending approximately north to north–northwest and with structural relief of about 1000 m. The Kaibab upwarp is regarded as a Laramide feature, although recurring deformation may have continued during the Cenozoic period. Monoclinal flexures, commonly regarded as Laramide in age, occur in various places in northwestern Arizona, including the Hualapai

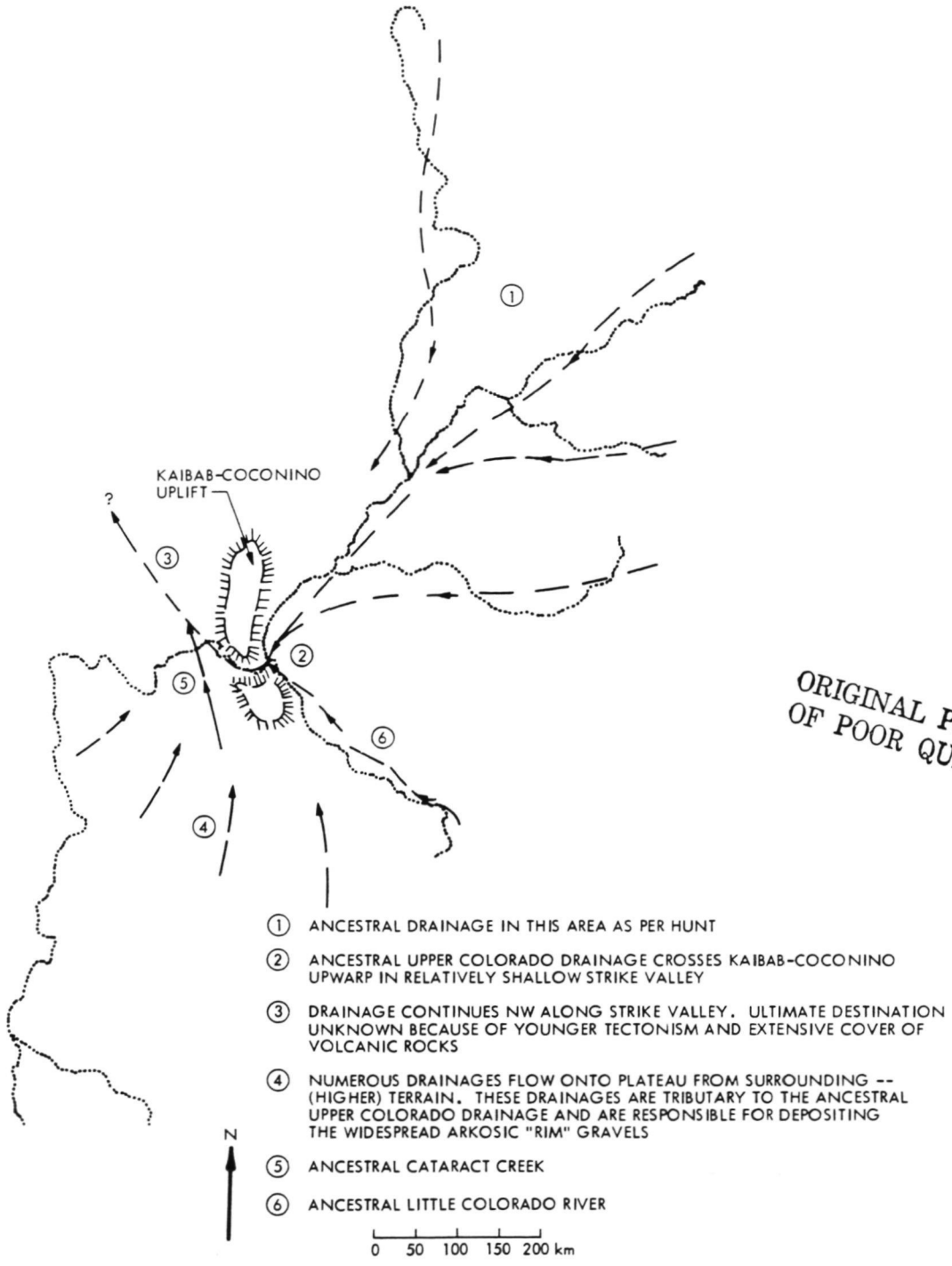

Figs. IV-B-10a. Lucchitta's hypothesis. Ancestral Colorado Drainage before basin–range faulting

Plateau directly south of the Shivwits. Other folding commonly is associated with major faults and consists of downwarping toward the fault on the downthrown block, generally accompanied by upwarping toward the fault on the upthrown block. There has been little agreement on interpretation of this feature, which has been called "reverse drag" by Hamblin (Ref. IV-B-27).

The faults and folds on the Shivwits Plateau generally parallel the Grand Wash and Hurricane faults, the master

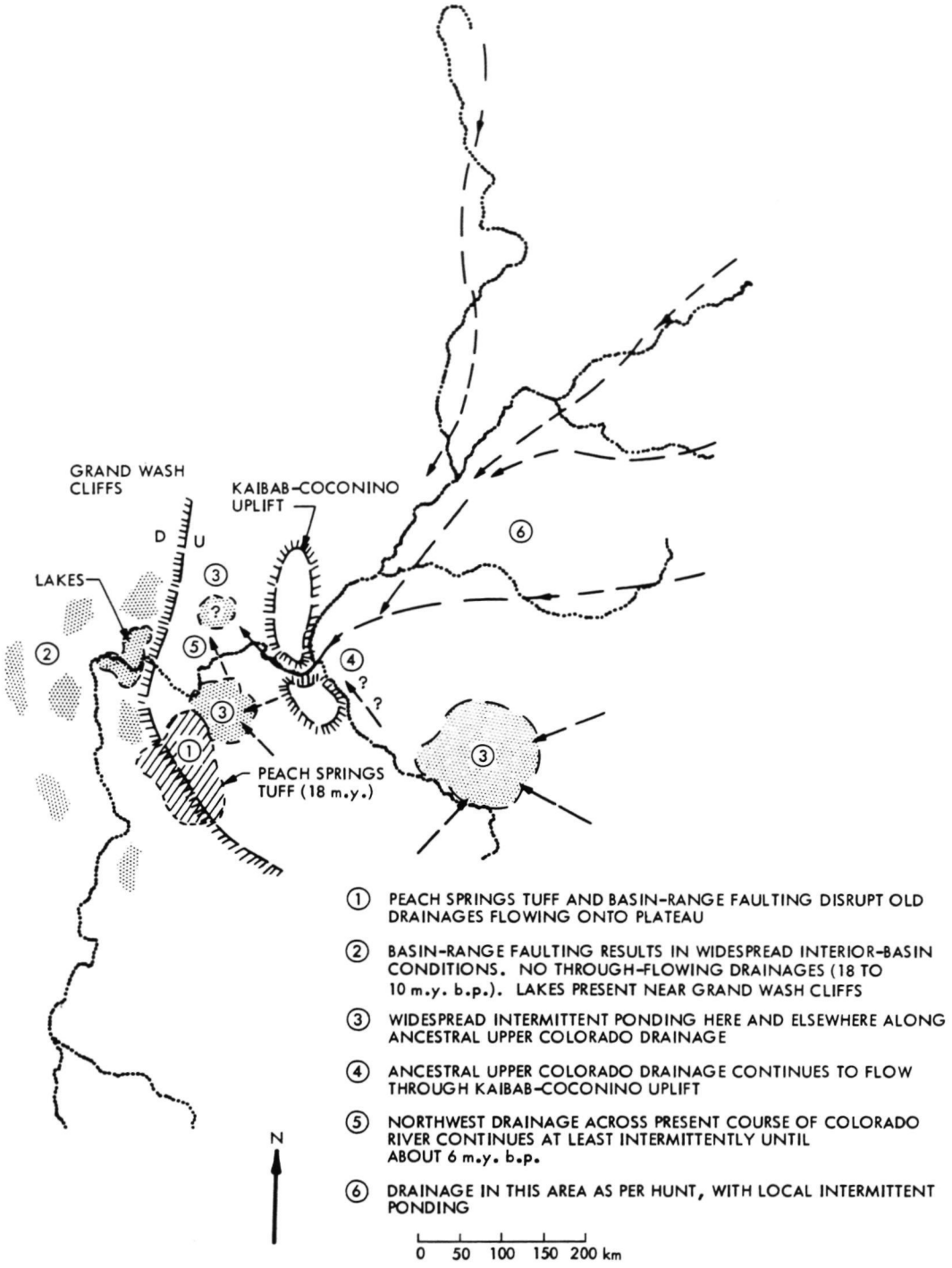

Fig. IV-B-10b. Lucchitta's hypothesis. Ancestral Colorado Drainage after basin–range faulting and effusion of Peach Springs Tuff

faults of the area, and are concentrated primarily in the eastern and western thirds of the area. The central part of the Shivwits is relatively unfaulted. Some faults have scissors movement. Strike lengths are measured in kilometers to tens of kilometers, and displacements in tens to hundreds of meters. Preferred orientations are northwest, north–northwest, and north–northeast (Fig. IV-B-11). Faults trending northeast are relatively few and generally

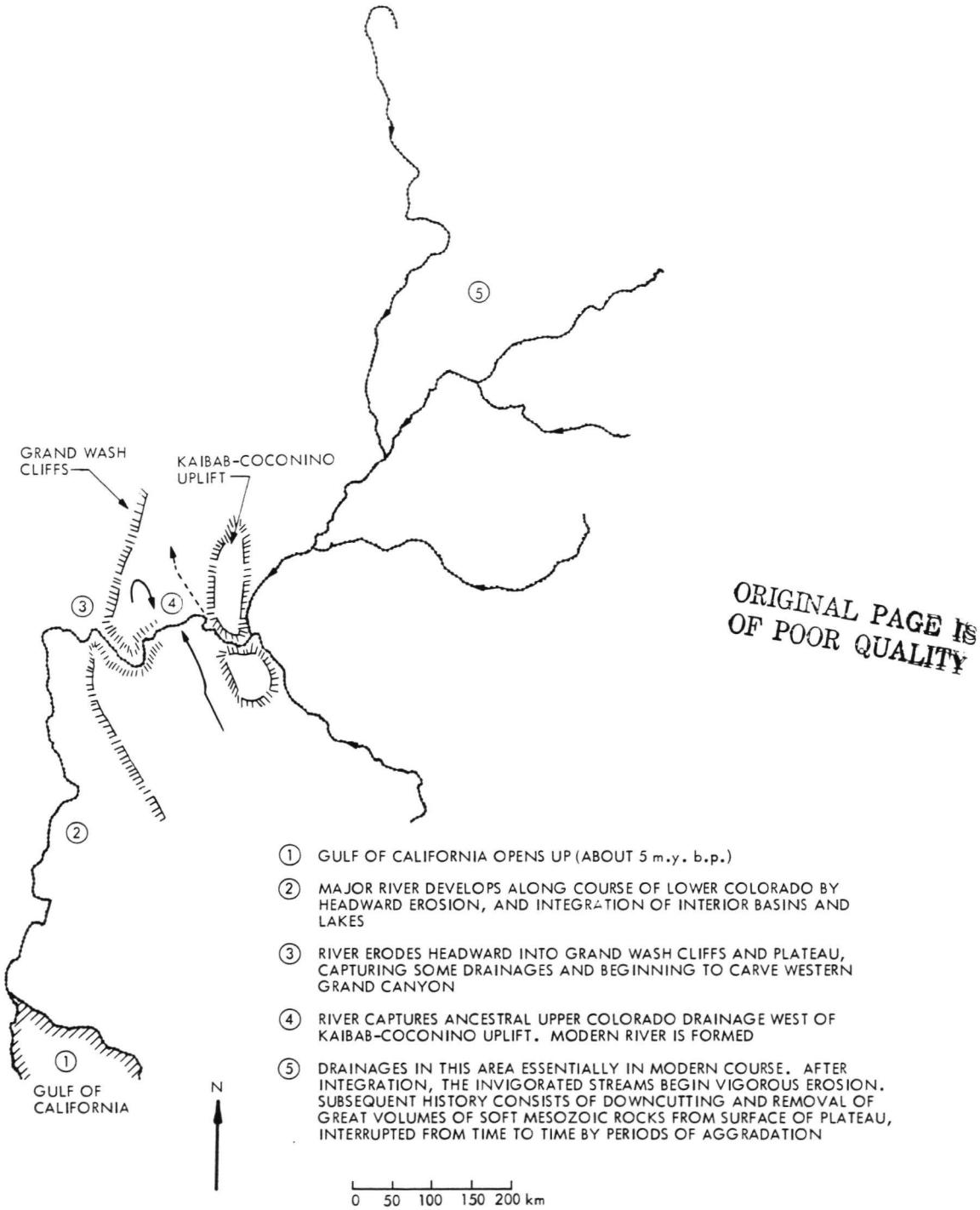

Fig. IV-B-10c. Lucchitta's hypothesis. Ancestral Colorado Drainage becoming modern Colorado River through headward erosion, capture, and integration after opening of the Gulf of California

aligned with, as well as parallel to, the northeast-trending segment of the southern great bend of the Hurricane fault. Graben, horsts, and tilted-block structures are common, especially in the eastern part of the plateau and in a belt trending approximately northeast and located between the two great bends of the Hurricane fault. Although faults with either the west or east side down are equally common throughout most of the plateau, near the western

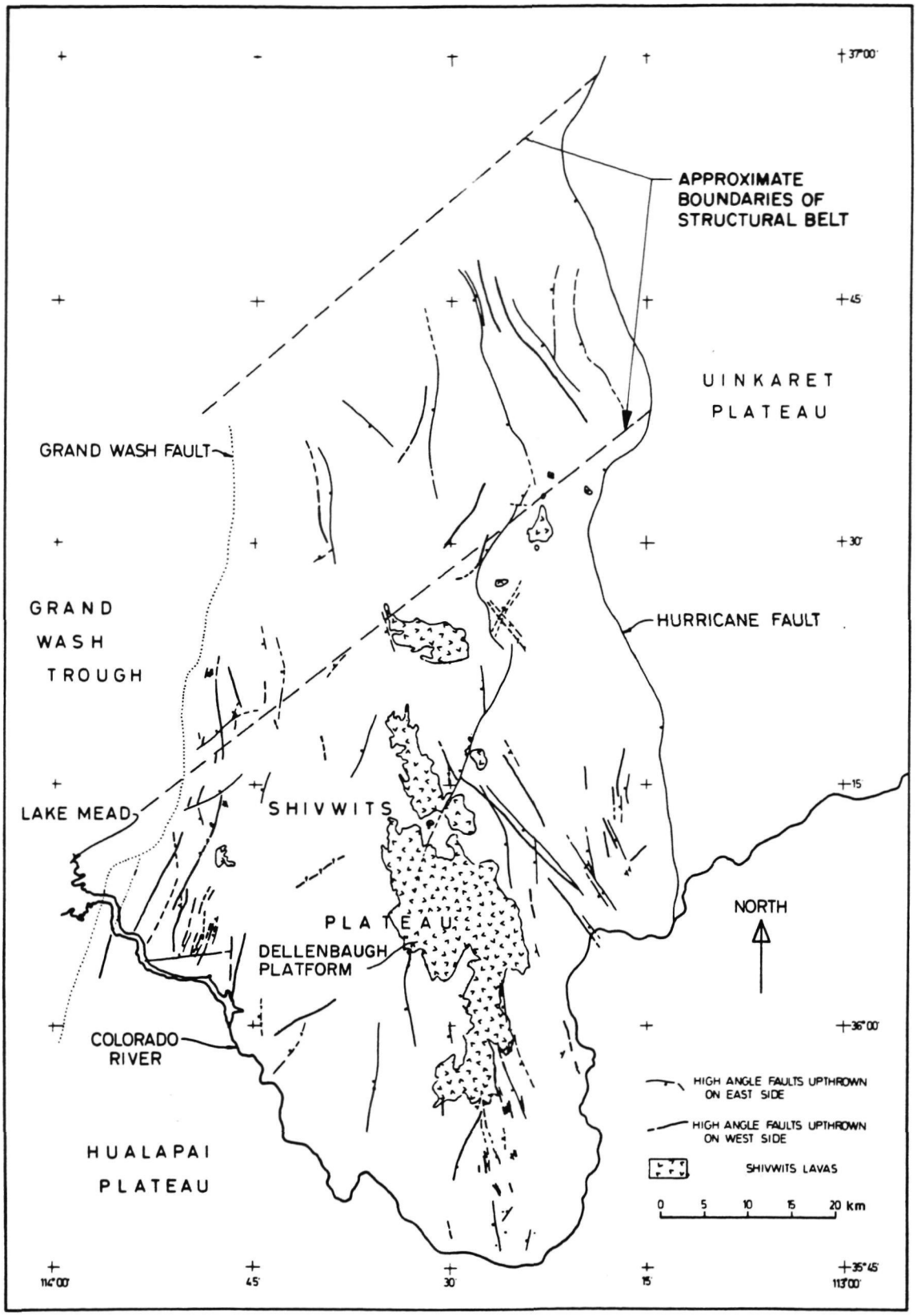

Fig. IV-B-11. Tectonic map of the Shivwits Plateau, Arizona

boundary faults are consistently up to the west and associated with gentle monoclinal flexures also upwarped to the west. In many instances, these monoclines pass along strike into faults. Strata of the Shivwits Plateau dip homoclinally to the northeast at 1° to 3°; near the western boundary, however, the dip increases to as much as 4° to 5°. This increase, combined with the elevation of the west side of faults and monoclines, results in a notable structural upwarping of the western edge of the Shivwits Plateau and of the Hualapai to the south of it, and thus of the western edge of the Colorado Plateau in this area.

Throughout most of the Shivwits Plateau area, the age of structural features can be determined no more precisely than post-Triassic. In lava-covered areas, faulting occurred before, during, and after effusion of the lavas. However, the relative scarcity of faults that cut the lavas suggests that most faults predate at least the youngest flows. Hamblin (Ref. IV-B-20 and Best et al. (Ref. IV-B-21) report ages of about 6 m.y. for the oldest lavas (Stage I) and 2 m.y. or less for younger ones. Lavas in the southern part of the Shivwits Plateau are for the most part Stage I, so that most faulting in that area probably occurred before 6 m.y. ago.

d. Tectonic relation of Shivwits part of the Colorado Plateau to adjacent Basin and Range. The area now occupied by the southwestern part of the Colorado Plateau has differed geologically from adjacent areas to the west throughout Phanerozoic time. Deformation has been slight; accumulation of Paleozoic sediments has been low; and topographic elevation has usually been the opposite of that of adjacent areas to the west (when these were high, the plateau was low, and vice versa). Although the present southern boundary of the plateau with the Basin and Range is relatively indistinct and marked by a transition zone about 100 km wide, the western structural and physiographic boundary is remarkably sharp and generally less than 10 km wide. From the top of the Grand Wash Cliffs at the western edge of the Shivwits Plateau, the view to the west consists of a seemingly endless succession of serrated ranges composed of tilted fault blocks and separated by deep structural basins that are in large part filled with sediments. The first of these basins, west of the Cliffs, is the Grand Wash Trough (see Fig. IV-B-2), probably 5000 to 6000 m deep (see Ref. IV-B-1) and bounded to the west by bedrock ridges whose strata dip 45° or more toward the Grand Wash fault. East from the observation point, by contrast, is a landscape of tablelands, scarps, and stripped surfaces developed in subhorizontal strata that dip gently northeast. This dip is not significantly increased by rotation of fault blocks, in spite of the considerable displacement on some of the faults, and is disturbed only by monoclinal flexures that occur in the immediate vicinity of the faults. Deep sediment-filled structural basins are absent.

The high structural elevation of the western edge of the plateau near the Grand Wash fault results from an increase in dip as compared with other areas, as well as from structural uplift of the west sides of flexures and faults. The orientation of the resulting structural slope does not correspond well to the grain of adjacent basin–range structures and cannot easily be attributed to the same stress field. The upwarp probably reflects pre-Basin and Range uplift of the terrain west and southwest of the plateau (Kingman Uplift) rather than deformation related to Basin and Range tectonism.

The style of deformation suggests that most of the structural features of the Shivwits Plateau were formed by an extensional stress field. Similarity in age and general parallelism with structural features in the adjacent part of the Basin and Range province suggest that the same stress field existed in both areas. The lesser degree of deformation of the Shivwits Plateau indicates either that the stress field is weaker east of the Grand Wash fault, or that the crust in that area is more competent than to the west.

As summarized by Shuey et al. (Ref. IV-B-28), crustal properties of the western plateau differ markedly from those of the Basin and Range. On the plateau the crust is thick, gravity is low, heat flow is low to normal, and aeromagnetic values are high. In the adjacent Basin and Range, the crust is thin, gravity is high, heat flow is high, and aeromagnetic values are low. Shuey et al. emphasize that the locus of maximum change in these properties, as well as a seismic belt of anomalously high geomagnetic variation, is a relatively wide zone, 50 to 80 km across whose axis is to the east of the present physiographic boundary of the plateau. Nevertheless, this zone, the present physiographic and structural boundary, the Wasatch line (eastern limit of Laramide thrusting and folding), and the Paleozoic hinge line coincide remarkably well when viewed at a perspective commensurate with the crustal blocks involved, which measure about 600 km (Plateau) and 400 to 800 km (Basin and Range) in an east–west direction.

Some type of geologic discontinuity has existed at or near the present western boundary of the Colorado Plateau since Paleozoic time, which suggests the following questions:

(1) What is the nature of the Plateau crustal block, a block that apparently has remained internally

coherent for 500 m.y., and that for the most part has behaved differently from its surroundings?

(2) What is the nature of the tectonic boundary between the Plateau block and the area to the west now occupied by the Basin and Range province?

Answers to these questions are fundamental not only to understanding the Colorado Plateaus and Basin and Range provinces, but also crustal processes and tectonic theory in general.

These questions are evaluated here, in the context of Cretaceous and Cenozoic deformation of the southwestern boundary of the Plateau, in the hope that this limited understanding will help to explain the general problems. Within this context, four hypotheses may be advanced to explain the structural and tectonic differences between the Plateau and Basin and Range provinces:

(1) The Plateau is being "consumed" at its western edge by Basin and Range structures, in effect slumping at a crustal scale into the Basin and Range province. This implies that the present boundary between the two provinces is ephemeral and has been moving eastward, and that the fault-bounded blocks of the western plateau represent a transition zone of incipient Basin and Range structures. The hypothesis also implies an eastward-migrating extensional stress field, a progressively younger age for plateau faults as one goes eastward, and a diffuse boundary between the Plateau and Basin and Range provinces. A major change in crustal properties across the boundary is not required.

(2) The Plateau and Basin and Range provinces are subject to and resulted from different crustal stress fields. This hypothesis does not require different crustal properties of the two blocks, nor a boundary between the two blocks that migrated with time, nor specifically a sharp or diffuse boundary. It does require a decoupling between the two blocks and perhaps also between the crustal blocks and the underlying mantle.

(3) The Plateau and Basin and Range provinces represent blocks that are subject to the same stress field, but with different crustal properties so that the stress field results in different styles of deformation in the two blocks. This hypothesis requires a relatively fixed and sharp boundary between the two blocks.

(4) The Plateau and Basin and Range were one geologic province before deformation and became subject to the same stress field, which decreased in intensity eastward. The present tectonic boundary between the two provinces marks the eastern boundary of the area in which stress was sufficiently great to cause major deformation. This hypothesis does not require different crustal properties, but does imply a boundary between the two provinces that is gradational and fixed in space. Consequently, Basin and Range structures would grade eastward into Plateau structures, and both should be equivalent in age.

In the subsequent paragraphs, several criteria are advanced that help in the evaluation of these hypotheses and selection of the one most likely to be correct.

Monoclinal flexures associated with faults. The common association between monoclines and faults suggests that the monoclinal flexures are the surface expression of zones of weakness in the competent basement and were formed under compressive stress conditions probably related to the Laramide orogeny to the west. These zones later localized high-angle normal faults when the area was affected by the extensional stress related to Basin and Range tectonics. The antiquity and repeated reversal of movement on faults, as well as the association of monoclines with faults at depth, are well documented for the Grand Canyon (Refs. IV-B-29 through IV-B-32). Huntoon (see Ref. IV-B-32) especially has recognized the importance of basement fractures in controlling deformation even under widely differing stress fields.

The monoclinal flexures and associated faults of the Plateau block in northwestern Arizona suggest that the:

(1) Block and the adjacent Basin and Range have been subjected to related stress fields.

(2) Resulting deformation has differed in degree (much more subdued) and perhaps in type from that farther west because of the greater competence and the buttress-like nature of the Plateau block.

(3) Zones of weakness, some very ancient, in the basement of the Plateau block have localized deformation even if produced by widely different stress fields.

These data support the third hypothesis, but not the others.

Structural upwarping of the western edge of the Plateau. The upwarp may reflect an ancient uplift (the Kingman Uplift) of probable Laramide age southwest of the Plateau (see Refs. IV-B-1 through IV-B-3). The main part of this uplift, was fractured and destroyed by basin–range faulting in Miocene time. Alternatively, the upwarp

may represent a monoclinal flexure of the type discussed previously and assoicated with the Grand Wash fault. In either case, the upwarp indicates that the western edge of the Plateau has been involved in repeated deformation involving the basement and at least in part reflecting stress fields that probably are relatively old and encompassed both the Plateau and the adjacent area to the west.

Sharpness and age of the Colorado Plateau-Basin and Range boundary. The present physiographic boundary in northwestern Arizona is remarkably sharp (10 km wide). The boundary based on geophysical data is more diffused, but still narrow (80 km or less) compared with the dimensions of the crustal blocks involved (600 km). The boundary would be diffuse if the various plateaus bounded by high-angle normal faults were a transition zone between areas of typical Plateau and typical Basin and Range structure. However, these plateaus, although exhibiting block faulting and extension tectonics, do not have the horsts (ranges) or graben (basins), the great structural relief, or the rotation of blocks typical of the adjacent Basin and Range terrain. Extension tectonics and block faulting are necessary but not sufficient to form basin-range structure. The plateaus could also be interpreted as a zone of incipient basin-range structure, but this is in poor accord with the ages of the associated faults, which are comparable to those of nearby faults in the Basin and Range. The plateaus probably represent neither basin-range structures that are just beginning to form nor structures that are older but have been arrested in their development. Consequently, the tectonic boundary, separating areas that differ markedly in structural style, is best placed at the western edge of the Shivwits Plateau, in coincidence with the physiographic boundary and with ancient tectonic boundaries such as the Paleozoic hinge line. In summary, the boundary is best viewed as old, relatively sharp, and relatively fixed. These properties are in poor accord with the first hypothesis. The markedly different structural styles and the sharpness of the boundary do not support the fourth hypothesis.

Alignment and distribution of structural features on the Plateau in comparison with the adjacent Basin and Range province. Faults at the western edge of the Colorado Plateau and the edge itself closely parallel the structural grain of the adjacent Basin and Range province. This indicates a common stress field.

On the Shivwits Plateau, faults trending northeast are concentrated in a zone also trending northeast and aligned with the southernmost bend of the Hurricane fault (Fig. IV-B-12). Other features with northeast trends in the same general area are:

(1) Straight segment of the Grand Canyon, about 75 km long, and closely paralleled by at least one long fault that is outside the area mapped for this study, but clearly visible in ERTS pictures and in high-altitude aerial photographs.

(2) Several diffuse, but long, lineaments visible in ERTS pictures.

(3) Northeast-trending segment of the Toroweap-Sevier fault.

West of the Plateau, a zone of conspicuous faults trending approximately northeast occurs north of Lake Mead, in alignment with the belt on the Plateau (see Fig. IV-B-12). In the western part of Lake Mead, this zone has demonstrable transcurrent movement (R. E. Anderson, personal communication, 1973) and may be part of the Las Vegas shear zone. Major structural features trending northeast are not common elsewhere in southern Nevada.

A belt about 60 km wide that trends northeast is aligned with the two bends of the Hurricane fault. This belt is characterized by a distinctive set of numerous and closely spaced graben, by bends in the traces of faults in correspondence with bends of the Hurricane fault, and by virtual absence of volcanic centers. By contrast, volcanic centers are abundant north and south of the belt.

The colinear nature of the fault zone in the Lake Mead area and of the anomalous belt on the Plateau probably reflects the same stress field rather than being fortuitous. According to this interpretation, in the Basin and Range block this stress field resulted in faulting that was at least in part transcurrent. In the Plateau block, by contrast, the stress field produced fractures with no demonstrable transcurrent displacement. Some of these fractures were followed by normal faults generated by an extensional stress field. Examples are the faults trending northeast on the Shivwits Plateau and the northeast-trending segments of the Hurricane fault.

In summary, the parallelism between structural features on the Plateau and in the adjacent Basin and Range province suggests that all of these structures were formed in response to the same stress field. The lack of displacement of plateau structures, compared with correlative structures in the Basin and Range, suggests that the Plateau has responded as a more competent block than has the Basin and Range. These characteristics tend to support the third hypothesis.

Conclusions. The southwestern part of the Colorado Plateau and the adjacent Basin and Range province differ

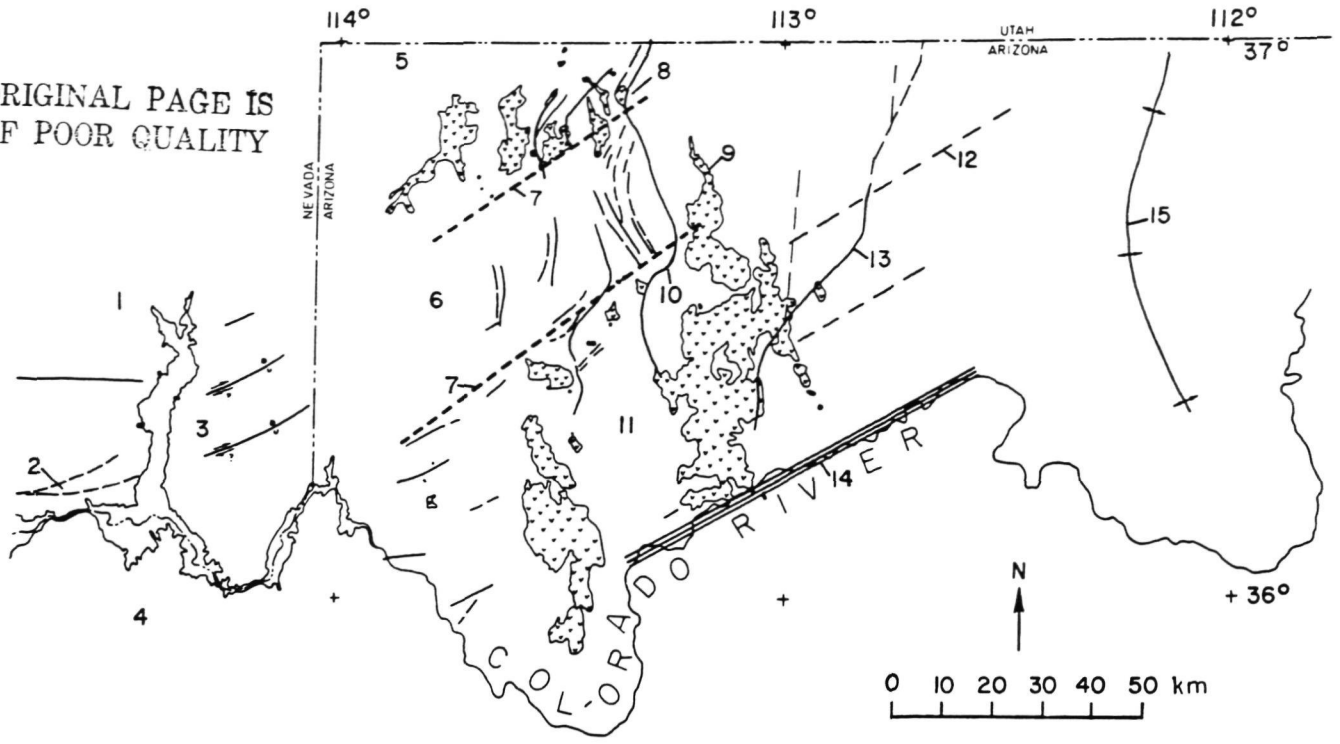

(1) Area of no volcanic centers
(2) Fault with transcurrent movement. Probably part of Las Vegas shear zone
(3) Faults with probable right-lateral component of movement
(4) Area of abundant volcanic centers
(5) Area of abundant volcanic centers
(6) Anomalous belt of closely spaced graben and no volcanic centers
(7) Approximate boundaries of anomalous belt
(8) Northern sigmoidal bend in Hurricane fault
(9) Lava flow whose vent is south of anomalous belt
(10) Southern sigmoidal band in Hurricane fault
(11) Abundant volcanic centers
(12) Lineaments visible on ERTS pictures. Locations shown are diagrammatic
(13) Northeast bend in Toroweap-Sevier fault
(14) Northeast-trending, structurally controlled segment of Grand Canyon
(15) Northeast bend of Kaibab upwarp

Fig. IV-B-12. Northeast-trending features in northwestern Arizona and in southeastern Nevada

markedly in physiography, structure, crustal properties, and geologic history. Most of these differences have existed through Phanerozoic time. The boundary between the two crustal blocks is best viewed as old, relatively sharp, and relatively fixed.

Parallelism between structural features of the Plateau and the adjacent Basin and Range suggests that both have been subject to the same stress fields; the much more subdued deformation on the Plateau results from its more competent crust. This is also suggested by a northeast-trending structural belt that crosses the boundary between the two blocks. In the Basin and Range, the belt shows transcurrent movement, but is reflected by anomalous northeast trends of structural features and by a set of graben that may indicate a shear movement of the stress field.

In the Plateau block, the basement has been dominant in controlling structural deformation. Zones of weakness, some very old, have localized deformation even under different stress fields. Many of these zones have been repeatedly active, commonly with reversed movement. Thus, the compressional stress field associated with the Laramide orogeny to the west resulted in reverse faulting in the basement and corresponding folding in the sedimentary cover. The later extensional stress field

associated with Basin and Range deformation to the west resulted in normal faulting along many of the same faults.

C. The Coconino Plateau

R. L. Squires and M. J. Abrams

1. Regional Setting

The Coconino Plateau (Fig. IV-C-1) lies in north-central Arizona, within the southwestern part of the Colorado Plateaus province. The central 3200 km^2 of the Plateau was mapped in an area extending north–south from the southern rim of the Grand Canyon to the Mt. Floyd volcanic field, and east–west from the 112th to 113th meridian.

The regional slope of the land surface on the Coconino Plateau is to the south. Altitudes along the southern rim of the Grand Canyon range from about 1850 to 2200 m above sea level. Ponderosa and piñon pine forests occur along the area immediately adjacent to the southern rim, with a gradual transition to juniper and piñon pine forests to the south. South and west of the Heather monocline (see Fig. IV-C-1), the forests yield to extensive grasslands that form the central plains of the Coconino Plateau. These plains, of which most of the mapped area consists, have an average elevation of about 1900 m. Cataract Creek, the principal drainage of the Coconino Plateau, is the major physiographic feature in the plains. The Mt. Floyd volcanic field to the south of the plains is covered primarily by juniper and piñon pine forests. The average elevation of the northern escarpment of the Mt. Floyd volcanic field is about 1850 m.

Because the southern rim has a higher average elevation than the rest of the Coconino Plateau, the amounts of snowfall and rainfall are highest there. According to Metzger (Ref. IV-C-1), the annual precipitation for the southern rim country is about 38 cm. A semi-arid climate characterizes the plains area, with an average annual precipitation of about 25 cm. Half of this precipitation falls in summer thunderstorms, and the other half falls as snow during regional storms in the winter.

Accessibility into the mapped area is excellent. U. S. Highway 180 and State Highway 64, which provide access to the Grand Canyon from the south, are along the eastern margin. The paved Frazier Wells road provides access into the northwestern sector of the mapped area. Many secondary roads criss-cross the entire area.

2. Previous Mapping

There has been no previous attempt to map the Coconino Plateau in detail. Although the Plateau is included in McKee's (Ref. IV-C-2) facies maps of the Alpha and Beta Members of the Kaibab Formation, he did not map the different members of the Kaibab Formation over the Plateau. Koons (Ref. IV-C-3), in his map of the western Grand Canyon, grouped the Kaibab and Toroweap Formations. His geologic map also includes the Rose Well area (see Fig. IV-C-1) of the Coconino Plateau. Moore et al. (Ref. IV-C-4) published a generalized geologic map of Coconino County and also grouped the Toroweap and Kaibab Formations over the Coconino Plateau. This same map was later incorporated into the Geologic Map of Arizona (Ref. IV-C-5).

Maxson (Ref. IV-C-6) included the area immediately adjacent to the southern rim on his map of the Bright Angel quadrangle, and his preliminary geologic maps of the Grand Canyon and vicinity in 1967 and 1969 also show the southern rim area. Shoemaker et al. (Ref. IV-C-7) mapped the principal faults that occur on the Coconino Plateau (see Section IV-A of this Report).

3. Stratigraphy

The Coconino Plateau is underlain primarily by flat-lying to gently dipping sedimentary rocks of Paleozoic age. These rocks, about 1200 m thick, consist of an alternating sequence of sandstone, shale, and limestone. The older Paleozoic rocks are exposed chiefly in the Grand Canyon and in side canyons tributary to the Grand Canyon.

Most of the Coconino Plateau is a stripped surface formed on the Kaibab Formation of middle Permian age. Locally, the Kaibab Formation is overlain by the Moenkopi Formation of Triassic age. At the southern edge of the Plateau, sediments and volcanic rocks of Tertiary and Quaternary age overlie the Kaibab and Moenkopi Formations. A generalized stratigraphic section of the rock units mapped on the Coconino Plateau is shown in Fig. IV-C-2.

The Kaibab Formation is the geologic unit of interest in this investigation. In accordance with McKee's convention (see Ref. IV-C-2), the Kaibab Formation is subdivided into the Beta Member at the base and the Alpha Member at the top. In this section, the contact between the Alpha and Beta Members was chosen at the base of the lowermost redbed in the Kaibab Formation. This contact, which can be mapped throughout the Coconino Plateau,

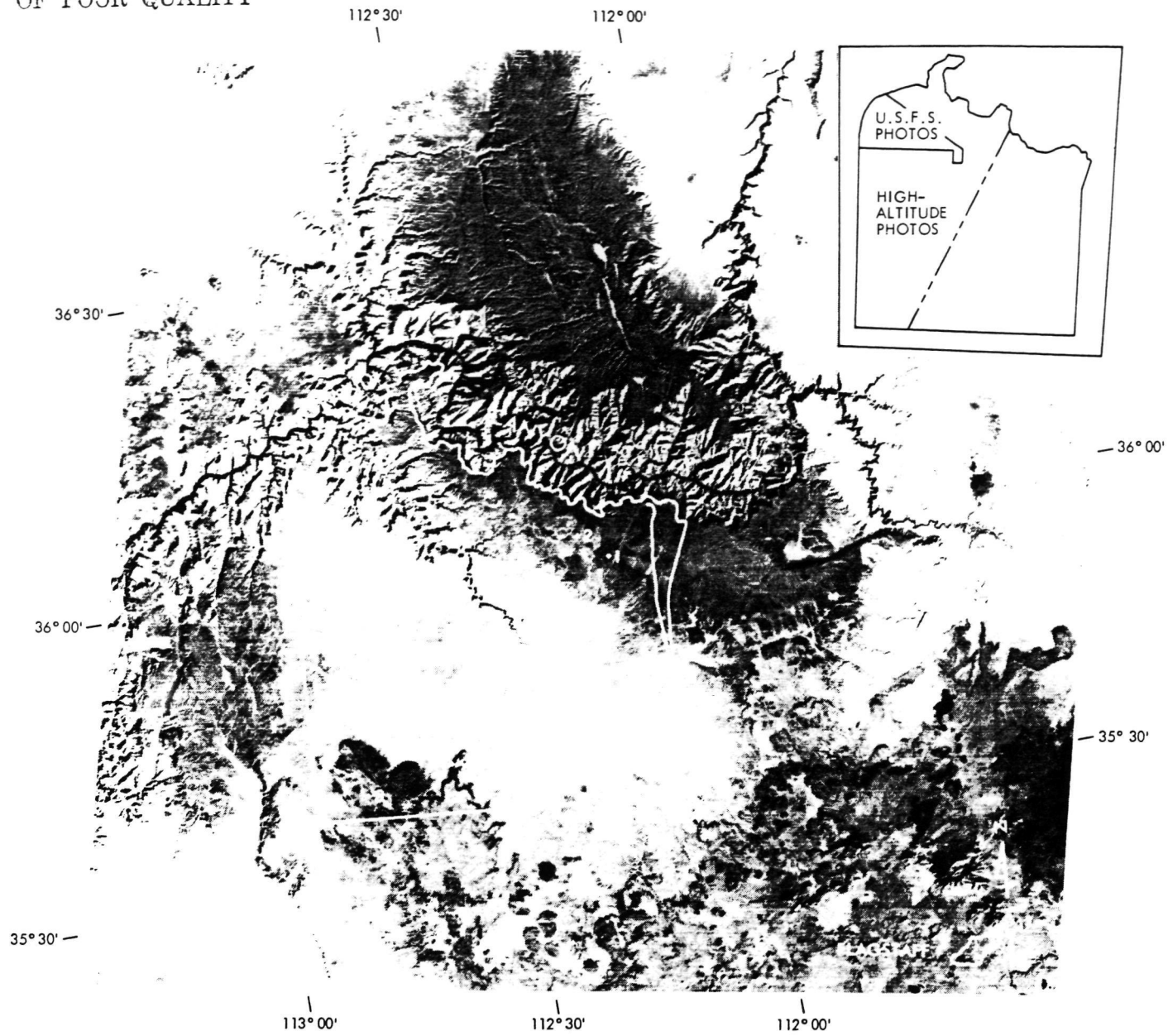

Fig. IV-C-1. ERTS picture of the Coconino Plateau, showing outline of mapped areas A and B and high-altitude and U. S. Forest Service photographic coverage: (1) Bright Angel fault, (2) Globe Ranch, (3) Heather monocline, (4) Cataract Creek, (5) Hualapai Hilltop Mesa, (6) Frazier Wells Road, (7) Rose Well, (8) Mt. Floyd volcanic field, (9) Long Point, (10) Moore Tank fault system, (11) Redlands Camp, (12) Howard Hill, (13) U. S. Highway 180 and State Highway 64, and (14) Valle (NASA picture ERTS E-1464-17354-6, Oct. 30, 1973)

differs slightly from that of McKee (see Ref. IV-C-2) and is about 15 m above his contact.

The Alpha Member, as studied in the mapped area, contains six mappable units: three red claystone, siltstone, and sandstone units (units 1, 3, and 5), which alternate with three relatively unfossiliferous dolomite (see Fig. IV-C-2) units (2, 4, and 6). Unit 1 is the basal unit of the Alpha Member. Locally, gypsum deposits occur within the clastic units, and nodular chert generally occurs within carbonate units 4 and 6. The upper parts of the Alpha Member (units 5 and 6) have been eroded away in some places. Where the complete section is present, the Alpha Member typically ranges in thickness from 33 to 40 m.

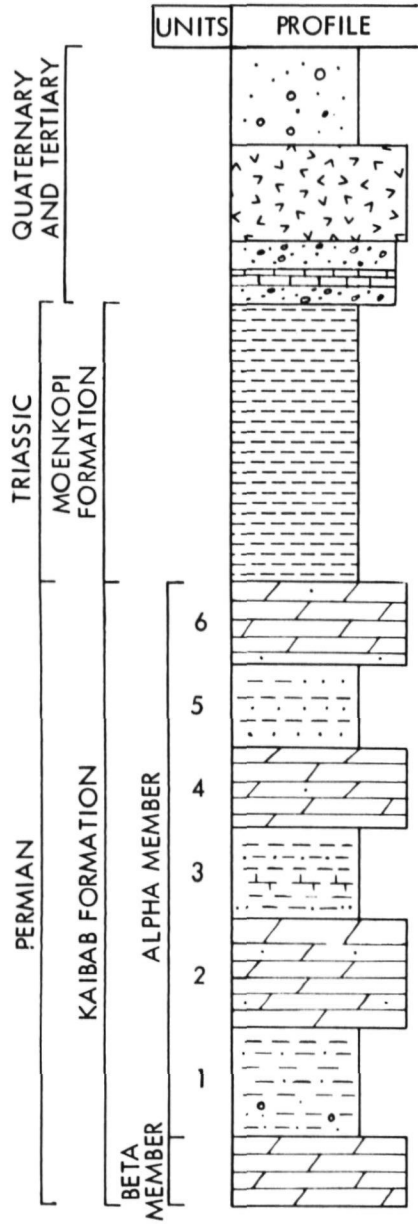

UNITS	PROFILE	GENERAL LITHOLOGY AND THICKNESS	WEATHERED COLOR
QUATERNARY AND TERTIARY		ALLUVIUM, LAG GRAVELS, LOESS. VARIABLE THICKNESS	RED TO TAN DEPENDING UPON SOURCE
		BASALT FLOWS, ASSOCIATED PYROCLASTIC ROCKS, RHYOLITE AND OBSIDIAN FLOWS. TALUS AND LANDSLIDE. 5 TO 100 m	BLACK
		SANDSTONE, CONGLOMERATE, AND LACUSTRINE LIMESTONE. MAXIMUM 50 m	RED AND WHITE SANDSTONE, GRAY LIMESTONE
TRIASSIC MOENKOPI FORMATION		SILTSTONE AND CLAYSTONE WITH INTERBEDDED FINE-GRAINED MASSIVE SANDSTONE. CHERT AND LIMESTONE PEBBLE CONGLOMERATE AT BASE. MAXIMUM 130 m	REDDISH SILTSTONE, GREEN AND RED BROWN CLAYSTONE, REDDISH SANDSTONE AND CONGLOMERATE. ENTIRE UNIT: 10R5/2
PERMIAN KAIBAB FORMATION ALPHA MEMBER	6	DOLOMITE, NODULAR WHITE AND PINK CHERT. SANDY AT TOP AND BASE, LOCALLY FOSSILIFEROUS. MAXIMUM 8 m	GRAY TO BUFF
	5	SANDSTONE, SHALE, AND GYPSUM. VERY FINE- TO MEDIUM-GRAINED LIMY QUARTZ SANDSTONE. LOCAL CONGLOMERATE. MAXIMUM 25 m	YELLOW BROWN AND PINKISH SANDSTONE, REDDISH SHALE, WHITE GYPSUM
	4	DOLOMITE, ABUNDANT WHITE CHERT AT TOP. SOME BEDDED CHERT, SANDY LAYERS, LOCALLY OSTRACODE. MAXIMUM 8 m	GRAYISH WHITE TO BUFF: 5YR8/1
	3	SHALE, SILTSTONE, AND GYPSUM. INTERBEDDED LIMESTONE AND FINE-GRAINED CALCAREOUS SANDSTONE. MAXIMUM 15 m	RED AND GREEN SHALE AND SILTSTONE, WHITE GYPSUM
	2	DOLOMITE WITH SANDY INTERBEDS, IRON NODULES COMMON AT TOP. LOCAL PYRITIC ROCKS AT BASE. LOCAL GASTROPOD AND BIVALVE. MAXIMUM 8 m	YELLOW BROWN: 10YR6/4
	1	CALCAREOUS SILTSTONE AND SHALE, INTERBEDDED DOLOMITE, LOCAL FINE-GRAINED SANDSTONE AND CONGLOMERATE SANDSTONE. MAXIMUM 9 m	RED TO BUFF SILTSTONE AND SHALE, BUFF TO YELLOW SANDSTONE
	BETA MEMBER	DOLOMITE, CHERTY AND FOSSILIFEROUS. LOCAL ABUNDANT PRODUCTID, SPONGE, GASTROPOD, AND CRINOID. MAXIMUM 100 m	GRAYISH WHITE

Fig. IV-C-2. Stratigraphic column of rock units on the Coconino Plateau

Locally, however, the total thickness may be 50 m where gypsum deposits thicken within one or more of the clastic units.

Although the clastic units are usually covered by slope wash, they are easily recognizable in the field because of their reddish color and slope-forming characteristics. The carbonate units, however, are more resistant and form white to yellow cliffs or broken outcrops. Distinctive fossil assemblages commonly could be recognized for the three carbonate units. Based primarily on these weathering, color, and fossil characteristics, all six units could be distinguished wherever they occurred through the mapped area. Other mappable units in the area include:

(1) Basal conglomerate in the Moenkopi Formation.

(2) Reddish siltstone and claystone with interbedded sandstone, which comprise the rest of the Moenkopi Formation.

(3) Tertiary age gravel.

(4) Tertiary age basalt flows of the Mt. Floyd volcanic field.

(5) Quaternary age basalt talus, landslide debris, and reworked gravel.

(6) Recent stream deposits.

4. Structure

The regional dip of the sedimentary rocks that underlie the Coconino Plateau is about 2° to the south. Normal faults and monoclines, structures typical of this part of the Colorado Plateaus province, offset these strata to a maximum of about 70 m. Within the area mapped, most of these structures trend northwest. Most of the faults occur in the Cataract Creek system (see Ref. IV-C-7).

In addition to the Cataract Creek system, there are two major northeast-trending fault systems, termed by Shoemaker et al. (see Ref. IV-C-7) the "Bright Angel and Sinyala systems," which may be related to fault zones in the crystalline Precambrian basement. Based on the study of an ERTS picture of the Coconino Plateau, the Bright Angel fault, of which only a small fraction along the southern rim had been previously mapped by Maxson, appeared as a through-going system across the Coconino Plateau.

Most of the northwest-trending faults have displacements down to the southwest, and most of the northeast-trending faults have displacements down to the southeast. Within the mapped area, there are many sags and domes; the most prominent dome is Howard Hill, which lies along the extension of one of the faults in the Bright Angel system.

5. Geologic Mapping

The geology of Area A of the Coconino Plateau (see Fig. IV-C-1) was mapped by M. Abrams and R. Squires from June 1973 to May 1974. Geology was compiled on black and white aerial photographs with a ground scale of about 1:60,000, from the U. S. Geological Survey, then recompiled using a 1:125,000 enlargement of an unenhanced ERTS picture as a base. In addition, the ERTS picture was used to help delineate large-scale structural features. High-altitude color photographs were available for the western half of the area, and low-altitude U. S. Forest Service color photographs also were used for the western part of the Kaibab National Forest adjacent to the southern rim of the Grand Canyon (see Fig. IV-C-1).

All 14 mappable units are depicted in Fig. IV-C-3, which is a simplified version of the original compilation, without cultural features or bedding attitudes.

6. Modified Geologic Map

Although 14 different geologic units were originally mapped and compiled for the area, only combined units were generally distinguishable on enhanced ERTS pictures. For the Alpha Member of the Kaibab Formation, these combined units consist of β-1-2-3, 4-5, and 6. In some places, however, individual units of the Alpha Member could be detected on ERTS pictures (see Section VI). The Moenkopi Formation was identifiable in some of the ERTS pictures, but the basal conglomerate could not be detected. Deposits of Quaternary and Tertiary age were recognizable only as two general units:

(1) Basalt flows, landslide debris, and basalt talus.

(2) Alluvium, reworked Tertiary gravel, and Tertiary gravel.

A modified geologic map, showing the distribution of all of the combined units mentioned, is shown in Fig. IV-C-4. The contacts for these units are based on the original geologic map.

Results of analyses of individual enhancements used in comparing ERTS pictures with field-mapped products are presented in Section VI.

7. Mapping of Area B

Although Area B (see Fig. IV-C-1) was not covered in the original field effort on the Coconino Plateau, it subsequently became a prime area in which to test the applicability to geologic mapping of photointerpretation

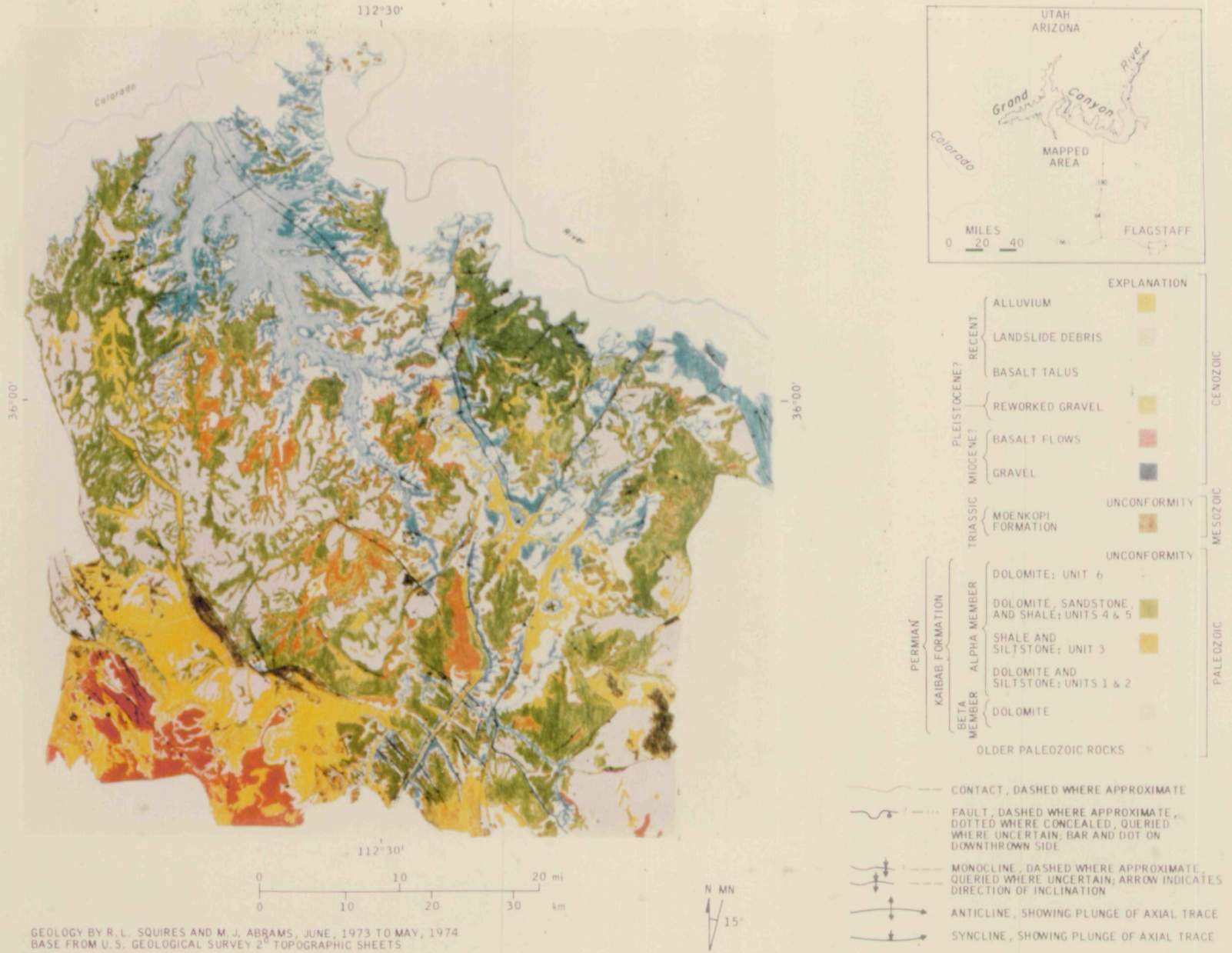

Fig. IV-C-3. Geologic map of part of the Coconino Plateau. Bedding attitudes and culture are omitted

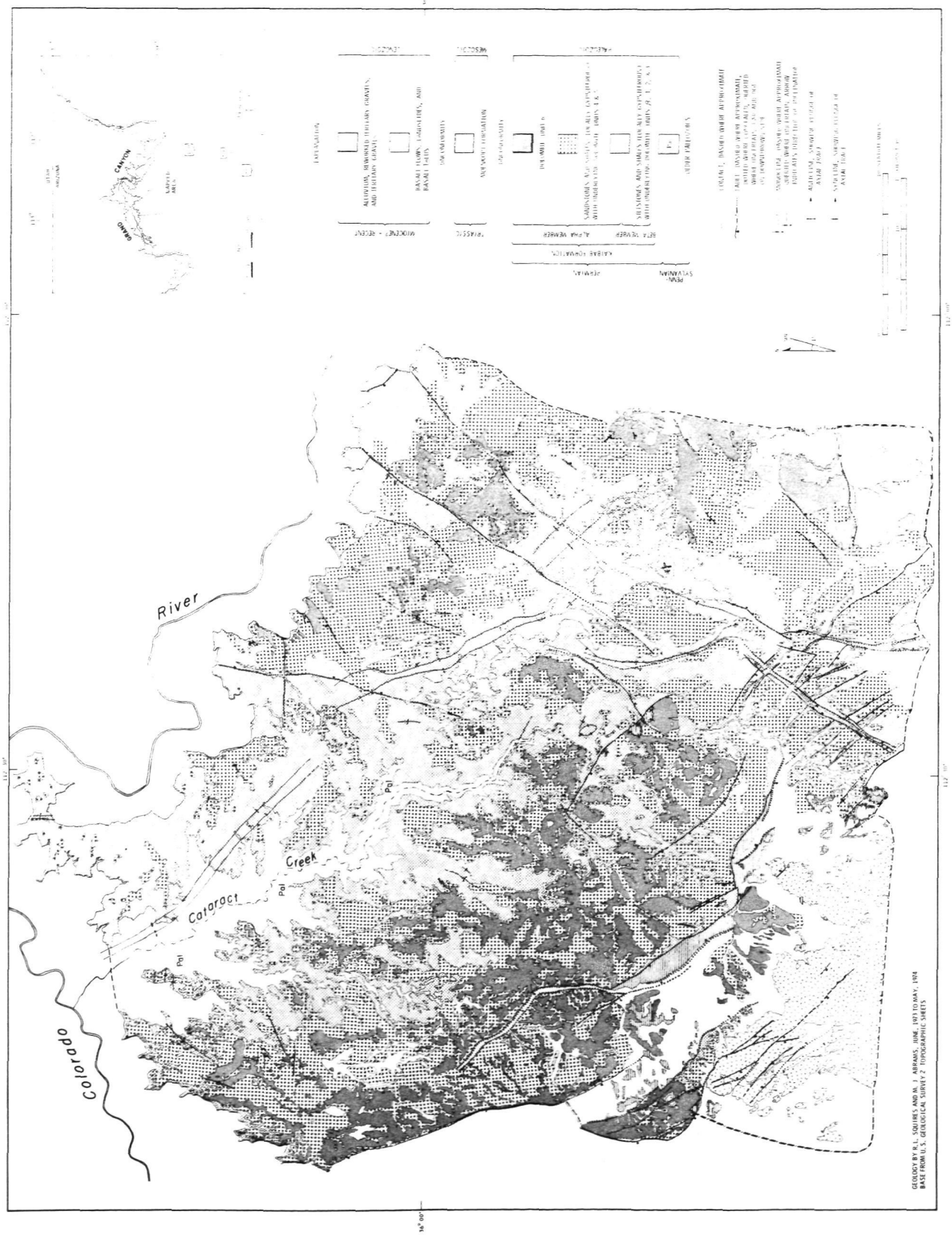

Fig. IV-C-4. Simplified geologic map of the Coconino Plateau, showing distribution of geologic units

techniques using both enhanced and unenhanced ERTS images. Some a priori information, available by inference from data collected in the adjacent Area A, was used to help to make decisions in the test area. However, the geologic map constructed from ERTS images was produced without any direct field evidence. Later, the test area was mapped in the field to evaluate the accuracy of the ERTS map. Figure IV-C-5 shows faults determined from the ERTS images and faults identified by field work. The geologic map compiled from ERTS data, the Geologic Map of Arizona (Ref. IV-C-5), and the map compiled from field data are shown in Fig. IV-C-6.

a. Structure. A comparison between the Geologic Map of Arizona and the ERTS-derived map of Area B shows that the ERTS map contains structural information entirely absent from the state map. Comparison with the field-derived map (see Fig. IV-C-5) shows that the two are in excellent agreement. All major faults recognized in the field were identified in the ERTS images. The short northwest–southeast faults mapped east of the Moore Tank fault system were not recognized in the ERTS images. Field studies indicate that these faults have only minor topographic expression and stratigraphic displacement, and therefore would be difficult to see in ERTS images. The two northeast-trending faults mapped from ERTS images east of the basalt outcrop could not be verified in the field, and no logical explanation for these features can be given.

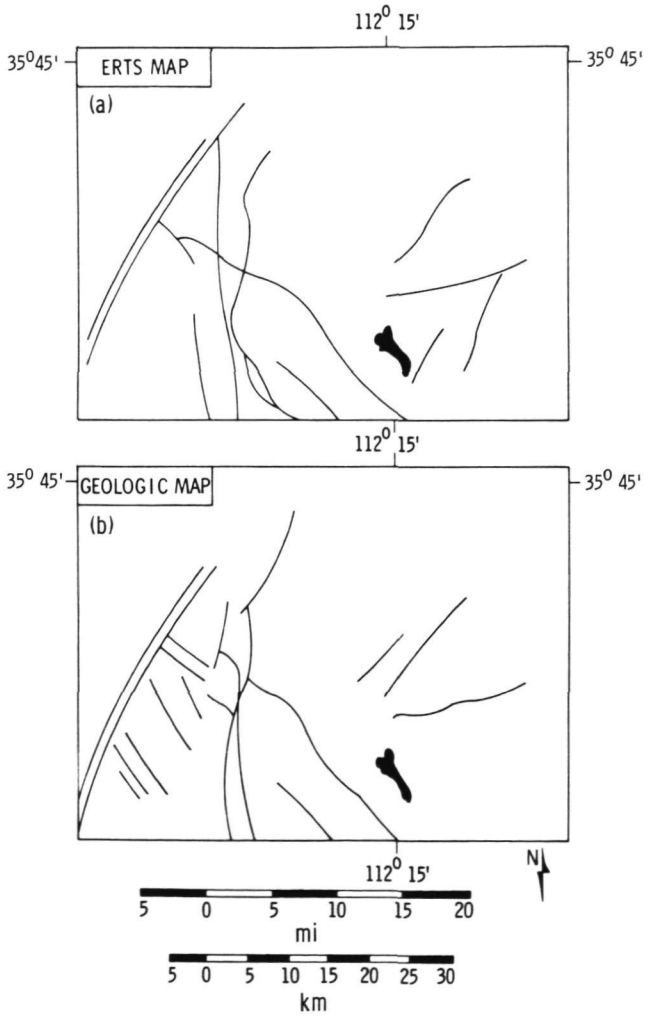

Fig. IV-C-5. (a) Fault map derived from ERTS images. (b) Fault map derived from field observations. Solid black feature is a basalt outcrop

b. Stratigraphy. Six different geologic formations were distinguishable in the ERTS images: basalt, Moenkopi, Kaibab unit 6, units 4 and 5, β-1-2-3, and alluvium.

Owing to the great difference in contrast, basalt outcrops and associated talus deposits were easily identified. Of the five areas of Moenkopi Formation mapped from ERTS images, four correspond accurately to field-mapped outcrops. The fifth area, on the southwest side of the railroad, corresponds to units 4 and 5. Confusion may be due to the similarity of Moenkopi Formation to the sandstone and shale of unit 5. With this exception, the Moenkopi Formation was accurately identified. The Geologic Map of Arizona identifies the general areas of basalt, but does not accurately map the Moenkopi Formations.

Excellent detail was recognizable in the ERTS images among units of the Kaibab Formation. The eastern third of the area was mapped from ERTS images as unit 6, which corresponds well to the actual field-mapped area of this unit; the other area of unit 6 in the center of the area corresponds fairly well to the actual area of unit 6. All areas mapped from ERTS images as units 4 and 5 are generally correctly identified. The small areas at the western edge of the map and the area along the southern edge are reasonably accurate, with somewhat less accuracy in the larger areas. Unit 2 was correctly mapped from ERTS images except for the south-central part of the area, which consists primarily of units 4 and 5. The two areas mapped as alluvium from the images correspond to actual field-mapped occurrences of alluvium.

Comparison with the Geologic Map of Arizona shows that the ERTS map is a significant improvement. No separation is made among the units of the Kaibab Formation on the Geologic Map of Arizona, where it is actually grouped with the underlying Toroweap Formation.

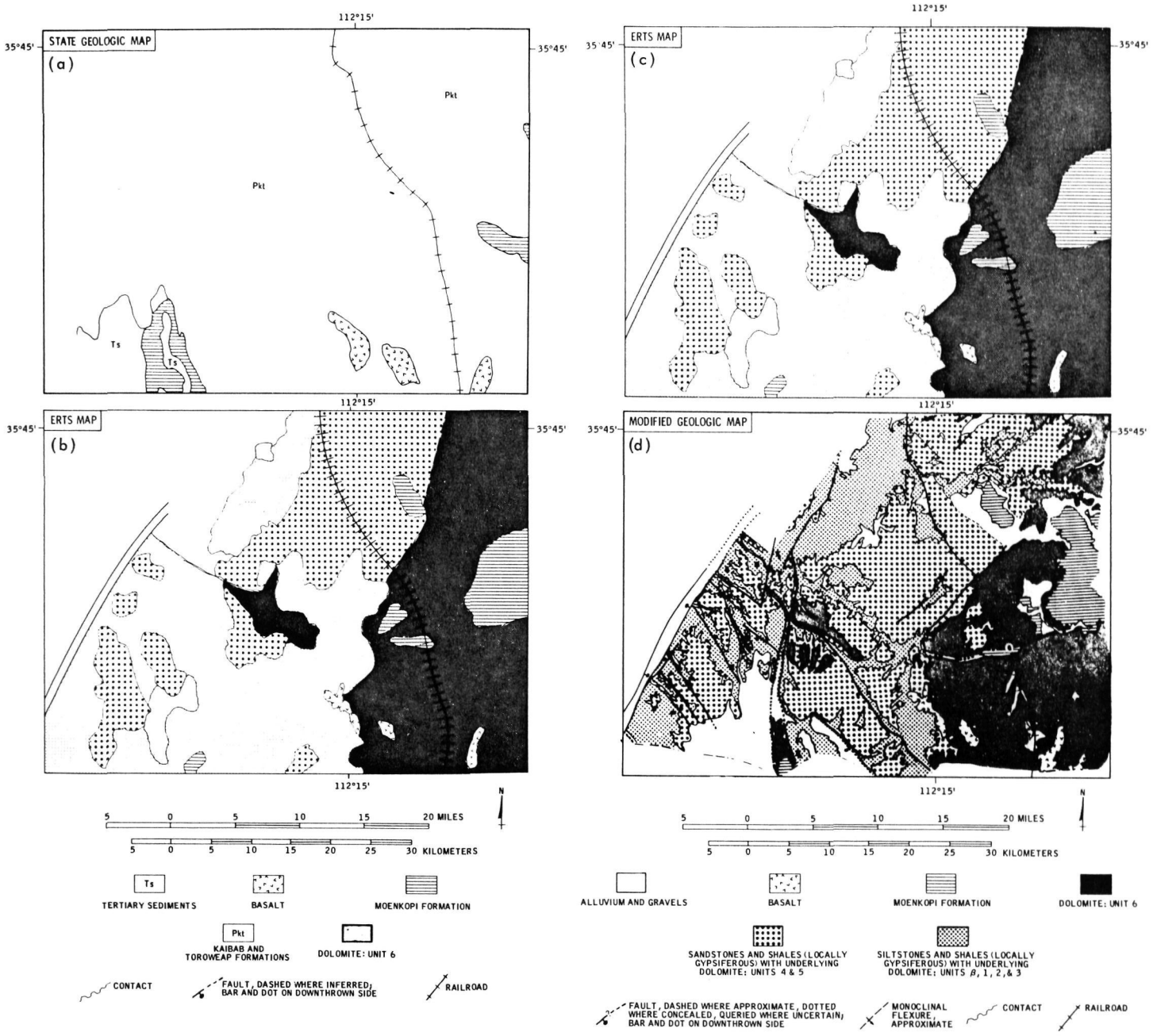

Fig. IV-C-6. (a) Geologic Map of Arizona showing Area B. (b) Geologic map made in the laboratory using unenhanced and computer-enhanced ERTS images. (c) Same as (b), except that extra stippling was used to distinguish unit from that in (d). (d) Part of the simplified geologic map (Fig. IV-C-4) covering Area B

8. Conclusions

Comparison between an ERTS-derived map and a field-derived map shows that a reasonable reconnaissance map can be produced from enhanced and unenhanced ERTS images. Structural details are readily apparent and can be delineated accurately.

Stratigraphic detail requires some degree of a priori information and familiarity with the general physiographic, topographic, structural, and geologic characteristics of the region. Careful enhancement of ERTS images is required to emphasize the maximum separation among units. Even then, an ERTS-derived map is no better than a combination soils and outcrop map, complicated by vegetation. However, with some key ground control, an ERTS-derived map can be greatly superior to existing reconnaissance maps, as evidenced by the excellent quality of the ERTS map compared with the present Geologic Map of Arizona.

D. The Verde Valley

D. P. Elston

The northern Arizona test site, centered approximately on the Verde Valley (see Fig. I-1), was selected originally because it offered excellent exposures and good geologic map coverage. In contrast to the Shivwits and Coconino Plateaus, this site includes areas that have been mapped in detail at scales of 1:48,000 and 1:62,500 (Refs. IV-D-1 through IV-D-8). However, a large part of the area has been mapped only in reconnaissance at 1:375,000 scale for the Geologic Map of Arizona (Ref. IV-D-9), which was published at 1:500,000 scale. Part of the Geologic Map of Arizona that includes the test site in north-central Arizona is shown, without explanation, in Fig. IV-D-1, to allow comparison with the ERTS-derived maps of geologic details in Precambrian and Phanerozoic terranes.

1. Geologic Map

ERTS-1 images allow details of the distribution of several of the geologic units to be improved with respect to the Geologic Map of Arizona. The images, employed with the detailed geologic maps, led to the monoscopic and stereoscopic identification of the units shown in Figs. IV-D-2a and IV-D-2b (see Fig. IV-D-2c for explanation). The product is a regional geologic map referenced to a near-orthographic photo-base. Geologic detail is degraded with respect to standard geologic quadrangle maps, but is improved with respect to areas that have been mapped only in reconnaissance. A geologic map referenced to an orthogonal photo-base allows evaluation of the relations of geologic units to physiographic, vegetational, and structural characteristics in a single display. The planimetric geology could be transferred to a 1:250,000-scale topographic base to produce a preliminary geologic map. The new photogeologic map has served as control for evaluating stratigraphic units in the computer-processed images.

Rock types exposed in the study area include reddish and light gray granitic rocks and dark gray mafic rocks of Precambrian age; red-brown to buff to light gray sedimentary strata of Paleozoic age; and gray basalts and light gray to white lake beds of late Tertiary age. Bedrock, or bedrock on which only sparse vegetation occurs, is extensively exposed in the region. However, the topographically highest parts of the area support extensive stands of Ponderosa pine, and the major stream courses (Verde River, Oak Creek, Beaver Creek, and Clear Creek) contain stands of cottonwood and sycamore trees and associated deciduous plants.

Basalt of late Tertiary age was easily discriminated on the ERTS images, but, not unexpectedly, appeared similar to gabbro of Precambrian age. A tuff-bearing area in a basaltic flow sequence was identified and mapped in the southeastern part of the mapped area. Such features are not represented on the state map. Quaternary and Tertiary sediments overlie and underlie the Tertiary basalts, and were mapped with fair ease. Details of their distribution were improved with respect to the state map. However, details of the stratigraphy in the Paleozoic rocks could not be resolved, although the red Supai Formation of Pennsylvanian and Permian age was apparent on false-color composites of the multi-spectral images. As a consequence, all Paleozoic rocks were mapped as one unit. In this respect, the Geologic Map of Arizona is far superior. In contrast, more Precambrian units could be identified in the ERTS images than are shown on the state geologic map, and the ERTS "photogeologic" map is an improvement for the older rocks. We conclude that ERTS images at about 1:200,000 scale, used with conventional photogeologic and field geologic techniques, can lead to improved geologic reconnaissance maps.

2. Fault and Lineament Map

The most striking geologic aspect of the ERTS images is the synoptic view provided of fracture and lineament patterns that occur in basement rocks and in surficial deposits that mask the bedrock and basement. Faults and lineaments in north-central Arizona are shown in Figs. IV-D-3a and IV-D-3b (see Fig. IV-D-2c for explanation). The faults are from published maps. In many cases, the trace of a fault was less clear than the trace of nearby

Fig. IV-D-1. Geologic map of north-central Arizona from Geologic Map of Arizona (see Ref. IV-D-9)

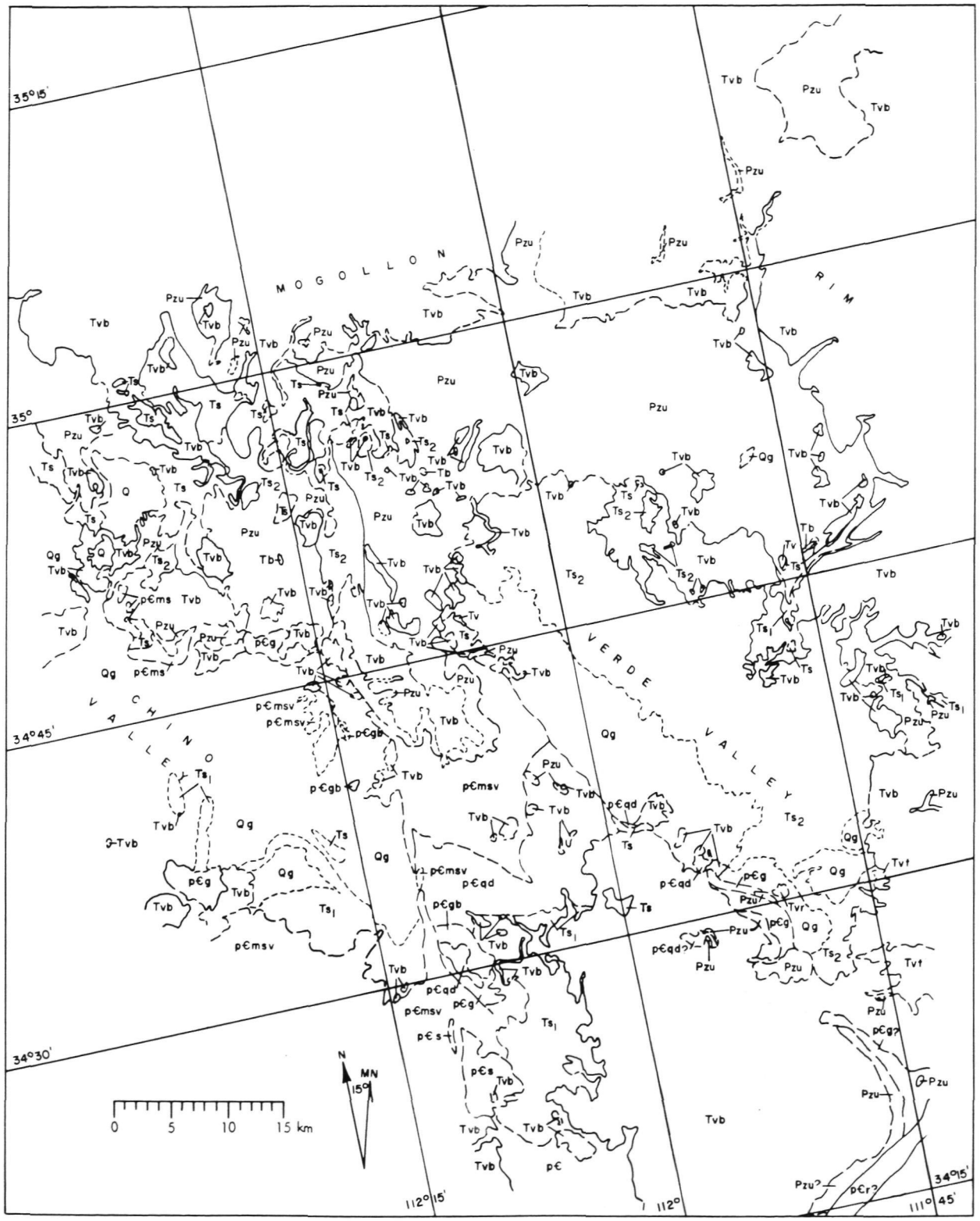

Fig. IV-D-2a. Geologic map of north-central Arizona compiled from published and unpublished information on ERTS-1 images

Fig. IV-D-2b. Geologic map of north-central Arizona shown in Fig. IV-D-2a superimposed on background of an ERTS-1 image

ORIGINAL PAGE IS
OF POOR QUALITY

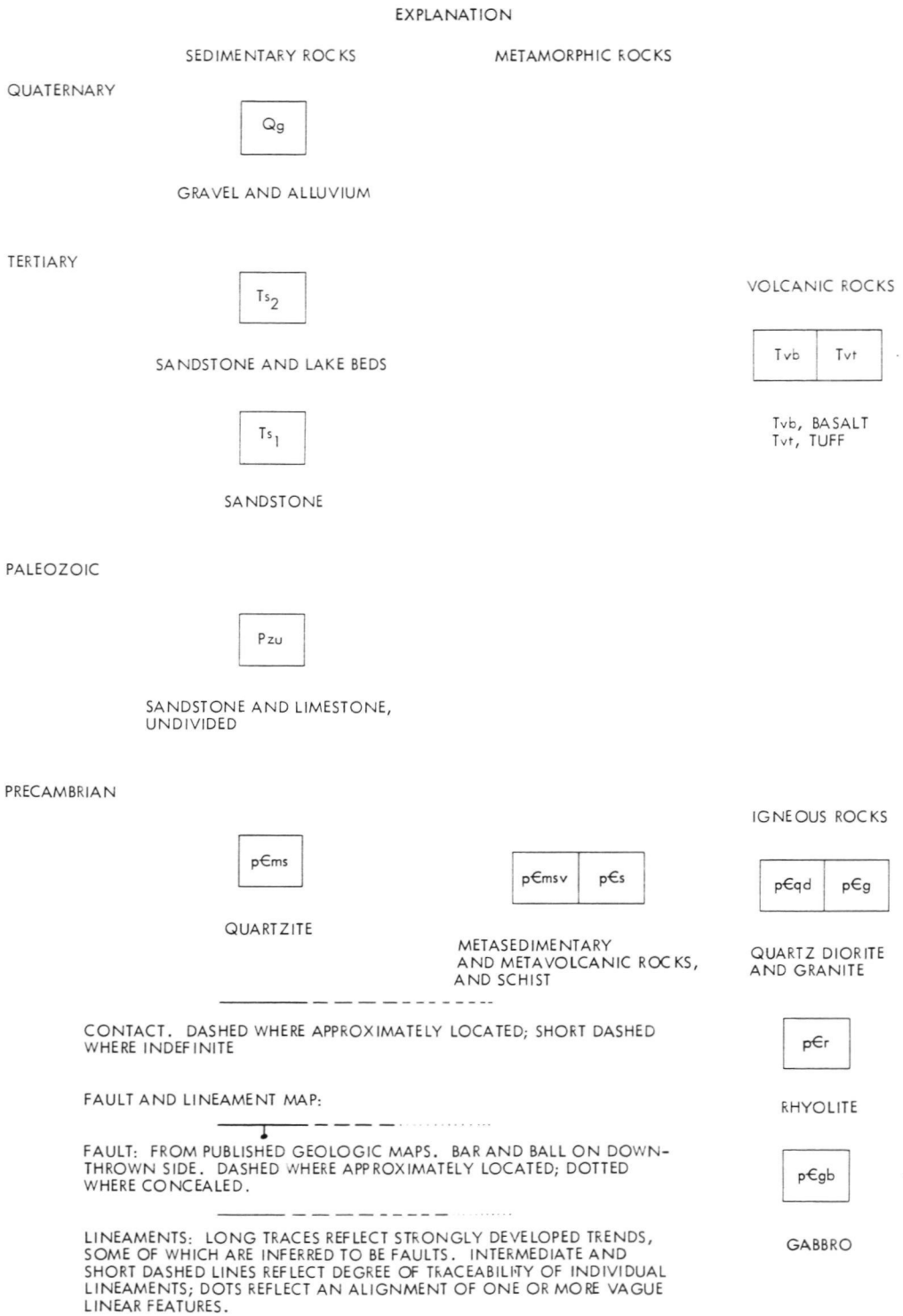

Fig. IV-D-2c. Explanation for Figs. IV-D-2a, b and IV-D-3a, b

lineaments. For purposes of illustration, faults are shown as heavy lines in Fig. IV-D-3 to allow them to be distinguished from the lineaments.

The test site in north-central Arizona lies within the structural boundary of the Colorado Plateaus province, and only comparatively simple high-angle normal or gravity faults displace the Paleozoic and Tertiary rocks. Thus, where Precambrian rocks are exposed, the structure observed principally reflects structure of Precambrian age. The dominant Precambrian fault and lineament systems trend northeast and north. In contrast, northwest-trending faults and lineaments appear mainly to reflect comparatively recent structural adjustments in the Tertiary period, and they lack the laterally continuous characteristic of the northeast- and north-trending systems. The Precambrian structural grain has been imparted to the overlying Phanerozoic rocks, and the major fault and lineament systems have been sites of renewed structural adjustments. The Oak Creek fault in the northeastern part of the mapped area, which is seen to displace only Paleozoic and Tertiary rocks, almost certainly overlies a north-trending fracture system in the basement analogous to the Shylock fault in the south-central part of the mapped area. Northeast-trending lineaments occur near Williams, Arizona, in the northern part of the mapped area (35°45′N, 112°12′W). Their trends parallel those of strongly developed Precambrian faults in the Grand Canyon to the north. Eruptive centers of the late Tertiary San Francisco volcanic field in the Colorado Plateau are localized along these lineaments. Presumably, northeast-trending Precambrian faults, analogous to the Chaparral and Spud faults in the southern part of the mapped area, underlie parts of the Plateau.

Results of the evaluation of computer-enhanced images for stratigraphic mapping and structural control are given separately in Section VI.

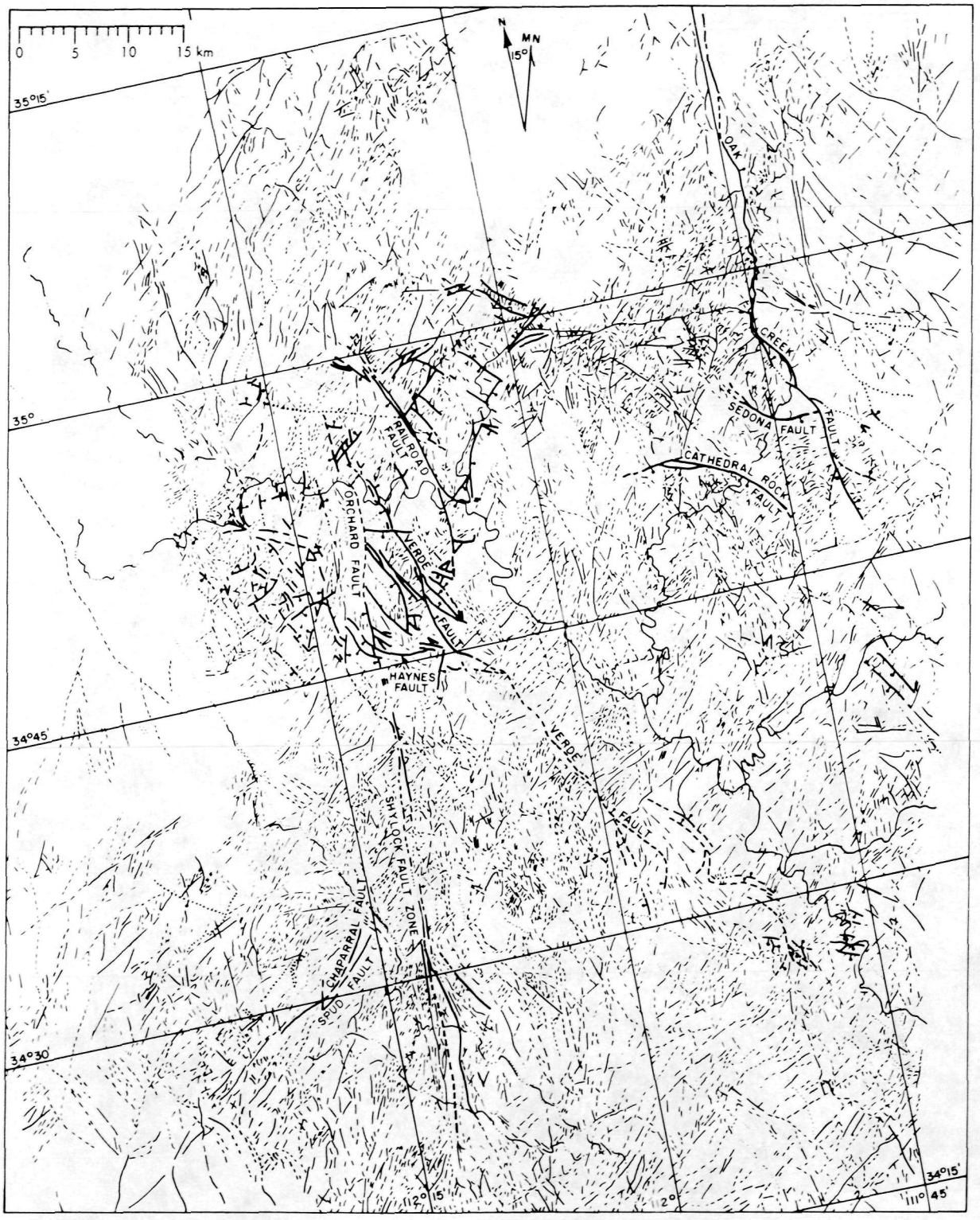

Fig. IV-D-3a. Fault and lineament map of north-central Arizona. Faults (heavy lines) are compiled from published information, lineaments from monoscopic and stereoscopic analyses of ERTS-1 images

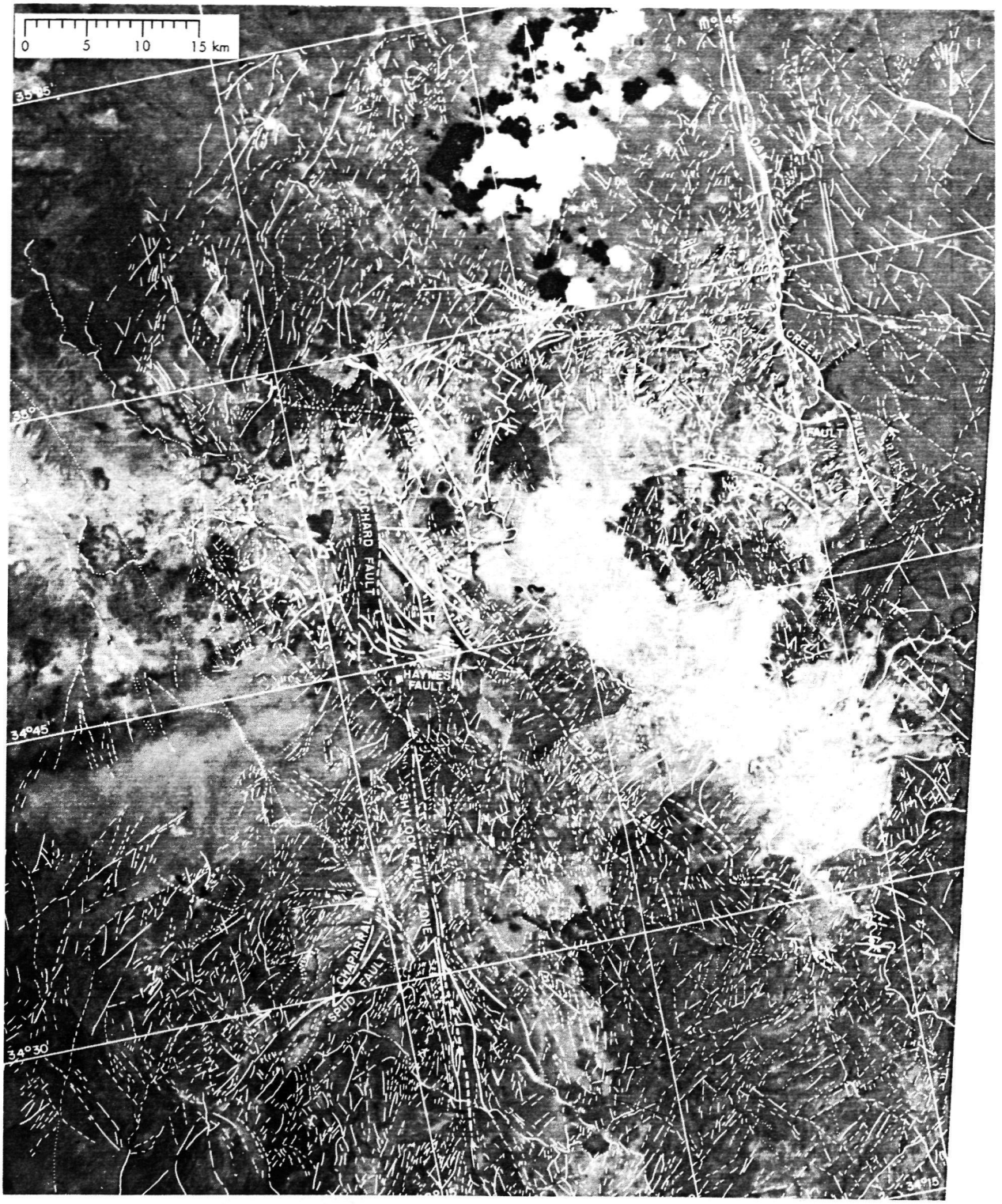

Fig. IV-D-3b. Fault and linement map of north-central Arizona shown in Fig. IV-D-3a superimposed on background of an ERTS-1 image

References

IV-A-1. Ransome, F. L., "Pre-Cambrian Sediments and Faults in the Grand Canyon of the Colorado," *Science*, Vol. 27, pp. 667–669, 1908.

IV-A-2. Darton, N. H., "A Reconnaissance of Parts of Northwestern New Mexico and Northern Arizona," *U. S. Geol. Survey Bull. 435*, 88 pp., 1910.

IV-A-3. Noble, L. F., "The Shinumo Quadrangle, Grand Canyon District, Arizona," *U. S. Geol. Survey Bull. 549*, 96 pp., 1914.

IV-A-4. Noble, L. F., and Hunter, J. F., "A Reconnaissance of the Archean Complex of the Granite Gorge, Grand Canyon, Arizona," *U. S. Geol. Survey Prof. Paper 98-I*, pp. 95–113, 1916.

IV-A-5. Noble, L. F., Geological History of the Bright Angel Quadrangle, Arizona, U. S. Geol. Survey, Text on Back of Topographic Sheet, Bright Angel Quadrangle, Coconino County, Arizona, 1918.

IV-A-6. McKee, E. D., "The Bright Angel Fault," *Grand Canyon Nature Notes*, Vol. 4, pp. 21–22, 1929.

IV-A-7. Maxson, J. H., and Campbell, I., "Faulting in the Bright Angel Quadrangle, Arizona" (abs), *Geol. Soc. Amer. Proc. 1933*, p. 301, 1934.

IV-A-8. Maxson, J. H., Geologic Map of the Bright Angel Quadrangle, Grand Canyon National Park, Arizona, Grand Canyon Nat. History Assoc., 1961.

IV-A-9. Sears, J. W., *Structural Geology of the Precambrian Grand Canyon Series, Arizona*, M. S. Dissertation, 100 pp., University of Wyoming, 1973.

IV-A-10. Sauck, W. A., and Sumner, J. S., Residual Aeromagnetic Map of Arizona, University of Arizona, Tucson, 1971.

IV-A-11. Sears, J. D., "Geology of Comb Ridge and Vicinity North of San Juan River, San Juan County, Utah," *U. S. Geol. Survey Bull. 1021-E*, pp. 176–207, 1956.

IV-A-12. Johnson, D., "A Geological Excursion in the Grand Canyon Region," *Boston Soc. Nat. History Proc.*, Vol. 34, pp. 135–161, 1909.

IV-A-13. Babenroth, D. L., and Strahler, A. N., "Geomorphology and Structure of the East Kaibab Monocline, Arizona and Utah," *Geol. Soc. Amer. Bull.*, Vol. 56, pp. 107–150, 1945.

IV-A-14. Krieger, M. H., "Geology of the Prescott and Paulden Quadrangles, Arizona," *U. S. Geol. Survey Prof. Paper 467*, 127 pp., 1965.

IV-A-15. Wilson, E. D., Moore, R. T., and Cooper, J. R., Geologic Map of Arizona, Tucson, Arizona, Arizona Bureau of Mines, 1969.

IV-A-16. Krieger, M. H., "Reconnaissance Geologic Map of the Picacho Butte Quadrangle, Yavapai County, Arizona," *U. S. Geol. Survey Prof. Paper 750-B*, pp. B157–B160, 1967.

IV-A-17. Cooley, M. E., Harshbarger, J. W., Akers, J. P., and Hardt, W. F., "Regional Hydrogeology of the Navajo and Hopi Indian Reservations," *U. S. Geol. Survey Prof. Paper 521-A*, 61 pp., 1969.

IV-A-18. Koons, E. D., "Geology of the Uinkaret Plateau, Northern Arizona," *Geol. Soc. Amer. Bull.*, Vol. 56, pp. 151–180, 1945.

IV-A-19. Twenter, F. R., "Geology and Promising Areas for Ground Water Development in the Hualapai Indian Reservation," *U. S. Geol. Survey Prof. Paper 1576-A*, pp. A1–A37, 1962.

IV-A-20. Blissenbach, E., "Geology of Aubrey Valley," *Plateau*, Vol. 24, pp. 119–127, 1952.

IV-A-21. Robinson, H. H., "The San Franciscan Volcanic Field, Arizona," *U. S. Geol. Survey Prof. Paper 76*, 213 pp., 1913.

IV-A-22. Condit, C. D., "Geology of Shadow Mountain, Arizona," *Geology of Northern Arizona with Notes on Archaeology and Paleoclimate, Part II*, p. 454, for Geological Society of America, Rocky Mountain Section Meeting, Flagstaff, Arizona, 1974.

IV-A-23. Gregory, H. E., "Geology of the Navajo Country—A Reconnaissance of Parts of Arizona, New Mexico, and Utah," *U. S. Geol. Survey Prof. Paper 93*, 161 pp., 1917.

IV-A-24. Williams, H., "Pliocene Volcanoes of the Navajo–Hopi Country," *Geol. Soc. Amer. Bull.*, Vol. 47, pp. 111–172, 1936.

IV-A-25. Gilbert, G. K., *Report on the Geology of the Henry Mountains*, U. S. Geog. and Geol. Survey, Rocky Mtn. Region, 160 pp., 1877.

IV-A-26. Baker, A. A., "Geology of the Monument Valley–Navajo Mountain Region, San Juan County, Utah," *U. S. Geol. Survey Bull. 865*, 106 pp., 1936.

IV-A-27. Hunt, C. B., "New Interpretation of Some Laccolithic Mountains and Its Possible Bearing on Structural Traps for Oil and Gas," *Amer. Assoc. Petroleum Geologists Bull.*, Vol. 26, pp. 197–203, 1942.

IV-A-28. Condie, K. C., "Crystallization Po_2 of Syenite Porphyry From Navajo Mountain, Southern Utah," *Geol. Soc. Amer. Bull.*, Vol. 75, pp. 359–362, 1964.

IV-A-29. Walcott, C. D., "Study of a Line of Displacement in the Grand Cañon of the Colorado, in Northern Arizona," *U. S. Geol. Survey Bull.*, Vol. I, pp. 49–64, 1889.

IV-A-30. Ford, T. D., and Breed, W. J., "Late Precambrian Chuar Group, Grand Canyon, Arizona," *Geol. Soc. Amer. Bull.*, Vol. 84, pp. 1243–1260, 1973.

IV-A-31. Pasteels, P., and Silver, L. T., "Geochronologic Investigations in the Crystalline Rocks of the Grand Canyon, Arizona" (abs), *Geol. Soc. Amer. Special Paper 87*, p. 124, 1966.

IV-A-32. Marshall, D. R., *Gravity Gliding at Gray Mountain, Coconino County, Arizona*, M. S. Dissertation, 83 pp., Northern Arizona University, 1972.

IV-A-33. West, R. E., and Sumner, J. S., Bouguer Gravity Anomaly Map of Arizona, Tucson, Arizona, University of Arizona, 1973.

IV-A-34. Ragan, D. M., and Sheridan, M. F., "The Archean Rocks of the Grand Canyon, Arizona" (abs), *Geol. Soc. Amer. Abs. With Programs*, Vol. 2, pp. 132–133, 1970.

IV-A-35. Anderson, C. A., "Precambrian Wrench Fault in Central Arizona," in "Geological Survey Research 1967," *U. S. Geol. Survey Prof. Paper 575-C*, pp. C60–C65, 1967.

IV-A-36. Anderson, C. A., Preliminary Geologic Map of the NW1/4 Mayer Quadrangle, Yavapai County, Arizona, U. S. Geol. Survey Mineral Inv. Field Studies Map MF-228, 1959.

IV-A-37. Anderson, C. A., and Creasey, S. C., "Geology and Ore Deposits of the Jerome Area, Yavapai County, Arizona," *U. S. Geol. Survey Prof. Paper 308*, 184 pp., 1958.

IV-A-38. Anderson, C. A., and Creasey, S. C., Geologic Map of the Mingus Mountain Quadrangle, Yavapai County, Arizona, U. S. Geol. Survey Geol. Quad. Map GQ-715, 1967.

IV-A-39. Anderson, C. A., Blacet, P. M., Silver, L. T., and Stern, T. W., "Revision of Precambrian Stratigraphy in the Prescott–Jerome Area, Yavapai County, Arizona," *U. S. Geol. Survey Bull. 1324-C*, pp. C1–C16, 1971.

IV-A-40. Blacet, P. M., "Unconformity Between Gneissic Granodiorite and Overlying Yavapai Series (Older Precambrian), Central Arizona," in "Geological Research 1966," *U. S. Geol. Survey Prof. Paper 550-B*, pp. B1–B5, 1966.

IV-A-41. Lehner, R. E., "Geology of the Clarkdale Quadrangle, Arizona," *U. S. Geol. Survey Bull. 1021-N*, pp. 511–592, 1958.

IV-A-42. Bowers, W. E., "The Canaan Peak, Pine Hollow, and Wasatch Formations in the Table Cliff Region, Garfield County, Utah," *U. S. Geol. Survey Bull. 1331-B*, pp. B1–B39, 1972.

IV-A-43. Shoemaker, E. M., "Structural Features of the Central Colorado Plateau and Their Relation to Uranium Deposits," in Page, L. R., "Contributions to the Geology of Uranium and Thorium," *U. S. Geol. Survey Prof. Paper 300*, pp. 155–170, 1956.

IV-A-44. McKee, E. D., Wilson R. F., Breed, W. J., and Breed, C. S., "Evolution of the Colorado River in Arizona—A Hypothesis Developed at the Symposium on Cenozoic Geology of the Colorado Plateau in Arizona, August 1964," *Mus. Northern Arizona Bull. 44*, 67 pp., 1967.

IV-A-45. Krieger, M. H., Creasey, S. C., and Marvin, R. F., "Ages of Some Tertiary Andesitic and Latitic Volcanic Rocks in the Prescott–Jerome Area, North-central Arizona," *U. S. Geol. Survey Prof. Paper 750-B*, pp. B157–B160, 1971.

IV-A-46. Young, R. A., and Brennan, W. J., "Peach Springs Tuff: Its Bearing on Structural Evolution of the Colorado Plateau and Development of Cenozoic Drainage in Mojave County, Arizona," *Geol. Soc. Amer. Bull.*, Vol. 85, pp. 83–90, 1974.

IV-A-47. Lucchitta, I., "Early History of the Colorado River in the Basin and Range Province," *Geol. Soc. Amer. Bull.*, Vol. 83, pp. 1933–1948. 1972.

IV-A-48. Lucchitta, I., "Structural Evolution of Northwest Arizona and Its Relation to Adjacent Basin and Range Province Structures," *Geology of Northern Arizona with Notes on Archaeology and Paloclimate, Part I*, for Geological Society of America, Rocky Mountain Section Meeting, Flagstaff, Arizona, 1974.

IV-A-49. Fuis, G. S., *The Geology and Mechanics of Formation of the Fort Rock Dome, Yavapai County, Arizona*, Ph.D. Dissertation, 278 pp., California Institute of Technology, Pasadena, 1973.

IV-A-50. Akers, J. P., Irwin, J. H., Stevens, P. R., McClymonds, N. E., and Chenoweth, W. L., Geology of the Cameron Quadrangle, Arizona, U. S. Geol. Survey Geol. Quad. Map GQ-162, 1962.

IV-A-51. McKee, E. D., and McKee, E. H., "Pliocene Uplift of the Grand Canyon Region: Time of Drainage Adjustment," *Geol. Soc. Amer. Bull.*, Vol. 83, pp. 1923–1932, 1972.

IV-A-52. Damon, P. E., Shafiqullah, M., and Leventhal, J. S., "K-Ar Chronology for the San Francisco Volcanic Field and Rate of Erosion of the Little Colorado River," *Geology of Northern Arizona with Notes on Archaeology and Paleoclimate, Part I*, for Geological Society of America, Rocky Mountain Section Meeting, Flagstaff, Arizona, 1974.

IV-A-53. Reiche, P., "Quaternary Deformation in the Cameron District of the Plateau Province," *Amer. J. Sci.*, 5th Ser., Vol. 34, pp. 128–138, 1937.

IV-A-54. Hunt, C. B., "Cenozoic Geology of the Colorado Plateau," *U. S. Geol. Survey Prof. Paper 279*, 99 pp., 1956.

IV-A-55. Hamblin, W. K., "Structure of the Western Grand Canyon Region," *Utah Geol. Soc. Guidebook 23*, pp. 3–19, 1970.

IV-A-56. Townley, S. D., and Allen, M. W., "Descriptive Catalog of Earthquakes of the Pacific Coast of the United States, 1769–1928" *Seismol. Soc. Amer. Bull.*, Vol. 29, pp. 1–297, 1939.

IV-A-57. Sturgul, J. R., and Irwin, T. D., "Earthquake History of Arizona and New Mexico," *Ariz. Geol. Soc. Digest*, Vol. 9, pp. 1–37, 1971.

IV-A-58. Coffman, J. L., and von Hake, C. A., "Earthquake History of the United States," *U. S. Nat. Oceanic and Atmospheric Adm. Pub. 41-1*, rev. ed. (through 1970), 208 pp., 1973.

IV-A-59. Maxson, J. H., Preliminary Geologic Map of the Grand Canyon and Vicinity, Arizona, Eastern Section, Grand Canyon Nat. History Assoc., 1967.

IV-A-60. Maxson, J. H., Preliminary Geologic Map of the Grand Canyon and Vicinity, Arizona, Western and Central Sections, Grand Canyon Nat. History Assoc., 1969.

IV-A-61. Pomeroy, J. S., Photogeologic Map of the Hurricane Cliffs–2 NW Quadrangle, Mohave County, Arizona, U. S. Geol. Survey Misc. Geol. Inv. Map I-293, 1959.

IV-A-62. Marshall, C. H., Photogeologic Map of the Hurricane Cliffs–2 NE Quadrangle, Mohave Country, Arizona, U. S. Geol. Survey Misc. Geol. Inv. Map I-252, 1957.

IV-A-63. Marshall, C. H., Photogeologic Map of the Lost Spring Mountain NW Quadrangle, Mohave, County, Arizona, U. S. Geol. Survey Misc. Geol. Inv. Map I-146, 1956.

IV-A-64. Pillmore, C. L., Photogeologic Map of the Short Creek NE Quadrangle, Mohave, County, Arizona, U. S. Geol. Survey Misc. Inv. Map I-142, 1956.

IV-A-65. Morris, R. H., Photogeologic Map of the Shinarump NW Quadrangle, Coconino County, Arizona, U. S. Geol. Survey Misc. Geol. Inv. Map I-139, 1956.

IV-A-66. McQueen, K., Photogeologic Map of the Shinarump NE Quadrangle, Coconino County, Arizona, U. S. Geol. Survey Misc. Geol. Inv. Map I-255, 1957.

IV-A-67. Wells, J. D., "Stratigraphy and Structure of the House Rock Valley Area, Coconino County, Arizona," *U. S. Geol. Survey Bull. 1081-D*, pp. 117–158, 1960.

IV-A-68. Marshall, C. H., Photogeologic Map of the Jacob Lake Quadrangle, Coconino County, Arizona, U. S. Geol. Survey Misc. Geol. Inv. Map I-194, 1956.

IV-A-69. Shoemaker, E. M., *Penetration Mechanics of High-Velocity Meteorites*, International Geol. Cong., 21st, Copenhagen, 1960, Report, pt. 18, pp. 418–434, 1960.

IV-A-70. Krieger, M. H., Reconnaissance Geologic Map of the Turkey Canyon Quadrangle, Yavapai County, Arizona, U. S. Geol. Survey Misc. Geol. Inv. Map I-501, 1967.

IV-A-71. Moore, R. T., "Geology of the Virgin and Beaverdam Mountains, Arizona," *Ariz. Bur. Mines Bull. 186*, 65 pp., 1972.

IV-A-72. Huntoon, P. W., *The Hydro-mechanics of the Ground Water System in the Southern Portion of the Kaibab Plateau, Arizona*, Ph.D Dissertation, 381 pp., University of Arizona, 1970.

IV-A-73. Phoenix, D. A., "Geology of the Lees Ferry Area, Coconino County, Arizona," *U. S. Geol. Survey Bull. 1137*, 86 pp., 1963.

IV-B-1. Lucchitta, I., *Cenozoic Geology of the Upper Lake Mead Area Adjacent to the Grand Wash Cliffs*, Arizona, Ph.D. Thesis, 218 pp., Pennsylvania State University, 1966.

IV-B-2. Lucchitta, I., "Early History of the Colorado River in the Basin and Range Province," *Geol. Soc. Amer. Bull.*, Vol. 83, pp. 1933–1948, 1972.

IV-B-3. Young, R. A., *Cenozoic Geology Along the Edge of the Hualapai Plateau, Arizona*, Ph.D. Thesis, 167 pp., Washington University, St. Louis, Mo., 1966.

IV-B-4. Young, R. A., and Brennan, W. J., "Peach Springs Tuff: Its Bearing on Structural Evolution of the Colorado Plateau and Development of Cenozoic Drainage in Mohave County, Arizona," *Geol. Soc. Amer. Bull.*, Vol. 85, pp. 83–90, 1974.

IV-B-5. Longwell, C. R., Pampeyan, E. H., Boyer, B., and Roberts, R. J., "Geology and Mineral Deposits of Clark County, Nevada," *Nevada Bur. Mines Bull. 62*, 218 pp., 1965.

IV-B-6. Dutton, C. E., "The Tertiary History of the Grand Canyon District," *U. S. Geol. Survey Mon. 2*, Atlas, 264 pp., 1882.

IV-B-7. Lucchitta, I., and McKee, E. H., "New Chronological Constraints on the History of the Colorado River and the Grand Canyon," *Geol. Soc. Amer., Abs. with Programs (Cordilleran Section)*, Vol. 7, p. 342, 1975.

IV-B-8. Davis, W. M., "An Excursion to the Grand Canyon of the Colorado," *Harvard Coll. Mus. Comp. Zoology Bull. 38*, pp. 107–201, 1901.

IV-B-9. Davis, W. M., "An Excursion to the Plateau Province of Utah and Arizona," *Harvard Coll. Mus. Comp. Zoology Bull. 42*, pp. 1–50, 1903.

IV-B-10. Koons, E. D., "Geology of the Uinkaret Plateau, Northern Arizona," *Geol. Soc. Amer. Bull.*, Vol. 56, pp. 151–180, 1945.

IV-B-11. Hunt, C. B., "Cenozoic Geology of the Colorado Plateau," *U. S. Geol. Survey Prof. Paper 279*, 99 pp., 1956.

IV-B-12. Hunt, C. B., "Geologic History of the Colorado River" in "The Colorado River Region and John Wesley Powell," *U. S. Geol. Survey Prof. Paper 669*, Sec. C., pp. 59–130, 1969.

IV-B-13. McKee, E. D., Wilson, R. F., Breed, W. J., and Breed, C. S., eds., "Evolution of the Colorado River in Arizona," *Mus. Northern Arizona Bull. 44*, 68 pp., 1967.

IV-B-14. Blackwelder, E., "Origin of the Colorado River," *Geol. Soc. Amer. Bull.*, Vol. 45, pp. 551–566, 1934.

IV-B-15. Lucchitta, I., "Structure and Physiography of the Shivwits Plateau, Arizona," *Proceedings of the Fourth Annual Conference on Remote Sensing in Arid Lands*, pp. 148–152, University of Arizona, 1974.

IV-B-16. Lucchitta, I., "Geomorphic Development of the Western Grand Canyon Region, Arizona," in preparation.

IV-B-17. Lucchitta, I., and Young, R. A., "Course of the Ancestral Colorado River Before Capture and Integration," in preparation.

IV-B-18. McKee, E. D., and McKee, E. H., "Pliocene Uplift of the Grand Canyon Region—Time of Drainage Adjustment," *Geol. Soc. Amer. Bull.*, Vol. 83, pp. 1923–1932, 1972.

IV-B-19. Damon, P. E., Shafiqullah, M., and Leventhal, J. W., "K-Ar Chronology for the San Francisco Volcanic Field and Rate of Erosion of the Little Colorado River," *Geology of Northern Arizona With Notes on Archaeology and Paleoclimate, Part I*, p. 221, for Geological Society of America, Rocky Mountain Section Meeting, Flagstaff, Arizona, 1974.

IV-B-20. Hamblin, W. K., "Structure of the Western Grand Canyon Region" in "The Western Grand Canyon District," *Utah Geol. Soc. Guidebook 23*, pp. 3–19, 1970.

IV-B-21. Best, M. G., Brimhall, W. H., and Hamblin, W. K., "Late Cenozoic Basalts on the Western Margin of the Colorado Plateaus, Utah and Arizona," *Brigham Young University Research Reports of the Dept. of Geology*, 69-1, 39 pp., 1969.

IV-B-22. Koons, E. D., "Geology of the Eastern Hualapai Reservation," *Plateau*, Vol. 20, pp. 53–60, 1948.

IV-B-23. Lovejoy, E. M. P., "Major Early Cenozoic Deformation Along Hurricane Fault Zone, Utah and Arizona," *Am. Assoc. Petroleum Geologists Bull.*, Vol. 57, pp. 510–519, 1973.

IV-B-24. Gardner, L. S., "The Hurricane Fault in Southwestern Utah and Northwestern Arizona," *Am. J. Sci.*, Vol. 239, pp. 241–260, 1941.

IV-B-25. Averitt, P. A., "Table of Post-Cretaceous Geologic Events Along the Hurricane Fault, Near Cedar City, Iron County, Utah," *Geol. Soc. Amer. Bull.*, Vol. 75, pp. 901–908, 1964.

IV-B-26. Damon, P. E., *Correlation and Chronology of Ore Deposits and Volcanic Rocks*, Arizona University Geochronology Labs, Annual Progress Report, COO-689-50, Contract AT (11-1)-689, to Research Division, U. S. Atomic Energy Commission, 157 pp., 1965.

IV-B-27. Hamblin, W. K., "Origin of 'Reverse Drag' on the Downthrown Side of Normal Faults," *Geol. Soc. Amer. Bull.*, Vol. 76, pp. 1145–1164, 1965.

IV-B-28. Shuey, R. T., Schellinger, D. K., Johnson, E. H., and Alley, L. B., "Aeromagnetics and the Transition Between the Colorado Plateau and the Basin and Range Provinces," *Geology*, Vol. 1, pp. 107–110, 1973.

IV-B-29. Noble, L. F., "The Shinumo Quadrangle, Grand Canyon District, Arizona," *U. S. Geol. Survey Bull. 549*, 100 pp., 1914.

IV-B-30. Strahler, A. N., "West Kaibab Fault and Kaibab Plateau, Arizona," *Geol. Soc. Amer. Bull*, Vol. 59, pp. 513–540, 1948.

IV-B-31. Maxson, J. H., Geologic Map of the Bright Angel Quadrangle, Grand Canyon National Park, Arizona, Text, Grand Canyon Nat. History Assoc., 1961.

IV-B-32. Huntoon, P., "Recurrent Movements and Contrary Bending Along the West Kaibab Fault Zone," *Plateau*, Vol. 42, pp. 66–74, 1969.

IV-C-1. Metzger, D. G., "Geology in Relation to Availability of Water Along the South Rim, Ground Canyon National Park, Arizona," *U. S. Geol. Survey Water-Supply Paper 1475-6*, pp. 105–135, 1961.

IV-C-2. McKee, E. A., *The Environment and History of the Toroweap and Kaibab Formations of Northern Arizona and Southern Utah*, Carnegie Institute Publication 492, 268 pp., 1938.

IV-C-3. Koons, E. D., "Geology of the Hualapai Reservation," *Plateau*, Vol. 20, pp. 53–60, 1948.

IV-C-4. Moore, R. T., Wilson E. D., and O-Haire, R. T., Geologic Map of Coconino County, Arizona, Arizona Bureau of Mines, 1960.

IV-C-5. Wilson, E. D., Moore, R. T., and Cooper, J. R., Geologic Map of Arizona, Arizona Bureau of Mines, 1969.

IV-C-6. Maxson, J. H., Geologic Map of the Bright Angel Quadrangle, Grand Canyon National Park, Arizona, Grand Canyon Natural History Association, 1961.

IV-C-7. Shoemaker, E. M., Squires, R. L., and Abrams, M. J., "The Bright Angel and Mesa Butte Fault Systems of Northern Arizona," in *Geology of Northern Arizona With Notes on Archaeology and Paleoclimate, Part I*, p. 355, for Geological Society of America, Rocky Mountain Section Meeting, Flagstaff, Ariz., 1974.

IV-D-1. Anderson, C. A., and Blacet, P. M., "Precambrian Geology of the Northern Bradshaw Mountains, Yavapai County, Arizona," *U. S. Geol. Survey Bull. 1336*, 82 pp., 1972.

IV-D-2. Anderson, C. A., Blacet, P. M., Silver, L. T., and Stern, T. W., "Revision of Precambrian Stratigraphy in the Prescott–Jerome Area, Yavapai County, Arizona," *U. S. Geol. Survey Bull. 1324-C*, pp. C1–C16, 1971.

IV-D-3. Anderson, C. A., and Creasey, S. C., "Geology and Ore Deposits of the Jerome Area, Yavapai County, Arizona," *U. S. Geol. Survey Bull. 1230-F*, pp. F1–F19, 1958.

IV-D-4. Billingsley, F. C., and Goetz, A. F. H., *Computer Techniques Used for Some Enhancements of ERTS Images*, presented at ERTS Investigator Symposium, Goddard Space Flight Center, Greenbelt, Md., March 5–9, 1973.

IV-D-5. Huff, C., Santos, E., and Raabe, R. G., "Mineral Resources of the Sycamore Canyon Primitive Area, Arizona," *U. S. Geol. Survey Bull. 1230-F*, pp. F1–F19, 1966.

IV-D-6. Krieger, M. H., "Geology of the Prescott and Paulden Quadrangles, Arizona," *U. S. Geol. Survey Prof. Paper 467*, 127 pp., 1965.

IV-D-7. Lehner, R. E., "Geology of the Clarkdale Quadrangle, Arizona," *U. S. Geol. Survey Bull. 1021-N*, pp. N511–N592, 1958.

IV-D-8. Twenter, R. F., and Metzger, D. G., "Geology and Ground Water in Verde Valley—the Mogollon Rim Region, Arizona," *U. S. Geol. Survey Bull. 1177*, 129 pp., 1963.

IV-D-9. Wilson, E. D., Moore, R. T., and Cooper, J. R., Geologic Map of Arizona (Scale 1:500,000), Arizona Bureau of Mines, 1969.

V. Applications

Although the water application was not a planned geologic study of the ERTS investigation, it was a beneficial and potentially significant offshoot. This section contains a discussion involving this application as it pertains to the three major areas of study.

A. Water on the Shivwits Plateau

I. Lucchitta

Although annual precipitation on the Shivwits Plateau is sufficient to support piñon-juniper forest as well as the rich grasslands that make the area especially suitable for cattle ranching, the Shivwits Plateau actually has little water. There are no flowing streams, few springs, and insufficient ground water shallow enough to be tapped economically by wells. Ranchers rely almost entirely on catchment basins (tanks) that fill with runoff on the infrequent occasions when the washes are flowing. In even moderate drought, water must be hauled for great distances. A geologic study such as the one involved in this investigation is one of the best ways to determine possible locations of shallow ground water.

The layered sequence of Paleozoic age that underlies the Shivwits Plateau is composed chiefly of carbonate rocks (limestone and dolomite), which generally are permeable and act as aquifers, interbedded with shaly rocks, which are impermeable and act as aquicludes (see Fig. V-A-1). Perched ground water, therefore, occurs at several levels in the Paleozoic section, wherever a substantial carbonate sequence overlies a "tight" shale. The most notable examples are the base of the Muav Limestone, which overlies the Bright Angel Shale, and the base of the Coconino Sandstone–Toroweap Limestone sequence, above the Hermit Shale (see Fig. V-A-1). Both are marked by spring lines. The Muav water is deep in the Grand Canyon, about 1100 m below the rim of the Shivwits Plateau, and thus inaccessible. The water at the top of the Hermit Shale is 200 to 330 m below the rim. Although some of the springs related to this water table have been developed, especially along the Grand Wash Cliffs at the western edge of the Shivwits Plateau, most of them are inaccessible.

The caprock over most of the Shivwits Plateau consists of the Beta and Alpha Members of the Kaibab Formation of Permian age. The Beta Member, more than 65 m thick, consists of carbonate and is highly permeable; it overlies the thick and relatively permeable Toroweap Formation, also of Permian age. The Alpha Member overlies the Beta and consists of gypsiferous siltstone and minor limestone. This unit also is permeable, and in many places has formed a karst topography through solution of the gypsum. Consequently, rain falling over much of the Shivwits Plateau sinks readily into the ground and finds an

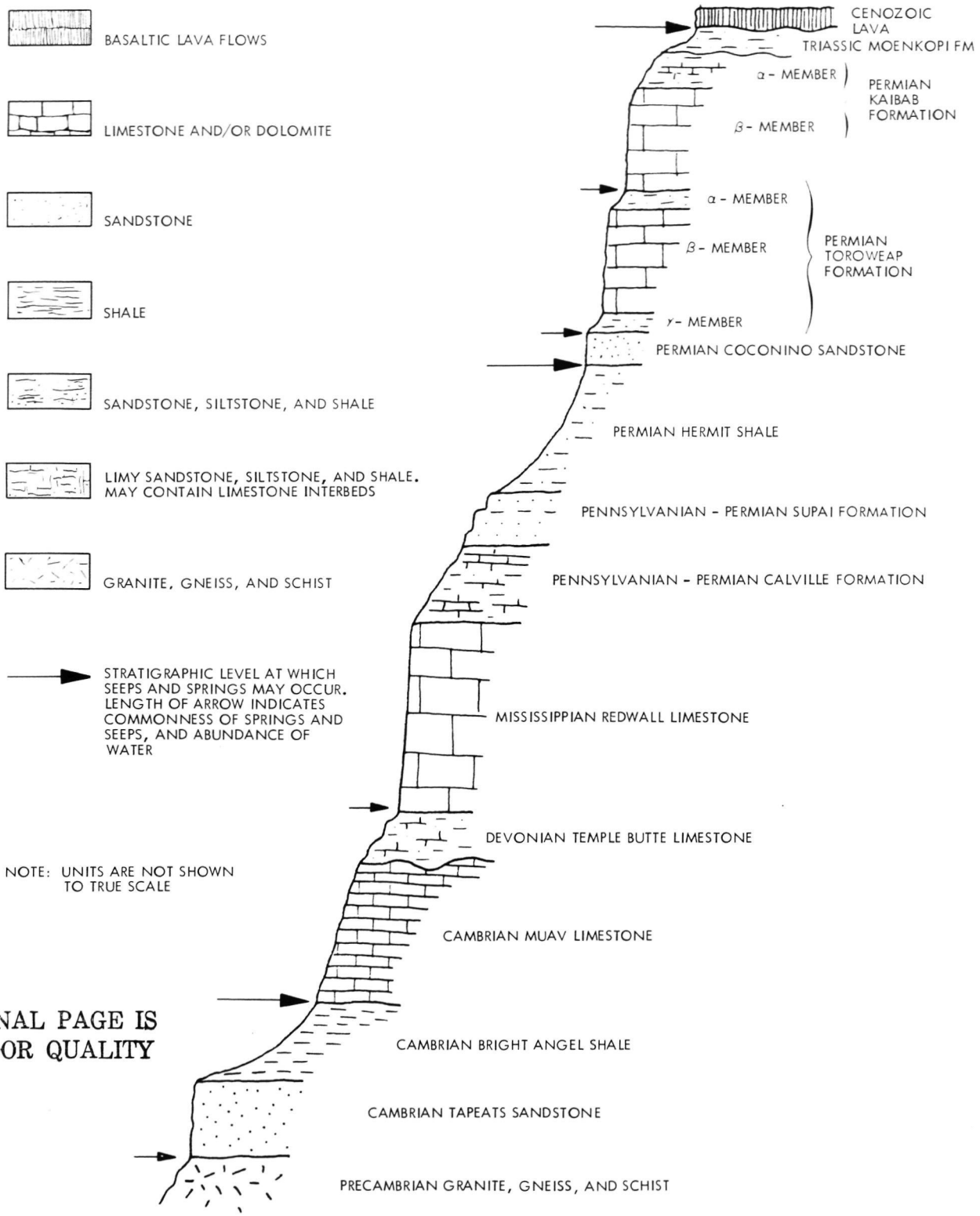

Fig. V-A-1. Diagrammatic stratigraphic section of the Grand Canyon region, showing lithologies and locations of main spring and seep lines. Not shown to scale

aquiclude to impede its downward progress only 150 m or more below the surface.

Part of the Shivwits Plateau is capped by basaltic lava flows and the associated effusive centers, all of Cenozoic age. These lavas are fractured and permeable. Field observations show that almost all springs on the Plateau are associated with the lavas, indicating that a perched water table exists at the base of these rocks wherever they overlie an aquiclude. This water table generally is less than 65 m below the surface.

Neither the Alpha nor the Beta Member of the Kaibab Formation forms good aquicludes; consequently, no perched water table and no springs exist where the lavas lie directly over this formation. Instead, all known springs associated with the lavas occur where the latter overlie either the shaly Moenkopi Formation of Triassic age, or clayey sediments of Cenozoic age. The most promising locations for development of ground water can be determined by first answering the following questions:

(1) What is the sub-lava distribution of the Moenkopi Formation and of the Cenozoic sediments?

(2) What is the direction of water flow at the base of the lavas?

(3) Are there any geologic features such as faults that are transverse to the direction of flow and thus can pond the water?

ERTS pictures and the Geologic Map of Arizona show that the lavas on the Shivwits Plateau are elongate in a north–northwest direction and typically blanket the erosional feather edge of the Moenkopi Formation on the underlying Kaibab. This pattern is repeated in many places in northwestern Arizona (Fig. V-A-2). Strata on the Shivwits Plateau dip gently northeast to east–northeast; thus, north–northwest is approximately the direction of strike. Lavas northeast of the axis of elongation of the flows rest on an erosion surface cut into the Moenkopi and sloping southwest toward the axis (Fig. V-A-3). In several places the lavas both overlie and are overlain by pebbles unmistakably derived from the Shinarump member of the Chinle Formation, a resistant ledge-forming conglomerate directly above the Moenkopi Formation. These relationships can be explained only by postulating that the lavas flowed down a broad strike valley, whose northeast side was formed by a scarp capped by the Shinarump, which shed its debris southwestward into the valley both before and after emplacement of the lavas (see Fig. V-A-3). The gentle southeast side of the valley was formed by strata of the Kaibab Formation dipping approximately northeast.

Field mapping of the basal contact of the lavas shows that, in the northern part of the lava field, the lavas flowed north–northwestward down the old strike valley, which also is the present direction of ground-water flow at the base of the lavas. East of the axis of the valley, the slope of the lavas' base, and therefore the direction of ground-water flow, is approximately west. Faults trending at a high angle to these flow directions tend to interrupt the flow of ground water, thus ponding the water on the upstream side of the fault.

Many faults on the Shivwits Plateau are older than the lavas and thus do not cut them. Of the faults that do cut the lavas and that have the orientation specified previously, the most prominent is one, well visible on ERTS pictures, that has a dip-slip displacement of more than 100 m and a strike length of 32 km (see Fig. V-A-2). Along most of its length, this fault is associated with springs, several of which have been developed. Two wells, both productive, have been drilled on the east side of the fault. Although small amounts of water probably can be obtained where the fault cuts the side of the old valley, the most promising place for future development is along the axis, where water tends to concentrate. It is likely that the shallow-water resources in this area have scarcely been tapped.

In the southern part of the Shivwits lava field, a regional direction of flow for the lavas can not be determined with certainty. The basal contact most commonly slopes gently to the west. If this slope is primary and not the result of post-depositional deformation, it probably represents the slope along the east side of the old valley. It is likely that ground water at the base of the lavas has no regional flow pattern, but rather flows toward local lows formed by pre-lava erosion and typically consisting of pre-lava stream channels.

Over most of the southern part of the lava field, the Moenkopi has been removed by pre-lava erosion. Consequently, there is no widespread aquiclude to perch water at the base of the lavas. However, pre-lava Cenozoic deposits are not uncommon. These deposits, which consist of lake beds, channel fill and regolith, in part clayey, tend to be concentrated in the pre-lava erosional lows. Most of these lows consist of broad channels, each of which is the lowest part of its drainage basin. The lows, therefore, form sumps for the ground water in the lavas; they are also the place in which impermeable Cenozoic deposits are most likely to be found. Because of this, the lows are the most, and probably the only, promising places for development of shallow-water resources in the southern part of the Shivwits lava field. This contention is supported by the

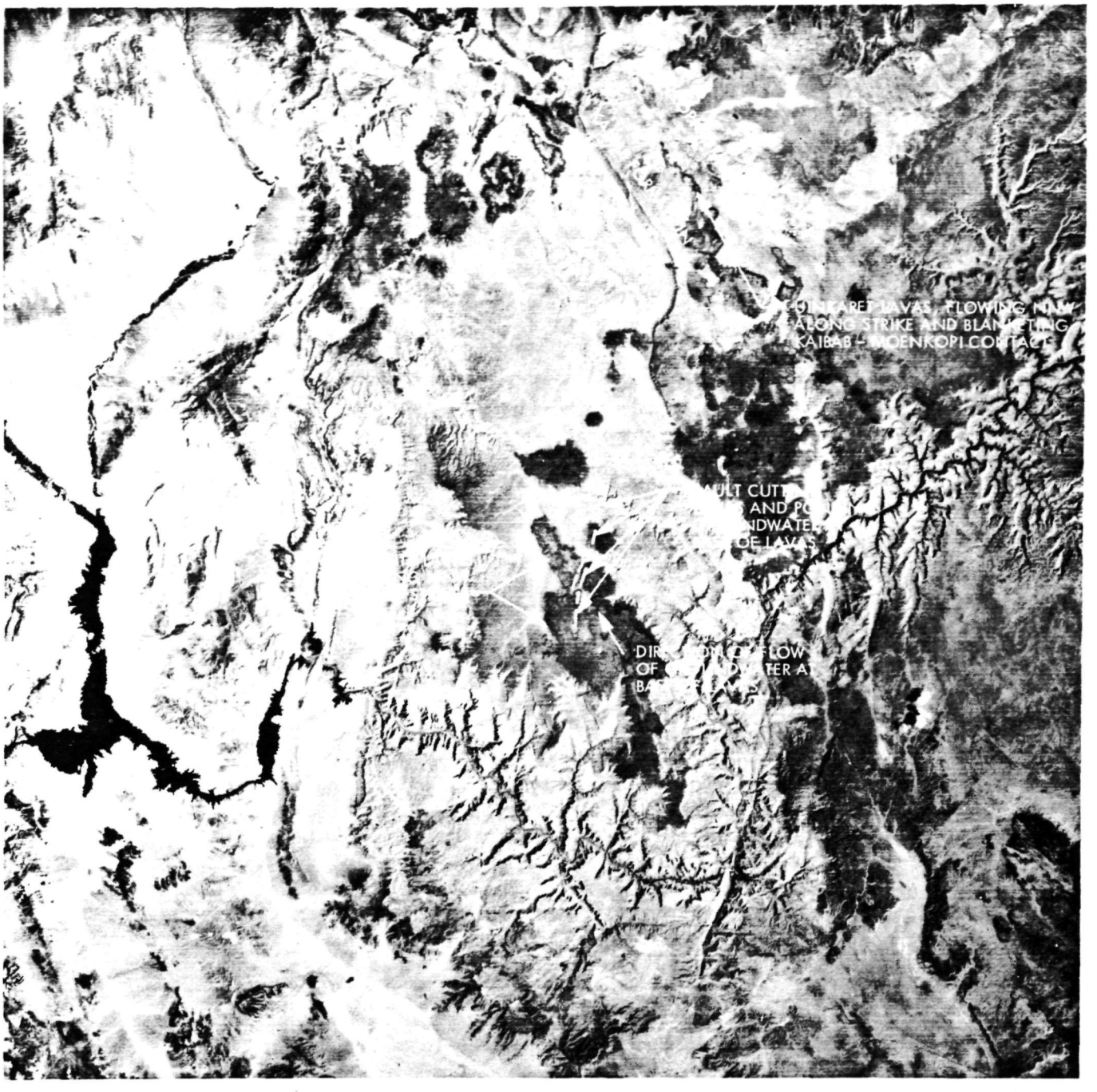

Fig. V-A-2. ERTS-1 picture of the western Grand Canyon region, centered on the Shivwits Plateau, showing the Shivwits and Uinkaret lavas flowing north-northwest in the direction of strike. Also shown is the Wildcat fault, which cuts the Shivwits lavas and ponds the shallow ground water in the lavas (NASA picture ERTS E-1015-17431, Aug. 7, 1972)

presence of one of the best springs of the Shivwits Plateau at the base of the biggest channel known, where Cenozoic deposits are especially thick.

The channels can be seen only where they are truncated by the sides of the Shivwits Plateau. Their continuations in the interior of the Plateau can not be determined by visual means or by geologic observations in the field. A project is being developed to determine the best geophysical techniques for finding these buried channels because, if this project is successful, the results can be widely applied in prospecting for water in the arid West.

Fig. V-A-3. Diagrammatic composite sections of the Shivwits Platea, showing sequence of events in late Cenozoic time. Distances and thicknesses are not shown to scale. Angles are exaggerated for clarity

B. Water on the Coconino Plateau

R. L. Squires, E. M. Shoemaker, and M. J. Abrams

The development of adequate supplies of water on the Coconino Plateau is critical for the livestock industry of the area, which in 1973 was about 45,000 head, and to some extent for the tourist industry. During investigations in the Cataract Creek Basin of the Plateau, it was recognized that shallow, perched ground water associated with the Kaibab Limestone could be found by the means discussed in this section.

Because of the aridity of the climate, and rapid downward percolation of the scant precipitation, water must be obtained through three principal sources:

(1) Tanks formed by earth dams bulldozed across natural drainages.

(2) Deep wells that reach the water table (see Fig. V-B-1).

(3) Water hauled at great cost from considerable distances.

Tanks are an unreliable source of water as most of the rocks that cap the Plateau are so pervious that there is little accumulation from runoff and, in many instances, tanks remain dry all year. At some ranches, the water obtained from a single existing well is distributed to strategically located storage tanks through an expensive system of pipes.

As a production capability of as little as 400 liters of water per day can be utilized profitably, a possible solution to the problem of adequate water supply is to develop shallow wells. One of the few such wells existing is at the Globe Ranch, near the rim of the Grand Canyon, where a small amount of water is produced from a shallow hand-dug well in a sandstone lens within the Alpha Member of the Kaibab Limestone. This well produces water for the ranch at a rate of 4000 liters/week. Through detailed mapping of the Globe Ranch area, it was found that the perched ground water was associated with a sandstone lens in unit 5 in the Alpha Member (see Section IV-C) of the Kaibab Limestone (see Fig. V-B-2). The sandstone is interbedded with red claystone and siltstone, which form an impervious layer beneath the sandstone. The perched water table is only 5 m beneath the surface at the site of the well. Recharge occurs from local runoff and from direct precipitation on the outcrop belt of the sandstone.

Unit 5 was mapped over an area of about 80 km^2 in the vicinity of the Globe Ranch (Fig. V-B-3) to explore the possibility of developing this aquifer. Subsequently, 14 exploratory wells were drilled near the hand-dug well, with negative results. Based on stratigraphic and structural considerations, a new location along a normal fault, about 8 km east of the Globe Ranch, was selected for drilling operations. It was anticipated that water might be structurally trapped within the downdropped block of the fault. Four shallow test holes were drilled, and all encountered water. These four water-bearing holes, now being monitored, will be tested to determine the potential production of water from the local sandstone aquifer.

Analysis of ERTS pictures can be a viable means of mapping unit 5, which is typically reddish-brown in color with red colluvial slopes developed on this clastic unit. The task of mapping its distribution is greatly facilitated by color difference pictures produced by computer from the raw data tapes (see Section VI). The results of this study show that shallow ground-water supplies in the Alpha Member of the Kaibab Limestone can be found by an inexpensive program of exploratory drilling in conjunction with ERTS-aided geologic mapping.

C. Water South of Flagstaff

D. P. Elston

R. DeWitt, ground-water geologist for the City of Flagstaff, in Arizona, reports that ERTS images of the north-central Arizona test site at 1:200,000 scale, with accompanying lineament map (see Fig. IV-D-3a), were used with conventional aerial photographs and with topographic maps to locate an area of inferred maximum fracturing in upper Paleozoic rocks along the north-trending Oak Creek fault in the Woody Mountain well field, south of Flagstaff. These pictures allowed the identification of apparent major fracture systems in strata beneath a cover of lava flows, and their projection into intersections with the Oak Creek fault. This led to selection of a location for a new, large-diameter ($\geq$50 cm), deep (~610 m) cable tool well for Flagstaff, which was started in October 1974 and will require 1 to 2 yr to complete.

A highly detailed lineament map (1:6,000 scale) of the Woody Mountain well field, made using the AP/C

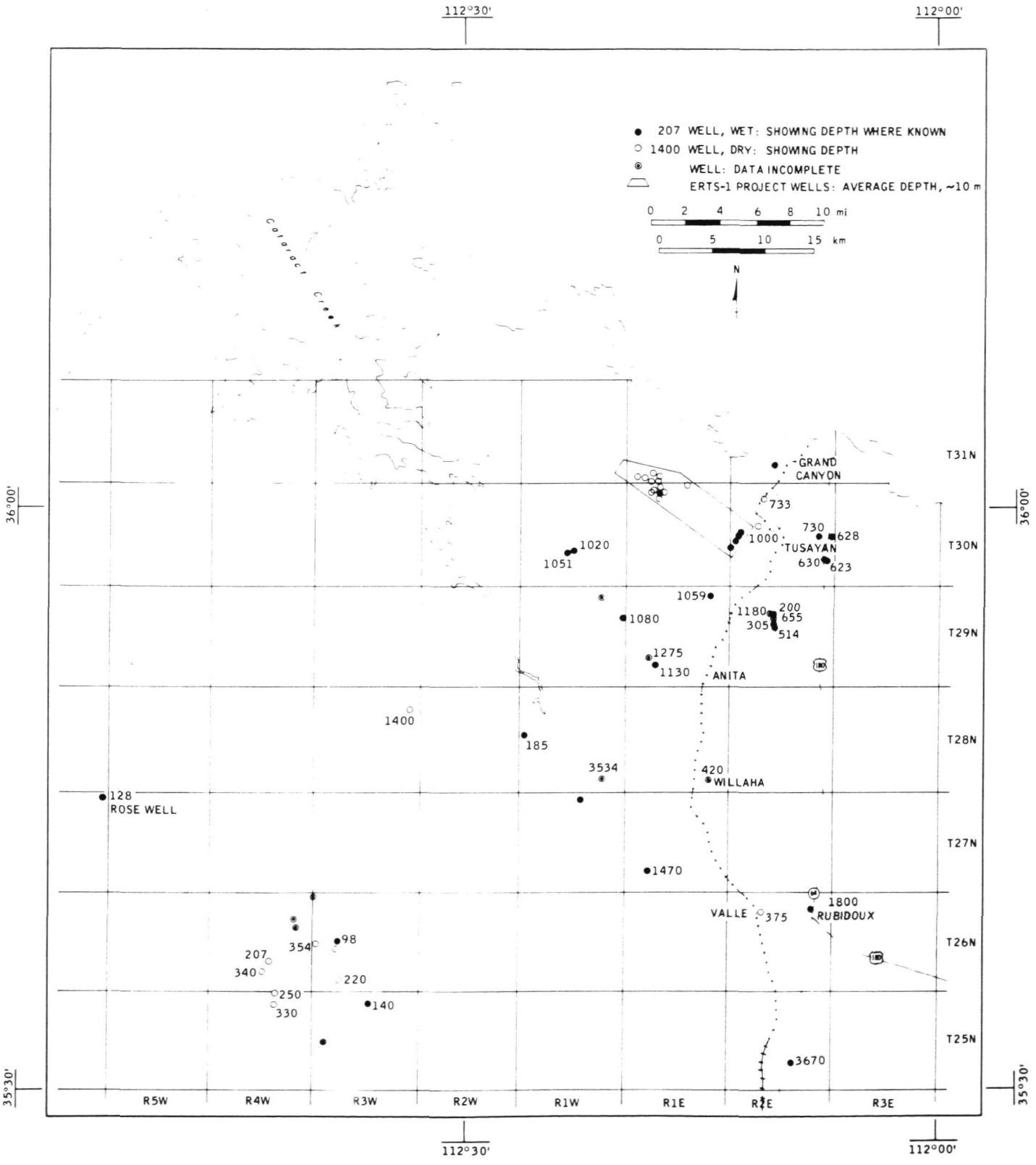

Fig. V-B-1. Existing wells on the Coconino Plateau. Wet or dry condition is indicated

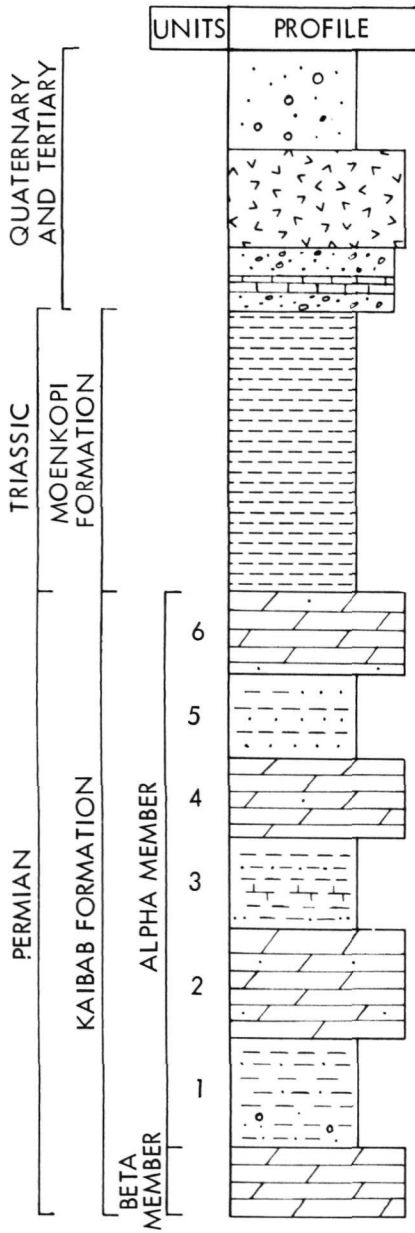

UNITS	GENERAL LITHOLOGY AND THICKNESS	WEATHERED COLOR
QUATERNARY AND TERTIARY	ALLUVIUM, LAG GRAVELS, LOESS. VARIABLE THICKNESS	RED TO TAN DEPENDING UPON SOURCE
	BASALT FLOWS, ASSOCIATED PYROCLASTIC ROCKS, RHYOLITE AND OBSIDIAN FLOWS. TALUS AND LANDSLIDE. 5 TO 100 m	BLACK
	SANDSTONE, CONGLOMERATE, AND LACUSTRINE LIMESTONE. MAXIMUM 50 m	RED AND WHITE SANDSTONE, GRAY LIMESTONE
TRIASSIC — MOENKOPI FORMATION	SILTSTONE AND CLAYSTONE WITH INTERBEDDED FINE-GRAINED MASSIVE SANDSTONE. CHERT AND LIMESTONE PEBBLE CONGLOMERATE AT BASE. MAXIMUM 130 m	REDDISH SILTSTONE, GREEN AND RED BROWN CLAYSTONE, REDDISH SANDSTONE AND CONGLOMERATE. ENTIRE UNIT: 10R5/2
PERMIAN — KAIBAB FORMATION — ALPHA MEMBER — 6	DOLOMITE, NODULAR WHITE AND PINK CHERT. SANDY AT TOP AND BASE, LOCALLY FOSSILIFEROUS. MAXIMUM 8 m	GRAY TO BUFF
5	SANDSTONE, SHALE, AND GYPSUM. VERY FINE- TO MEDIUM-GRAINED LIMY QUARTZ SANDSTONE. LOCAL CONGLOMERATE. MAXIMUM 25 m	YELLOW BROWN AND PINKISH SANDSTONE, REDDISH SHALE, WHITE GYPSUM
4	DOLOMITE, ABUNDANT WHITE CHERT AT TOP. SOME BEDDED CHERT, SANDY LAYERS, LOCALLY OSTRACODE. MAXIMUM 8 m	GRAYISH WHITE TO BUFF: 5YR8/1
3	SHALE, SILTSTONE, AND GYPSUM. INTERBEDDED LIMESTONE AND FINE-GRAINED CALCAREOUS SANDSTONE. MAXIMUM 15 m	RED AND GREEN SHALE AND SILTSTONE, WHITE GYPSUM
2	DOLOMITE WITH SANDY INTERBEDS, IRON NODULES COMMON AT TOP. LOCAL PYRITIC ROCKS AT BASE. LOCAL GASTROPOD AND BIVALVE. MAXIMUM 8 m	YELLOW BROWN: 10YR6/4
1	CALCAREOUS SILTSTONE AND SHALE, INTERBEDDED DOLOMITE, LOCAL FINE-GRAINED SANDSTONE AND CONGLOMERATE SANDSTONE. MAXIMUM 9 m	RED TO BUFF SILTSTONE AND SHALE, BUFF TO YELLOW SANDSTONE
BETA MEMBER	DOLOMITE, CHERTY AND FOSSILIFEROUS. LOCAL ABUNDANT PRODUCTID, SPONGE, GASTROPOD, AND CRINOID. MAXIMUM 100 m	GRAYISH WHITE

Fig. V-B-2. Stratigraphic column of mapped rock units

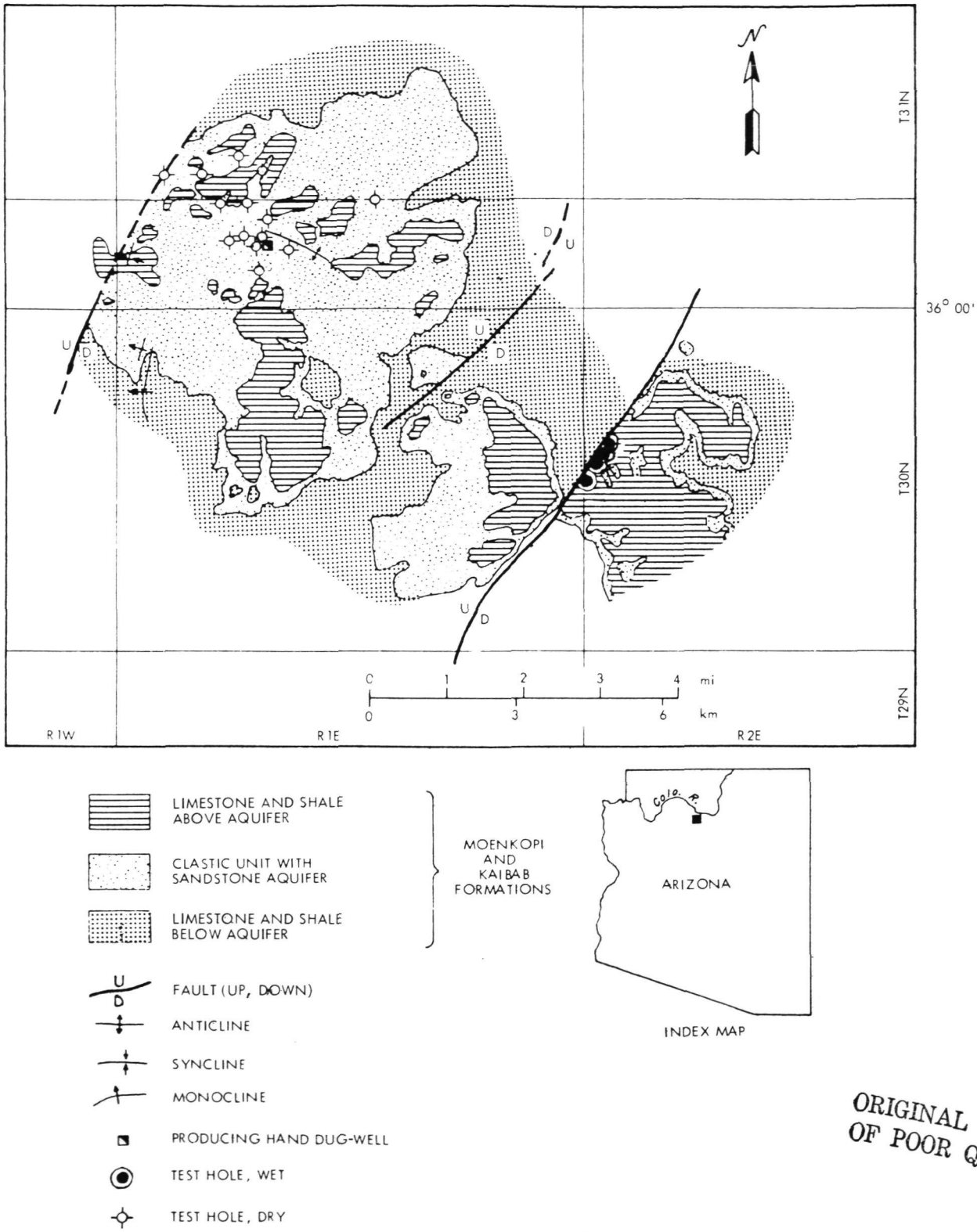

Fig. V-B-3. Simplified geologic map of the Globe Ranch area, Coconino County, Arizona, showing test hole locations

photogrammetric plotter at the U.S. Geological Survey, Flagstaff, and low-altitude aerial photographs, when compared with existing subsurface information, was not considered useful for predicting fractured ground beneath the basalt cover in the well field. Apparently, minor crackling of the basalt flows that overlie the Paleozoic strata near the Oak Creek fault does not reflect the pattern of major fracturing in the underlying strata.

VI. Evaluation of Computer-Enhanced Image Products

A. F. H. Goetz, R. L. Squires, I. Lucchitta, D. P. Elston, and M. J. Abrams

Computer enhancement of ERTS images is necessary to extract a subset of the 200 million bits of information contained in each frame, which is useful to the investigator. Experience has shown that only about one-tenth of the full informational content of an ERTS image can be usefully displayed at one time on film for interpretation. In general, certain types of enhancements are useful for a wide variety of areas; others are useful only if scene-dependent parameters are incorporated in the enhancement procedure.

In order to avoid duplication, the use of computer-enhanced products was mentioned but not discussed in the geologic mapping studies reported in Section IV. The evaluation and use of images enhanced by computer image processing, as given in Section III and in Appendix B, are discussed in the subsequent parts of this section. The three areas (Shivwits Plateau, Coconino Plateau, and Verde Valley region) are considered together under the discussion of each type of enhancement product. Because the primary effort in image evaluation was made in the Coconino Plateau, this area is considered first in each enhancement discussion. Other areas are mentioned by comparison only.

Evaluations of the enhanced products were made by the individual most familiar with the area. No cross checks were attempted. Each individual selected a number of features, structural, physiographic and stratigraphic, and subjectively rated them for detectability on a scale of 1 = poor, 2 = fair, and 3 = good. The results from each area were compiled in a slightly different way, as apparent in Tables VI-1 through VI-3.

In the Shivwits area, the evaluations were made mainly with color composites of several spectral bands viewed on an International Imaging Systems (I^2S) viewer. Table VI-1 shows the types of enhancements and the number of combinations evaluated. In order to permit comparison of the overall value of the various combinations of transparencies, the percentages of poor, fair, and good ratings were tabulated for each combination in the categories of structure and stratigraphy. The percentages were then multiplied by ten and added within each category for a total point value for each combination. A sample of this procedure is given in Table VI-2. A final tabulation is given in Table VI-3. A discussion of the results of the Shivwits analysis is given below.

A. Contrast Stretches

The simplest form of image enhancement is a contrast stretch in which the brightness data distribution is expanded or stretched to fill the dynamic range of the

Table VI-1. Types and number of observations made on I²S viewer in the Shivwits Plateau region

Combination of enhanced transparencies (three used at a time)	Color-filter combinations applied to each group of enhanced transparencies	Number of geologic observations made
Gaussian stretch, negative 5G, 4G, 6G	14	238
Ratio, negative, with atmospheric correction 5:7, 4:5, 4:6	18	324
Ratio, positive, with atmospheric correction 4:7, 4:5, 5:4	18	324
Ramp CDF, positive 4C, 6C, 7C	6	108
Difference, negative 5-4, 4-7, 4-5	3	54
Log ratio, positive, with atmospheric correction 4:5, 4:6, 5:7	2	36
Individual linear stretch, positive 4I, 6I, 7I	3	54
Standardized linear stretch, positive 4S, 6S, 7S	1	18
Log difference, positive 7-4, 5-4, 6-4	3	54
Totals	68	1210

display medium, in this case film (see Section III). Black and white transparencies are made of each band or band combination and are evaluated in the I²S viewer alone, in pairs, or in triplets.

Automatic or standard stretches in which a previously defined quantity of data (usually 6%) is intentionally lost to saturation at the dark and light end of the display are performed on the data automatically. Individual stretches require the judgment of the analyst in determining what part of the data is to be discarded in order to maximize the display of useful information. Nonlinear contrast stretches, to expand a portion of the data in the display domain at the expense of properly displaying the remainder, are extremely useful. Because of the log dependence of film density on exposure, a type of nonlinear stretch already is inherent in the film display. For this reason, both negative and positive film transparencies are made routinely.

In the study of the Coconino Plateau area, a detailed analysis was made of contrast-stretched images. Stratigraphic nomenclature is given in Fig. IV-C-2.

1. Standard Linear Stretch

In images of the Coconino Plateau, 13 different structural, physiographic, and lithologic features were chosen with which to determine the value of the products. Table VI-4 shows the features chosen and the evaluations for each band of the standard linear-stretch image.

Although the positives taken collectively are superior to the negatives in terms of contrast and amount of useful geologic information (see Table VI-4), the band 4 positive was generally poor in terms of fault information. This particular band in the other stretches contains some of the best resolution for faults.

Individual negatives of bands 6 and 7 show details of drainages along the highlands between Heather monocline and the southern rim, whereas the negatives of bands 4 and 5 did not.

The poor discrimination of rock types obtained in the combination of two or three of the positives (5, 6, and 7) is inadequate to distinguish salient stratigraphic differences throughout the plains area. Only the vegetation-caused broad color zone north of Valle could be differentiated.

In one of the combinations of the negatives (4, 5, 7), there is some distinction of the Triassic Moenkopi (Ṛm) at Valle, but the distinction is not that conclusive. Elsewhere, the Ṛm and the plains redbeds are totally indistinguishable. Stratigraphic details in the plains for this specific picture, as well as with various other combinations tried, are essentially nonexistent. With the 5, 6, 7 negative combination, the vegetation-caused color zone north of Valle is apparent. Combinations of only two standard linear-stretch images are much less useful in terms of usable information than are the ternary combinations.

Table VI-2. Cumulative points for the combination of difference picture transparencies 5-4 (negative), 4-7 (negative), and 4-5 (negative)

Filters	Category	Number of poor ratings	Number of fair ratings	Number of good ratings	Points
Points for individual transparency-filter combination					
5-4 blue 4-7 green 4-5 red	Structure Stratigraphy	4 (×1) + 1	2 (×2) + 2	1 (×3) = 7	11 26
	Total	5	4	8	37
5-4 green 4-7 red 4-5 blue	Structure Stratigraphy	3 2	3 3	1 5	12 23
	Total	5	6	6	35
5-4 white 4-7 blue 4-5 green	Structure Stratigraphy	2 0	3 5	2 7	14[a] 31[a]
	Total	2	8	9	45[a]

Category	Number of determinations	Number of poor ratings	Number of fair ratings	Number of good ratings
Percentages of poor, fair, and good ratings for transparency combination				
Structure	21	9	8	4
Percentage		42.9	38.1	19.0
Stratigraphy	32	3	10	19
Percentage		9.4	31.3	59.4
Total	53	12	18	23
Percentage		22.6	34.0	43.4

Cumulative points for transparency combination

Structure: $10[(42.9 \times 1) + (38.1 \times 2) + (19.0 \times 3)] = 1761$

Stratigraphy: $10[(9.4 \times 1) + (31.3 \times 2) + (59.4 \times 3)] = 2502$

Total: $10[(22.6 \times 1) + (34.0 \times 2) + (43.4 \times 3)] = 2208$

[a]Denotes best value in each class.

2. Individual Linear Stretch

To produce an individual linear stretch, the analyst studies the histogram of the image (frequency of DN vs DN) as well as the image itself and determines which features must be enhanced and which can be sacrificed when the brightness distribution is stretched to fill the dynamic range of the film.

As with the other stretch images, the positives of the individual stretch images have better contrast than do the negatives. The positives, taken individually, are useful for the analysis of faults and limestone contacts. The combination of 4, 5, and 7 also provides excellent fault details, especially for the Moore Tank fault system. This combination is judged to be one of the best pictures for fault details, but it is not as outstanding for the plains area

Table VI-3. Cumulative points for transparency combinations analyzed

Transparency combination	Structural feature	Stratigraphic units	Total
Standardized linear stretch, positive 4, 6, 7	1286	1500	1412
Individual linear stretch, positive 4, 6, 7	2190[a]	2089	2130
Gaussian stretch, negative 5, 4, 6	1580	1408	1465
Ramp CDF, positive 4, 6, 7	2002	2158	2101
Ratio, with atmospheric correction, positive 4:7, 4:5, 5:4	1704	1747	1731
Ratio, with atmospheric correction, negative 5:7, 4:5, 4:6	1331	1282	1305
Log ratio, with atmospheric correction, positive 4:6, 4:7, 5:7	2002	1550	1737
Difference, negative 5-4, 4-7, 4-5	1761	2502[a]	2208[a]
Log difference, positive 7-4, 5-4, 6-4	2136	2129	2132

[a]Denotes best value in category.

as the band 7 gaussian stretch. No distinctive rock types could be discriminated with any random combination of two or three of the images. In fact, in most combinations, the fault details were negated and the limestone contacts were blurred.

The only outcrops that could be discriminated in the combinations of the negatives (4_R, 5_G, 6_B) and (4_G, 5_B, 7_R) were those of Trm in the Valle area. Scattered outcrops of Trm elsewhere, as well as scattered redbeds throughout the plains, have the same characteristic color as the outcrops around Valle. The Trm outcrops at Valle and Redlands Camp are sharply delineated, but elsewhere the Trm and other redbeds are less distinct and somewhat blurred. In the combination (4_R, 5_G, 6_B) the larger outlier of volcanic rock southeast of Valle shows up quite distinctly, and there is a faint suggestion of a vegetation-caused color zone just north of Valle. The combination of (5, 6, 7) yielded excellent depiction of the faults just west of Howard Mesa, but no useful lithologic differentiations could be obtained except around Valle. Table VI-5 gives an evaluation of the individual linear-stretch images.

The individual linear-stretch color combination of bands 4, 5, and 7 produced the most usable image of the Verde Valley test site in north-central Arizona. Stratigraphic units as well as structure were more usable on this image than on any other combination of enhanced images. Comparisons of this image and the ratio combinations are given elsewhere in this section. In the Coconino Plateau region, the combination of individually stretched bands 4, 6, and 7 yielded the best rating of any enhancement for structural features, as shown in Table VI-3.

3. Gaussian Stretch

The gaussian contrast stretch is designed to force the brightness distribution function to closely resemble a gaussian function. Although in many instances the distribution already approximates a gaussian curve, some distributions are skewed in such a way that most of the image would become abnormally light or dark when stretched linearly.

In the Coconino Plateau image, the gaussian positives of bands 4 and 7 deserve special mention because of their remarkable resolution of structural features of the plains area in Area A (see Fig. IV-C-1). Band 4 is the most outstanding of all processed ERTS images in its depiction of the monoclines in the area. It also has usable information regarding the distribution of limestone contacts, primarily between units 4 and 6, in the plains area. Band 7 is the most outstanding of all processed ERTS images on the Coconino Plateau for physiographic and secondary roads details (Fig. VI-1).

The combination picture of these two positives (4_{Green}, 7_{Red}) yields an excellent representation of the faults, monoclines, physiography, and cultural details. In the northwestern plains area, there is faint differentiation

Table VI-4. Evaluation of features in a Coconino Plateau standard linear-stretch image

Category	4 (pos)	5 (pos)	6 (pos)	7 (pos)	4 (neg)	5 (neg)	6 (neg)	7 (neg)
Structure								
Faults	1	2	2	2	2	2	2	2
Moore Tank fault system	2	3	3	3	2	1	1	2
Faults in Tb	1	2	2	2	1	2	2	2
Heather monocline	3	3	3	3	3	2	2	1
Total	7	10	10	10	8	7	7	7
Lithology								
Tb escarpment (including Tb outliers)	1	2	2	3	1	3	3	2
Qb escarpment	1	1	1	1	1	1	2	1
Red Butte	1	2	2	1	1	1	1	1
Tb vs rim vegetation	1	1	1	1	1	1	1	1
5 vs 6 Hualapai Hilltop	1	1	1	1	1	1	1	1
LS contacts	1	2	2	1	1	1	1	1
Total	6	9	9	8	6	8	9	7
Physiography								
Physiography	1	2	3	3	1	2	2	2
Cultural features	1	3	2	3	1	2	2	2
Total	2	5	5	6	2	4	4	4
Structure	58	83	83	83	67	58	58	58
Lithology	33	50	50	44	50	44	50	39
Physiography	33	83	83	100	33	67	67	67
Total enhancements: 54								

between β-1-2-3 and 4-5-6 outcrops. Elsewhere, the limestone contacts between 4 and 6 are faintly visible. The features of the Mt. Floyd volcanic field and the southern rim are not clearly represented. Vegetation is a uniform color throughout the area.

Three-component composites of the gaussian positives fall within two general types. Those that included band 4 show some discrimination of rock types. In these cases, units β through 4 are distinguishable from units 5, 6, $\bar{T}$rm, and Qal. Such stratigraphic discriminations, however, are much more subtle than those encountered in ratio images. The composites that did not include band 4 show no stratigraphic differentiation. The same effects were observable with the ternary combinations of the gaussian negatives. The stratigraphic separations, obtained when the band 4 negative was used, were faint and inferior in contrast compared with the positives. Results of the gaussian image analysis are given in Table VI-6.

In the Verde Valley images, the color combinations using gaussian stretch images yielded superior discrimination of detail in high albedo units. The gaussian stretch images of the Shivwits Plateau yielded generally poor results compared with other enhancements. As evidenced in later comparisons, the value of a specific enhancement is scene-dependent for which no hard rules have been devised.

Table VI-5. Coconino Plateau individual linear-stretch image evaluation. Results in percentages

Category	4 (pos)	5 (pos)	6 (pos)	7 (pos)	4 (neg)	5 (neg)	6 (neg)	7 (neg)
Structure	83	75	83	83	58	58	58	75
Lithology	50	44	39	39	39	39	33	33
Physiography	38	38	63	85	38	25	25	50
Total enhancements: 52								

4. Ramp CDF Stretch

The ramp cumulative-distribution-function (CDF) stretch is formed by defining the sum of succeeding values of members of pixels in the brightness distribution, beginning at 0 DN, to form a linear ramp function. This type of enhancement has the property of increasing the separation among low pixel values in the display at the expense of separation in bright areas.

In the Coconino Plateau region, ramp CDF positives are far superior to negatives in terms of apparent contrast, as can be seen in Table VI-7. In the combinations of two or three positives, there is some discrimination of rock types. Areas of redbeds, including Pkm and Qal, are discernible from non-redbeds. Combinations without band 4, however, show less distinctive rock-type discriminations. The combination 4_G (pos) 5_R (pos) 7_B (pos) was unusual in that the Pkm outcrops are slightly different colored than the Alpha Member redbeds in the plains area. As with the other ternary combinations of the positives, the Heather monocline is enhanced, and there is no distinction between Tb and southern rim vegetation.

The discrimination of rock types is extremely poor in the ternary combinations of ramp CDF negatives. Stratigraphic and physiographic details are blurred or almost blacked out in the plains area. Just north of Valle, a broad color zone is distinctive in most of the pictures. This color zone is due to vegetation effects. In none of the combinations is there any distinction between Tb and southern rim vegetation. The combination of the band 5 and 7 negatives shows excellent fault details in Area B near Quivero. In fact, this combination is judged to be the most outstanding of all examined ERTS images for this area. With the addition of band 6 to this 5 and 7 combination, the drainage system along the southern rim becomes more apparent.

The ramp CDF stretch rated highly in defining both structure and stratigraphic units on the Shivwits Plateau, as seen in Table VI-3. As might be expected in the Verde Valley images, structure and physiographic detail were strongly enhanced in the dark basalt areas and dark red Paleozoic sediments at the expense of the lighter units.

B. Ratio Images

The reasons for producing an image of two ERTS spectral bands is given in Section II. Suffice it to say that it allows for a substantial increase in contrast by removing brightness variations due to topographic relief. However, as discussed below, ratio images are useful for lithologic discrimination in areas otherwise lacking contrast.

Evaluation of the ratio images for the Coconino Plateau was conducted in a different, more complete manner than the preceding contrast-stretch evaluations. As ratio images were shown to be more useful for determining boundaries between lithologic units and vegetation groups, a new set of seven separate categories or discriminators was chosen. Table VI-8 is a compilation of results obtained for both ratio and log ratio images. There is little to distinguish among the two types in the relative ranking of individual ratios. Therefore, they were not listed separately in the table. Also included in Table VI-8 are the rankings for ratios with atmospheric correction, as discussed in Section II.

The differences between the apparent information content of positives and negatives are vanishingly small so that no separate listings are given in Table VI-8. Similarly, the reciprocals of the stated ratios can be considered to contain an equal amount of information. However, when two reciprocal ratios, for instance 4:7 and 7:4, are

Fig. VI-1. Gaussian contrast-stretch print (band 7, negative), showing superior display of structure within areas of vegetation on the Coconino and Kaibab Plateaus

sandwiched, the result is not a uniform gray because of the nonlinear film-transfer curve. This fact allows color presentation of data in both light and dark areas of the image. The 4:7/7:4 combination is especially useful because these images contain the main lithologic boundary discrimination data in the flatland areas of the Coconino Plateau.

Color combinations of any two positives or any two negatives, in general, contain about as much informative

Table VI-6. Coconino Plateau gaussian-stretch image evaluation. Results in percentages

Category	4 (pos)	5 (pos)	6 (pos)	7 (pos)	4 (neg)	5 (neg)	6 (neg)	7 (neg)
Structure	92	67	67	92	67	42	42	58
Lithology	44	44	44	44	33	39	39	56
Physiography	33	50	50	100	50	50	50	83

Total enhancements: 56

Table VI-7. Coconino Plateau ramp-CDF-stretch image evaluation. Results in percentages

Category	4 (pos)	5 (pos)	6 (pos)	7 (pos)	4 (neg)	5 (neg)	6 (neg)	7 (neg)
Structure	83	75	67	83	50	33	42	33
Lithology	50	39	50	50	33	33	44	39
Physiography	50	67	67	100	33	33	33	33

Total enhancements: 51

data as the color combinations consisting of three positives or three negatives. The dual and ternary combinations of positives or negatives that contained an image from the group (4:6, 6:4, 4:7, 7:4) have fairly good contrast and sharpness of details. Dual-ratio pictures that involved a combination such as 5:6, 6:7 are poor. The composites judged to be the most noteworthy consisted of ternary colored combinations of either positives or negatives which involved a mixture of images from the (4:6, 6:4, 4:7, 7:4) group and the other images. Composites utilizing a 4:5 (or 5:4) and 5:7 (or 7:5) image yield distinctions among vegetations in the Mt. Floyd volcanic field, southern rim, and Valle area. Such effects are true for both positives and negatives, but color filter selection is critical for bringing out the full measure of the vegetation differences. The image $4{:}5_G$, $5{:}7_R$, $7{:}4_B$ (positives) was better than most in distinguishing: (1) β-1-2-3-4 from 5-6, Moenkopi, and Qr derived from Moenkopi, (2) vegetation differences within the Mt. Floyd volcanic field, and (3) vegetation zone north of Valle. The same combination of images in $4{:}5_G$, $5{:}7_R$, $7{:}4_{White}$ (negatives) is especially useful in distinguishing Qb outcrops and Alpha Member stratigraphic details in Area B and along the Moore Tank fault system.

In the Verde Valley region, the ratios were strikingly poor in their ability to present accurate lithologic boundaries. As can be seen by comparing the two images in Fig. VI-2, the color composite made from the individually stretched bands 4, 5, and 7 is superior to the color ratio composite. At first glance, this fact is puzzling in view of the successful application of ratios to the Coconino Plateau. However, the albedo contrasts among Verde Valley basalts, marls, and red Paleozoic sediments are large and any discarding of data by means of computer processing will destroy the pre-existing high contrast among units. Difference pictures on the Shivwits Plateau, which represents an intermediate case, proved to have the greatest information content.

1. Log Ratio Images

Log ratio images are produced by applying a log stretch to a ratio image. This increases the contrast in the dark part of the image. On the Coconino Plateau, ratio and log ratio images were most useful in differentiating among lithologic units. The color combination of $4{:}5_G$, $4{:}7_R$, $7{:}4_{White}$ (negative) shown in Fig. VI-3 proved to be the

Table VI-8. Ranking extending from 1 to 6 of ratio images with and without atmospheric correction in the Coconino Plateau

Category	Area	4:5	4:6	4:7	5:6	5:7	6:7
I	Structures and limestone contacts						
	Without correction	3	2	1	5	4	6
	With correction	3	2	1	5	4	6
II	Faults in Tertiary basalts						
	Without correction	1	5	4	3	2	6
	With correction	1	5	4	3	2	6
III	Vegetation in Tertiary basalts						
	Without correction	1	6	5	3	2	4
	With correction	1	6	5	3	2	4
IV	Grand Canyon, southern rim: vegetation						
	Without correction	1	6	5	3	2	4
	With correction	6	5	4	2	1	3
V	Tertiary basalt escarpment						
	Without correction	1	3	2	5	4	6
	With correction	1	6	5	3	2	4
VI	Quaternary basalt						
	Without correction	3	2	1	5	4	6
	With correction	1	3	2	5	4	6
VII	Moenkopi Formation						
	Without correction	3	2	1	5	4	6
	With correction	3	2	1	5	4	6

most outstanding in terms of stratigraphic information of all other composites examined in this study. In general, there is no significant difference between results oobtained from ratio or log ratio images.

2. Ratio and Log Ratio Images with Atmospheric Correction

The application of an atmospheric correction has the most effect upon band 4. The result is a general decrease in contrast because of the first-order removal of residual topographic shading. In some cases, the limestone contacts are enhanced, but in areas in which the physiographic information is an important parameter, the atmospheric correction is detrimental. All ratios studied on the Shivwits Plateau contained an atmospheric correction. In general, they were inferior to difference pictures.

C. Difference Pictures

Difference pictures are made by taking the difference between images in two spectral bands. If the numerous factors such as instrument calibration and atmospheric transmittance were known, the result would be the slope of the spectral reflectance curve. However, these factors are not well known, and no attempt is made to account for them. The difference picture can be considered to be a product intermediate between a linear-stretch image and a ratio image. Some brightness effects due to topography and overall albedo remain, while a greater contrast stretch is available than in a single image.

In the Coconino Plateau, the ratio images offered only slightly more information than the difference pictures. Ranking among the difference pictures is identical to that shown in Table VI-8 for the ratios using these same bands.

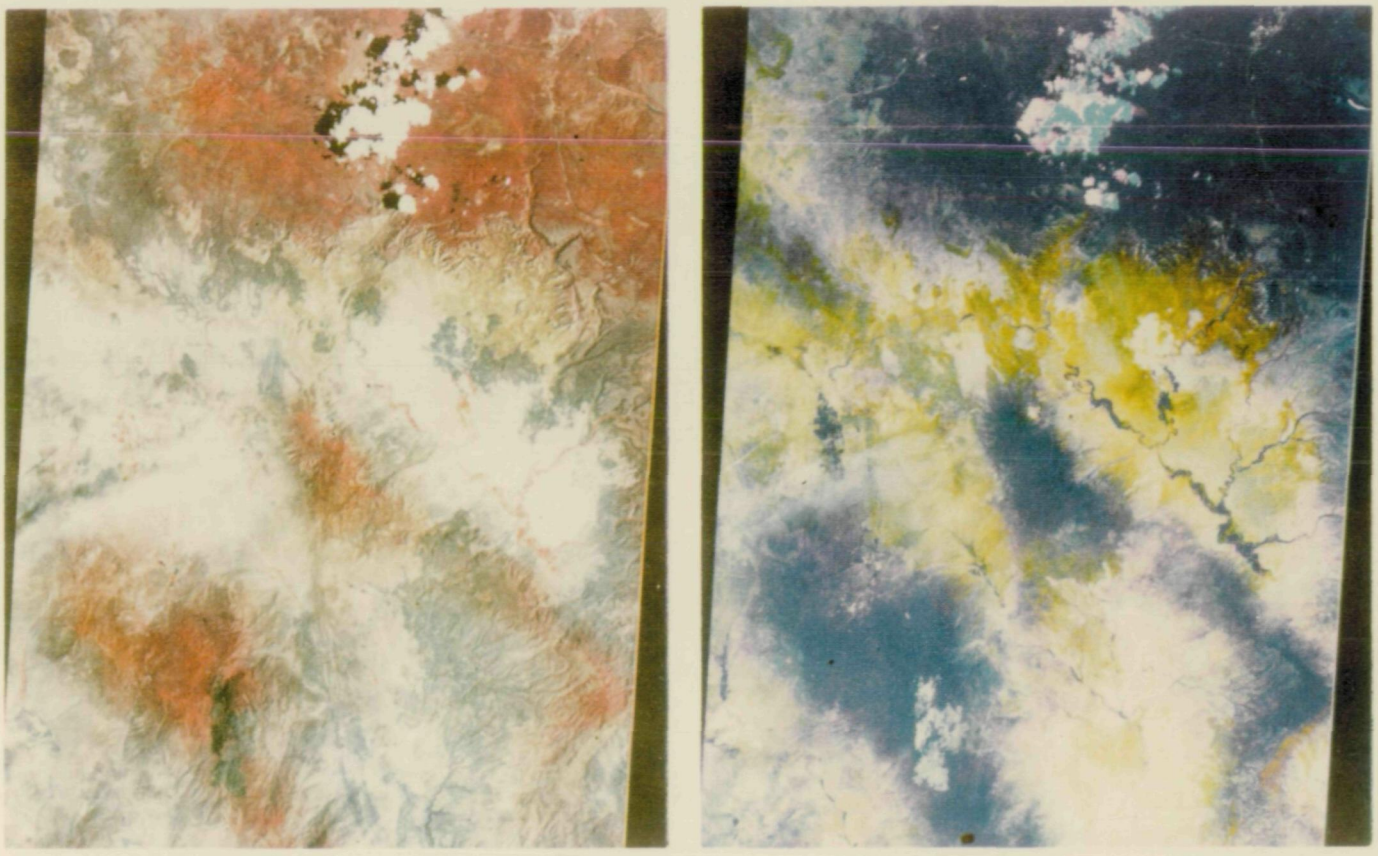

Fig. VI-2. (a) Individual stretch, color additive composite of the Verde Valley region. (b) Color ratio composite of the same area (4:5, 5:6, 6:7). Note the blending of lithologic boundaries

In the Verde Valley region, the difference pictures were superior to the ratio images, but were still greatly inferior to the stretched color additive composite.

In the Shivwits Plateau, the difference pictures proved to be superior in separating stratigraphic units and were superior overall in separating structural and stratigraphic units in the same image. Qualitatively, this result correlates with the fact that the general albedo contrasts are intermediate between those found in the Verde Valley and on the Coconino Plateau.

D. Combinations of Various Processed Images

Various processed images were combined in the I²S system in an attempt to discover further-enhanced stratigraphic and structural information. These combinations included:

(1) Positives and negatives of ratio images.

(2) Various ratio images.

(3) Stretch images vs ratio and difference images.

(4) Various stretch images.

Numerous composites were made of mixed positives and negatives of ratio images (R) taken two, three, and four at a time. None of these, however, was an improvement over ratio composites made up of only positives or negatives. The combination of R 7:4 (positive) and LRA 7:4 (positive) resulted in no discrimination of rock types in the plains area.

Dual and ternary composites (positives and negatives separate) involving individual stretch (I) and ratio (R) images produced nothing outstanding. In fact, the uncombined images are usually better for sharpness of details than the combined images. One composite, however, is worth mentioning. By adding I 5 (positive) to R (5:6, 7:4, 7:5) (positives), there is more physiographic detail at the mouth of Cataract Creek. There is also some enhancement of the β-1-2-3 areas in the vicinity of Hualapai Hilltop Mesa and some enhancement of monoclines and faults near Redlands Camp. Adding I 5

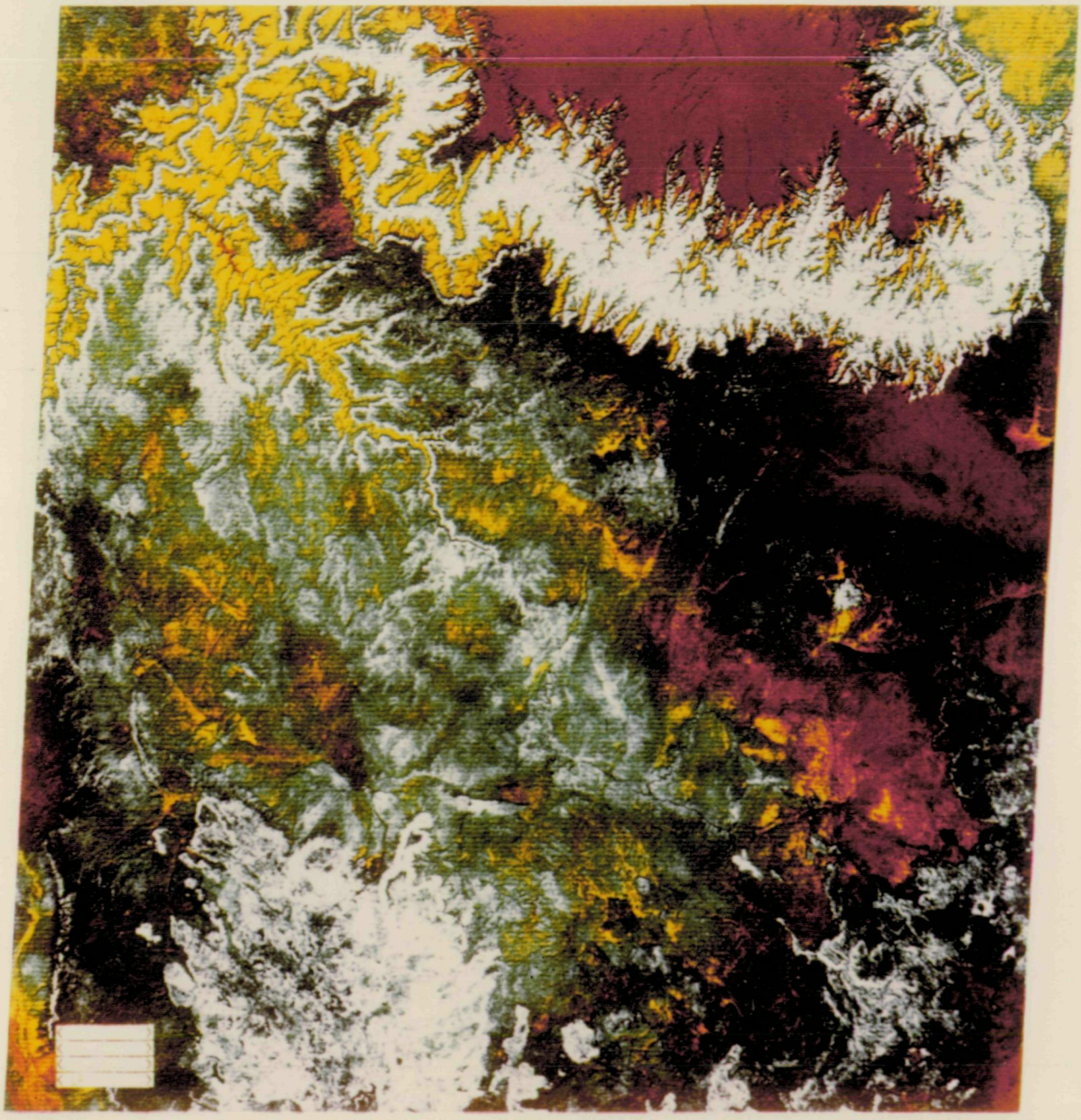

Fig. VI-3. Log ratio color composite of the negative transparencies of bands 4:5, 4:7, and 7:4 printed as green, red, and white, respectively

(positive) to R 7:4 (positive) results in more physiographic detail and less stratigraphic information in the area just west of Hualapai Hilltop Mesa and along the western edge of Cataract Creek.

In the combination of R 7:4 (positive), LRA 7:4 (positive), and I 7 (positive), there is some enhancement of the monoclines and drainages throughout the plains. Adding R 7:4 (positive) to I (5, 6, 7) (positives) resulted in some discrimination of rock types in the plains, but there was an associated blurring effect.

In general, without a strong physical reason for combining different types of products, random combinations of different enhanced images can not be expected to

be of value because of the almost unlimited number of possible combinations.

E. Filtered Images

The portion of NASA picture ERTS E-1014-17373 (and 5), covering the Coconino Plateau, was processed using spatial filtering techniques to enhance structural features. Figure VI-4a shows the effect of a 1- by 35-element horizontal line filter, and Fig. VI-4b shows the use of a 35- by 1-element vertical line filter. These filters are designed to enhance high spatial-frequency detail at the expense of radiometric information (see Appendix B). The contrast in local areas is increased to the maximum without reference to the rest of the scene. Thus, low-contrast, small features in the original scene are emphasized as much as are the features with high contrast; features that trend in the direction of the long axis of the filter are removed, while perpendicular-trending features receive maximum enhancement. This characteristic is demonstrated in Fig. VI-4a, which exhibits no horizontal striping, while Fig. VI-4b shows enhanced striping perpendicular to the direction of the vertical filter. However, filters of this type exhibit "ringing" effects which can be seen as apparent conjugate jointing pattern trending approximately 20° to the direction of the filter. This artifact must be considered during interpretation of the image.

A comparison was made for structural detail between filtered images and simple contrast-enhanced frames. An overlay was constructed which showed lineaments derived from both filtered images. The map produced was not significantly better than that produced from the unfiltered image. However, this may be because the major directions of structural features are northwest and northeast. Filters oriented perpendicular to these directions would provide superior results.

F. Sequential Image Differencing

Temporal differencing of ERTS images is useful for change detection as well as for possible identification of units based on differences in the photometric function or scattering properties. An attempt was made to observe differences in surface units based on sub-resolution texture by examining differences in the sidelap regions of ERTS images taken 1 day apart. The approximate 8° difference in photometric phase angle was not expected to be sufficient to separate any but the largest differences between units.

Figure VI-5a was formed by registration and differencing of ERTS pictures E-1014-17373, August 6, 1972, and E-1015-17431, August 7, 1972. The registration is obviously not perfect because of the inherent stereo information in the images and because of the extra pixels introduced to normalize the scan line length (see Appendix B).

If no differences in albedo or photometric function were present, the image would appear uniformly gray. Light and dark areas are, respectively, lighter or darker in the August 7 frame than in the August 6 frame. Clouds were present in the northwest corner of the August 6 frame. The cloud just north of area 3 was present in the August 7 frame.

Part of the image coincides with the area on the Coconino Plateau mapped for this report. In order to determine whether the anomalous areas corresponded to lithologic units, an overlay of the geologic map was made to fit the image. The light area (1) coincides with extensive exposures of Moenkopi Formation. There is not complete agreement, however, as adjacent outcrops of Kaibab Formation units 2, 4, and 6 also appear light. Outcrops of Moenkopi Formation to the west of area 1 are not anomalously light.

A second broad, light area (2) extends from the Aubrey Cliffs across the Mt. Floyd volcanic field, in which there is no correlation with either areas of basalt outcrop or areas mantled by alluvium. The anomaly crosses boundaries indiscriminately. Southwest of the volcanic field, the anomaly is in an area of Kaibab Formation, and again crosses unit boundaries within the Kaibab Formation.

Area 3 occurs in the vicinity of Frazier Well, and area 4 to the south in Aubrey Valley. To determine whether there was any coincidence of the anomalies with geologic units, a tracing of Twenter's geologic map (1962) was overlain with the difference picture. Area 3 is associated with Kaibab Limestone. However, to the south the anomaly is associated with Quaternary alluvium. Area 4 also coincides with alluvium. Moenkopi Formation exposed at Frazier Wells does not coincide with any anomaly.

The dark areas coincide to some extent, but not completely, with vegetation cover as identified on the 5:6 ERTS ratio and on the Williams 2° topographic sheet.

It is clear from this discussion that the light areas are not associated with one lithology. A more logical explanation is moist ground due to spotty precipitation on August 6. On that day 0.18 cm of precipitation was recorded at Seligman, according to U.S. Department of

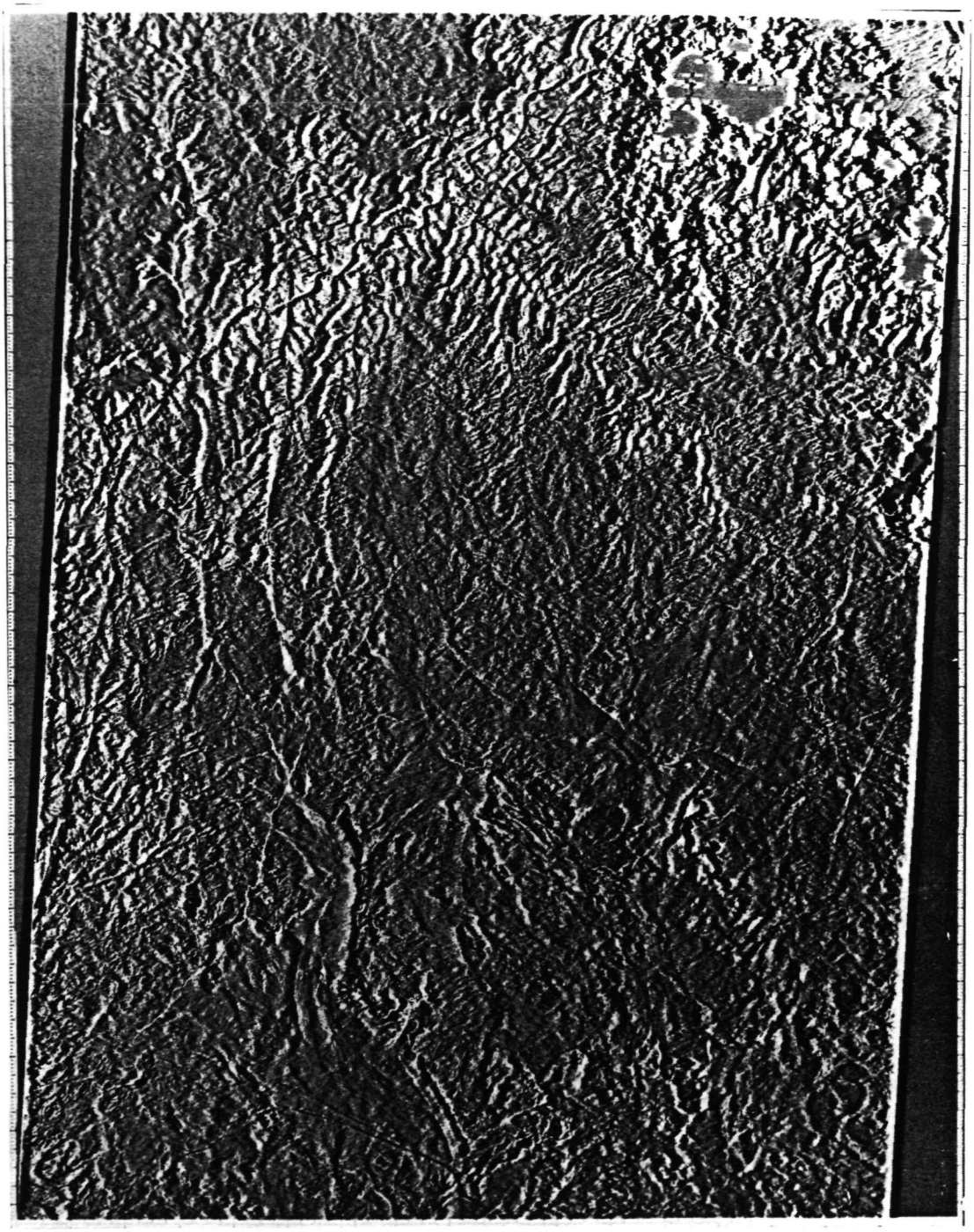

Fig. VI-4. NASA picture ERTS E-1014-17375-5 processed to enhance high spatial-frequency detail. (a) Processed using a horizontal line filter. (b) Processed using a vertical line filter.

Commerce climatological data. Because the anomalies appear when compared with data from the next day, rapid drying must have occurred.

In order to test the validity of the anomalies, an 18-day difference picture (Fig. VI-5b) was made between the August 6 image and the August 24, 1972, image (NASA picture ERTS E-1032-17373). Area 1 is equivalent in Figs. VI-5a and VI-5b and has approximately the same shape. This is significant because heavy rainfall was reported on August 13 and 14, with Grand Canyon Village recording 2.84 cm and Seligman 0.12 cm. The dark area north of

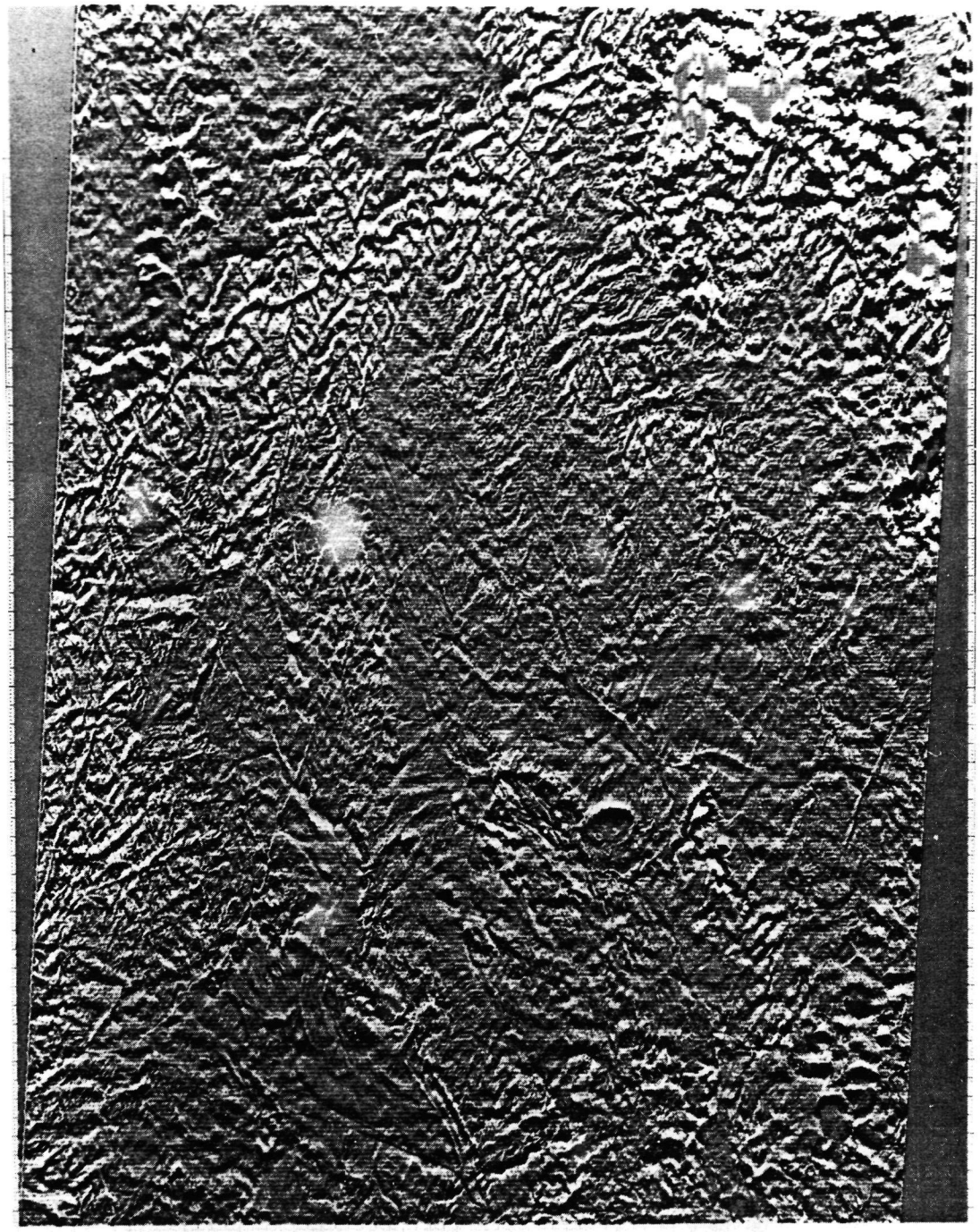

Fig. VI-4. (contd)

area 1 in Fig. VI-5b may be residual dark soil on August 24.

Note that, in the overlap region between Figs. VI-5a and VI-5b, a dark region in Fig. VI-5a which corresponds to the vegetation area does not appear in Fig. VI-5b. As the photometric geometry is almost identical in the images comprising Fig. VI-5b, no dark area would be expected. Therefore, a probable explanation for the dark area in Fig. VI-5b is a difference in photometric or scattering function between vegetation and non-vegetation areas, a logical explanation since the points observed in

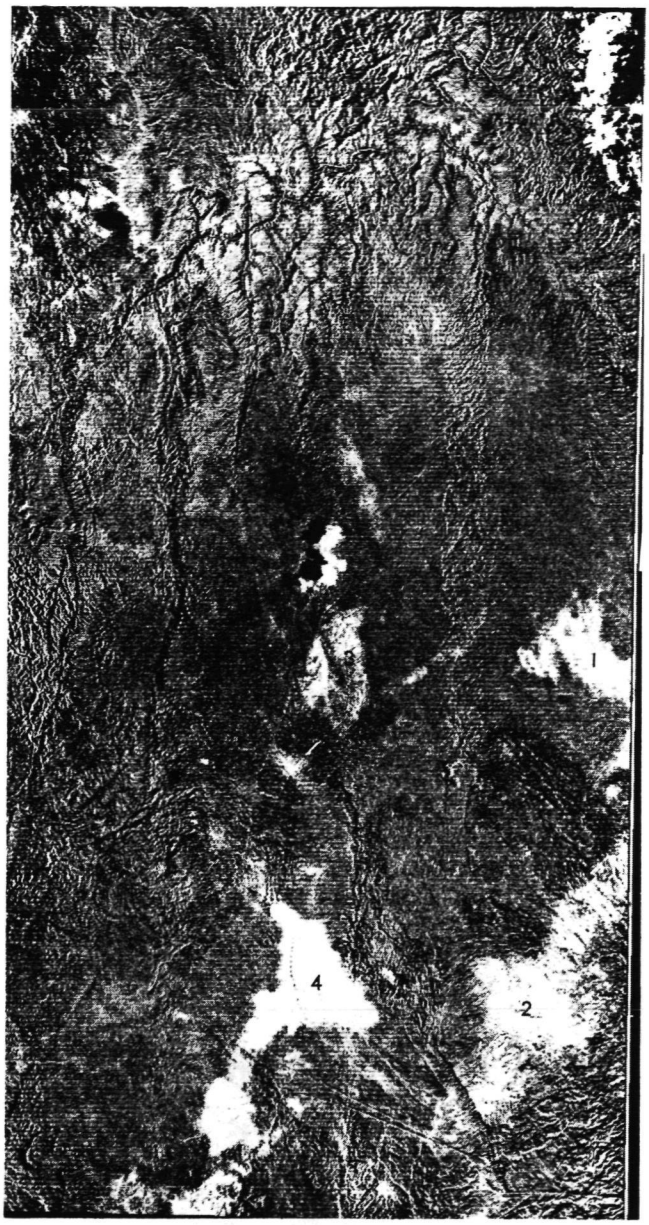

(a) IMAGES ACQUIRED 1 DAY APART (AUG. 6 AND 7, 1972) IN BAND 7

Fig. VI-5a. Difference pictures showing temporal changes in the Coconino Plateau. Misregistration is attributed to parallax. ERTS was 150 km farther west on Aug. 7 than on Aug. 6. (NASA pictures ERTS E-1014-17375 and E-1015-17431)

the right half of the August 7 frame were observed by the spacecraft at a greater phase angle than the same points in the left half of the August 6 frame. Because the photometric function of the vegetation, especially needle trees, is more peaked at zero phase, the vegetation should appear darker than soil with a more Lambertian scattering behavior. A more thorough study of difference images is required to verify the value of using photometric-function differences to identify remote-sensing units.

G. Summary

Computer-enhanced image products, in general, display more useful information than does an unenhanced image. Contrast-enhanced images without mixing different spectral bands are the most useful products for locating structural, physiographic, and cultural features. The best type of enhancement to use is scene-dependent and in most cases subscene-dependent. That is, it is necessary to survey the unenhanced image taking into account the relative and absolute brightness of the features before deciding on a particular enhancement. On the Coconino Plateau, comparisons of Tables VI-5 through VI-7 show that overall there is little to choose among different linear and nonlinear stretches, but that individual feature classes show large variations in evaluation of usefulness.

Ratio and difference images are generally better than single-band stretched images for the detection of stratigraphic details except in areas in which large albedo differences exist. Here, such as in the Verde Valley, a suitably stretched additive color composite provides the best lithologic differentiation.

In general, atmospheric correction does not help to discriminate among units, although it is of some value when spectrum matching on an absolute basis is attempted.

Scene-dependent processing based on the skill and experience of the interpreter seems to be the best means of obtaining the ultimate information from an ERTS MSS scene.

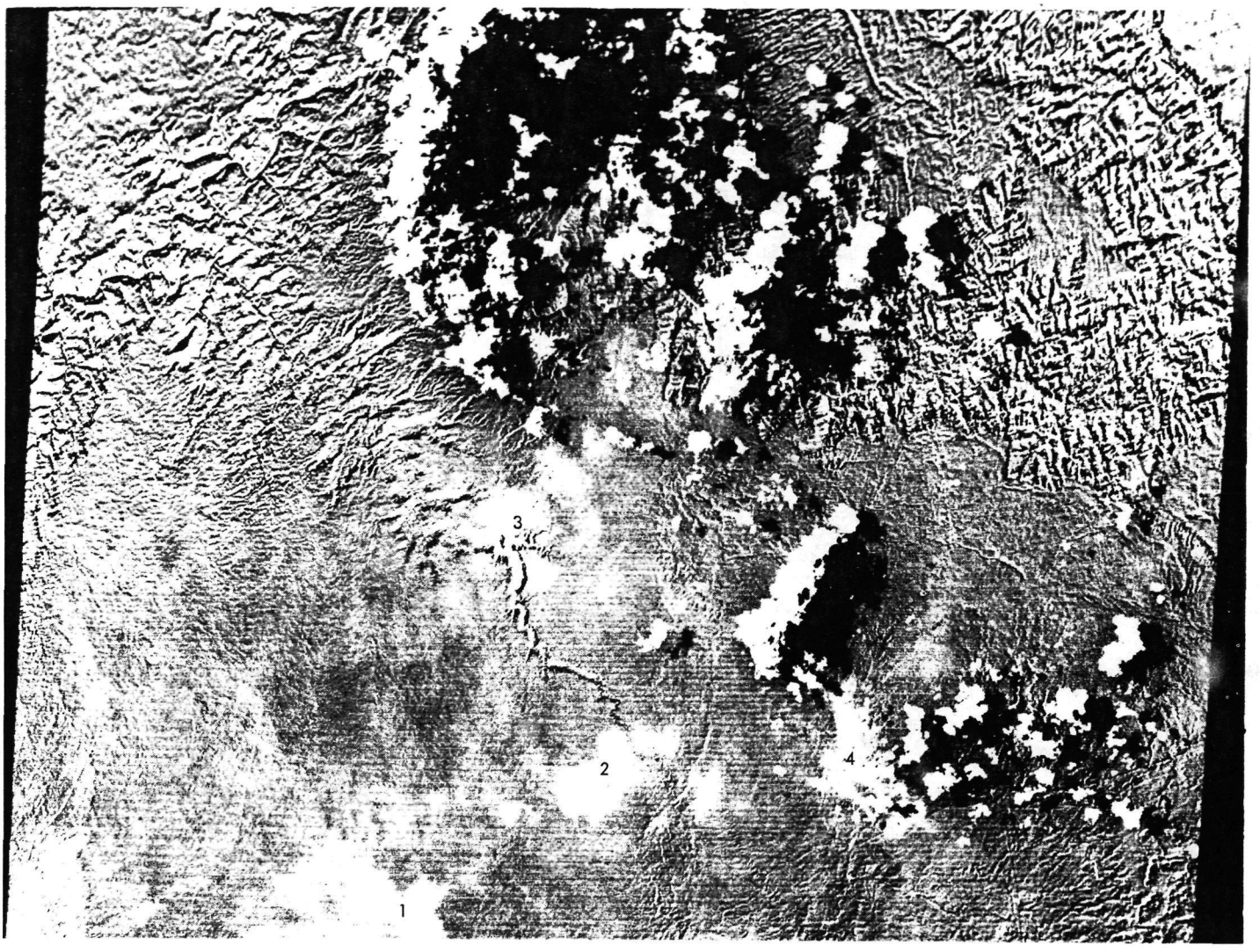

(b) IMAGES ACQUIRED 18 DAYS APART (AUG. 6 AND 14, 1972) IN BAND 7

Fig. VI-5b. Difference pictures showing temporal changes in the Coconino Plateau. Misregistration is evident in areas of high relief. Clouds, cloud shadows, and ground wet from recent thundershowers are visible temporal changes (NASA pictures ERTS E-1014-17375 and E-1032-17373)

VII. Conclusions and Recommendations

A. F. H. Goetz

A. General Remarks

ERTS images proved valuable in this investigation to obtain a broad synoptic view of the terrain. Unprocessed ERTS images, particularly those taken at low sun angles, revealed a wealth of new structural information and enabled a broad regional study to be made of the tectonic history of the southwestern Colorado Plateau. Because of the lack of regional continuity available in air photo mosaics and the lack of time and manpower to carry out such a study by conventional means, this study might not have been possible without the use of ERTS images.

It must be emphasized, however, that ERTS images are only a tool in the geologists' arsenal, albeit a very useful one. Reconnaissance mapping is feasible with ERTS images, but even with the aid of computer image processing, as demonstrated in the mapping of Area B on the Coconino Plateau, ambiguities are evident which can be resolved only by field checks.

B. Image Processing

Computer image processing has been shown to be both valuable and necessary in the extraction of the proper subset of the 200 million bits of information in an ERTS image to be applied to a specific problem. The methods, which include modulation-transfer-function correction, contrast stretching, and color ratio compositing, among others, facilitate for the geologist a display of pertinent data which can not be obtained from unprocessed images. An example is the comparison of Fig. IV-C-1, an unprocessed image of the Coconino Plateau, with the color ratio composite of Fig. VI-3. This comparison shows the dramatic increase in the amount of lithologic information available to the interpreter, as evident in Fig. VI-3.

The types of image enhancement best suited to a specific area vary. As demonstrated in this investigation, simple contrast enhancement, before forming a color-additive composite of three bands, is all that is necessary in areas such as the Verde Valley region in which large albedo variations are present among geologic units of interest. Difference pictures formed by color compositing three spectral difference images seem to provide the best separation among geologic units in areas such as the Shivwits Plateau, where moderate contrast is visible in unprocessed images. Ratio and log ratio color composites provide the best contrast among rock and soil units which show little or no separation on unprocessed black and white images. The Coconino Plateau is an example of an area in which a ratio image can be used most effectively.

C. Spectral Information

Spectral reflectivity information obtained from the four MSS bands can be correlated with in situ spectral reflectance measurements after path radiance effects have been removed and a proper normalization has been made. However, the absolute identification of lithologies is

precluded by the non-uniqueness of spectral reflectivity information in the wavelength region covered by ERTS. The data are most valuable for mapping purposes in distinguishing among telegeologic units that can be identified later by field checks.

D. Geologic Results

A new detailed map of the major fault systems in a 90,000-km^2 area in northern Arizona was compiled from high-altitude photographs and pre-existing published and unpublished map data. With the use of ERTS images, three major fault systems, the Sinyala, Bright Angel, and Mesa Butte, were identified and their full extent measured. Each system was extended to almost twice its previously mapped length. Although the displacements are small within the Phanerozoic rocks, correlation with gravity and magnetic anomalies suggests that these systems are related to Precambrian structural trends. In order to explain aligned linear margins of the anomalies, large displacement of the crystalline Precambrian rocks is postulated to have occurred on these faults.

A study of the boundary region of the southwestern part of the Colorado Plateau and Basin and Range province shows that the boundary between the two crustal blocks is old, relatively sharp, and has been more or less fixed since the beginning of Phanerozoic time. The two regions have been subject to the same stress fields, but a more competent crust within the Colorado Plateau has resulted in much more subdued deformation.

A new hypothesis for the late history of the Colorado River has been formulated. In Miocene time and earlier, the Lower Colorado Drainage did not exist. The Upper Colorado crossed the Kaibab Uplift and flowed northwestward. The Little Colorado River and Cataract Creek flowing in the same general direction were tributary to it. During or shortly after the opening of the Gulf of California, 4 to 6 m.y. ago, a stream developed in the Basin and Range province approximately along the present Lower Colorado River. This stream eroded headward and eventually captured the Upper Colorado Drainage west of the Kaibab Uplift, forming the course of the present day river.

E. Applications

A byproduct of the regional studies in each of the three areas was the identification of possible sources of shallow ground water, a scarce commodity in these regions.

On the Shivwits Plateau it was recognized that the Shivwits lavas fill an old strike valley, part of which is underlain by Moenkopi Formation, an aquiclude. Local runoff water is trapped at the base of the porous lavas along the axis of the valley. Near the northern end of the flow a prominent dip-slip fault interrupts the sub-lava drainage forming springs, some of which have been developed. However, a promising place for future development of shallow water resources in this arid area is along the axis of the old valley.

On the Coconino Plateau it was recognized that sandstone lenses, underlain by clay, within unit 5 of the Alpha Member of the Kaibab Limestone, form perched aquifers, collecting local runoff water in structurally favorable areas. Drilling on the Globe Ranch confirmed this hypothesis. The extent of unit 5 has been mapped over a 5000-km^2 area, and a potential for water at less than 15-m depth exists throughout the area.

South of Flagstaff lineaments detected first on ERTS frames were verified on conventional aerial photographs, and the resulting map was used to infer maximum fracturing in upper Paleozoic rocks along the north- to-south-trending Oak Creek fault in the Woody Mountain well field. A site for a large-diameter, deep cable tool well for Flagstaff was chosen; drilling began in October 1974.

F. Recommendations

The ERTS-1 multi-spectral scanner (MSS) system provided magnificent pictures in four spectral bands from a vantage point new to most geologists. The moderate resolution and small subtended angle in the image provided an uncluttered view of large areas and provided insights not obtainable using conventional aerial photography. There are, however, several shortcomings that should be considered in future Earth-observing instruments.

1. Resolution

The desire is always for increased rather than decreased resolution. In the case of ERTS, an increase of a factor of 3 in linear resolution would make possible the further use of textural and geomorphic information as well as provide an added ability to detect stratigraphic units. The former is important because the geologist uses a great deal of spatial context information to arrive at decisions in photointerpretation. This ability is severely hampered with the present ERTS system.

2. Number and Location of Spectral Bands

In order to obtain a greater separation among geologic units when using multi-spectral information, the bandpasses should be chosen optimally based on field spectral information. A study is underway to use the spectral reflectance data obtained with the portable field reflectance spectrometer (see Appendix E) to make objective decisions on bandwidths and band positions. A preliminary conclusion is that a band centered in the 1.6- and 2- to 2.5-μm region would be valuable in separating soils and rock types.

3. Overflight Times

A significant bias has been introduced into the structural interpretations based on ERTS data by the restricted range of sun azimuths encountered with a sun-synchronous orbiting spacecraft system. On ERTS images all northwest-trending structures are made almost invisible. A different view would be obtained by using afternoon overflights. It is hoped that digital filtering techniques can be developed to overcome this problem largely by enhancing preferred directions and adding them to the original image.

4. Radiometric Calibration

Better radiometric calibration and higher signal-to-noise systems are required to eliminate the disconcerting striping problems encountered in ERTS-1 data. In order to facilitate better absolute determination of spectral reflectance for more accurate rock identification, new systems should contain inflight-calibration procedures of the full optics system.

Appendix A
Image Processing System Considerations and VICAR

F. C. Billingsley

Many practical factors must be considered in the design of a digital image processing system in order to achieve maximum efficiency of the total system, including the analyst. Some of these are discussed below, followed by a brief discussion of the software and hardware systems used in the processing for this investigation.

1. Throughput Speed

Two primary factors that affect throughput are the efficiency of the operator in the input and output (I/O) operations and the actual computer running time. The considerations here and in the section on software philosophy are based on the use of general-purpose computers for digital processing.

In a production system, the required throughput quantities soon become sufficiently high that the efficiency of the operator/analyst in defining image areas to be scanned, determining reference areas, and inputing other data become major considerations. Because a major part of the operation time of the system may be occupied by the analyst, his efficiency must be given top priority short of sacrificing processing capabilities.

Because the data in a digital image number typically in the millions, and each of these must be separately manipulated by the computer to perform even the simplest image processing task, careless programming almost invariably leads to programs that are limited by the arithmetical speed of the computer, not by I/O data rate. However, careful use of techniques such as lookup tables significantly reduces the amount of arithmetic required. Therefore, it is anticipated that any modern central processor with instructions for manipulating individual pixels of data is adequate for digital image processing.

The required core size is dominated by the number and distribution of the picture elements in the input picture(s) which influence the photographic density at each point in the output picture. In functions such as geometric transformation or spatial filtering, the number can be large. Typical programs can operate with as many as six lines of input data and two lines of output data being required simultaneously. Assuming a maximum of 4000 picture elements (pixels) per line, these buffers alone require 32,000 bytes of core. The program itself requires additional space.

In a total digital image processing system, the computer is interfaced to external input and output devices. The I/O interface of the central computer must, therefore, be flexible.

A most important factor in the throughput of a system is its own peripherals, i.e., its tape drives and disks. A 4000- by 4000-pixel picture recorded at one picture line per logical record occupies a full 740-m reel tape at 800-bpi packing intensity. Because the computer is often likely to be I/O bound, the time required to read a picture from tape can be taken as a basic image processing time unit. This time unit is almost 4 min for a fast tape drive. For the standard slow tape drives often tied to mini-computers, this time becomes 30 min. A large disk is required to contain one 4000- by 4000-pixel picture; an IBM 2311 disk is only half of the required size.

Throughput speed can be drastically altered by using special devices such as parallel processors or hybrid peripherals in conjunction with a normal computer. For example, the use of a parallel processor for convolution operations involved in convolution filtering or cross correlations can reduce the time for these operations by a factor of between 5 and 10. Peripherals such as convolution and Fourier transformation hardware, and computer-controlled optical or analog electrical processors can be considered during system design to minimize expected lengthy processes.

2. Software Philosophy

Even in a production environment, the task of continually developing new software is never complete. Therefore, a programming system is needed to facilitate the development of new software and to provide simple means for its incorporation and use. The system should require a minimum of programming knowledge and data inputs from the analyst, and should perform the I/O

processing and routine bookkeeping. This language should be designed to allow the analyst to perform easily and quickly multiple processes automatically on one or more pictures.

A general set of design desiderata could be stated as follows:

(1) The fundamental philosophy of the system is that the image analyst, in accomplishing his picture processing, calls for execution of one or more of a group of programs from the system library. He can enter parameters at the time of execution to suit his particular needs, as the library programs will be written to be flexible in application. These programs will have been previously debugged and documented, and will be available to any analyst upon request. A continually growing system is thus provided as various analysts require new processes and write the required executable programs.

(2) Processing programs will be written so that each performs one useful function; however, a complete job may require from two to twenty to be run sequentially. A shorthand notation is required for doing repetitive jobs, and data-set handling must be automated and eliminated from the user's worry.

(3) Much picture processing can be accomplished using normal general-purpose computers and the standard Fortran batch processing software. As this is not particularly efficient, however, with large numbers of pictures to be processed, special attention in writing the processing programs must be given to reducing or bypassing the inefficient parts of the Fortran language and/or programming in machine language.

(4) If the computer is dedicated to this application, there is no a priori reason to use its operating system. However, the operating system normally provides basic data-set management capabilities along with reasonable I/O routines and program cataloging and fetching techniques. It is, therefore, appropriate to use the operating system as the supervisor for the machine and to avoid any modifications to it in order to save time and effort in learning, modifying, and debugging the system.

(5) As parameters for different routines necessarily vary, there is no completely standard format possible. However, it is desirable to keep parameters simple and easy to use so that manuals will not have to be repeatedly consulted for each program in order to set up a job.

(6) Normal production runs involve many pictures. Frequently, there are 25 or more pictures placed on one tape normally separated by file marks, which is a natural and efficient way to separate pictures.

(7) Much redundant effort would be expended by many programmers if each had to include tape-positioning, parameter readers, label updating, unblocking, and buffering routines that were similar. It is desirable to remove these and other repetitive processes from the programmer and place them once in a supervisor, which also saves core and ensures standardization of these functions.

(8) The designed system must reduce the core requirements of programs, as core shortage is a continuous problem.

(9) Identifying historical information for tape and disk files will be printed whenever a file is used. Apparent device independence between tape and disk will be supplied by common I/O routines.

3. VICAR: JPL Image Processing Language

An image processing laboratory should make available to the analyst an efficient data-handling system for the development of algorithms and for recording, processing, and displaying pictures. To facilitate the use of the system by the analyst and to enable him to call rapidly for new processes, an image processing software system based upon English language commands has been designed for the JPL Image Processing Laboratory (IPL). This system requires a minimum of programming knowledge and data inputs from the analyst, and automatically performs the I/O processing and routine bookkeeping. This language has been designed to allow the analyst to perform easily and quickly multiple processes automatically on one or more pictures. This is accomplished with a simple set of commands which, together with the required numerical parameters, are submitted as a card deck or via an interactive console.

Only a supervisory program is permanently resident in core. Various processing programs as required are read from the disk libraries to the core by the control commands, thus minimizing the amount of core that must be reserved for programs. The system contains special-purpose I/O routines designed for picture handling. These routines are used instead of the normal Fortran I/O routines, which saves considerable space in the program libraries and obviates the necessity of writing them for each processing program. As a result, the writing of

processing programs (which may be either assembly language or Fortran) is considerably simplified.

a. Standard format. A standard format has been established for both tape and disk data sets. All of the standard video image communication and retrieval (VICAR) processing programs are designed to operate with this standard data-set format.

Video samples are normally represented as 8-bit data bytes. With the data converter feature of the IBM 360 tape controller, both seven- and nine-track tapes may be logically equivalent. The standard tape format in use at JPL is an IBM-compatible seven- or nine-track tape written with odd parity at 800 bpi. Each reel of tape may contain up to 99 files, determined only by the size of the files. Each file contains one video frame and is followed by a trailing file mark. The last file on a reel must be followed by two trailing file marks.

All data are recorded in an 8-bit mode, compatible with that specified in IBM SRL A22-6866. On seven-track tape, the 8-bit data samples are written in a mode where three 8-bit data bytes are recorded on tape as four 6-bit characters.

Tapes from outside sources should meet these standards generally, but may be at other tape densities. For use within the system, these tapes are transcribed; standard EBCDIC labels containing picture identification and size data are added because the system uses this information in setting up and carrying out the various tasks.

b. Writing the processing program. As indicated by the previous discussion, the various programs called for execution must have previously been written and debugged and be available in the system library. These programs may be written either in Fortran IV or in assembly language.

To eliminate the Fortran I/O package, programs are normally designated as subroutines, in which case reading or writing of the picture, reading cards, and printing messages on the line printer must be handled by special CALLS that are available in the system library. The read and write CALLS are especially designed for picture processing, and will input or output one line of a picture or a segment of a line each time encountered. The various data conversion and printing CALLS provide their functions in formats appreciably simpler than that used by Fortran.

Because routine bookkeeping, tape handling, and other housekeeping functions are provided by VICAR, the executable processing program is appreciably simplified. The processing program is organized approximately as follows:

(1) After the normal Fortran INTEGER, REAL, EQUIVALENCE, etc., set-up statements (if Fortran is used), the required data sets are defined and the parameters called.

(2) Any required preprocessing using the parameters is then performed.

(3) One or more lines of the picture(s) are called using CALL READ.

(4) Required processing is performed on these picture lines.

(5) Resulting output picture line is written on the output data set using CALL WRITE.

(6) More lines are read, processed, and written until the end of the picture.

c. Advantages. This system has been in use at JPL since 1966 on an IBM 360/44 computer. The language has proved to be easy to use, after an initial learning period, and makes possible much simpler and more error-free deck setups than would be possible without it. The supervisor and system concept have simplified the programming of applications programs by about 25% and have made the programs more efficient in execution, using less core than would have been possible without the system.

Primary advantages over separate programs are:

(1) Easier to use due to standardization of procedures and formats and reduction in the number of control cards.

(2) Saves time and money in programming by providing buffering, housekeeping, label processing, and many other capabilities to the programmer.

(3) Allows interaction between programs which would otherwise be difficult for a user to control.

(4) Can be improved in the future without necessarily modifying all programs.

(5) Faster execution because of elimination of returns to the operating system between tasks.

The various programs utilized in this experiment are described in Appendix C.

4. JPL Image Processing Laboratory

IPL, which has evolved over the past decade to support the growing requirements of the unmanned planetary exploration program, is the laboratory in which all of the ERTS image processing described in this report has been accomplished. The system, as shown in Fig. A-1, is described in subsequent paragraphs.

a. Central computer. The central computer is an IBM 360/44 equipped with four IBM 2400 tape drives, four IBM 2314 disk drives, a multiply-summation processor (MSP), a standard complement of I/O peripheral devices, and an interface unit for on-line connection to external electronic equipment such as the present interactive console and the Image 100 system and parallel processor.

The system operates under the IBM 44 Programming System (44PS) using a special-purpose supervisor (VICAR) as the primary user language (described above).

Recently, a two-partition (foreground/background) version of 44PS has been installed which allows two concurrent data queues to be processed. The capability allows an analyst to work interactively on the console described below, while not unduly slowing down the batch processing in the other partition.

The interactive console has been developed to facilitate on-line image processing with operator interaction. The development of image processing techniques and the determination of the parameters to be applied during the processing are frequently subjective, and require the continued attention of the analyst. In this interactive procedure, the analyst examines his latest results and selects further processing accordingly until the desired result is achieved. To optimize the use of analyst and machine time, the interactive console may display before and after images at each step in the processing. The operator interacts through the keyboard, calling up the processes he desires and entering parameters. Principal components of the console include two scan-converter storage systems, television monitors for high-quality 1039-line video display, and a Polaroid/CRT recording display capable of high-quality 1024- by 1024-pixel images.

b. Video film converter. The video film converter (VFC) provides a flexible means of transferring images from optical to digital form and vice versa. Image data can be entered into the computer from digital tape or 70-mm film. Processed images can be transferred directly between these media through the translator in an off-line mode.

The VFC is a high-resolution flying-spot scanner/film-recorder device on which film images are either scanned for input or exposed on output. The minimum scanning spot, 25 μm in diameter, is stepped at the rate of 150 μs/element. In the input mode, samples are digitized to 8 bits, providing 256 levels of gray. Beam positioning is repeatable to within 5 μm. The VFC active film area is approximately 55 by 75 mm, allowing it to handle pictures up to about 2000 by 2500 pixels. Horizontal and vertical pixel spacings are independently adjustable.

The converter translator contains a mini-computer for some simplified picture operations, such as simple contrast stretches and masking and annotating the images, which are related to scanning and recording. Three digital tape decks are provided to allow maximum operational overlap and throughput capability.

c. Photolab. The IPL operates its own small photolab for developing film under precise photometric control and for making enlargement prints. The regular JPL Photolab is utilized for color printing.

d. Image 100 console. This console contains a stand-alone image processing system of moderate capability, solid-state refresh memory with color television monitor and a hardware multi-spectral classifier and preprocessor. It is operated stand-alone and eventually will be used as a smart terminal to the 360/44.

e. Coordinate digitizer. This device allows digitizing of coordinate locations to increments of 25 μm over a 1- by 1-m area. It produces computer tapes that can be read and processed by VICAR programs in the 360/44.

f. Precision film scanner. This scanner can scan color or black-and-white films over an area of 25 by 25 cm at variable spacings down to about 1 μm. The output consists of computer tape, which can be read and processed by VICAR programs in the 360/44.

ORIGINAL PAGE IS
OF POOR QUALITY

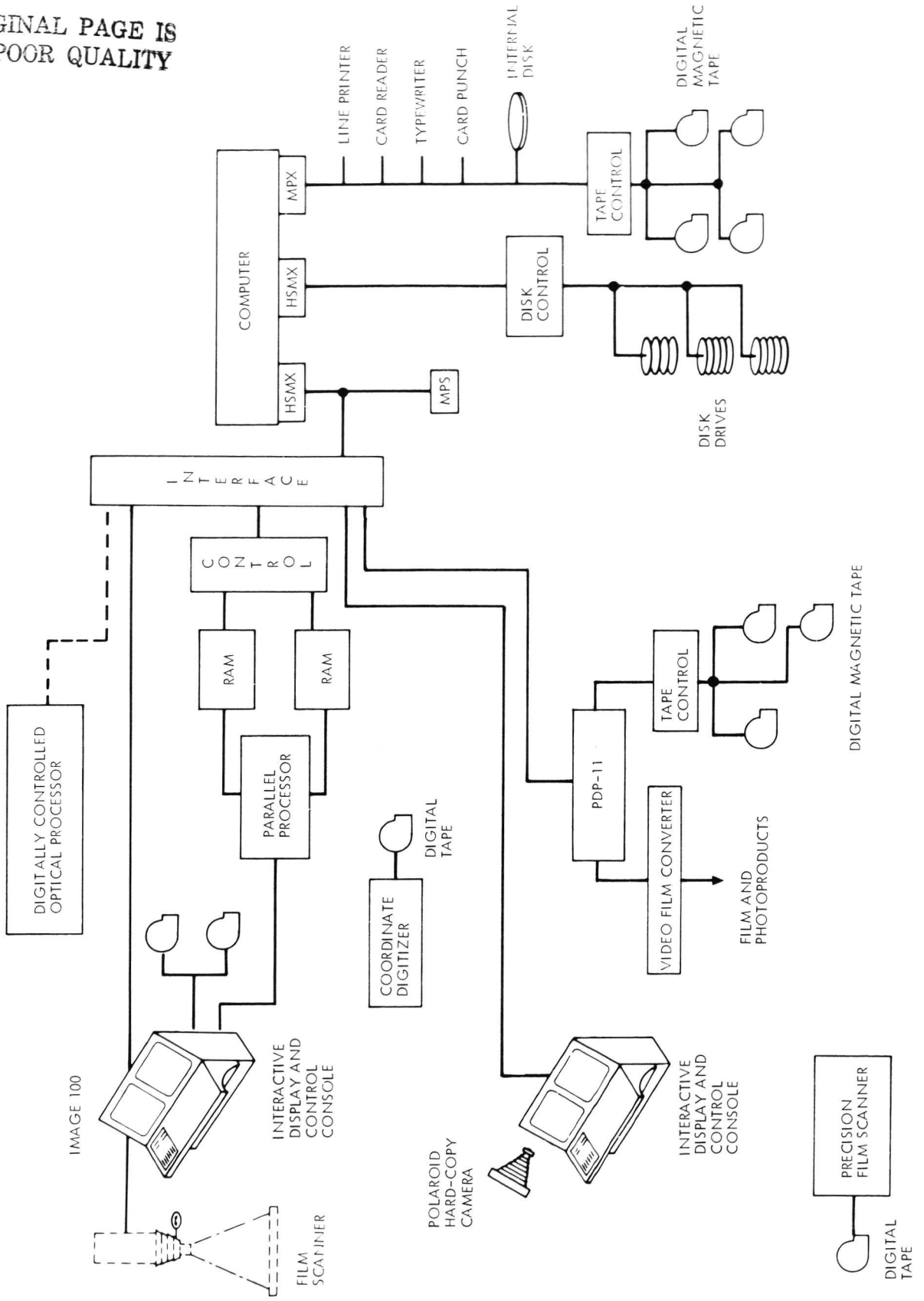

Fig. A-1. Image processing system

Appendix B
Digital Processing of ERTS Images

A. R. Gillespie and F. C. Billingsley

Procedures and goals of image processing are discussed in this appendix in the following categories: (1) Image Preparation, (2) Rectification, (3) Cosmetics, (4) Analysis, and (5) Display. A detailed description of the ERTS multispectral scanner (MSS) is given in Refs. B-1 and B-2.

I. Image Preparation

EROS supplies users with ERTS images stored in a spectrally interleaved format on four computer-compatible tapes (CCTs). Each tape contains two records of annotation describing the imagery and one-quarter of the four-channel image. Some calibration data describing the response of the 24 MSS sensors to an illuminated gray scale of known density are stored in tapes 1 and 4, which also contain the left and right edges of the image.

Images are supplied in EROS format and must be converted to VICAR format before processing at the JPL Image Processing Laboratory (IPL) to take advantage of existing software. VICAR (see Appendix A) is an image processing supervisor originally developed by IBM for JPL. It is characterized by simple, standardized input/output (I/O) and usage rules and by an extensive library of applications programs and procedures. Its format requires from one to five 360-byte records appended to the digital image. These records contain picture dimensions and annotations describing the scene and processing history. This information is extracted from the two EROS label records.

Under VICAR, the different channels of a multi-spectral image are usually not interleaved so that a complete ERTS image of four spectral channels is stored as four separate images, each containing the entire scene in a different spectral region. Because data can be conveniently stored and accessed in 8-bit bytes (2^8 or 256 gray levels), ERTS images are rescaled from the supplied 7-bit data (MSS bands 4, 5, and 6) or 6-bit data (MSS band 7) to fill the entire available 8 bits. This rescaling is required before MSS band 7 can be compared with the other channels.

II. Rectification

Images acquired by the ERTS MSS contain several geometric and radiometric distortions that must be corrected to allow accurate comparison with data from other sources. Rectification is the name given to this process. There are two broad classes of distortion: systematic and scene-dependent. Systematic distortions are caused by idiosyncracies of the satellite and imaging system; they are easily identified and removed. Scene-dependent distortions are more difficult to define than systematic distortions, and thus more difficult to correct. An example of scene-dependent geometric distortion is parallax; an example of scene-dependent radiometric distortion is detector hysteresis.

A. Geometric Rectification

Geometric rectification is accomplished by programs (see GEOM, LGEOM, SKEW, ASPECT, EGEOM in Appendix C) that rearrange the location of features in an image. This can be accomplished in two ways:

(1) The actual location of the picture elements (pixels) can be changed.

(2) The pixel grid can be retained and the individual pixels assigned new gray levels, which is called "resampling."

Although both approaches are used at IPL, the first technique is used only for simple geometric corrections such as correction of the aspect ratio, which is the ratio between the scales (meters per pixel) in the horizontal (sample) and vertical (line) directions of an image. Resampling is a flexible, powerful technique, and there are several different approaches (see Figs. B-1 and B-2). In all of them, some attempt is made to recreate or model the scene which was sampled to form the image. This modeled scene is then resampled to yield an image with the desired geometric characteristics. Because of limitations in the size of the memory of most computers, it is necessary to model the scene only locally, in the vicinity of a desired resampling site. This can still consume a large amount of time. Unfortunately, the severity of image degradation resulting from resampling increases as the size of the local area and the computation time decrease.

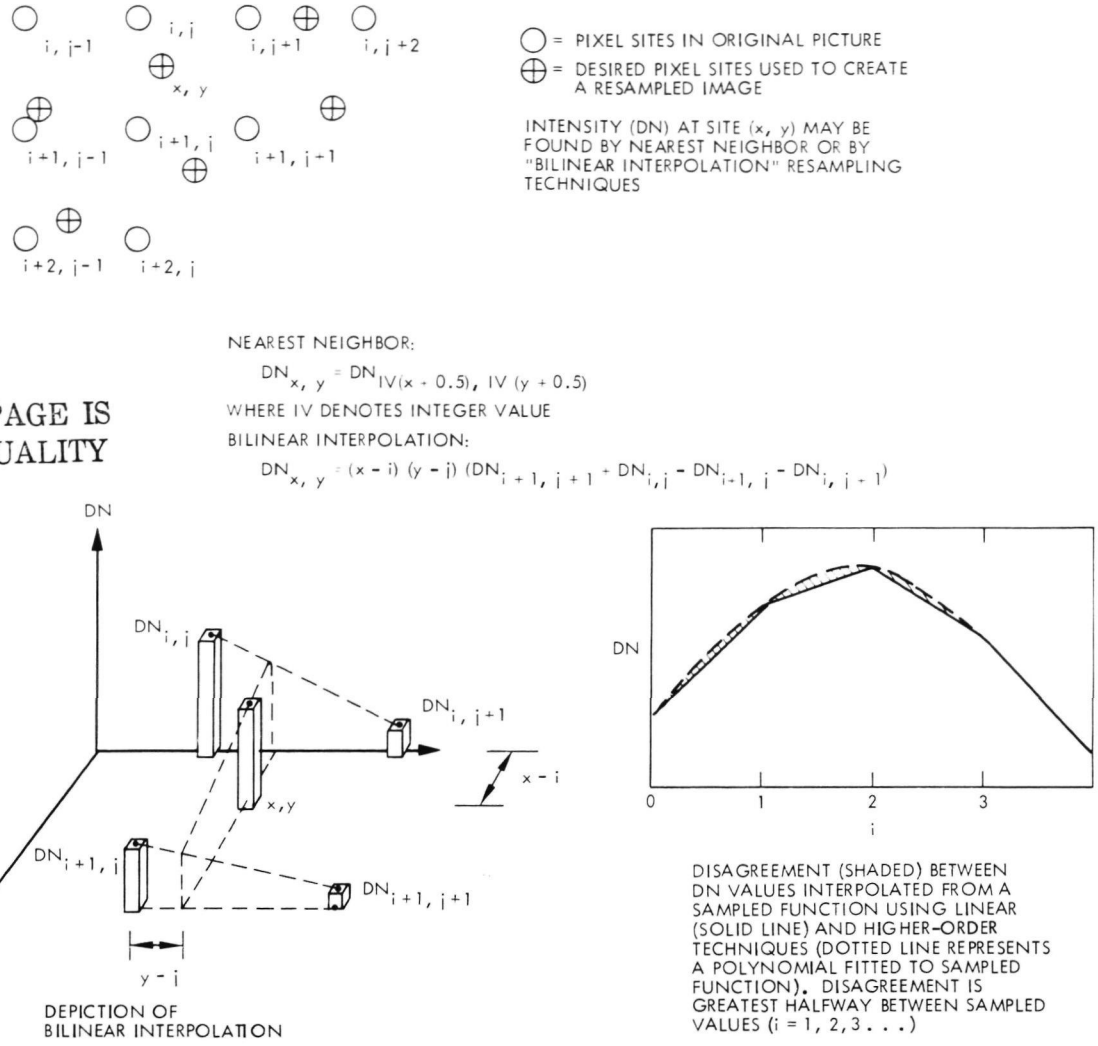

Fig. B-1. Nearest neighbor and bilinear interpretation resampling techniques

In resampling an image, a feature in the scene to be located at pixel (i,j) in the geometrically correct image being constructed will be found at (x,y) in the distorted image. Only rarely will x and y coincide with pixel centers in the input image. Resampling techniques differ in the method by which the gray level (DN), which should be stored at pixel (i,j) of the output picture, is derived from the input picture. Principal algorithms to accomplish this are discussed below.

1. Nearest neighbor algorithm. $DN_{i,j}$ is assumed to be the same as the DN of the pixel closest to the location (x,y) in the input picture. The closest pixel (k,l) is found by:

$$k = \text{integer part of } (x + 0.5)$$

$$l = \text{integer part of } (y + 0.5)$$

so that

$$DN_{i,j} = DN_{k,l}$$

Nearest neighbor algorithms are generally the fastest of the resampling algorithms; however, they suffer from the defect that the local geometry may be inaccurate by up to $2^{1/2}$ of the instantaneous field of view (IFOV), or the size of a pixel on the ground. Worse yet, the pixel from which the gray level is derived shifts suddenly from the pixel just before the correct resampling location x,y) to the pixel just after it. This problem becomes annoying during digital picture comparisons because, while the registration of detail in the two images may be perfect in one location, elsewhere there is misregistration. This is illustrated in

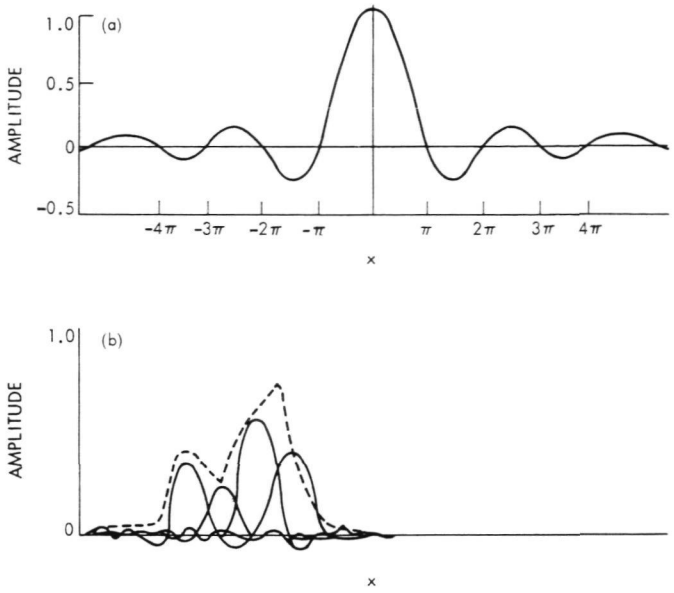

Fig. B-2. Resampling by convolution. (a) Cross section of response of diffraction-limited imaging system to an impulse of unit intensity at x = 0. Amplitude = sin (x)/x (sinc function). (b) A scene (dotted line) can be reconstructed by the superposition of sinc functions centered at the various sampling locations (pixels). Resampling requires computation of the intensity of the scene only at specified locations (resampling sites)

Fig. B-3, which depicts a time difference picture showing changes in Arizona over 1- and 18-day periods. The vertical bands in Fig. B-3a result when sudden jumps in the resampling positions in the two pictures, from which the difference pictures were made, are out of phase.

ERTS images supplied by EROS have typically been resampled using a nearest neighbor algorithm to force the number of samples per line to be constant.

2. Bilinear interpolation algorithm. DN_{ij} is found by using an interpolation scheme with the four nearest pixels surrounding resampling location (x,y) to determine the DN at (x,y) (see Fig. B-1). If (x,y) lies between samples k and $k + 1$ and lines l and $l + 1$, then the gray level at (x,y) can be found by using Eq. (B-1):

$$DN_{xy} = (y - l)\left[(x - k)(DN_{l,k+1} - DN_{lk}) - (x - k)(DN_{l+1,k+1} - DN_{l+1,k})\right]$$

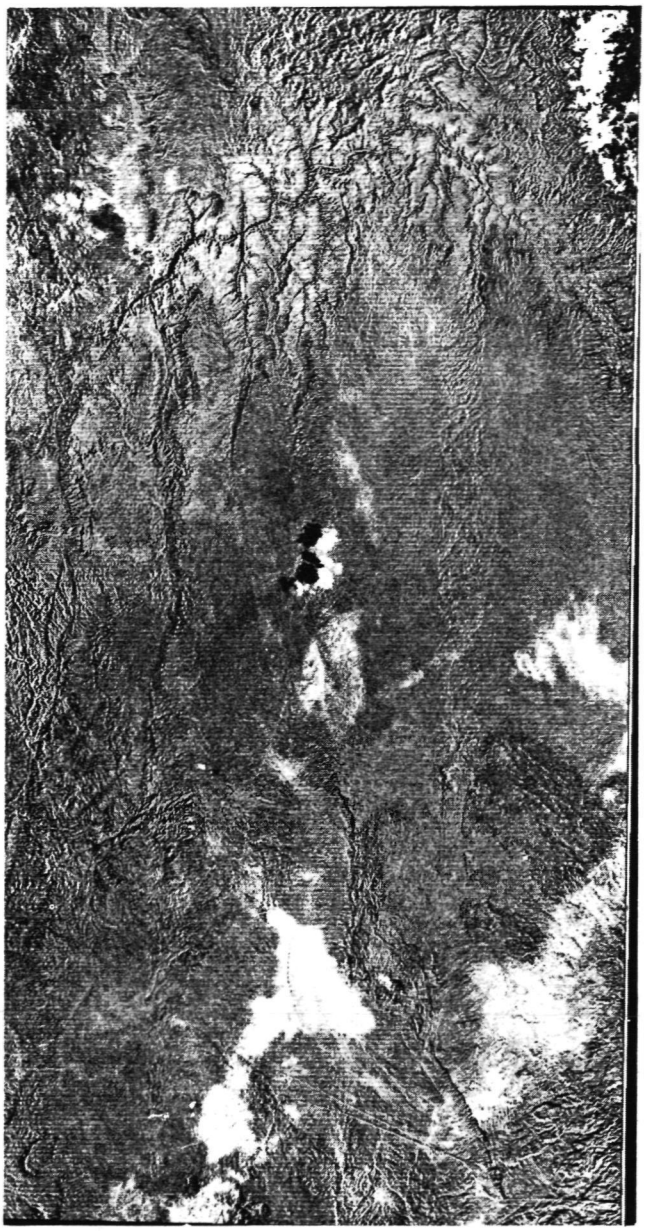

(a) IMAGES ACQUIRED 1 DAY APART (AUG. 6 AND 7, 1972) IN BAND 7

Fig. B-3a. Difference pictures showing temporal changes in the Coconino Plateau. Misregistration is attributed to parallax. ERTS was 150 km farther west on August 7 than on August 6. Vertical swaths of misregistered data (see right center) are artifacts introduced by nearest neighbor interpolation (NASA pictures ERTS E-1014-17375 and E-1015-17431)

which reduces to:

$$DN_{xy} = (x - k)(y - l)\,DN_{l,k+1} + DN_{l+1,k} - DN_{lk} - DN_{l+1,k+1} \qquad \text{(B-1)}$$

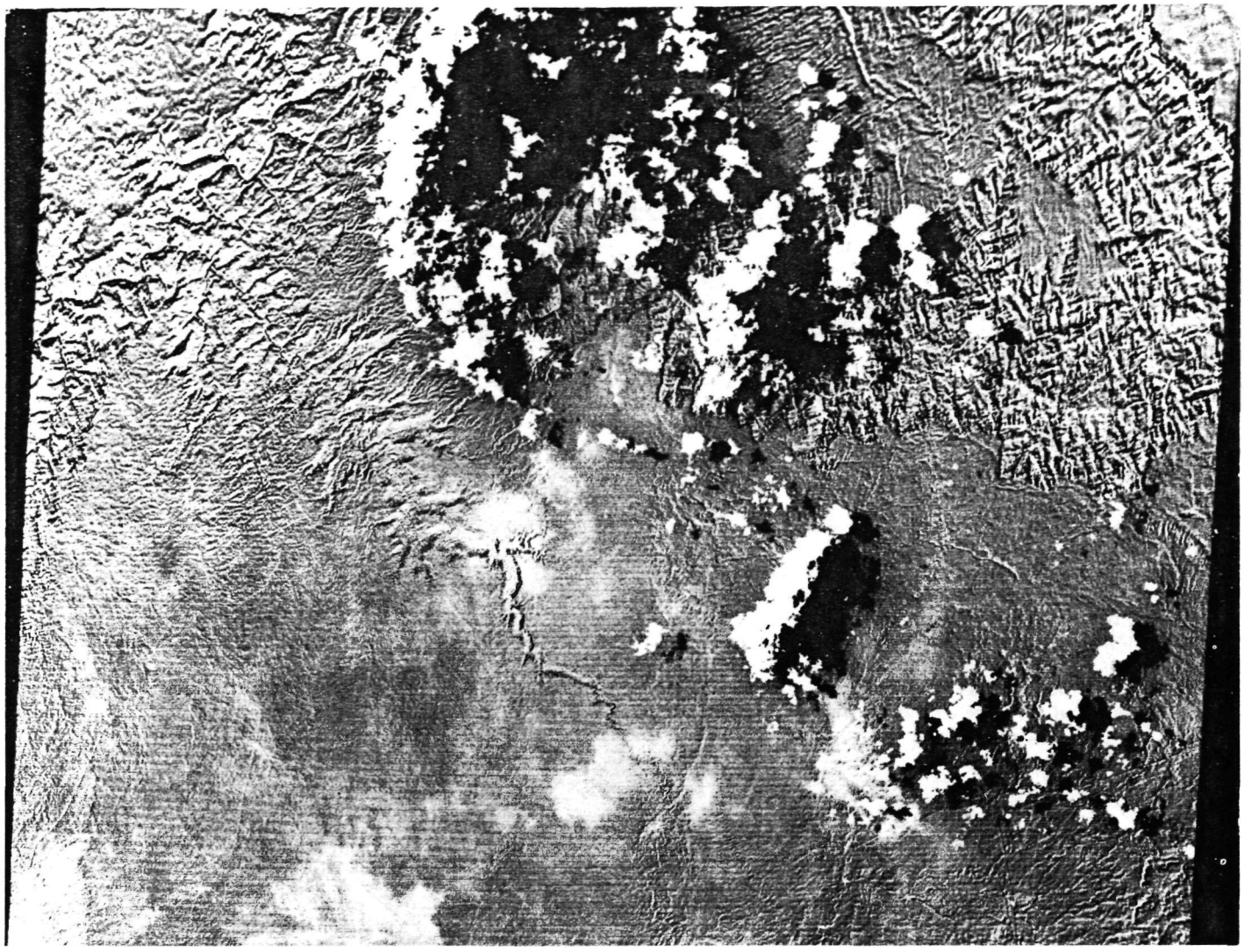

(b) IMAGES ACQUIRED 18 DAYS APART (AUG. 6 AND 14, 1972) IN BAND 7

Fig. B-3b. Difference pictures showing temporal changes in the Coconino Plateau. Misregistration is evident in areas of high relief. Clouds, cloud shadows, and ground wet from recent thundershowers are visible temporal changes (NASA pictures ERTS E-1014-17375 and E-1032-17373)

The frequency response in one dimension can be found by taking the Fourier transform of the triangular convolution kernel (h) shown in Fig. B-4d:

$$h_{bilinear} = \underset{-a \qquad +a}{\wedge} = \left(1 - \frac{x}{a}\right)_{x=0}^{a} + \left(1 + \frac{x}{a}\right)_{x=-a}^{0} \tag{B-2}$$

$$H_{bilinear} = \int_{-a}^{a} h\, e^{-i2\pi f_x x}\, dx$$

where f_x is the frequency in the x direction and $1/a$ is the sampling interval. The integral in Eq. (B-2) may be rewritten as:

$$H_{bilinear} = \left(\frac{\sin \pi f_x a}{\pi f_x a}\right)^2 \tag{B-3}$$

This function has zeros at integer multiples of $f_x = 1/a$ cycles/sample.

In normal resampling of digital imagery, $a = 1$; also, the convolution kernel is not the continuous function

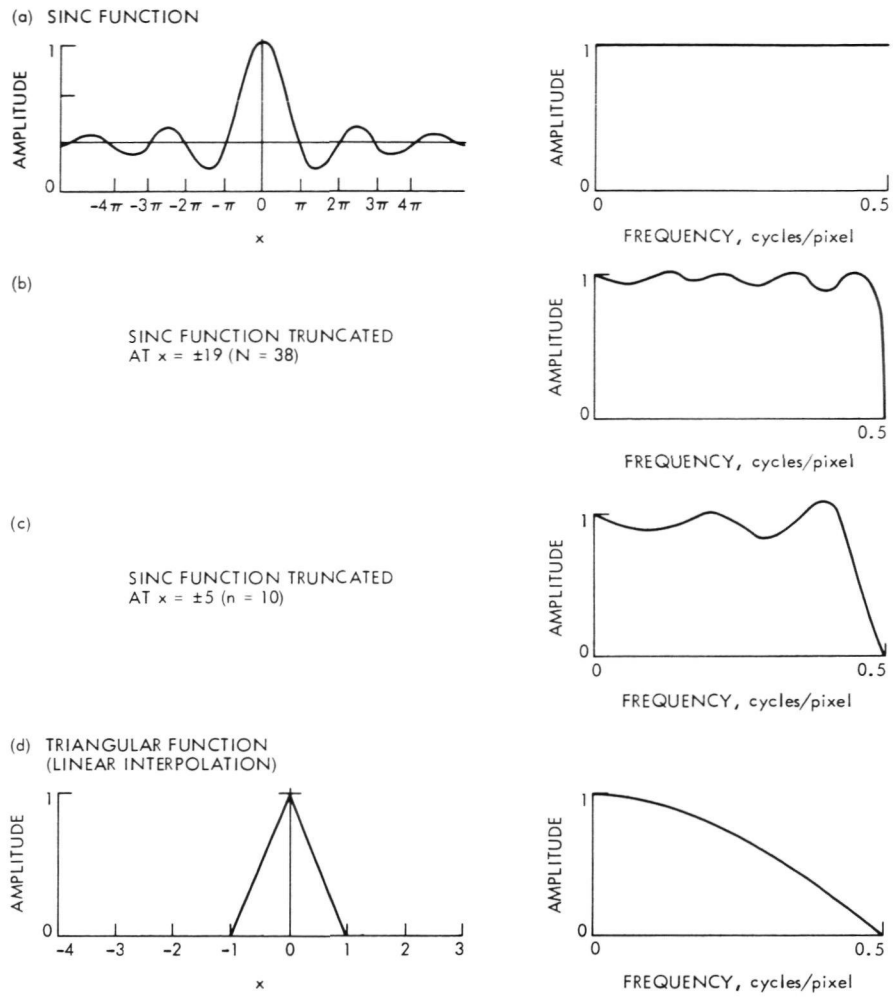

Fig. B-4. Image degradation during resampling when the resampling site is midway between original samples

described in Eq. (B-2), but consists of weights which are the amplitude of the parent function h at values of x determined by the distance of the resampling site from the nearest samples. Thus, if the resampling site is 25% of the distance from sample n to sample $n + 1$, the two weights are found at $x = -0.25$ and $x = 0.75$. The frequency degradation increases as x goes to 0.5 (Fig. B-4d). Extension of the above argument to two dimensions is straightforward.

3. Convolution algorithms. Resampling using a bilinear interpolation algorithm involves more computation time than resampling using a nearest neighbor algorithm, but it is significantly more accurate. Accuracy can be improved further by increasing the number of pixels in the vicinity of the resampling location from the nearest 4 to the nearest 16 or more.

Image degradation caused by a multi-spectral scanner should be spatially independent (examination of ERTS MSS images supports this contention), and the radiometric response of an MSS is essentially linear (or can be made linear). Therefore, spatial-frequency degradation is constant over an image. The superposition theorem is valid under these circumstances.

If a function is band-limited (the Fourier transform of the image has zero energy at frequencies higher than some ω_0), the function can be reconstructed exactly from a set of discrete samples:

$$f_n = f_{n\Delta x}$$

where $n = \ldots -1, 0, 1 \ldots$, provided that $2\pi/\Delta x > 2\omega_0$ (i.e., 0.5 cycle/sample at ω_0).

The reconstruction formula in one dimension is:

$$f(x) = \sum_n f_{n\Delta x} \frac{\sin[\pi(x - n\Delta x)/\Delta x]}{(x - n\Delta x)/\Delta x}$$

$$= \sum_n f_{n\Delta x} \operatorname{sinc}[\pi(x - n\Delta x)/\Delta x] \qquad \text{(B-4)}$$

Reproduction of f using a series of sinc functions results in a uniform spatial-frequency response out to a frequency of $\omega_0 = \pi/\Delta x$, so that the relative spatial frequency content of the image is undisturbed. Because of this, the original continuous function will be reproduced exactly at all points between the samples as well as at the samples themselves. Thus, the resampling process consists of:

(1) Reconstruction of the continuum function in two dimensions from neighboring samples.

(2) Resampling the reconstructed continuum at the desired points to produce a new image.

It is generally too expensive and time consuming to compute the site in an image corresponding to each pixel in the resampled image. Because systematic distortions generally change slowly over an image, a control grid can be established for the resampled image in which the distortion is measured about every 50 pixels. Resampling sites for pixels that do not coincide with control points are formed by interpolation from neighboring points (see Fig. B-5).

The optimum function with which to reconstruct the continuum is sinc x, as indicated in Eq. (B-4). However, this function decays slowly; we have found that as many as ±19 samples (in one dimension only) are required for adequate reconstruction. Figure B-4 shows the modulation transfer function (MTF) for an impulse located at the origin in an image that has been resampled at $x = 0.5$, $y = 0.5$ using summation limits of $\pm\infty$, ±19, and ±5. The MTF is the modulus of the Fourier transform of the response of a system to an impulse (the point-spread function, PSF). Thus, the MTF can be described as the function whose amplitude is given by Eq. (B-5).

$$amp_f = \left(R_f^2 + I_f^2\right)^{1/2} \qquad \text{(B-5)}$$

where amp is the amplitude at frequency f, and R and I are the real and imaginary parts of the transform.

Clearly, amplitude at higher spatial frequencies in the MTF of the resampled picture decreases as the summation limits are decreased. At limits of ±5, this technique yields results comparable to bilinear interpolation.

Rifman (Ref. B-3) and Simón (Ref. B-4) have experimented with various functions to use in place of the sinc function in Eq. (B-4). These functions do not require as large summation limits as the sinc function, but their MTFs retain a high amplitude at frequencies less than $\omega_0 = \pi/\Delta x$ (the Nyquist frequency). Two of these functions and MTFs of impulses resampled by using them are shown in Fig. B-6. The Fourier transformation and its properties are discussed in Refs. B-5 through B-7.

It is important not to confuse loss of frequency response during resampling with degradation during acquisition of the image. The goal of resampling is to minimize computing time while preserving the original frequency response in the resampled image. Image intensity degradation during resampling is most severe for resampling sites that are far from existing pixels, and negligible for sites close to existing pixels.

Compensation for the spatial-frequency response of the ERTS MSS is accomplished using a different set of programs than those used for resampling because the scene intensity between pixels need not be computed. The spatial-frequency response of the ERTS MSS is controlled primarily by the sampling aperture. Figure B-7 shows the approximate aperture size compared with the x (sample) and y (line) spacings.

A real scene is composed of an infinite number of impulses, or point sources. An image can be considered to be made by the superposition of all impulse response functions (also known as aperture functions or PSFs) obtained from each of the individual impulses in the scene. Thus, we can write:

$$i(x,y) = \iint s(u,v)\, h(x+u,\, y+v)\, du\, dv + noise(x,y) \qquad \text{(B-6)}$$

where $i(x,y)$ is the image in the x,y plane; $s(u,v)$ is the scene in the u,v plane; and $h(x = u,\, y + v)$ is the PSF, centered at x,y.

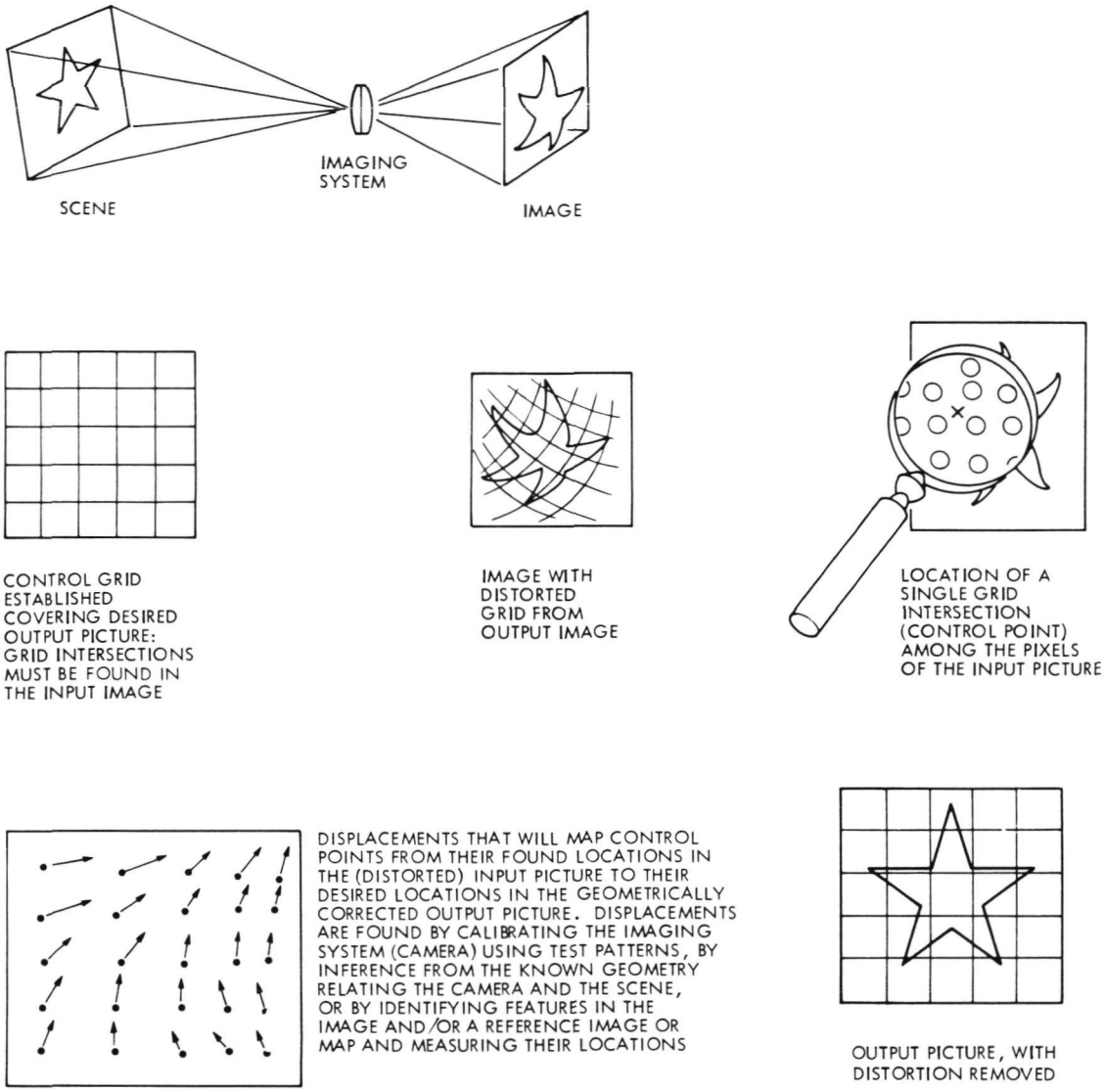

Fig. B-5. Displacements that will map control points from their found locations in the (distorted) input picture to their desired locations in the geometrically corrected output picture

By recognizing the relation between convolution and the Fourier transformation and ignoring the noise term, we can express Eq. (B-5) as:

$$I(x,y) = S(u,v)\, H(x+u,\, y+v) \qquad \text{(B-7)}$$

where I, S, and H are the Fourier transformations of the image, scene, and impulse response, respectively.

By performing this transformation for the aperture shown in Fig. B-7, we have:

$$H_{aperture} = \frac{1}{2a2b} \int_{-a}^{+a} \int_{-b}^{+b} e^{-i2\pi(f_x s + f_y y)}\, dx\, dy$$

where $2a$ and $2b$ are the dimensions of the IFOV in the line and sample directions; x and y are the distances between pixel centers in the line and sample directions; and f_x and f_y are the frequencies at which the first zeros of H occur. This yields, after some manipulations:

$$H_{aperture\ x} = \left[\frac{\sin(2\pi f_x a)}{2\pi f_x a}\right]$$
$$H_{aperture\ y} = \left[\frac{\sin(2\pi f_y b)}{2\pi f_y b}\right] \quad \text{(B-8)}$$

The first zeros of this function occur at $2\pi f_y b = \pi$ and $2\pi f_x a = \pi$. Thus, because $2b \approx 0.9y$ and $2a \approx 1.3x$,

$$f_y = \frac{1}{0.9} = 1.1 \text{ cycles/sample}$$

$$f_x = \frac{1}{1.3} = 0.77 \text{ cycle/sample}$$

The PSF of the imaging system thus can be considered to be a low-pass filter with a spatial-frequency amplitude response as displayed in its MTF in Fig. B-7.

The Fourier transform of the scene is recoverable from an image for which the impulse response is known:

$$S(u,v) = I(x, y)\, H^{-1}(x+u, y+v) \quad \text{(B-9)}$$

where H^{-1} is the inverse of H, provided that H has no zeros in the range of interest.

Frequency response can be restored either by convolution of the image with a filter kernel created from H^{-1}, or by multiplying the transform of the image by H^{-1} (Eq. B-9), and then taking the Fourier transform of the product to yield a corrected image (Fig. B-8). In either case, it is necessary to know the PSF of the MSS. In the absence of ground calibration data, this can be found by examination of the image of an impulse or of a sharp boundary between two homogeneous regions of significantly different brightness. From the Fourier transform of an intensity profile across such a feature, which contains all spatial frequencies in the known proportions, the degradation of response of the MSS, as the spatial frequency approaches the theoretical limit of $\omega_0 = \pi/(2\Delta x)$ (0.5 cycle/pixel), can be calculated. Figure B-9 shows the MTF of MSS band 4 in the scan (sample) and track (line) directions, measured from agricultural fields in the Mojave Desert in California.

Equation (B-9) states that perfect frequency response (at frequencies less than ω_0) can be achieved by transforming the product of the transform of the degraded image (I) and the inverse of the transform of the *PSF* (H^{-1}). However, H typically becomes small at high frequencies, and its inverse becomes large. Figure B-8 shows the effect of using such a function to restore frequency response in an image with "white" noise. The overall signal-to-noise ratio for the corrected image is worse than before because the noise does not decrease in amplitude at high frequencies. To overcome this difficulty, H^{-1} is modified to reduce its amplitude at ω_0. A Wiener filter is one scheme for modifying H^{-1} (Ref. B-8):

$$H_\omega^{-1'} = \frac{OTF_\omega^2 + SN_\omega^{-2}}{OTF_\omega} \quad \text{(B-10)}$$

where *OTF* (optical transfer function) is the Fourier transform of the PSF, *SN* is the signal-to-noise ratio, and ω is the frequency. For additive noise, *SN* decreases with ω; thus, $H^{-1'}$ becomes increasingly smaller than H^{-1} as ω approaches ω_0.

In practice, frequency restoration is performed by convolution because it is expensive to transform large images. The filter kernel (h in Eq. B-6) is the Fourier transform of the modified H^{-1} and can be represented typically by a 15-line by 15-sample matrix of weights. Figure B-10 compares a frequency-restored image made from a CCT to a picture of the same image supplied by EROS.

4. Systematic geometric distortions encountered in MSS imagery. Systematic distortions introduced in ERTS MSS images include skewing and scale distortions.

Skewing is caused by the rotation of the Earth during the 25 s required for ERTS to scan a single frame (185 km on a side). Typically, this skew is about 3°, but varies with latitude as the angle between the tangential component of the rotation of the Earth and the velocity of ERTS changes:

$$\vec{E}'(\phi) = \vec{E}(\phi) - \vec{T}(\phi) \quad \text{(B-11)}$$

where $\vec{E}'(\phi)$ is the velocity of ERTS projected onto the rotating Earth, $\vec{E}(\phi)$ is the velocity of ERTS projected onto an inertial Earth, and $\vec{T}(\phi)$ is the tangential velocity of the Earth at geocentric latitude ϕ (Fig. B-11). Obviously, $|\vec{E}'(\phi)| \neq |\vec{E}(\phi)|$, which is nearly constant [$|\vec{E}(\phi)| \approx 7.4$ km/s]. Because the scale in meters/pixel in the line (track) direction is a function of $|\vec{E}'(\phi)|$, and the scale in the sample direction is a function of the scan mirror velocity and thus independent of $|\vec{E}(\phi)|$ or $|\vec{E}'(\phi)|$, the aspect ratio (ratio of meters per line to meters per sample) also changes as a function of latitude.

An additional complication is introduced because the ERTS MSS acquires six lines at a time. Thus, compensa-

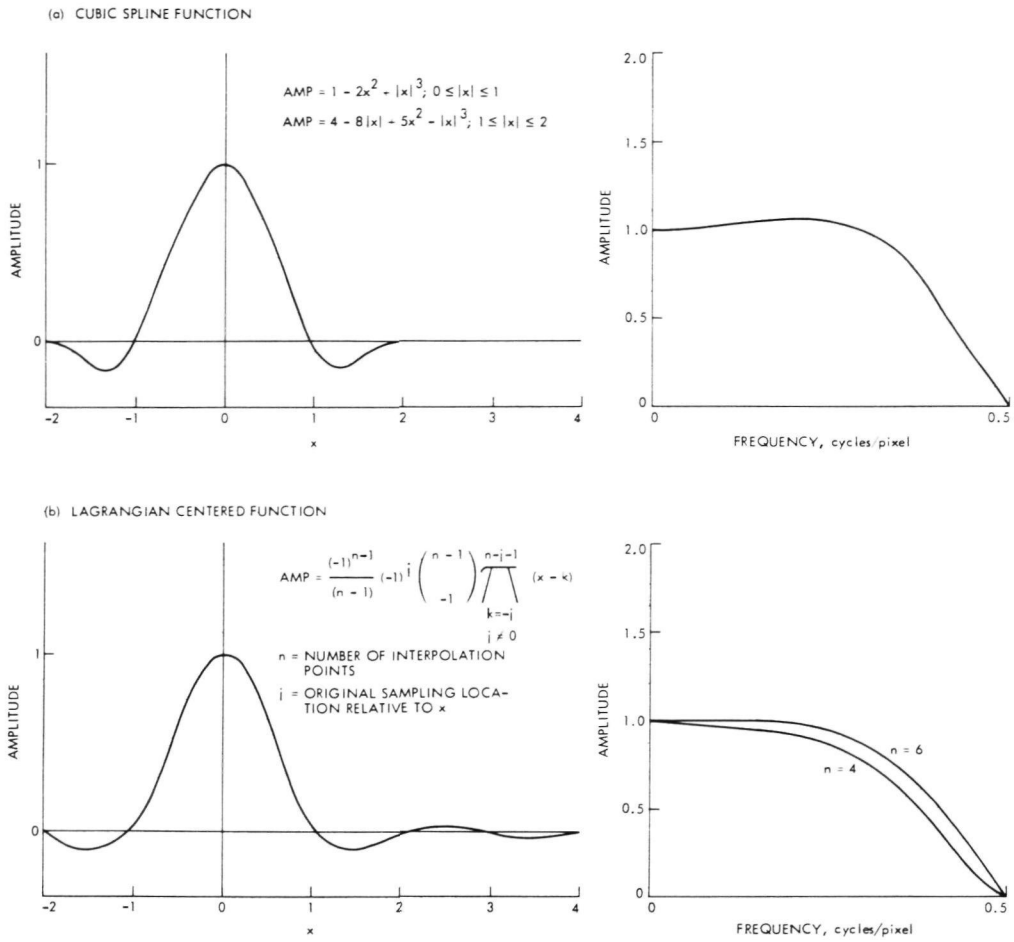

Fig. B-6. Image degradation during resampling. Fourier transformation of an impulse after resampling by convolution with a cubic spline function (see Ref. B-3) and a lagrangian centered function (see Ref. B-4). Resampling site is midway between original samples

tion for skew must not disturb the geometry within these six line groups, or swaths, which is independent of spacecraft position. Samples from successive lines in a single channel are acquired one-twelfth of the dwell time apart; consequently, each line within a six-line swath must be offset to the east by one-twelfth sample (or about 5 m) from the preceding line.

Correction for skewing requires two pieces of information: angle of skew and correct aspect ratio. The correct aspect ratio (A) is found by using Eq. (B-12):

$$A = \frac{\left|\vec{E}'(\phi)\right|/(6p)}{2(a - R_\phi)\tan(\theta/2LLC)} \qquad \text{(B-12)}$$

where p is the scan frequency (13.62 Hz), a is the distance of ERTS from the center of the Earth (7285.82 km), R_ϕ is the distance from the surface of the Earth to the center at the geocentric latitude ϕ, θ is the field of view of the MSS in the cross-track direction (11.56°), and LLC is the number of samples taken per scan (usually about 3220). The value of R_ϕ can be determined in many ways, Eq. (B-13), which assumes the Earth to be an oblate spheroid, is probably sufficient:

$$R_\phi = \frac{R_{0\circ}}{(1 - \epsilon_2^2 \sin^2 R_{0\circ})^{1/2}} + elev \qquad \text{(B-13)}$$

$$\epsilon_2 = \left[\frac{(R_{0\circ})^2 - (R_{90\circ})^2}{(R_{90\circ})^2}\right]^{1/2}$$

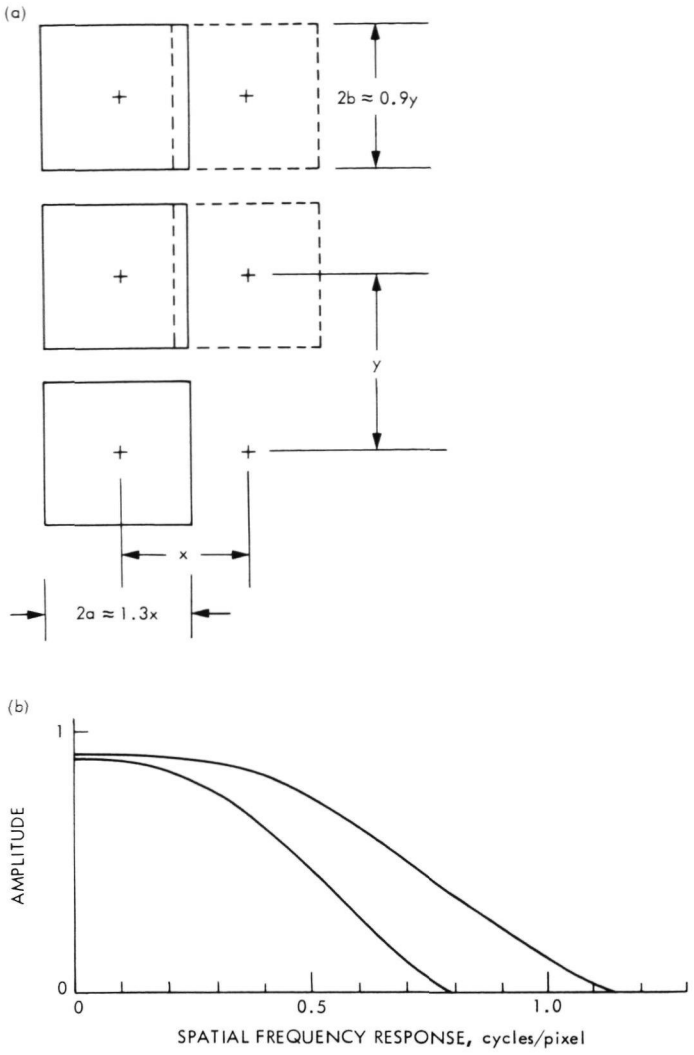

Fig. B-7. Sampling intervals and field of view of the ERTS MSS. (a) x is in the cross-track (scan, or sample) direction; y is in the track (line) direction. Instantaneous field of view at sample i is indicated by solid lines, and at sample i + 1 by dashed lines. Pixel centers are represented by +. Cross sections of optical fibers in the MSS are square. (b) MTF in the line and sample directions is controlled by the sampling aperture

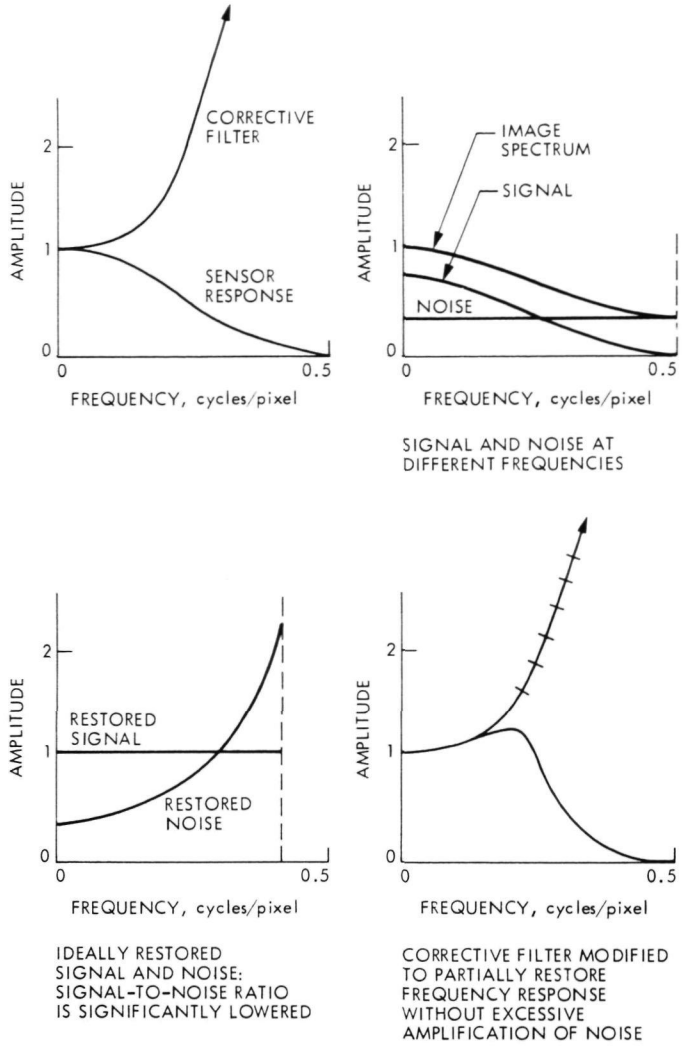

Fig. B-8. Restoration of correct frequency response

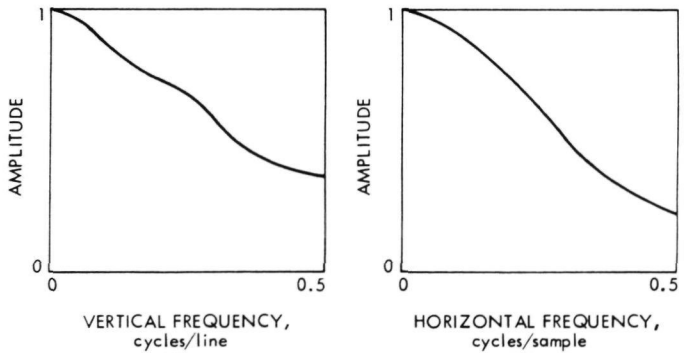

Fig. B-9. Measured frequency response of MSS band 4

Here ϵ_2 is the Earth's second eccentricity and *elev* is an altitude correction that compensates for deviations from the spheroid.

$$\left|\vec{E}'(\phi)\right| = \left[\left|\vec{E}(\phi)\right|^2 + \left|\vec{T}(\phi)\right|^2 - 2\left|\vec{E}(\phi)\right|\left|\vec{T}(\phi)\right|\cos(az_\phi - 90°)\right]^{1/2} \quad \text{(B-14)}$$

where az_ϕ is the azimuth of the projected ERTS velocity $\vec{E}(\phi)$ and ϕ is again the geocentric latitude at the sub-ERTS point. The sub-ERTS point is specified in the ERTS

(a) PORTION OF ERTS 1102-17274, MSS BAND 5, SHOWING THE WILCOX PLAYA (ARIZONA)

(b) SAME SCENE PRODUCED FROM THE CCT

(c) SAME SCENE AS (b) AFTER RESTORATION OF CORRECT FREQUENCY RESPONSE, USING CONVOLUTION FILTERING

Fig. B-10. Frequency-response correction. (a) Fourth-generation picture of the master retained at EROS Data Center. This picture is typical of film products available to the user. (b) Bit errors have been removed in this second-generation picture and the pixel density increased to suppress frequency-response degradation from the film recorder. (c) Pattern revealed after restoration (see lower-left corner) is a new subdivision

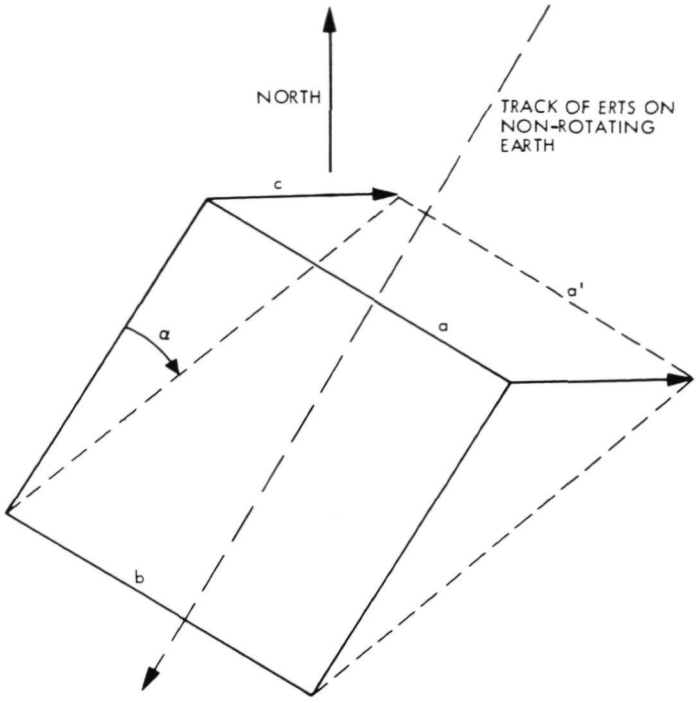

α = FIRST LINE OF IMAGE

b = LAST LINE OF IMAGE, TAKEN 25 s AFTER a. DURING THAT TIME, ROTATION OF EARTH HAS CARRIED THE SCENE RECORDED AT a BY A DISTANCE c EASTWARD TO a'.

α = ANGLE OF SKEW

Fig. B-11a. Skewing of image caused by the Earth's rotation. Change in aspect ratio is caused by component of c in track direction

data by its geographic, or geodetic, latitude (see Fig. B-11b). Geocentric and geodetic latitudes can be related by using Eq. (B-14):

$$\phi = (1-\epsilon_1^2)\tan\phi' \qquad \text{(B-15)}$$

where ϕ' is the geodetic latitude and ϵ_1 is the Earth's first eccentricity:

$$\epsilon_1 = \left[\frac{(R_{0^\circ})^2-(R_{90^\circ})^2}{(R_{0^\circ})^2}\right] \qquad \text{(B-16)}$$

The magnitudes of $\vec{E}(\phi)$ and $\vec{T}(\phi)$ can be found by using Eqs. (B-17) and (B-18):

$$|\vec{T}(\phi)| = \frac{2\pi R_\phi \cos\phi}{SD} \qquad \text{(B-17)}$$

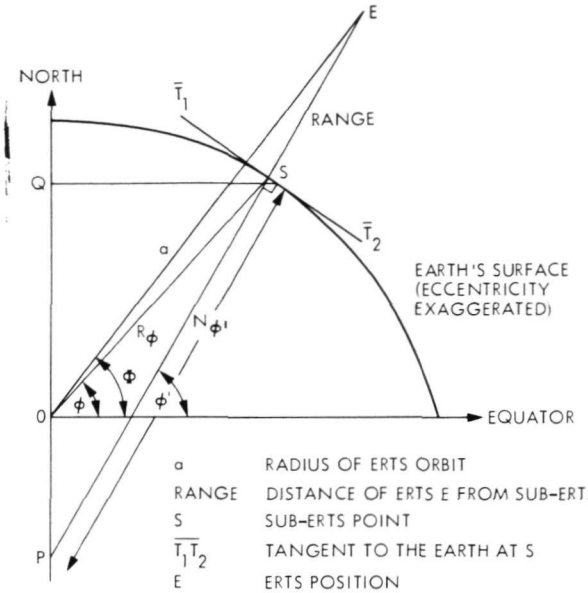

a	RADIUS OF ERTS ORBIT
RANGE	DISTANCE OF ERTS E FROM SUB-ERTS POINT S
S	SUB-ERTS POINT
$\overline{T_1T_2}$	TANGENT TO THE EARTH AT S
E	ERTS POSITION
0	CENTER OF EARTH
P	INTERSECTION OF SURFACE NORMAL WITH POLAR AXIS
ϕ	GEOCENTRIC LATITUDE OF S
ϕ'	GEODETIC LATITUDE OF S
Φ	GEOCENTRIC LATITUDE OF E
R_ϕ	RADIUS OF EARTH AT LATITUDE ϕ (AT S)
$N_{\phi'}$	RADIUS OF CURVATURE NORMAL TO MERIDIAN AT LATITUDE ϕ' (AT S) = $\|PS\|$
ϵ_1	FIRST ECCENTRICITY OF EARTH
$\|OQ\|$	$= R_\phi \sin\phi = N_{\phi'}(1-\epsilon_1^2)\sin\phi'$
	$\epsilon_1^2 = \frac{R_{0^\circ}^2 - R_{90^\circ}^2}{R_{0^\circ}^2}$
$\|QS\|$	$= R_\phi \cos\phi = N_{\phi'}\cos\phi'$

Fig. B-11b. ERTS and Earth geometry

where SD (= 86164 s) is the duration of the sidereal day;

$$|\vec{E}(\phi)| \cong \frac{2\pi R_\phi}{\tau\cos(\phi'-\Phi)} \qquad \text{(B-18)}$$

where τ (= 6216 s) is the period of ERTS and Φ is the geocentric latitude of ERTS. Φ must be computed from ϕ':

$$\Phi = \phi' + \cos^{-1}\left[\frac{a}{N_{\phi'}(1-\epsilon_1^2)\cos^2\phi' - R_\phi\cos\phi\sin\phi}\right] \qquad \text{(B-19)}$$

$$N_{\phi'} = \frac{R_{0\circ}}{\left(1 - \epsilon_1^2 \sin^2 \phi'\right)^{1/2}} \qquad \text{(B-20)}$$

A theorem of Clairaut (Ref. B-9) defines the azimuth of ERTS as:

$$az_{\Phi} = \sin^{-1}\left(\frac{c}{\cos \Phi}\right) \qquad \text{(B-21)}$$

for c = constant = sin i, where i (= 99.114°) is the inclination of the orbit at the ascending node. Equation (B-21) is valid for a circular orbit. The azimuth at the sub-ERTS point of the orbit projected onto the Earth can be found by using Eq. (B-22):

$$az_{\phi} = \tan^{-1}\left[\frac{\tan (az_{\Phi})}{\cos (\phi' - \Phi)}\right] \qquad \text{(B-22)}$$

az must be found to solve Eq. (B-14).

The skew angle (α) can now be found from Eqs. (B-14 and B-17) using the law of sines:

$$\alpha = \sin^{-1} \frac{|\vec{T}(\phi)|}{|\vec{E}'(\phi)|} \sin (az_{\phi} - 90°) \qquad \text{(B-23)}$$

(For a detailed discussion of this problem, see Ref. B-9.)

The actual compensation for skew is generally performed in two steps. The first step (program SKEW) offsets swaths from their neighbors by an integer number of pixels such that, when the correction to the correct aspect ratio is made, the angle between a vertical line in the correct image and the edge of data will be α. SKEW thus uses a nearest neighbor resampling algorithm. The second step may be performed during playback, in which case lines in the picture being created on film are spaced A times farther apart than the samples (see Eq. B-12 and Fig. B-11a). Alternatively, the image output by SKEW can be resampled in the line or sample direction using an interpolation algorithm to normalize the aspect ratio in the image itself. Lines and samples in a picture created from such an image would be the same distance apart. Because some playback devices are not built to handle data with a non-unity aspect ratio, both approaches are useful.

Scale distortions in ERTS MSS data have a variety of causes. Variations in the altitude of ERTS cause changes in its angular velocity, and also changes in the arc of surface subtended by a scan. However, the scale change in the line direction, which is linear with the angular velocity, is not the same as the scale change in the sample (scan) direction because the angular velocity varies with $a^{3/2}$ (Kepler's third law), while the arc subtended by a scan varies. Scale distortions caused by changes in altitude thus result in a different aspect ratio and can be corrected as discussed. However, altitude variations in the orbit of ERTS are slight (5 km out of 914 km) and result in small scale changes only, so altitude generally is ignored as a cause of geometric distortion.

Changes in the ERTS attitude introduce a more significant distortion in the MSS imagery. Nominally, the MSS is aligned with the local zenith (pointed toward the center of the Earth), and the scan mirror oscillates normal to the direction of motion. Yaw is the rotation of the spacecraft about the local zenith vector, and is reported not to exceed ±0.7°. However, only the heading of ERTS is reported with the imagery, and that only to the nearest degree, so the yaw must be inferred from the difference between the reported heading and the computed azimuth. Because of truncation or roundoff errors in the heading, the expected error in the value of the yaw is as large as the yaw itself. The yaw affects imagery as an additional skew, whose magnitude varies from about 25% of the total skew at the equator to 100% at ϕ = ±81°, where $\vec{E}$ and $\vec{T}$ are colinear. The yaw, if identified, can be removed at the same time as the skew distortion.

Pitch, or rotation of the spacecraft in the direction of motion, does not change the distance between swath centers, but only the line dimension of the individual IFOV. This results in some geometric distortion and frequency-response modification, but is not corrected at the IPL.

Roll, or rotation of the spacecraft around $\vec{E}(\phi)$, does introduce some error in the sample direction of the image, which is similar to and removed with the distortion caused by foreshortening at the edges of a scan (see Fig. B-12).

Because the dwell time (integration period for each sample) is independent of the scan mirror deflection, the difference between pixel centers, as well as the IFOV in the sample direction, is a function of the deflection. The ERTS roll effectively adds a constant to that deflection, so that:

$$\Delta x(n) = 0.5 \text{ range} \left\{ \cos\left[(n+1)t_d f\theta/2 + \theta_r\right] - \cos\left[(n-1)t_d f\theta/2 + \theta_r\right] \right\} \quad \text{(B-24)}$$

where Δx is the IFOV in the sample direction at time $t = nt_d f\theta/2$, or at sample n, both measured from zero at the time the scan mirror deflection is zero; a and R_ϕ have already been introduced as the radii of the ERTS-1 orbit and the Earth's surface, t_d is the dwell time of the MSS (9.95 μs), f is the scan mirror oscillation frequency, θ is the total deflection of the scan mirror during an oscillation, and θ_r is the roll of ERTS. The distance of ERTS from the sub-ERTS point can be found using the law of cosines (see Fig. B-11b):

$$range = \left[R_\phi^2 + a^2 - 2R_\phi\, a \cos(\Phi - \phi)\right]^{1/2} \quad \text{(B-25)}$$

Foreshortening causes a scale change of about 0.05% from the center of a scan to the edge, resulting in a cumulative distortion of about 0.62 km, or about 11 pixels. A roll of 1° will increase this to about 1.83 km, or about 32 pixels. Thus, the removal of distortion attributable to foreshortening and roll is important, particularly if the MSS image is to be compared with an image taken at a different time by a different camera. The program GEOM is used to remove foreshortening and roll and is computed using a spheroidal Earth rather than the flat Earth of Eq. (B-24). Control points are established every 25 samples.

Unfortunately, neither the roll nor the pitch of ERTS is reported on the CCTs, and the user must deduce them from the supplied sub-spacecraft and line-of-sight coordinates. While this is possible, precision is limited by the failure to report the yaw.

The attitude of ERTS is corrected periodically. We have observed distortions of about 15 pixels, which we attribute to this cause, in the relative position of identifiable features near the corners of a 7-1/2-min topographic map. Currently, we either do not compensate for attitude correction or compensate for it during image registration by identifying features in two images, or in an image and a map, and forcing their coincidence. Registration is discussed below in more detail.

Systematic geometric distortion is also introduced in the sample scale by irregularities in the scan mirror velocity. Because the mirror oscillates back and forth instead of rotating, it must accelerate and decelerate each scan. Cumulative distortions on the locations of features are as much as eight samples. The scan velocity distortions can be removed at the same time foreshortening is corrected.

Changes in the period of the oscillating scan mirror over a long period of time result in a different number of samples per scan, because the dwell time is constant. When the user receives a CCT, the number of samples has been adjusted to 3240, using the nearest neighbor resampling algorithm. Typical acquired line lengths range from 3216 to 3224; thus, the number of samples per line is increased by an average of 20. This is accomplished by periodically inserting a "synthetic" pixel, which is assigned the DN of its neighbor. The scheme used for line-strength adjustment is clearly identified in Ref. B-1 and is not repeated here. It is important to remove these synthetic pixels and to normalize the sample scale by interpolation if the image is to be compared to any other, as discussed earlier (see Fig. B-3). The sample scale is normalized using program ASPECT at the same time the aspect ratio is adjusted.

5. Scene-dependent geometric distortions. The only scene-dependent distortions encountered in ERTS imagery are introduced by deviations of the shape of the Earth from its model (an oblate spheroid is used at the IPL) and by parallax where there is considerable local topographic relief. A deviation of 10 km in the radius of the Earth from its predicted value results in a change of scale of only 1%; nevertheless, the deviation from the predicted radius is accepted by program SKEW as a user-supplied parameter. Parallax presents a more difficult problem. A feature with a height of 1 km at the edge of an ERTS MSS image will be displaced two samples compared with its location if it has a height of 0 km.

If the same feature is visible in an adjacent image, it will be displaced 2 pixels in the opposite direction (see Fig. B-13); thus, the relative displacement is 4 pixels. This effect hinders temporal comparison of images, because it makes registration of images containing any topographic relief a tedious, time-consuming chore (see Fig. B-3).

Registration of different images of the same scene generally involves locating the same features in both images and resampling one or both images to cause their coincidence. The selection of features is usually done manually, but the precise translation required to cause their coincidence can be found using an automatic cross-correlation program (REGISTER). However, coherent noise, such as the six-line striping present in ERTS imagery, confuses REGISTER and similar programs, so some caution must be exercised in their use.

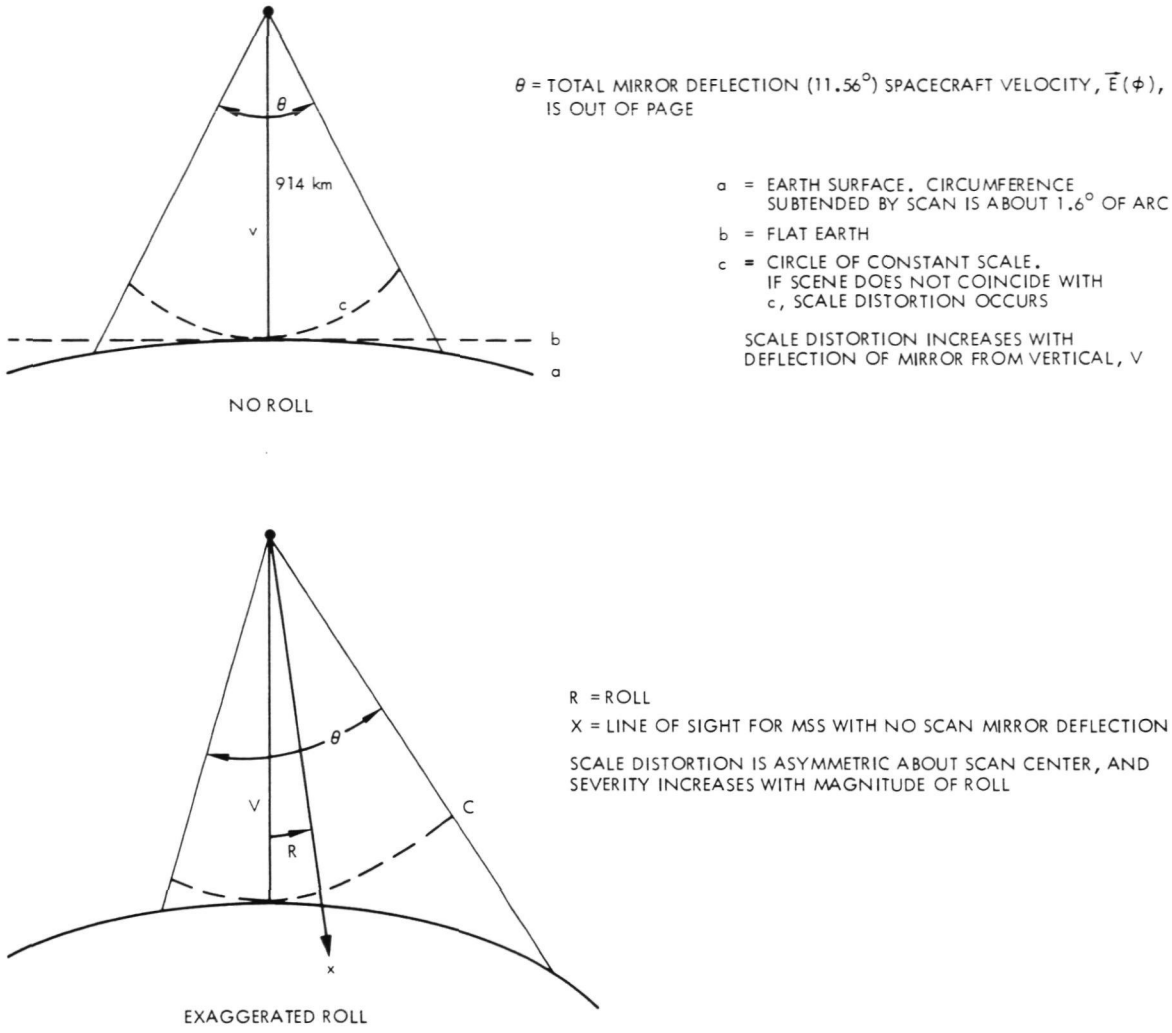

Fig. B-12. Effect of spacecraft roll on MSS viewing geometry

In theory, digital altitude maps (Fig. B-14) could be used to predict distortions caused by parallax as well as to predict various radiometric conditions. However, this remains to be done, at least on a production basis, at the IPL and elsewhere.

B. Radiometric Rectification

The goal of radiometric rectification applied to ERTS imagery is to cause the digitally encoded gray levels (DN) in the image to be a linear representation of the scene brightness. Systematic distortions are introduced by each of the 24 sensors comprising the MSS, and more distortion may occur as optical parts become dirty or as the electronics age. The calibration of the 24 sensors is described in Ref. B-1. Each of the six sensors in a single spectral band has a slightly different spectral response in addition to differences in sensitivity. Coefficients for linear equations were devised to normalize the response of each sensor to the Goddard Space Flight Center (GSFC) illuminating sphere. In flight, the voltage output by each sensor is recorded as the sensor views a linear neutral density wedge which is illuminated by an incandescent tungsten lamp. The gray scale is scanned each 147 ms, and the response of each sensor is used to modify its characteristic linear equation. However, the response to the gray scale (which is included in the calibration data in tapes 1 and 4 of the CCTs) is reported only six times, with redundant measurements at three different densities.

A typical calibration report from a CCT is shown in Fig. B-15. The presence of residual striping in MSS imagery after GSFC's radiometric normalization prompted, in April 1973, an empirical revision of the constants used in the linear corrections. However, the

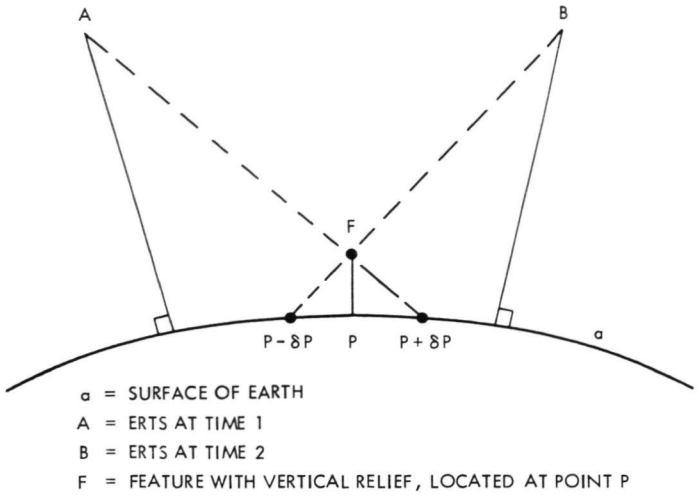

Fig. B-13. Parallax in adjacent ERTS images. Viewed from A, point F has an apparent displacement of δP; viewed from B, the displacement is –δP

continued presence of subtle striping is still annoying to the analyst. This striping becomes more noticeable as the image is adjusted for optimum contrast, and often becomes the most dominant feature after ratioing of channels (Fig. B-16) or classification.

The origin of the striping is difficult to identify, and hence the striping is difficult to remove. Removal of the radiometric rectification imposed by GSFC can be achieved because the coefficients of the linear correction equations are reported in the calibration data. However, the simulated raw picture can have more, or less, or about the same striping as the rectified image. Rectification using second-order polynomials fit to the reported calibration sequence instead of a linear approximation yields in conclusive results. Certainly, some striping can be attributed to truncation, and perhaps some to nonlinearities in the sensor response, but sudden onsets of severe striping within an image suggest a source external to the sensors themselves. If some striping is imposed externally and if it varies with time, then its removal based on the internal calibration data is not possible, and other approaches must be tried.

Before the sensor response can be normalized, it must somehow be characterized. One possible method requires finding a number of large, homogeneous regions of different albedo which will be observed by ERTS in the same frame. If the reflectance spectrum at each site can be monitored on the ground while ERTS is overhead, then satisfactory light-transfer characteristics can be devised. However, the scarcity of suitable sites coupled with the difficulty and expense of simultaneously monitoring their reflectivity reduces the usefulness of this approach.

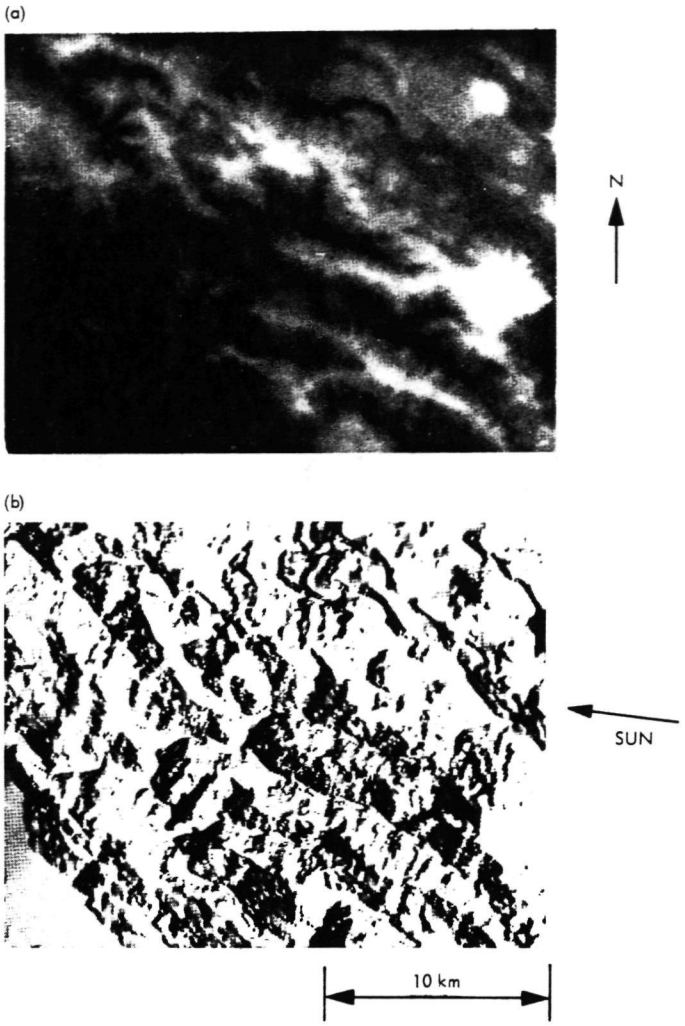

Fig. B-14. (a) Digital topographic map. Elevation ranges from sea level (DN = 0, black) to 1275 m (DN = 255, white) in 5-m increments. (b) Irradiance map. Irradiance for any sun position S can be predicted. The map was created with the sun's azimuth = 97° and elevation = 39°. By varying the sun's position, the analyst can predict optimum lighting conditions for a scene

Locally, each sensor comprising an ERTS spectral channel can look at a different target; however, over a sufficiently large region, each sensor will encounter the same types of scenes in the same proportions. Thus, the probability-density function (PDF) of each sensor from the same channel should be similar. Any differences can be attributed to irregularities in the sensor response. It follows that manipulating the data from each sensor in a way that causes the sensor PDFs to resemble each other will reduce radiometric noise. For instance, the means and standard deviations of the six sensor PDFs for a given MSS

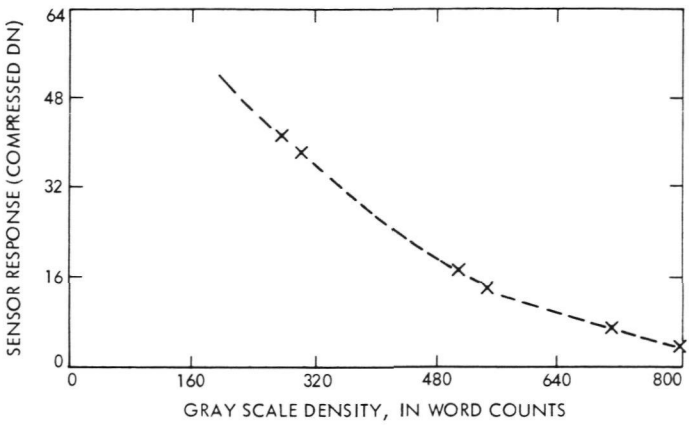

Fig. B-15. In-flight sensor calibration for NASA picture ERTS E-1111-04340, MSS band 4, sensor 1 only. Sensor response is reported in compressed DNs so that the reported DN is proportional to the log of the sensor voltage. If the sensor response were linear to scene radiance, compressed DNs would be linear with gray-scale density. Crosses indicate reported samples (from CCTs)

band can be made to agree by applying a different linear contrast stretch (Eq. B-21) to the data from each sensor:

$$DN'_{ijk} = aDN_{ijk} + b \qquad \text{(B-26)}$$

where DN is the gray level at line i sample j of MSS sensor k, and a and b are empirically determined constants. However, some striping still persists after the means and standard deviations of the PDFs agree.

Assuming that deviations (e.g., skew) of the sensor PDFs from gaussian distributions invalidated the above approach, we attempted to cause agreement by enforcing Eq. (B-27). This equation redistributes gray levels so that the total frequency of occurrence from $DN = 0$ to $DN = N$ is the same (or almost so) for each sensor:

$$\sum_{DN=0}^{N} P(DN,k) = \sum_{DN=0}^{N} P(DN,K_{ref}) \qquad \text{(B-27)}$$

$$\text{for all } N = 0 \leq n \leq 255$$

where P is the frequency of the occurrence in sensor k of a gray level DN.

The persistence of striping after application of the contrast manipulation described by Eq. (B-26) suggests that striping may be attributable, in part, to scene-dependent effects.

1. Scene-dependent radiometric distortions. The scene being imaged by the MSS may introduce distortion in two ways:

(1) Because the spectral responses of the sensors comprising an ERTS band differ slightly, the relative response may be different for a strongly colored (saturated) scene than for a pastel (unsaturated) scene.

(2) ERTS MSS sensors, like most photo sensors, may suffer from hysteresis (Fig. B-17).

The first effect could introduce striping locally, and may not be removed if the scene were treated in aggregate. The second condition exists when the response of a sensor to a stimulus is partly dependent on the recent history of the sensor. For instance, a sensor that has been saturated usually requires a short time to regain the sensitivity it possessed before it was over-stimulated. If the hysteresis of a sensor can be specified, its effects on the radiometry can be removed by convolution filtering; however, the filter kernel will differ for different scene brightnesses.

VICAR application program POLYFLTR applies a convolution filter whose kernel is a function of a parameter of the image being filtered, but because we have not defined the hysteresis characteristic of the ERTS MSS sensors, we have not explored its use.

Efforts to relate MSS radiometry to "ground truth," determined by observers using the portable field reflectance spectrometer (PFRS) in selected study areas while ERTS was overhead, are given in Appendix E and in Section II.

III. Cosmetics

Cosmetic programs attempt to make a picture look better to a human observer, even though the information content of the picture is not increased. The removal of coherent noise is a particularly important application. MSS striping removal belongs in this category, and in fact is the only application of cosmetic programs to ERTS imagery generally required.

Severe striping can be removed after identifying the sensor producing it, usually by careful inspection. Each line produced by the offending sensor can be replaced by interpolation from adjacent lines. In the case of striping so severe that recovery through rectification techniques is hopeless, offending lines can be easily identified by

(a) MSS BAND 5 AS AVAILABLE ON CCT. SOME STRIPING HAS BEEN REMOVED BY GSFC

(b) MSS BAND 5 ENHANCED TO PROVIDE OPTIMUM CONTRAST .

(c) MSS BAND 6 ENHANCED TO PROVIDE OPTIMUM CONTRAST

(d) RATIO PICTURE OF MSS 6/5

Fig. B-16. Residual radiometric striping in NASA picture ERTS E-1072-18001

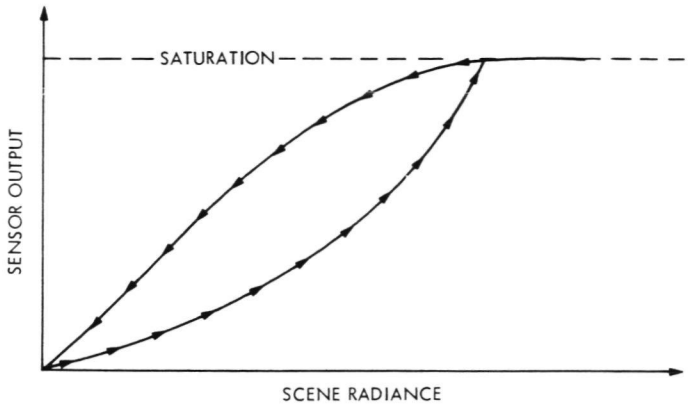

Fig. B-17. Hysteresis. Hysteresis occurs when an instrument response to a stimulus is a function of the recent history of the instrument. Figure shows the sensor response as scene radiance is first increased, then decreased

automated examination of the PDFs. Program ERTSFIX performs automated identification of striping and random bad lines of data, followed by replacement of the offending lines by interpolation.

Subtle striping also can be reduced by unsupervised convolution filtering, typically using a one-line subtractive box filter with from 31 to 301 weights in the sample direction. Such a filter suppresses low-frequency variations in DN, displaying only local departures from average number.[1] By examining only one line at a time, gross brightness differences between lines are reduced.

Striping also can be removed by supervised convolution filtering. The filter is oriented in the vertical (track) direction; the weights are found from the Fourier transformation of a "notch" filter, which is fit to a power spectrum of the image (Fig. B-18). The notches are centered on the frequencies at which noise is observed (0.166, 0.333, and 0.500 cycles/pixel). The shape of the notches is specified to ensure that the product of the filter spectrum and image spectrum shows no noise spikes. Such convolution filters tend to have a large number of weights (about 301), so it is generally economical to rotate both the image and the convolution filter 90° before filtering.

Finally, for small images or sections of images, striping can be removed directly in the Fourier transformation. While automated procedures exist that will identify as noise those spikes having an amplitude greater than ambient by a specifiable amount, it is often more convenient for the analyst to identify noise by inspection. Identified noise in the Fourier transform is replaced by interpolation, and the cleaned image is recreated by a second Fourier transformation.

For a discussion of convolution filtering, the reader is referred to Ref. B-10, and for a discussion of the removal of coherent noise in the spatial domain to Refs. B-11 and B-12.

IV. Analysis

Analysis of ERTS images is a diverse field limited only by the ingenuity and resources of the analyst. Nevertheless, programs created to assist the analyst fall into three categories: (1) statistical procedures, designed to extract information from a single image; (2) comparison procedures, designed to relate or compare different images of the same scene; and (3) classification procedures, designed to interpret a multi-channel image with the analyst's supervision.

A. Statistical Procedures

The analyst can compute and display any statistical measure of image data over any area contained in the image. The most common measure examined is a histogram describing the PDF. The PDF indicates the frequency of occurrence of each brightness level, or DN, over the area examined, and is a necessary input to programs that modify the contrast within an image. The PDF can also be computed for two or more dimensions (channels), but display of the PDF is difficult for more than two channels. One use of a two-dimensional PDF is shown in Fig. B-19 and discussed in Section 5 of this appendix.

The mean and variance or standard deviation of DNs within local regions can be found from the local PDF. By choosing training areas representative of themes the analyst wishes to discriminate in an image, the analyst can estimate the effectiveness of an image or a single channel within a multi-channel image at separating the desired themes.

A common measure of separability between two classes of data is given in Eq. (B-28):

$$d_{ijk} = \omega_{ik}\,\omega_{jk} \left\{ \frac{\left[\mu_{0(ik)} - \mu_{0(jk)}\right]^2}{\mu_{1(ik)} + \mu_{1(jk)}} \right\}^{1/2} \quad \text{(B-28)}$$

[1] The number of weights in the sample direction determines the degree of low-frequency suppression.

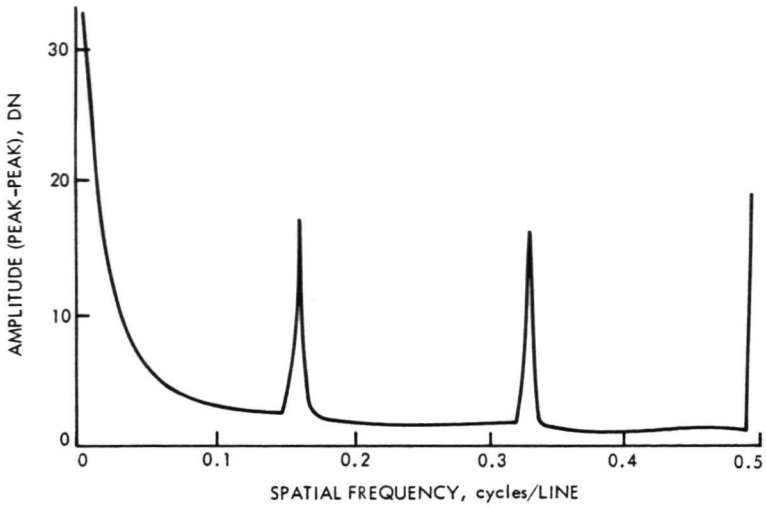

(a) ONE-DIMENSIONAL SPECTRUM OF NASA ERTS 1014-17373 SHOWING RADIOMETRIC STRIPING AT FREQUENCIES 1/6, 1/3, 1/2 cycles PER LINE

(b) ERTS 1014-17373, MSS BAND 4, BEFORE FILTERING TO REMOVE STRIPING (VISIBLE EXPECIALLY IN THE CLOUDS)

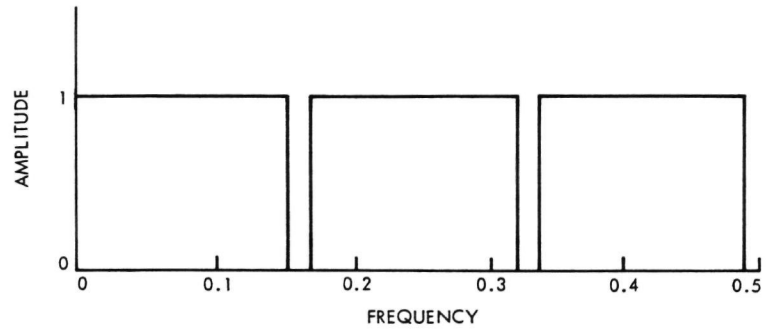

(c) "NOTCH" FILTER DESIGNED TO REMOVE STRIPING MEASURED IN SPECTRUM

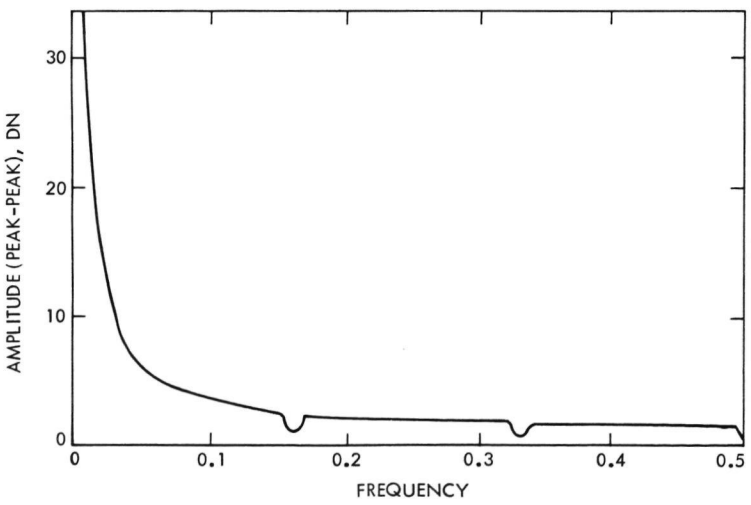

(d) SPECTRUM OF ERTS 1014-17373 AFTER FILTERING. THE FILTER USED (c) WAS TOO STRONG, EFFECTIVELY ADDING LOW-AMPLITUDE STRIPING OF OPPOSITE SENSE TO IMAGE. THIS MAY BE CORRECTED BY ADJUSTING FILTER AMPLITUDE IN THE "NOTCHES"

(e) NASA ERTS 1014-17373 AFTER FILTERING TO SUPPRESS STRIPING

Fig. B-18. Removal of radiometric striping using "notch" filters

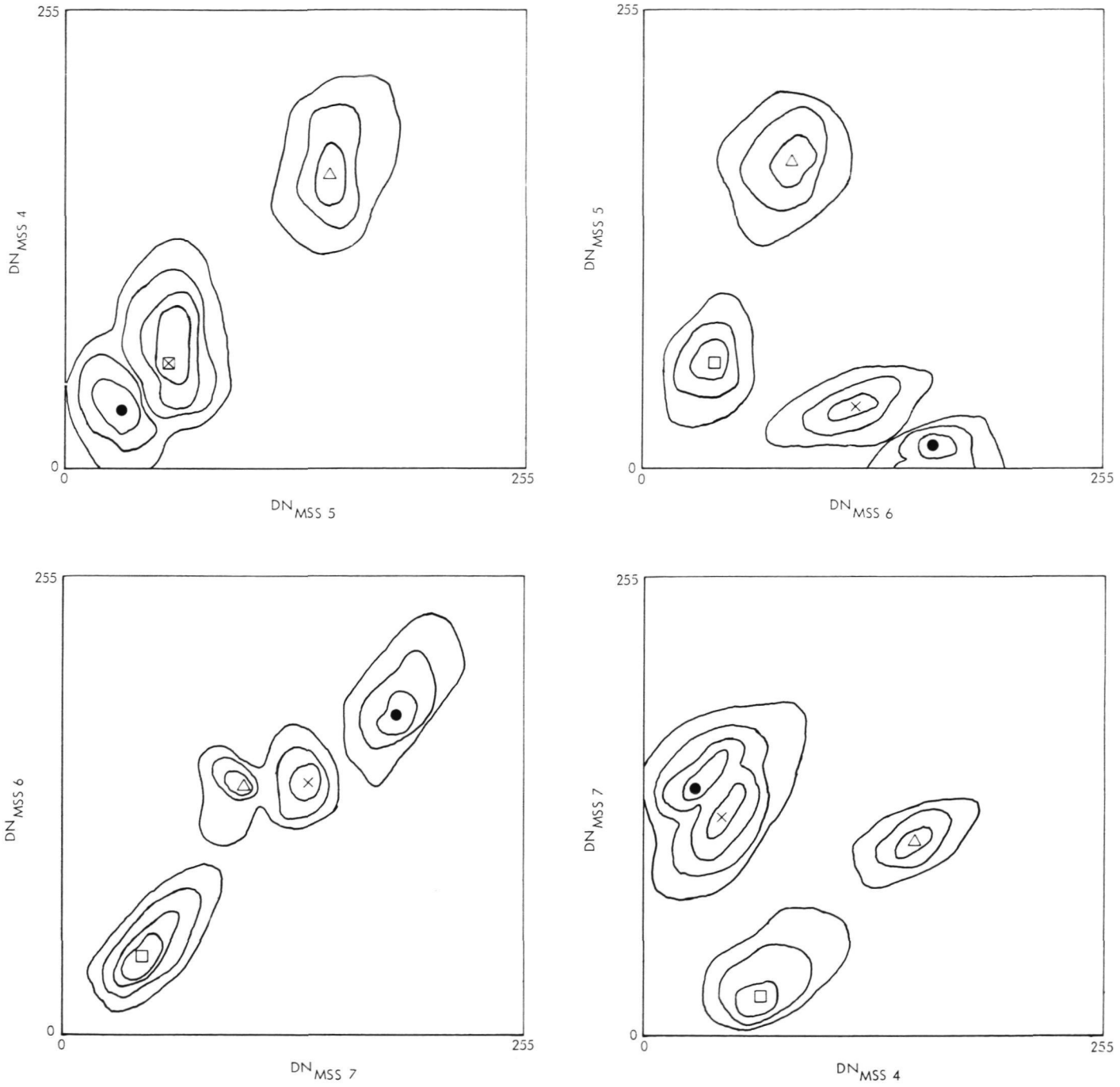

Fig. B-19. Use of "decision" spaces to describe classes of materials. Each decision space is a two-dimensional PDF depicting the frequency of occurrence of DN pairs associated with the four classes of data: alfalfa (solid circle), grass (cross), sand (triangle), and loam (square). Higher-dimension decision spaces are difficult to depict

where d_{ijk} is the distance separating class i from class j in channel k, μ_0 is the mean DN, and μ_1 is the variance within a class.

$\omega(i)$ and $\omega(j)$ are weights that can be assigned to a class, and can be used as a measure of reliability of μ_0 and μ. This technique can be extended to estimate the effective-

ness of a single channel at separating large numbers of themes or classes:

$$D_k = \sum_{i=1}^{n} \sum_{i=1}^{n} d_{ij} \qquad \text{(B-29)}$$

Channels of an image can thus be ranked in effectiveness at separating specified themes by ordering them in terms of D_k, called the divergence.

Equations (B-28) and (B-29) can be extended to measure the distance between data clusters in the n-dimensional space created by a multi-channel image (Ref. B-13):

$$D_k = \sum_{i=1}^{n} \sum_{j=1}^{n} \omega_{ik}\omega_{jk} \left(M_{ik} - M_{jk}\right)^T K^{-1} \left(M_{ik} - M_{jk}\right) \qquad \text{(B-30)}$$

where K is the covariance matrix:

$$K_{ij} = \frac{1}{n}\left[x(i) - \frac{1}{n}\sum_{l=1}^{n} x(l)\right] \times \left[y(j) - \frac{1}{n}\sum_{l=1}^{n} y(l)\right] \qquad \text{(B-31)}$$

and M is the mean vector.

The above techniques form a procedure for selecting those channels necessary and sufficient for image classification (discussed below).

Statistical measures, which are made of many local areas within an image, can themselves be displayed as a picture, thus preserving spatial relationships. Typically, such a picture is created by convolution filtering of an image. Thus, the local mean of perhaps a 3- by 3-pixel area, or "window" can be created using a convolution filter with a 3 by 3 weight matrix in which each weight is equal to 1/9 (a simple low-pass filter). Similar filters can be devised to represent other statistical measures. Two such filters that have been used create a directional gradient picture in which the one component of the gradient of the brightness or intensity of an image is itself represented as a DN, and a "laplacian" picture in which the one- or two-dimensional second derivative is measured at each pixel and displayed as brightness. Other procedures can be used to compute the variance or standard deviation locally and display that measure as a brightness in an image. Pictures such as these last four discussed emphasize scene detail, or "activity." They are dark where there is little high-frequency information on an image, but bright where there is more. Thus, they can be used to help select training areas, for classification of an image, which should be homogeneous (or dark). Conversely, although bright high-activity areas are poor for training areas, they are good control points for cross-correlation programs seeking to register the same region in different images. Results can sometimes be improved by performing the actual cross-correlation using the laplacian picture instead of the original picture.

Filtering techniques, either by convolution or in the spatial frequency domain, can be used to enhance or suppress features with certain spatial frequencies or orientation. However, feature selection in remotely sensed data has proved unsatisfactory to date for geologic applications, largely because real features on Earth are difficult to define carefully. For instance, linear features such as earthquake fault zones, jointing in crystalline rocks, and exposed lithologic boundaries are easily recognized by all beginning photogeologists. However, this recognition is performed by a sophisticated brain which has had years of experience imposing linear structure on scenes and patterns. Detailed inspection shows that the fault is locally not visible; the lithologic boundary is not truly straight. Nevertheless, simple pattern enhancement and recognition has proved useful in some fields, especially in analyses of internal ocean waves in ERTS imagery (Ref. B-14).

B. Image Comparison

Information obtainable from an image can be increased by using more than one spectral channel or monitoring a scene over a period of time.

Detection of temporal changes occurring in a scene is most naturally accomplished by subtracting one image of a scene from another taken at a different time. Figure B-3 is a "difference picture," made between ERTS images of the Coconino Plateau on August 6 and 7, 1972. The bright regions correspond to soil darkened by rain that fell in periods between the times the pictures were taken.

Because the images were acquired from different positions (at latitude 36°N, ERTS passes about 150 km farther west each day), the images had to be carefully registered before comparison. However, especially in mountainous or hilly portions of the scene, residual

misregistration is apparent. The difference in DN between a pixel in one image and a corresponding pixel in the other may range from −255 to +255; usually, however, this value is close to zero unless some change in the scene has occurred. Thus, encoded DN differences must be rescaled so that all data lie within the permitted range of 0 to 255 DN, and there must be sufficient contrast for the analyst to see changes in the picture. This is accomplished by a linear contrast stretch, so that:

$$DN'_{ij} = a\left[DN_{1(ij)} - DN_{2(ij)}\right] + b \qquad \text{(B-32)}$$

where DN_1, DN_2, and DN' are brightnesses at pixel (i,j) in the input pictures (1,2) and the difference picture, and a and b are constants determined empirically from the PDF of a sample difference picture, or predicted. Typical values of a and b are 2 and 128, respectively, so that "no change" is represented as midscale gray $DN = 128$), and differences of ±64 DN are saturated white and black.

Multi-spectral comparisons usually involve image ratioing techniques rather than image differencing, because one goal is to exaggerate color differences (deviations from gray) at the expense of albedo information. The DN difference of the same feature in green light and in red light at noon and at 4:00 p. m. reflects the change in illumination intensity, even though the color has not changed. However, if light scattered from the sky is ignored (i.e., illumination color), the ratio between the DN in red and in green does not change. Articles documenting the development of this procedure are listed in Section III of this report.

The algorithm used to construct a "ratio picture" is similar to Eq. (B-32):

$$DN'_{ij} = a\left[\frac{DN_{1(ij)}}{DN_{2(ij)}}\right] + b \qquad \text{(B-33)}$$

The coefficients a and b are required to scale the ratio information, which can range from 0 to ∞, to 256 gray levels for storage. Despite the great potential range available, ratio values that occur in comparisons of ERTS MSS bands generally fall between 0.25 and 4.0. The coefficients a and b are determined empirically from the PDF of a sample of the image to be ratioed, just as they were for temporal comparisons. They are chosen to maximize the contrast while centering the PDF on mid-gray ($DN = 128$). A typical value for a is about 400 and for b is −300, but these vary considerably with different scenes and spectral bands.

Ratio pictures are extraordinarily useful in geologic applications, because they exaggerate subtle color differences in a scene, and many geologic problems require the distinction between rock types which may appear to be quite similar. However, ratioing suppresses the ability of the analyst to discriminate between rocks with strikingly different albedos, but similar reflectance spectra (for instance, between dark basalts and bright marls; see Section VI).

Ratio techniques also enhance random noise, or coherent noise that is not correlated in different bands. Thus, even subtle striping, which may not be noticeable or objectionable in a contrast-enhanced single-channel image, may become severe (Fig. B-20).

Atmospheric effects may also become visible in ratio pictures, because diffuse light scattered onto a scene is strongly colored blue. As the incident angle of direct solar illumination decreases, the blue light scattered onto the scene assumes a larger share of the total illumination. To a sensor viewing this scene, the effect is that the color of the scene is partly a function of topography. Because the scattered light from the sky can be predicted (as a function of altitude and aerosol content; see Refs. B-15, B-16, and Section VI) and because it does not change too significantly over an ERTS MSS scene, it can be removed by modifying Eq. (B-33):

$$DN'_{ij} = a\left[\frac{DN_{1(ij)} - atm_1}{DN_{2(ij)} - atm_2}\right] + b \qquad \text{(B-34)}$$

where atm_1 and atm_2 are the DNs that the MSS sensors would record if the scene were illuminated only by light scattered from the sky. These quantities can be estimated by examination of dark, gray features shaded from the sun by large clouds (see Section II). In some cases, removal of atmospheric scattering does increase contrast between features, but the signal-to-noise ratio is decreased.

Contrast between features in ratio pictures is greater if the ratio of DNs is larger than unity than if it less. To illustrate this, assume that there is a scene with two features viewed in two channels, A and B (see tabulation below). Feature 2 is colored; feature 1 is gray. The separation between features 1 and 2 in ratio picture A:B is 0.5, but between the same features in ratio picture B:A it is 1.0, twice as great.

	DN(1)	DN(2)
Channel A	100	50
Channel B	100	100
Ratio A:B	1.0	0.5
Ratio B:A	1.0	2.0

The characteristics of the ratio picture are explicitly stated in Eqs. (B-35) through (B-37), where x and y are DNs of the input pictures.

$$R = x/y \tag{B-35}$$

$$R/x = 1/y \tag{B-36}$$

$$R/y = -x/y^2 \tag{B-37}$$

There is less contrast between features if the DN of the numerator picture is smaller than the DN of the denominator picture, as demonstrated in Eq. (B-35). Another way of looking at this is that for half of the possible combinations of x and y, $x < y$. Yet for $x < y$, $0 \leq R < 1$, while for $x > y$, $1 < R \leq \infty$.

This situation can be modified by examining the logarithm of the ratio picture:

$$R = a \ln(x/y) + b \tag{B-38}$$

$$\partial R/\partial x = a/x \tag{B-39}$$

$$\partial R/\partial y = -a/y \tag{B-40}$$

Thus, equal changes in the DN of the numerator and the denominator pictures result in equal changes in the log ratio picture. If the analyst must examine images with features of different colors, so that the numerator picture is brighter in one instance and the denominator picture in another, the log ratio may be preferable to the ratio picture because the average contrast between features will be greater.

All image comparison algorithms discussed above can be executed with the single program RATIO, which utilizes a 256- by 256-byte lookup table to perform the actual arithmetic. The use of a lookup table considerably decreases the execution time for large images.

Image differencing can be considered as a matrix operation. Thus, Eq. (B-32) can be rewritten as:

$$DN' = a\,(1\ \ -1)\begin{pmatrix} DN_1 \\ DN_2 \end{pmatrix} + b \tag{B-41}$$

Dimension rotation involves a similar matrix operator:

$$\begin{pmatrix} DN_3 \\ DN_4 \end{pmatrix} = a \begin{pmatrix} \cos\theta & \sin\theta \\ -\sin\theta & \cos\theta \end{pmatrix} \begin{pmatrix} DN_1 \\ DN_2 \end{pmatrix} + b \tag{B-42}$$

where DN_1 and DN_2 are input channels, DN_3 and DN_4 are output change channels, θ is the angle of axis rotation, and a and b are required to locate the output DN within the permitted range of 0 to 255. Clearly, Eq. (B-41) is a special case of dimension rotation in which only DN_3 is computed, for an angle of -45°. The angle θ can be chosen to optimize feature separation (see Section III and Ref. B-17). Such an operation can be performed to reduce the number of channels input to a classification program without significantly reducing the information input (Ref. B-18).

C. Image Classification

In recent years considerable effort has been devoted to multivariate analysis, or classification of multi-spectral images.[2] A simple example will help to explain multivariate analysis. Figure B-21 shows the Mojave Desert viewed by the ERTS MSS in bands 4, 5, 6, and 7 (corresponding to green, red, and reflective infrared light).

Agricultural fields in the three bands are dark in green and red light, but bright in infrared. Bare desert soil is gray in all bands, and the alluvial fan and some of the bare rocks are dark in all bands. Thus, crops can be discriminated from bare soil by identifying pixels with low DNs in bands 4 and 5, but high DN in band 7.

Figure B-22 depicts the spectral response of the four materials visible in Fig. B-21 (NASA ERTS picture E-1144-18015): alfalfa, grass, sand, and loam. Figure B-19 shows the locations of these four materials in each of four "decision spaces," each of which displays the correlation of feature DNs in channel pairs. Such a decision space is a two-dimensional PDF.

The two colored materials, alfalfa and grass (whose brightness varies in different spectral bands), occupy different regions of each two-dimensional space. Each of

[2] Some of the discussion of this section is taken from Ref. B-18.

(a) DIFFERENCE

$DN' = 4.90\ (DN_{MSS\ 4} - DN_{MSS\ 5}) - 147.11$

(b) LOG DIFFERENCE

$DN' = 2118.38 \log\ (DN_{MSS\ 4} - DN_{MSS\ 5} + 256.00) - 4959.75$

(c) RATIO (WITH ATMOSPHERIC CORRECTION)

$$DN' = 490.3 \left(\frac{DN_{MSS\ 4} - 27}{DN_{MSS\ 5} - 15} \right) - 245.0$$

(d) LOG RATIO (WITH ATMOSPHERIC CORRECTION)

$$DN' = 451.9 \log \left(\frac{DN_{MSS\ 4} - 27}{DN_{MSS\ 5} - 15} \right) + 251.0$$

Fig. B-20. Comparison pictures of Verde Valley

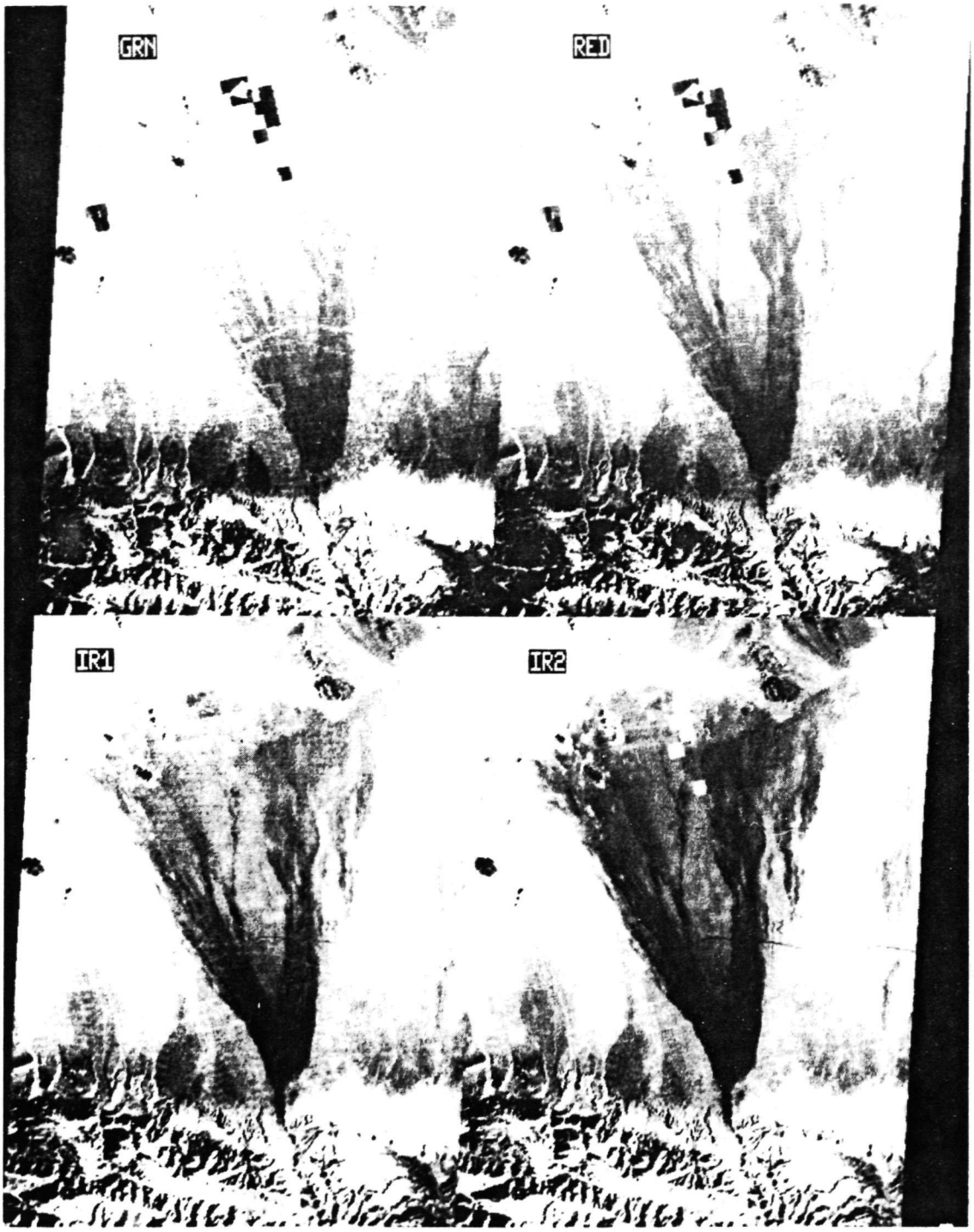

Fig. B-21. Mojave Desert viewed by MSS in four bands on December 14, 1972. GRN = band 4, RED = band 5, IR1 = band 6, and IR2 = band 7 (NASA picture ERTS E-1144-18015)

the four classes of material has a unique spectral signature; that is, each class can be distinguished from the others based on its position in the decision space. It is important to recognize that consideration of a hypothetical fifth class could remove one or more of the original classes from "unique" status. The decision space is not limited to two dimensions; however, a simple graphical representation is not possible for more than three dimensions.

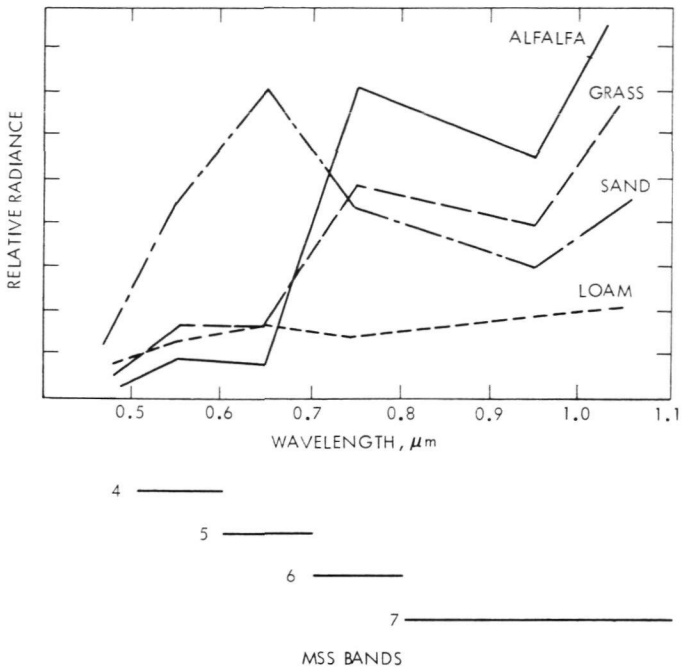

Fig. B-22. Relative radiances of four surface materials viewed by ERTS in the Mojave Desert (see Fig. B-21)

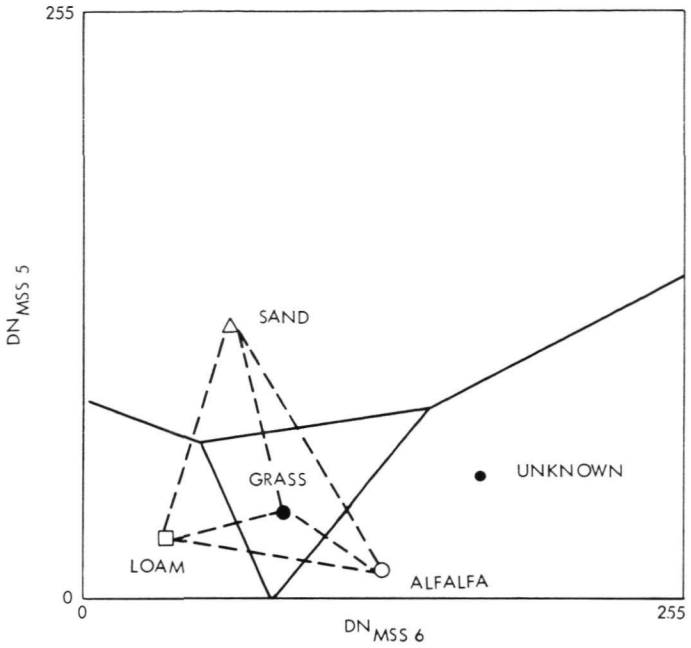

Fig. B-23. Simple decision boundaries. Division of the MSS 5/MSS 6 decision space with equal probability boundaries, assuming equal variances in the four class clusters. Boundaries are thus perpendicular dividers of lines joining cluster pairs. Usually, cluster variances are different, and more elaborate schemes are required

Classification of an image involves partitioning the n-dimensional decision space into zones defined by the positions of the classes specified as significant by the analyst. Each pixel from the image will lie within one zone or another, and thus can be called similar to the pixels used to define that specific class. Figure B-23 illustrates one simple division of a two-dimensional space into four defined zones.

In this case, the centerpoint of each class is determined first. Then the locus of points equidistant from these three centroids is plotted, producing the three line segments as shown.[3] These lines form decision boundaries. In this example, the unknown point would be associated with the class "alfalfa." Many similar schemes for partitioning the decision space have been devised.

Bayesian classification methods are based on the assumption that data for each defined class form a "cluster" in the n-dimensional decision space which acts as a gaussian distribution. Decision boundaries form hyperellipsoids whose dimensions are specified by the analyst as a function of the scatter within the cluster. Typically, the length of the axes of the ellipsoid are from 1 to 2 standard deviations. During classification, each pixel is assigned to the class with the closest cluster center. If the DN $n$tuplet is not enclosed by any decision boundaries, the pixel is classified "unknown."

The demonstrated success of bayesian classification in separating agricultural themes (or classes) attests to the validity of the assumption of gaussian statistics, at least for some situations. However, data clusters in nonagricultural arid regions, largely devoid of vegetation, are not necessarily gaussian, but can and do form a continuum with neighboring clusters. Such clusters may be strongly oriented, with a great amount of scatter in one or more directions. In this case, the analyst may wish to define decision boundaries. Figure B-24 shows a simple scheme in which the boundaries are parallelepipeds in the n-dimensional decision space. This scheme allows rapid classification (by table lookup) and is satisfactory when the various materials cluster far apart. Irregular boundaries can be approximated to a satisfactory degree by grouping a number of parallelepipeds into a single defined class that may more closely match the set of training samples.

At the IPL, bayesian classification is performed by VICAR program BAYES, while parallelepiped classification is performed by FASTCLAS. Because a parallelepiped does not adequately describe a gaussian cluster whose

[3] When more than two dimensions (spectral bands) are used, this locus becomes a surface rather than a line.

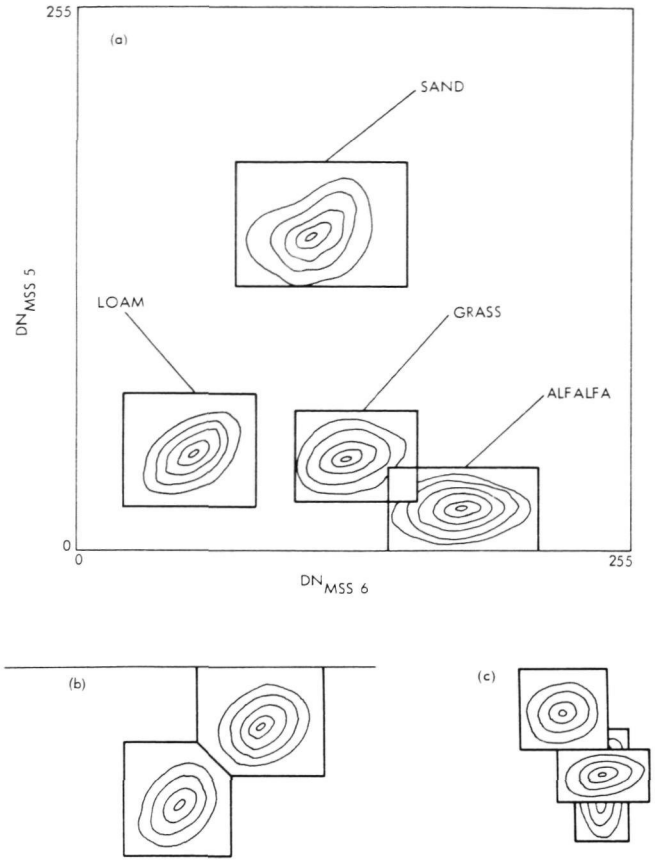

Fig. B-24. Parallelepiped decision boundaries. (a) Division of cluster space by surrounding each center with rectangles whose size is related to variances of each material and the relative importance of making correct decisions about each. (b) Treatment of overlap areas when a decision must be made without using any more dimensions. (c) Buildup of irregular decision space by grouping rectangles

major axis is not aligned with any axis of the decision space, FASTCLAS has a provision to use the bayesian algorithm as required.

Perhaps the most important and difficult task in image classification is not the application of the classification algorithm, but the selection of data classes that adequately delimit and define the themes of interest to the analyst. To be useful, a class must be separable from all others and must be significant to the analyst. For example, it is purposeless to define a class describing a theme called "iron ore deposits" if the spectral response of the iron ore is not distinct from other materials in the image to be classified. There also is no reason to define such a class if no one is interested in locating iron ore deposits in the region under study.

There are three approaches to obtaining data from which decision boundaries can be established. Only one approach is fully developed; that approach requires the analyst to specify areas which, in his opinion, typify the list of themes he has chosen. These are referred to as "training areas." Statistics gathered by examination of the training areas are used to establish the clusters that define a class of information. In an extension of this approach, a "signature bank" may be established which contains statistics defining a very large number of themes. Thus, the analyst can extract the statistics from the "signature bank" rather than from training areas in his image. In a further extension, called "unsupervised" classification, the analyst may allow the computer itself to define themes by inspection and separation of the n-dimensional PDF (decision space) into clusters. Neither of the last two approaches has yet been completely successfully implemented.

Clearly, careless definition of themes or specification of training areas can result in a poorly classified or even misleading thematic map. The thematic map produced by image classification is itself an image. Each theme specified by the analyst is assigned a unique gray level, so that all pixels belonging to the same theme have the same DN.

D. Evaluation and Comparison of Image Enhancement and Classification Techniques

Image enhancement and classification techniques are used to allow the human analyst to see more information in a processed picture than is evident without processing. However, the two approaches are quite different. Enhancement procedures are used to optimize the display of a parameter or parameters implicit or explicit in the image. A user may wish to display the color within a scene; he can ratio images of the scene viewed in different spectral bands, or he can decompose blue, green, and red intensity images to form images describing hue, saturation, and intensity. In either case, he has isolated information describing the color of a scene, in the first case by excluding spatial-intensity variations and in the second case by isolating them. The analyst has now isolated spatial color variations, which he can interpret to create a map of the scene, but the computer has not yet interpreted the image in any way. Before the user allows the computer to classify an image, he must supply an interpretive scheme to the machine. Usually, as described above, this is done by example: the user names training areas that typify classes of materials in the scene in which he is interested. The computer then decides, pixel by pixel, which defined class or training area most closely resembles the local scene. In this manner, an interpretive

map is constructed which describes the scene to the analyst.

Each example has its advantages. Classification allows the analyst to use a large number of channels (currently 12 at JPL) to interpret a scene. These channels may represent disparate parameters such as texture, intensity, and temporal differences, or any scalar field that can be measured (Refs. B-19 through B-21). Using enhancement only, it is difficult to construct a meaningful image relating channels that represent different parameters of a scene. It is also difficult for an analyst to interpret multiple pictures of a scene (Ref. B-22) because it is difficult to remember detail from the first n pictures while examining the $(n + 1)$th picture. Multiple-image display techniques can increase to three (color) or four (color and stereo) the number of enhanced images that can be viewed simultaneously; however, this remains a drawback inherent in enhancement methods.

A classified image is actually a thematic map, which can be interpreted easily by persons who may not be sophisticated photointerpreters. However, the process of classification is inherently exclusive; only the actual decision is available to the viewer, while the large amount of data from which the classification was made is discarded. Consequently, the viewer does not have the necessary information to resolve ambiguities (when a pixel equally resembles more than one defined class) and uncertainties (when a pixel resembles no defined class). In fact, without supplementary images, the user may not even be able to determine when a decision is ambiguous or uncertain. In many disciplines it is sufficient to note that the thematic map constructed has a confidence level of, for example, 2 standard deviations; that is, all pixels classified fell within 2 standard deviations of the centroid of the cluster defining a class. However, this is not always satisfactory.

Classification requires more manipulation of data than does enhancement, and thus can be significantly more expensive. The cost of a bayesian classification is roughly proportional to $mn(n + 1)$, if m is the number of defined classes and n is the number of channels. Enhancement techniques are variable, but tend to be more economical. For example, construction time of a ratio picture is only slightly greater than the time required for the computer to read the two input pictures and write the ratio picture. This time can be from one to two orders of magnitude smaller than the time required to classify an image.

We have found enhancement techniques to be superior in differentiating different lithologic units in three arid regions in Arizona and Nevada. In each area, the geology was well known from conventional mapping.

1. Coconino Plateau. Figure B-25 shows a comparison of a thematic map constructed by bayesian classification with a color display made from three different log ratio pictures; also shown is a geologic map of the same area.

The thematic map accurately depicted the distribution of basalt. Alluvium and units 4 and 4 near Moore Tank (see the stratigraphic column in Fig. IV-C-2) were generally correctly identified. Recognition of the β-1-2-3 unit northeast of Redlands Camp was fair, as it was in the areas north and northwest of Long Point and near Moore Tank. However, unit 6 (Moenkopi Formation) could not be distinguished in the thematic map.

The color ratio picture allows the analyst to distinguish all six units. The best separation was achieved for the Moenkopi Formation and basalt; for these units, the ratio picture is almost as accurate as the geologic map. Recognition of the other four units ranged from good to poor.

2. Verde Valley. Figure B-26 is a comparison of a geologic map of the Verde Valley with a false-color composite picture with enhanced contrast and a thematic map made by image classification.

Two geologic units were accurately depicted in the thematic map: Qg and Ts_2 (see Fig. IV-D-2c for explanation of terms). Although Tvb and pCmsv were generally well distinguished, in the south they were misidentified, primarily because of the vegetation cover and confusion of bedrock-derived alluvium with its source. pCqd and pCgb were correctly identified locally; pzu, Ts_1, and pCg were not recognized at all.

Interpretation of the enhanced false-color picture was successful in identifying Ts_2 and Tvb; these units have high contrast with their surroundings. Ts_1 and pCgb were difficult to distinguish. The other units were correctly identified, at least locally.

3. Goldfield. Figure B-27 is a comparison of a color ratio picture of Goldfield, Nevada, with a thematic map, constructed with no confidence threshold, so that each pixel is assigned to the most similar class. The color-coded legend deciphering the color ratio picture was constructed from the mean DN of the ratio pictures in the frames taken in regions chosen as training areas for the classification map. (The actual classification was performed by VICAR program LARSYS, based upon the bayesian algorithm developed and implemented at the Purdue

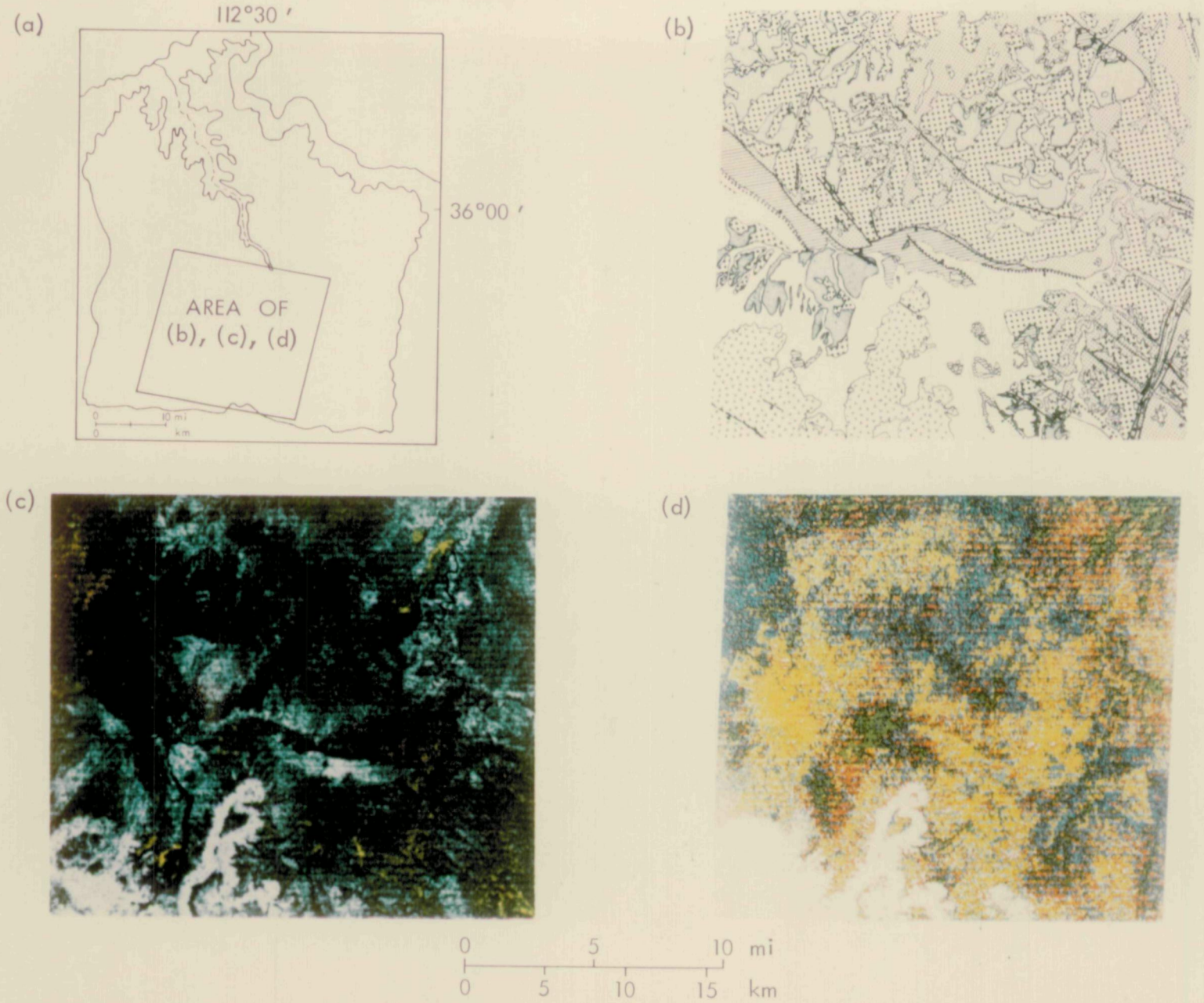

Fig. B-25. Classification vs enhancement for part of the Coconino Plateau. (a) Index map. (b) Geologic map (for explanation of units, see Fig. IV-C-5). (c) False-color composite of ratio pictures. (d) Computer-classified image. Pink = basalt, green = unit 2, orange = alluvium, red = Moenkopi Formation, blue = units 4 and 6

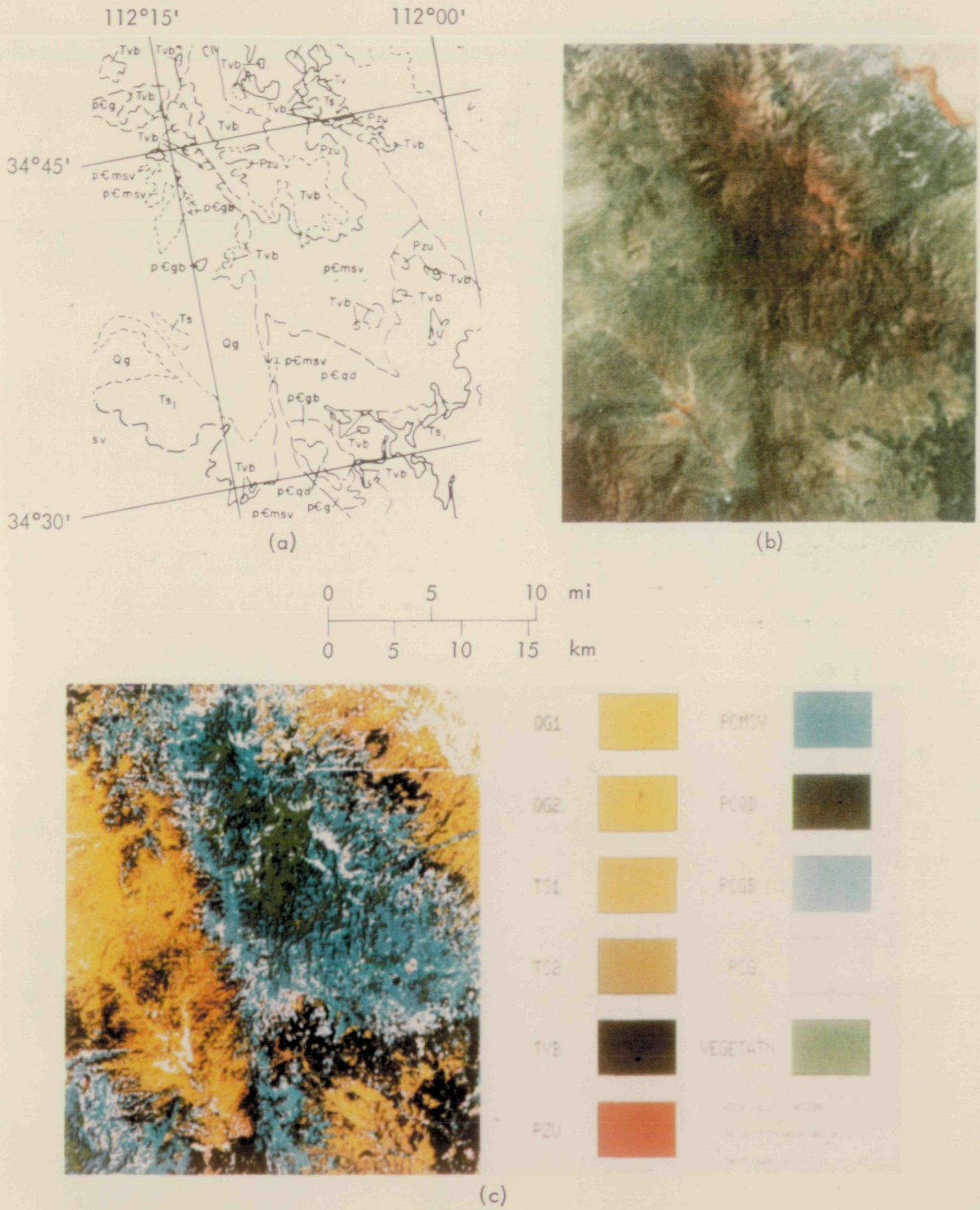

Fig. B-26. Classification vs enhancement for part of the Verde Valley. (a) Geologic map. (b) False-color composite of enhanced ERTS MSS Bands 4, 5, and 7. (c) Computer-classified image

Laboratory of Applied Remote Sensing and available commercially. Subsequent extensive modifications to the algorithm have resulted in the replacement of LARSYS by BAYES at the IPL.)

The color ratio picture and the thematic map were fairly successful in agreeing with the geologic map, with perhaps two interesting exceptions. The thematic map identified a wider range of alluvial deposits and detritus-covered pediments as PLAYA, LT. (green). This is not surprising, because the playas are filled with material derived from neighboring rocks, transported by streams. However, the color ratio picture shows emphatically the wide range of materials classified as ALT. LIM. (altered zone with limonite). In part, the difference between the two versions is illusory. The ratio picture includes ALT. LIM. as one end (brown) of a continuum extending to PLAYA, LT. (orange), and the thematic map depicts only the extremes, using the dissimilar colors red and green. In this case, representation of the entire continuum is appropriate because of the actual similarity of the materials. In other instances, the extra separation in visibility afforded by arbitrary color assignment is warranted. It is interesting that while neither approach unambiguously identifies the rich altered zone at Goldfield and distinguishes it from its surroundings, the color ratio is more successful at this task.

V. Display

Display procedures are designed to present to the human viewer as much information as possible in a convenient useful format. Perhaps among the most useful of these procedures is the family of contrast enhancements, or stretches.

Photographic prints have excellent spatial resolution, but only mediocre density resolution. Transparencies, which can range from complete absorption to complete transmission of light, are somewhat better. They are,

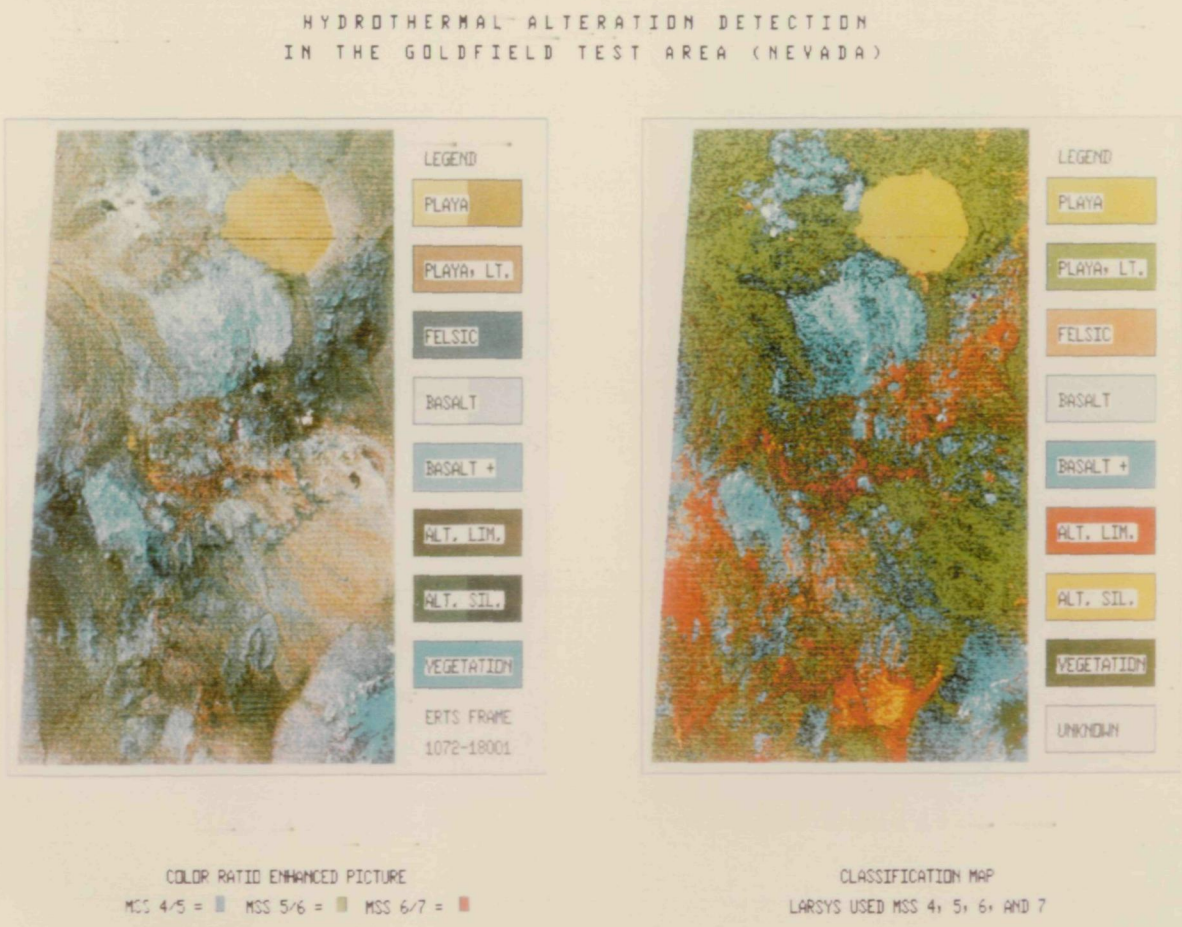

Fig. B-27. Hydrothermal alteration detection in the Goldfield, Nevada, test area

however, limited by the photographic process, which must represent the entire range of brightness (which is infinite) as a finite medium. Only a limited range of brightness can be faithfully represented; this is called the "dynamic range."

A digital image does not suffer from as severe a restriction of dynamic range as the picture. To display the dynamic range of the ERTS MSS in a picture requires 127 recognizable density levels. A densitometer can discriminate between gray levels only 0.02 density units apart, so the density range thus required exceeds the 1.8-unit range typical of recorded digital images.

The second problem that complicates photographic display of digital images is that the human eye is not as discerning as a densitometer. The human may be able to distinguish 15 or 20 discrete gray levels, if adjacent and with sharp boundaries. Thus, in order for a human eye to see subtle variations in brightness contained in a digital image, the contrast must be increased. This is inconvenient to do onboard ERTS, as one sensitivity setting of the photosensors must be able to record the wide range of brightness encountered over the Earth with minimum saturation. The contrast is therefore modified before display, so that gray levels actually are encountered on an image are separated as much as possible in the photographic picture of the image.

Figure B-28 shows a raw picture, and three different versions of it created by applying different contrast stretches. The histograms below each picture depict the PDF of the stretched image.

The linear stretch (Fig. B-28b) is created by mapping each DN encountered in the raw picture (Fig. B-28a), pixel by pixel, to the stretched picture being created using a linear equation.

$$DN'_{ij} = aDN_{ij} + b$$

where i is the line and j the sample of a specific pixel, and a and b are specified coefficients. In practice, coefficients for linear and other stretches are found automatically by algorithms (e.g., ASTRTCH2) that allow a certain amount of saturation at each end of the PDF of the stretched picture.

The gaussian and ramp CDF stretches (Figs. B-28c and B-28d) are performed by distributing gray levels to force the envelope containing the PDF to resemble a gaussian distribution on a ramp. The ramp CDF stretch requires some elaboration. The cumulative distribution function (CDF) is:

$$CDF(n) = \sum_{DN=0}^{n} P(DN) \qquad \text{(B-43)}$$

where P is the probability or frequency of occurrence of a given DN in a picture, and n is a DN within the dynamic range. The CDF of the stretched picture resembles a ramp, or the envelope containing the PDF resembles a line with a positive slope. Ideally, the ramp CDF picture has equal numbers of pixels at each gray level.

Occasionally, an image of a scene with a high brightness range may be encountered, so that any contrast stretch performed will saturate large portions of the original PDF. Spatial filtering to suppress gross changes of brightness over the image while exaggerating local (higher-frequency) changes can be employed to increase the analyst's ability to discriminate detail; however, there is a loss of ability to relate brightness from one locality to another. (Figure III-5 shows a picture filtered in this way.) Usually, filtering is conducted by convolution because it is more economical for large pictures.

Spatial filtering also can be used to display structural features, which are characterized by a certain spatial frequency range and orientation. Figure B-29 shows a region in the relatively featureless Coconino Plateau before and after filtering with a horizontal line filter.

When choosing the appropriate stretch to display an image, the analyst must also consider the peculiarities of the film recorder. Most film recorders, including the video film converter and the Optronics film recorder at the IPL, have transfer functions that map DN linearly to film density. Thus, light transmitted through a transparency is proportional to 10^{DN}. However, the DN in an image is often proportional to scene radiance (this is true of ERTS MSS images), so that the light transmitted through the transparency is really an exponential function of the scene radiance. To linearize this transfer function, the digital image must be stretched so that the DN is proportional to the log of the scene radiance. Other complications can arise from irregularities in the density DN transfer function. This can be corrected by means of a table stretch in which the correct output DN is specified for each input DN.

The film recorder also can act as a low-pass filter when it produces a picture from an image. This can occur if the actual spot or pixel on the picture being created has a

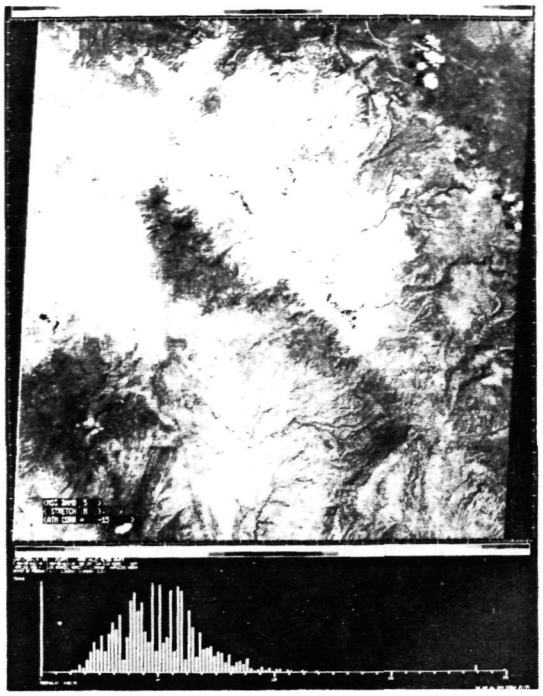

(a) DATA AS CONTAINED ON CCT. EMPIRICAL ATMOSPHERIC SCATTERING CORRECTION HAS BEEN MADE:

DN' = DN-15

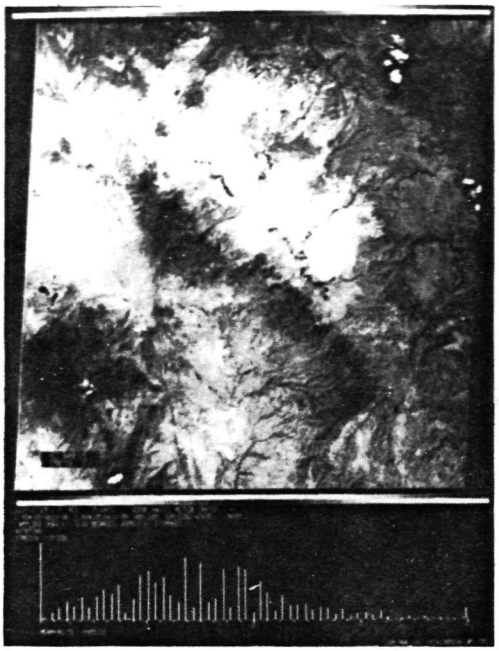

(b) LINEAR CONTRAST STRETCH:

DN' = 2.23 DN - 82.5

(c) GAUSSIAN STRETCH

(d) RAMP CDF STRETCH

Fig. B-28. Contrast stretches. (a) Image as received from EROS with atmospheric correction applied. (b) Linear contrast stretch. (c) Gaussian stretch. (d) Ramp CDF stretch. (NASA picture ERTS E-1337-17325-5)

(a) BEFORE FILTERING

(b) AFTER CONVOLUTION FILTERING USING 1-LINE, 35-SAMPLE WEIGHT MATRIX

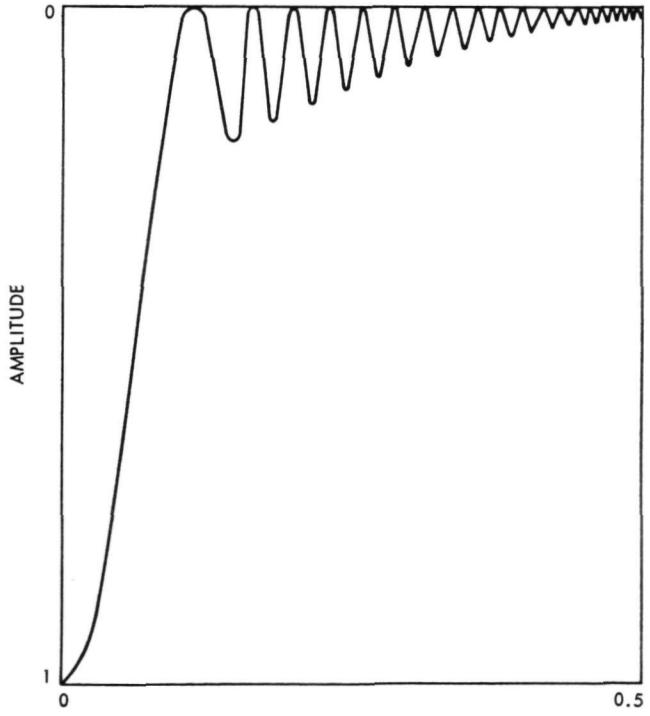

(c) MTF OF FILTER IN BAND 6

Fig. B-29. Box filtering to enhance structural features. (a) Picture before filtering. (b) Picture after convolution filtering. (c) MTF of filter (NASA picture ERTS E-1014-17373-2)

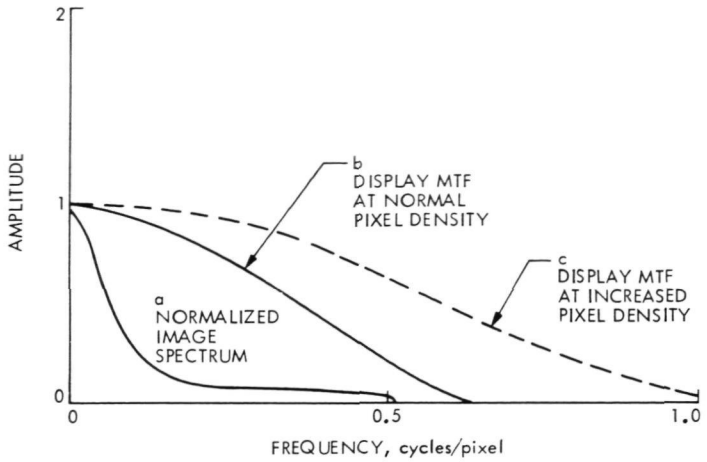

Fig. B-30. Increased pixel density by resampling image. Severity of the low-pass filter is lessened without sacrificing flat-field reproducibility

gaussian cross section, so that the actual density at a pixel center is derived in some part from the density at neighboring pixels. This effect can be lessened by reducing the spot size, but this could have unwanted consequences. In a region of homogeneous brightness (a flat field), individual pixels become increasingly visible, first as ripples in the supposedly uniform surface, as the magnitude of the intensity of the pixels between pixel centers is reduced, and finally as discrete bright points set in a grid. The introduction of such a coherent pattern to the picture is all the more undesirable because the human eye is sensitive to coherent signals (or noise).

One solution is to increase the pixel density in the display picture by resampling the image. This effectively reduces the severity of the low-pass filter without sacrificing flat-field reproducibility (Fig. B-30), but is expensive.

A practical way to increase the amount of information that can be displayed in a single picture is to use color. To convey information, there are three variable parameters in a color picture: hue, saturation, and intensity. The use of color allows the viewer to recognize a greater number of classes of data than does a black and white picture. (The color picture also can incorporate all gray levels.) Because of this advantage, color has been exploited as a tool to optimize the display of single-channel images (Refs. B-23 and B-24). Color display of classified pictures is an example of this technique. Color display is accomplished by the application of three different table stretches to a picture, creating three color component pictures. Each DN or DN range in the input picture can be represented by a unique DN triplet in the three output pictures. Each output picture is then assigned a primary color (blue, green, and red), and a color composite created using an additive color viewer, or a color film recorder. By substituting different image channels for each of the three component pictures, the analyst can create a false-color picture from ERTS imagery which has the same color scheme as conventional infrared color film. However, the user also can use difference or ratio pictures as color component frames. The value of these color display techniques has been illustrated above.

Just as a raw ERTS image makes a flat low-contrast picture in black and white, so does it make a flat low-contrast picture in color. A simple solution is to contrast stretch the component pictures, which must be done carefully. The analyst must create a picture utilizing the full range of available lines. By stretching the component pictures so that their PDFs look similar, this effect can be achieved. However, more precise control is available if the analyst first converts his component blue, green, and red pictures (these need not be acquired in blue, green, or red light) to more suitable dimensions.

Conversion to chromaticity coordinates is straightforward. Let DN_1 = DN of the blue picture, DN_2 the DN of the green picture, and DN_3 the DN of the red picture. We can define three new dimensions, g, r, and intensity (INT), which are related to the acquired DN by Eqs. (B-44) through B-46).

$$INT = DN_1 + DN_2 + DN_3 \tag{B-44}$$

$$g = DN_2/INT \tag{B-45}$$

$$r = DN_3/INT \tag{B-46}$$

g and r (along with $b = DN_1/INT$) are known as tristimulus coordinates (Ref. B-25). A more usable chromaticity space, defined by the Commission Internationale de l'Éclairage (CIE) in 1931 is given by Eqs. (B-47) and (B-48):

$$x = \frac{0.490r + 0.310g + 0.200b}{0.66697r + 1.13240g + 1.20003b} \tag{B-47}$$

$$y = \frac{0.17897r + 0.81240g + 0.01063b}{0.66697r + 1.13240g + 1.20063b} \tag{B-48}$$

INT is the same as in Eq. (B-44).

A chromaticity diagram (see Fig. B-31c) relates all possible display colors (i.e., all hues and saturations) to the

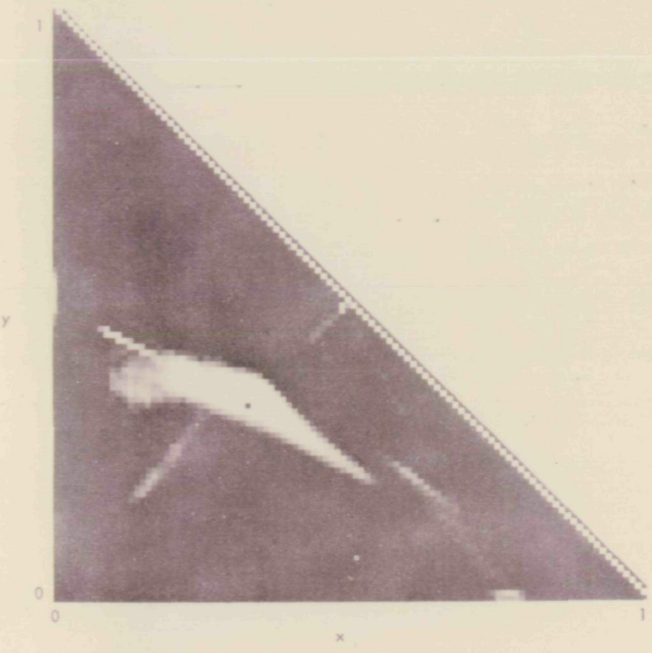

(a) DATA AS STORED ON CCT

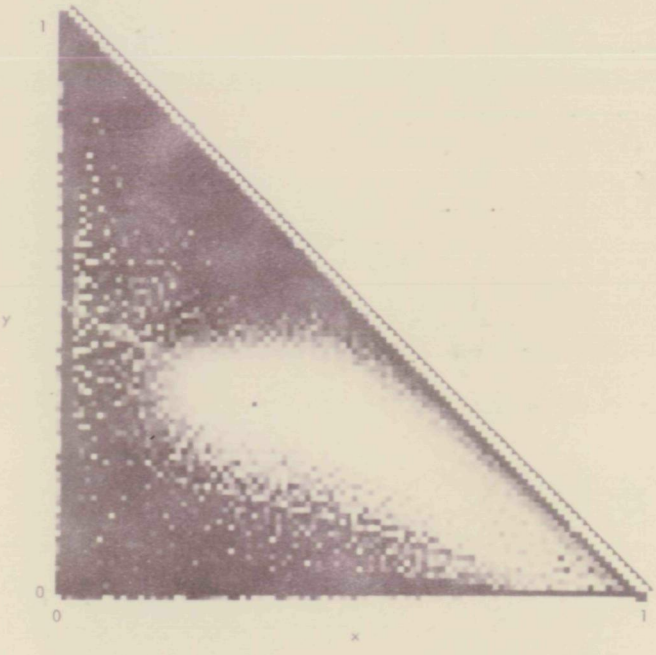

(b) INDIVIDUAL LINEAR STRETCH APPLIED TO EACH CHANNEL

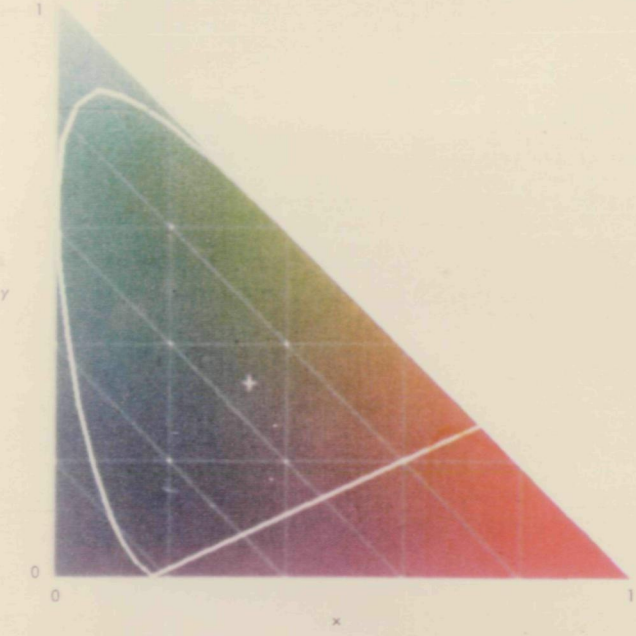

(c) STANDARD CHROMATICITY DIAGRAM. CURVILINEAR LINE DEPICTS CIE COORDINATES CORRESPONDING TO THE VISIBLE SPECTRUM. + IS THE ACHROMATIC (EQUAL ENERGY) POINT

(d) COLOR PICTURE DESCRIBED IN (b) (ERTS E-1242-05054) MSS 4 = BLUE, MSS 5 = GREEN, MSS 7 = RED

Fig. B-31. Chromaticity PDF. The frequency of occurrence of colors in a three-color picture can be described by a two-dimensional PDF

possible x- and y-coordinates (Ref. B-26). Notice that the sum of x and y cannot exceed INT. Figure B-31a and B-31b show relations of the probability density in raw and stretched ERTS data to the x and y coordinates, respectively, for a picture of a scene with a wide range of color. Instead of stretching the blue, green, and red images to create a good color picture, we can stretch x and y pictures to control hue and saturation, and the INT picture to control intensity. Subsequently, the blue, green, and red pictures can be recreated and the color picture made. However, it is also possible to decompose the blue, green, and red images that describe hue (HUE), saturation (SAT), and INT (Fig. B-32).

All DN triplets must lie within one octant of a Cartesian space bounded by the positive DN_1, DN_2, and DN_3 axes. The line on which the three DNs are equal is associated with the color gray and can be called the "achromatic" or "equal-energy" axis. However, DN_1, DN_2, and DN_3 represent intensities, and INT is the scalar sum of DN_1, DN_2, and DN_3. We must rescale the DNs in the blue, green, and red images so that we can consider INT as a vector. Thus, we seek a value k such that

$$INT = \left(k^2 DN_1^2 + k^2 DN_2^2 + k^2 DN_3^2\right)^{1/2} \quad \text{(B-49)}$$

By using the identity of INT (Eq. B-44), we see that

$$k = \frac{DN_1 + DN_2 + DN_3}{\left(DN_1^2 + DN_2^2 + DN_3^2\right)^{1/2}} \quad \text{(B-50)}$$

Our rescaled blue, green, and red DNs are:

$$DN_1' = DN_1 \quad \text{(B-51)}$$

$$DN_2' = DN_2 \quad \text{(B-52)}$$

$$DN_3' = DN_3 \quad \text{(B-53)}$$

We can now define a spherical coordinate system in which the north vector corresponds to the achromatic axis and with an origin that coincides with the origin on the $(DN_1, DN_2, DN_3)'$ space. Let us constrain the new coordinate system so that the projections of the $(DN_1, DN_2, DN_3)'$ axes into the equatorial plane lie at longitudes of $-120°$, $0°$, and $+120°$, respectively. We now define hue as the angle about the polar (achromatic) axis, measured from green $= 0°$; saturation is defined as the co-latitude. The two reference systems are related by two rotations. The first rotates $(DN_1, DN_2, DN_3)'$ 45° about DN_2' so that DN_1' is in the equatorial plane of (HUE, SAT, INT); the second rotates $(DN_1, DN_2, DN_3)''$ by $\cos^{-1}(0.667^{1/2})$ about DN_1'' so that DN_2''' coincides with the achromatic axis. Now HUE and SAT can be defined in terms of DN_1, DN_2, and DN_3. INT has already been defined.

$$HUE = \tan^{-1}(DN_1''/DN_3'') + \tau \quad \text{(B-54)}$$

$$SAT = \cos^{-1}(DN_2'''/INT) \quad \text{(B-55)}$$

Equation (B-54) reduces to

$$HUE = \tan^{-1}\left(\frac{DN_1' - DN_3'}{DN_1' - 2DN_2' + DN_3'}\right) + \pi \quad \text{(B-56)}$$

and Eq. (B-55) reduces to

$$SAT = \cos^{-1}\left(\frac{DN_1' + DN_2' + DN_3'}{3^{1/2}\, INT}\right) \quad \text{(B-57)}$$

Saturation can be represented better as the ratio between the found saturation and the maximum saturation allowed at a given hue, remembering the constraint that all data lie within a single octant of $(DN_1, DN_2, DN_3)'$.

Now a three-channel image can be expressed as three new channels: one describing hue, one saturation, and one the intensity of the original image. By using any available VICAR program, each of these pictures can be manipulated freely as an independent image before reconstruction of a new (DN_1, DN_2, DN_3) image to be used in color construction (Fig. B-33). As an example among the limitless possibilities, saturation can be set to 100%, intensity to 300 DN, and hue can be adjusted with a ramp CDF stretch so that the reconstructed color picture contains only saturated hues in equal amounts at a constant intensity. Alternatively, a picture displaying only vegetation (which is red in the standard false-color scheme) can be modified so that variations in red or the original picture, reflecting subtle changes in vegetation, are stretched to occupy the entire spectrum.

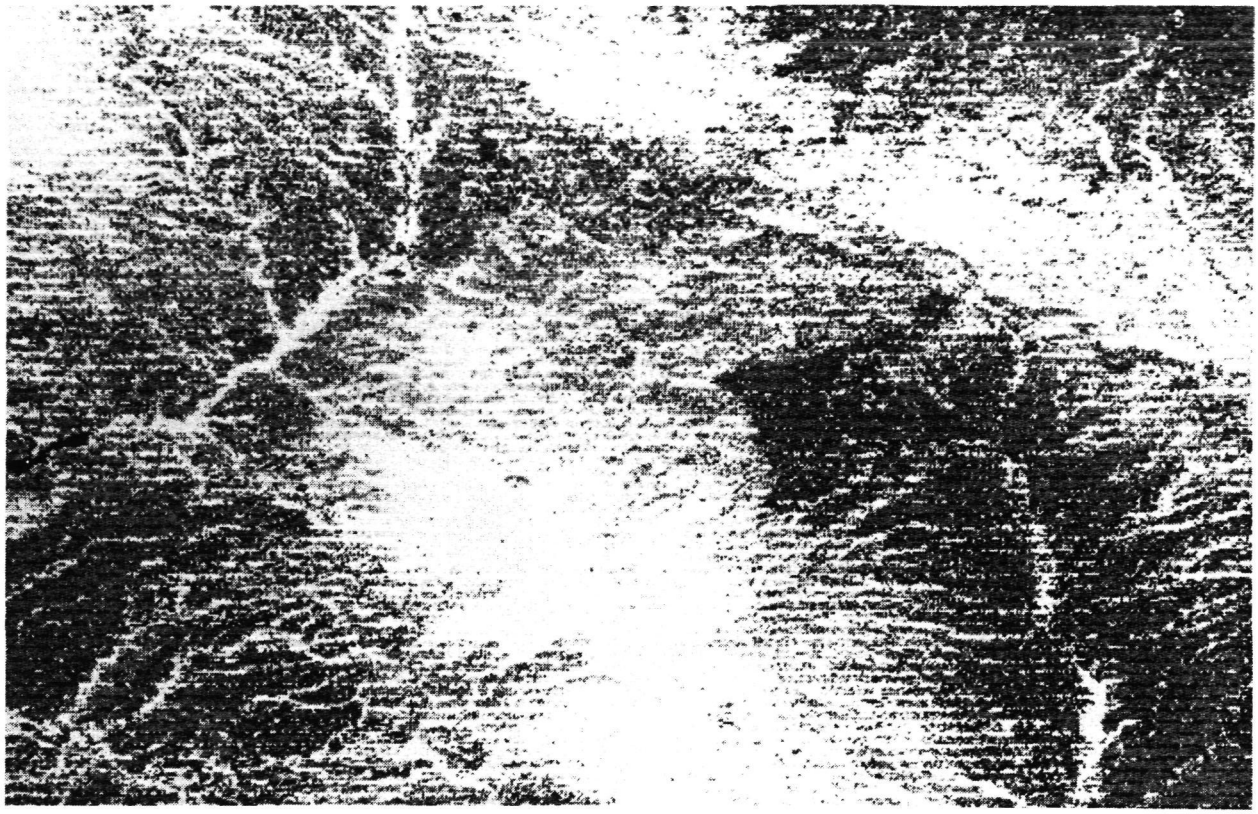

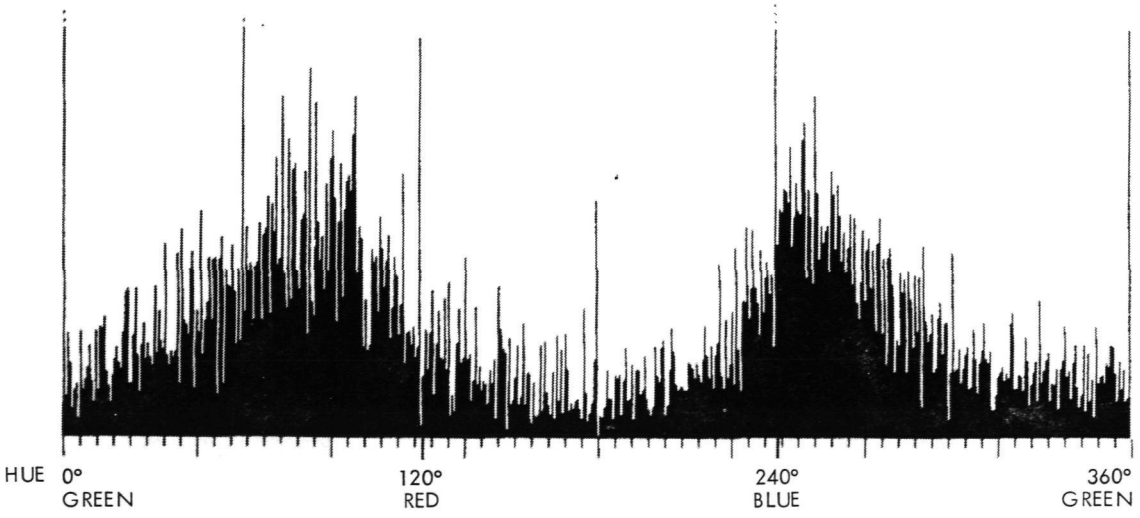

(a) HUE

Fig. B-32. Construction of pictures representing hue, saturation, and intensity from a triplet of ratio pictures (NASA picture ERTS E-1156-17280)

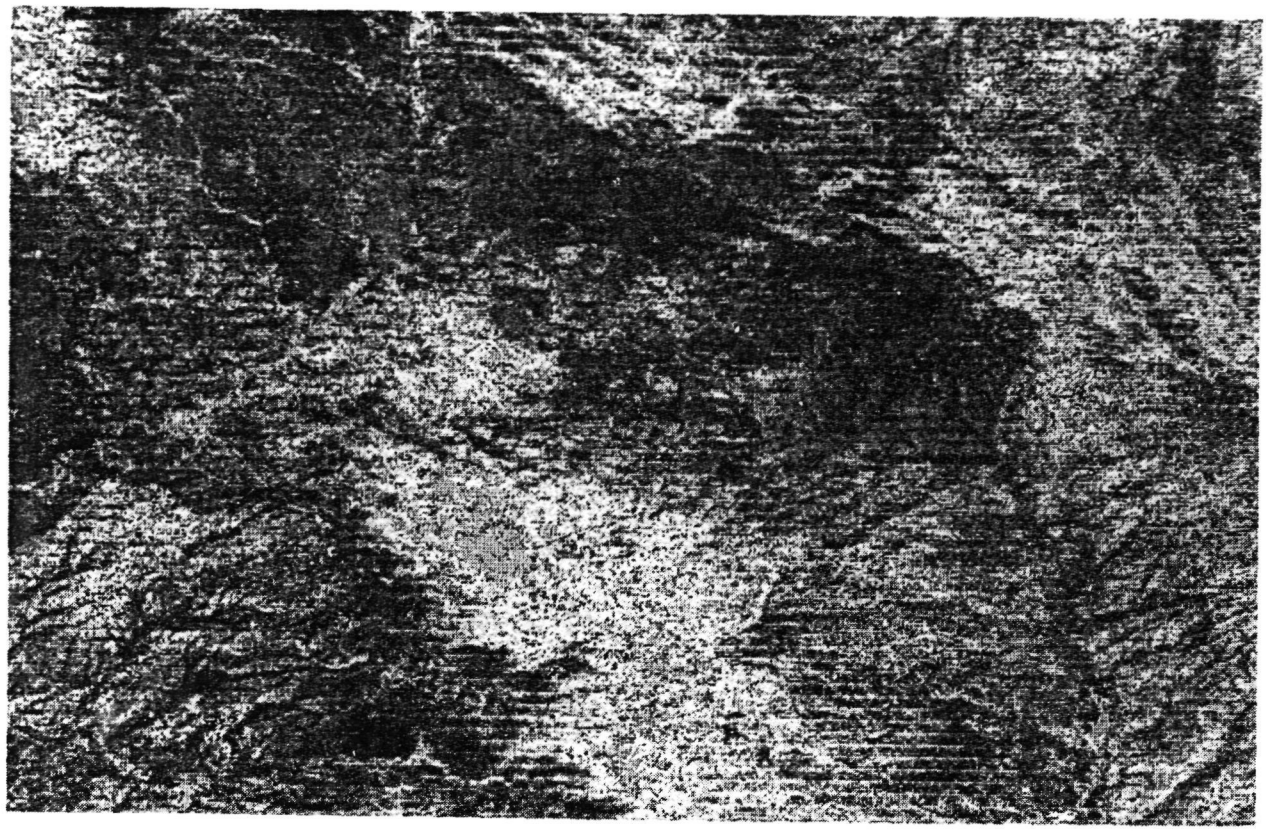

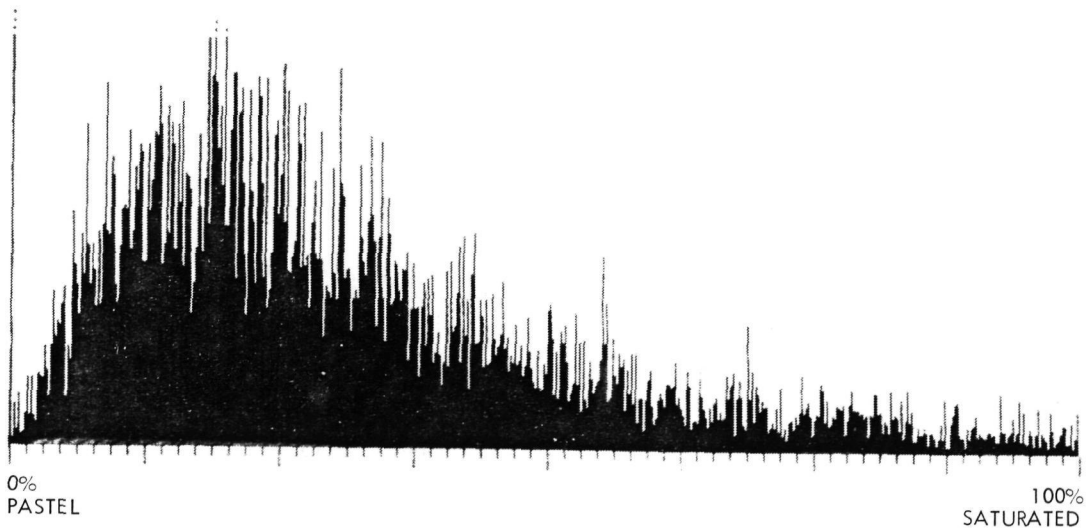

(b) SATURATION

Fig. B-32. (contd)

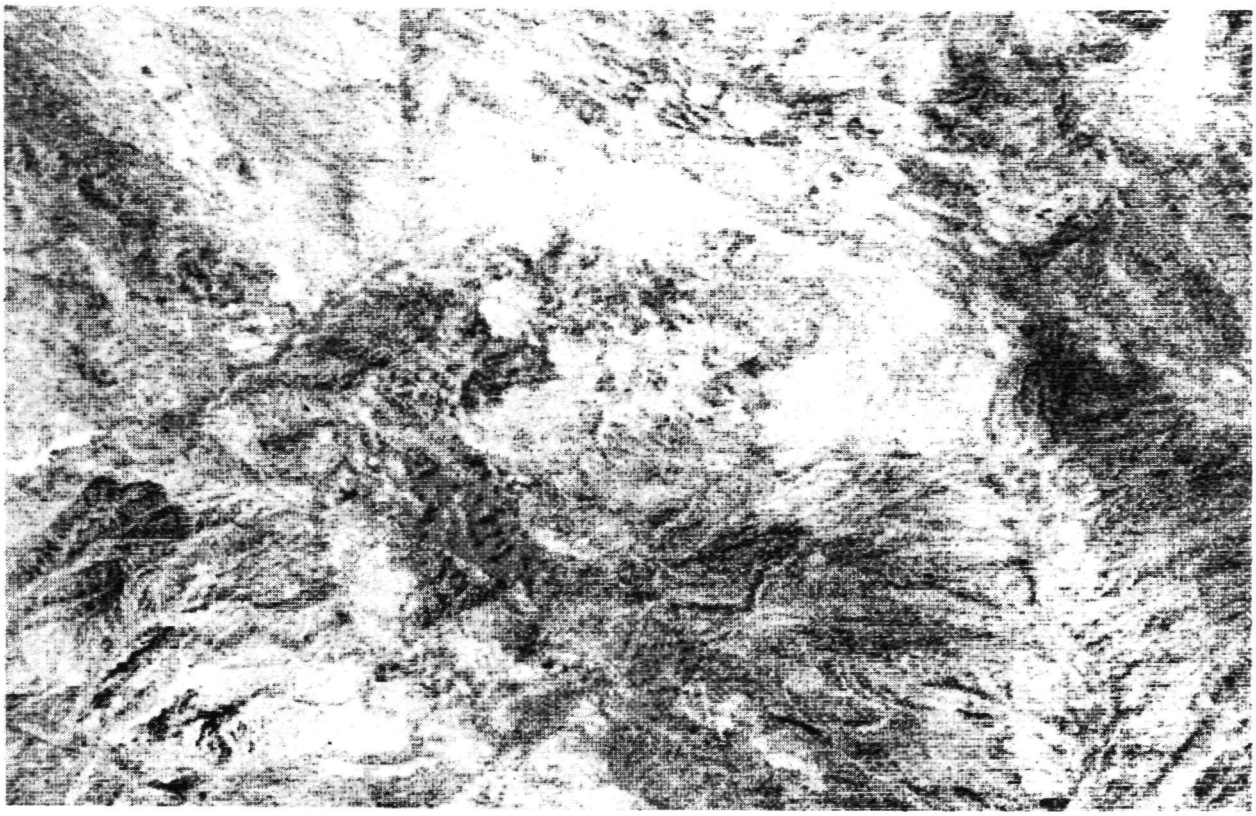

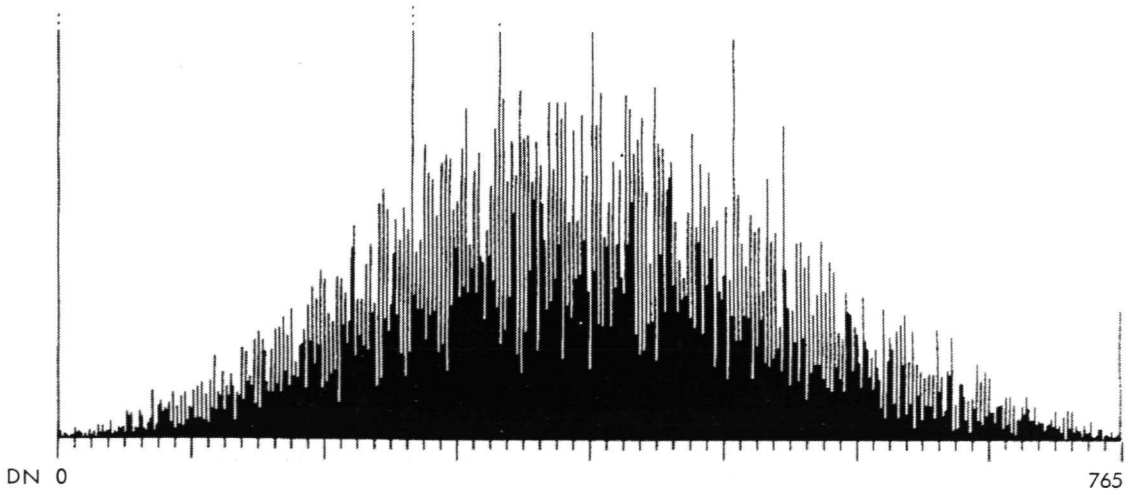

(c) INTENSITY

Fig. B-32. (contd)

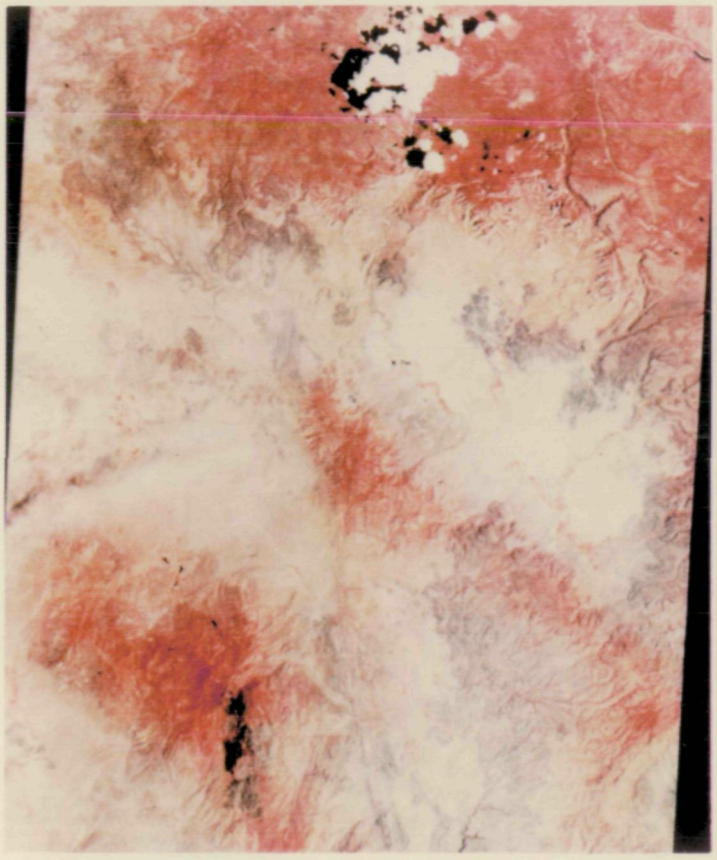

(a) NASA ERTS E-1014-17375

MSS 4 = BLUE
MSS 5 = GREEN
MSS 7 = RED

* COLOR COMPOSITE WAS CREATED FROM CCTs WITHOUT ENHANCEMENT

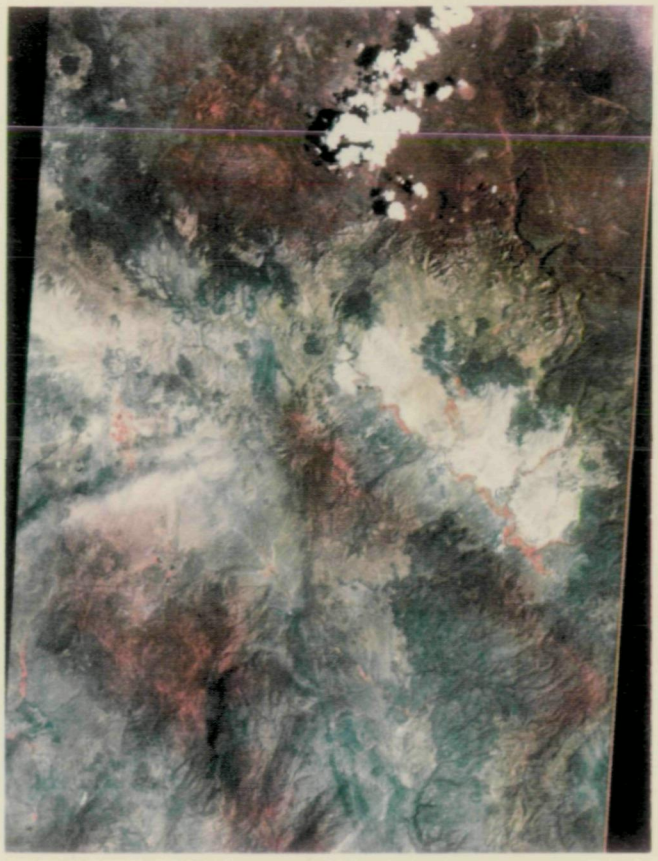

(b) NASA ERTS E-1014-17375
SAME SCENE AS (a) AFTER CONTRAST STRETCH OF EACH INPUT PICTURE:

DN* = 1.6 DN

* HUE IS SIMILAR, BUT INTENSITY AND SATURATION HAVE BEEN INCREASED

Fig. B-33. Color and contrast enhancement

References

B-1. *Earth Resources Technology Satellite Data Users Handbook*, Goddard Space Flight Center, Greenbelt, Md., 1972.

B-2. Norwood, V. T., Fernelia, L. R., and Tadler, G. A., *Final Report, Vol. I., Multispectral Scanner System for ERTS*, Hughes Aircraft Report HS324-5214, 1972.

B-3. Rifman, S. S., "Digital Rectification of ERTS Multispectral Imagery," *Symposium on Significant Results Obtained From Earth Resources Technology Satellite-1*, NASA SP-327, pp. 1131–1142, National Aeronautics and Space Administration, Washington, D. C., 1973.

B-4. Simón, J. C., *Functional Signal Representation in Connection With Precision*, 1970.

B-5. Goodman, J. W., *Introduction to Fourier Optics*, McGraw Hill, 1968.

B-6. Blackman, R. B., and Tukey, J. W., *Measurement of Power Spectra*, Dover Publications, 1959.

B-7. Bracewell, R., *The Fourier Transform and its Applications*, McGraw Hill, 1965.

B-8. Helstrom, C. W., "Image Restoration by the Method of Least Squares," *J. Opt. Soc. Am.*, Vol. 57, No. 3, Mar. 67.

B-9. Richardus, P., and Adler, R. K., *Map Projections*, North Holland Publishing Co., 1972.

B-10. Selzer, R. H., *Use of Computers to Improve Biomedical Image Quality*, pp. 817–834, Fall Joint Computer Conference, 1968.

B-11. Nathan, R., "Image Processing for Electron Microscopy: I. Enhancement Procedures," *Advances in Optical and Electron Microscopy*, Vol 4, pp. 85–125, Academic Press, 1971.

B-12. Rindfleisch, T., Dunne, J. A., Frieder, H. J., Stromberg, W. D., and Ruiz, R. M., "Digital Processing of the Mariner 6 and 7 Pictures," *J. Geophys. Res.*, Vol. 76, pp. 394–417, 1971.

B-13. Fu, K. S., *Sequential Methods in Pattern Recognition and Mach Learning*, Academic Press, 1968.

B-14. Goetz, A. F. H., and Billingsley, F. C., "Digital Image Enhancement Techniques Used in Some ERTS Application Problems," *Third Earth Resources Technology Satellite-1 Symposium*, NASA SP-351, pp. 1911–1993, National Aeronautics and Space Administration, Washington, D. C., 1973.

B-15. Rogers, R. H., and Peacock, K., "A Technique for Correcting ERTS Data for Solar and Atmospheric Effects," *Symposium on Significant Results Obtained From Earth Resources Technology Satellite-1*, NASA SP-327, pp. 1115–1122, National Aeronautics and Space Administration, Washington, D. C., 1973.

B-16. Crane, R. B., "Preprocessing Techniques to Reduce Atmospheric and Sensor Variability in Multispectral Scanner Data," *Proceedings of the 7th Symposium on Remote Sensing of the Environment*, p. 1345, University of Michigan, 1971.

B-17. Andrews, H. C., *Introduction to Mathematical Techniques in Pattern Recognition*, Wiley-Interscience, N. Y. , 1972.

B-18. Landgrebe, D. A., *Systems Approach to the Use of Remote Sensing*, LARS Information Note 041571, Laboratory for the Application of Remote Sensing, Purdue University, Lafayette, Ind., 1971.

B-19. Gramenopoulos, N., "Terrain Type Recognition Using ERTS-1 MSS Images," *Symposium on Significant Results Obtained From Earth Resources Technology Satellite-1*, NASA SP-327, pp. 1229–1241, National Aeronautics and Space Administration, Washington, D. C., 1973.

B-20. Haralick, R. M., and Shanmugam, K. S., "Combined Spectral and Spatial Processing of ERTS Imagery Data," *Symposium on Significant Results Obtained From Earth Resources Technology Satellite-1*, NASA SP-327, pp.

1219–1228, National Aeronautics and Space Administration, Washington, D. C., 1973.

B-21. Haralick, R. M., and Bosley, R., "Spectral and Textural Processing of ERTS Imagery," *Third Earth Resources Technology Satellite-1 Symposium*, NASA SP-351, pp. 1929–1969, National Aeronautics and Space Administration, Washington, D. C., 1973.

B-22. Tanguay, M. F., Hoffer, R. M., and Miles, R. D., "Multispectral Imagery and Automatic Classification of Spectral Response for Detailed Engineering Soils Mapping," *Proceedings of the 6th Symposium on Remote Sensing of the Environment*, pp. 33–63, 1969.

B-23. Lamar, J., and Merrifield, P. M., "Pseudocolor Transformation of ERTS Imagery," *Symposium on Significant Results Obtained From Earth Resources Technology Satellite-1*, NASA SP-327, pp. 1187–1198, National Aeronautics and Space Administration, Washington, D. C., 1973.

B-24. Nielsen, V., "Agfacontour Film for Interpretation," *Photogrammetric Engineering*, p. 1099, 1972.

B-25. Wyszecki, G., and Stiles, W. S., *Color Science*, Chapter 3, John Wiley and Sons, Inc., New York, 1967.

B-26. Committee on Colorimetry of the Optical Society of America, *The Science of Color*, Chapter 7, Optical Society of America, Washington, D. C., 1966.

Appendix C

Computer Program Descriptions

A. R. Gillespie

AFILTER: Performs two-dimensional asymmetrical convolution filtering.

ARROW: Draws a north-pointing arrow on ERTS pictures.

ASPECT: Performs one-dimensional resampling (bilinear interpolation).

ASPECT2: Performs two-dimensional resampling (using bilinear interpolation, lagrangian centered function, or spline function).

ASSURE: Tests a classified picture (thematic map) for proximity to the indicated spectral cluster; pixels exceeding a specified distance are reclassified as "unknown."

ASTRTCH2: Performs an automatic linear, ramp cumulative-distribution function (CDF), or gaussian contrast stretch on an image. The percentage of the input picture allowed to saturate black or white is controllable. A ramp CDF contrast stretch redistributes input digital numbers (DN) to enforce the condition that all gray levels in the output picture have the same frequency of occurrence. A gaussian contrast stretch modifies the input histogram to resemble a gaussian distribution.

AUTOSAR: Finds pixels whose DN deviates by more than a specified amount from the average of adjacent pixels. Digital numbers that exceed the allowed variation are replaced by interpolation. AUTOSAR is used to remove bit errors and bad line segments.

BAYES: Classifies an image with up to 12 channels to produce a thematic map using the bayesian algorithm.

BOXFLT: Applies a two-dimensional low-pass "box" convolution filter (with all weights = 1) to an image.

CHROMDIA: Creates a chromaticity frequency diagram from a three-channel input image. Coordinates of the chromaticity diagram (x, y) are the same as those used in standard colorimetry. The output picture depicts the frequency of occurrence of DN triplets with chromaticity values (x, y). The x- and y-axes are discretized into 201 levels, ranging from 0 to 100%. No coordinates above the line $x = -y + 100\%$ can be occupied.

CHRMHST: Computes histograms of the x- and y-chromaticity coordinates from a chromaticity diagram. The x-histogram represents the projection of the frequency distribution onto the x-axis; similarly, the y-histogram is the projection onto the y-axis.

CHRMWGT: Weights the histogram output by CHRMHST to compensate for the fact that the chromaticity diagram is a triangle. Because of this, the x- and y-chromaticity-coordinate histograms showing a uniform frequency distribution would be ramps.

COLORSTR: Transforms a three-channel image into color coordinates of hue, saturation, and intensity or x- and y-chromaticity coordinates, and intensity.

CONCAT: Creates a composite (concatenated) picture from up to 10 input pictures of the same size.

CONTOUR: Creates a contour map showing iso-DN levels from an input picture and optionally overlays it on an image. In this way, topography, temperature, or any scalar field can be directly and visually related to scene detail.

CROSS: Determines the translation necessary to register scene information between rectangular areas in two images. Calculates the sum of the squares of the differences between corresponding DN levels of a rectangle in image 1 and a rectangle in image 2. This process is repeated, moving the rectangle in image 2 by 1 pixel each time, until a matrix of registration coefficients is constructed. The minimum value yields the best registration.

DIFFPIC: Arithmetically computes the DN difference between two input pictures, scales the difference, and creates from it an output image. The input images can be displaced from each other.

DISPLAY: Displays a picture or portions of a picture on a line printer using the high-order 6 bits of data (64 gray levels) to determine which character to print.

EGEOM: Performs geometric transformations of an input picture. Requires a rectilinear grid of control points similar to GEOM, but intensity resampling is performed using bilinear interpolation, a lagrangian centered function, or spline function.

ERTSCAL: Linearizes the light-transfer function of each sensor in ERTS multispectral scanner (MSS) imagery using inflight calibration data.

ERTSFIX: Removes "striping" in ERTS MSS imagery by forcing agreement of means and standard deviations for each of the six sensor histograms per spectral band. Replaces spectral bands by interpolation as an option.

EXPAND: Increases the size of an image by repeating each pixel rather than by interpolation.

F: Fast and flexible byte arithmetic program accepting one or two input pictures. Utilizes a 256- by 256-byte lookup table to apply a chosen function. The table may be generated under parameter control or may be read from a disk or tape storage.

FANCY: Creates color-separation pictures from an input picture with up to 51 gray levels. Designed to create color maps from classified pictures.

FASTCLAS: Classifies an image using statistics produced by STATS to create a thematic map. Spectral clusters in n-dimensional space are approximated by parallelepipeds. In case of ambiguity, the cluster may be approximated as a hyperellipsoid and bayesian classification performed.

FASTFIL1:
FASTFIL2: Convolve an image with a high-pass filter in one (sample only) or two dimensions. Filter used is a subtractive equal-weight filter with dimensions n by m. As an option, FASTFIL2 creates the low-pass picture and/or histograms of the output.

FFT1:
FFT2: Compute the one- or two-dimensional complex Fourier transform. An option exists for the computation of the inverse transform. Transforms must have horizontal and vertical dimensions equal to powers of 2.

FFTIL: Performs one-dimensional frequency space filtering of harmonic noise using the fast Fourier transformation algorithm. Noise spikes are removed one line at a time by either amplitude notching or by linear interpolation of the complex spectrum of each line across the harmonic noise spectral spikes. The output picture is the retransformed image including spectral corrections. POWER can be used to determine frequencies to be filtered.

FFTPIC: Processes VICAR format complex Fourier transforms or complex pictures extracting, reorganizing, and automatically scaling various functions of the complex data for image display. Available functions of the complex input include amplitude, intensity (squared amplitude), phase (with or without sign), real part, and imaginary part. Linear or logarithmic scaling before output can be performed for all functions except phase.

FILTER: Performs two-dimensional convolution filtering followed by a linear transformation to scale the output. FILTER differs from AFILTER in that the filter weights must be symmetrical about the vertical and horizontal lines passing through the filter center.

FLOT: Rotates a picture 90° clockwise or counterclockwise, or rotates at 180° out of the image plane about its horizontal or vertical axis.

FOTO: Creates a polaroid picture of an image.

GEOM:
LGEOM: Effects geometric transformation of images using bilinear interpolation resampling algorithms. Geometric control is input via a rectilinear grid of control points over the output picture, describing the location of the same points in the input picture. LGEOM is a multipass version of GEOM and is more efficient if large vertical translations are required.

GEOMA: Differs from GEOM in that it accepts a nonrectilinear control grid, but still performs bilinear intensity interpolations.

HD: Stretches pictures to compensate for nonlinearities in the $D - \log E$ response of the video film converter. User may specify a desired gamma for his film output.

HIST2:
CLSTR: Construct two-dimensional histogram depicting correlation of DN in two channels.

HISTO: Creates histogram data set in VICAR format for use in display programs and contrast modification programs such as ASTRTCH2.

HISTLOC: Assigns specified output DN to all pixels with DN pairs falling within specified rectangles in the two-dimensional histogram.

HSTAD: Adds from two to ten histograms in VICAR format to create a new histogram.

INSECT: Combines two pictures of unequal size to form a composite picture. May be used to mosaic two pictures or to replace a portion of one picture with a portion of another.

LAVE: Calculates DN averages of a row or column in a digital image.

LEGEND: Annotates classified pictures, constructing rectangles of constant DN used to denote a spectral class and labeling them with English descriptions.

LIST: Produces decimal printouts of a picture or portions of a picture. Optionally displays histograms of the examined regions.

LPLOT:
LPLOT2: Provide analog plot of DN values along an arbitrary straight line through a picture. LPLOT produces data in a format compatible with a stand-alone Calcomp plotter. LPLOT2 produces a VICAR format image of the same data.

LSIGMA: Calculates DN standard deviation for a line of data in a digital image.

MAG: Generates parameters for GEOM. Fetches GEOM to alter picture size and aspect ratio.

MAPGRID: Overlays pixel reference grid on an image. (Grid interval is 25 pixels.) Each grid line consists of alternating black and white 5-pixel segments.

MASK: Prepares digital image in VICAR format for display as a film picture. Pixel grids, gray scales, wall clock date and time, and the VICAR processing history label are shown along with the picture.

MOSAIC: Mosaicks up to ten input pictures to form a composite output picture.

NSPACE: Performs matrix multiplication of n-dimensional images.

OPTRONIX: Pre-stretches a picture to compensate for nonlinearities in the light-transfer function of the Optronics film recorder.

PICAVE: Arithmetically averages up to ten input pictures to create an average image. Input images may be displaced from one another.

PIXC: Performs complex arithmetic on two complex (i.e., complex *8) input arrays, one or both of which may be specified as constant. Addition, subtraction, multiplication, and division are possible options. One or both input images may be conjugated.

PIXGRAD: Calculates local DN gradients and displays them in two pictures. One picture contains the scaled gradient magnitude; the other contains the gradient direction encoded as an integer.

PIXH: Performs fractional fixed-point arithmetic on pictures using half-word storage.

PIXJRK: Removes synthetic pixels inserted by Goddard Space Flight Center (GSFC) in ERTS MSS images to standardize sample scale.

PIXPIK: Extracts each n^{th} line and each m^{th} sample to reduce the size of a picture.

PIXSTAT: Calculates statistical quantities in local areas surrounding each pixel in an input picture. These quantities are scaled and written in the corresponding pixel of the output picture.

POLYFLTR: Applies convolution filter to a picture. Filter weights used may belong to one of five different filters; the appropriate filter can be varied during processing, based on some parameter of the image being filtered (e.g., local brightness or variance of brightness).

POWER: Computes one-dimensional power spectrum of a specified portion of a picture. The square root of the power spectrum is displayed on the line printer, and a file is written on an output tape suitable for plotting on a stand-alone Calcomp plotter.

PSAR: Adjusts DN in up to 100 polygonal areas (specified by vertices) or rectangles by user-specified amounts.

QSAR: Adjusts DN in rectangular areas only by user-specified amounts.

RATIO: Computes parameters for F, causing F to apply

$$DN' = a \frac{DN_1 - constant_1}{DN_2 - constant_2} - b \tag{1}$$

$$DN' = \log \left(a \frac{DN_1 - constant_1}{DN_2 - constant_2} - b \right) \tag{2}$$

$$DN' = a\,(DN_1 - DN_2) - b \tag{3}$$

or

$$DN' = \log \left[a\,(DN_1 - DN_2) - b \right] \tag{4}$$

to produce a digital image comparing two input pictures. Determines coefficients a and b so that the resulting probability-density function (PDF) optionally occupies a 256-level dynamic range, and the distribution is centered on $DN' = 128$.

REGISTER: Aligns two images depicting the same scene, based on correlation of selected regions within the input pictures. Parameters are generated that allow GEOM or GEOMA to effect the desired geometric transformation.

ROTATE: Rotates a picture ±90°.

ROTATE2: Rotates a picture any number of degrees about a specified point. ROTATE2 is slower than ROTATE.

SAC: Orders MSS input pictures in decreasing effectiveness at separating specified "classes" of information. Selects minimum number of input pictures required for classification. Fetches FASTCLAS or BAYES to perform the actual classification.

SAR: Copies pictures from one data set to another. Replaces specified rectangular areas with data interpreted from the perimeter.

SCALE: Appends distance scale (kilometers and miles) and/or gray-level scale to picture.

SHADY: Introduces shading and contour lines on an image.

SKEW: Compensates ERTS images for geometric distortions caused by Earth's rotation and satellite's orbit during data acquisition.

SKEWCON: Concatenates two pictures that have been SKEWED.

SLICE: Performs density slicing on a single input picture. Produces three output pictures for color combination.

SPREAD6: Causes the six individual sensor PDFs (histograms) to resemble a specified sensor PDF in ERTS image.

STATS: Produces data set required by classification programs FASTCLAS, BAYES, and SAC, which contains means and covariance matrices describing polygonal regions in multi-spectral images specified by the analyst. A maximum of 12 channels of data is allowed.

SYNBLU: LUTSFBPG: Accept the green, red, and first infrared bands (MSS 4, 5, 6) of an ERTS image and predict a blue band that may be used to synthesize a "natural" color image.

TAPE2: Manipulates data stored on tape.

TEXTAD: Superimposes user-specified English messages and/or outlines rectangular areas on an image.

TRNAREA: Finds DN means and standard deviations for polygonal areas in an input image with up to 10 input channels. (i.e., accepts up to 10 registered input pictures).

VMSS: Converts ERTS images from the GSFC EROS format to VICAR format. Specifically, data are segregated by spectral channel; each individual channel image is assigned a standard 360-byte VICAR label and is subsequently managed as though it were an independent picture.

WTGEN: WTSIN: WTGN1: Generate convolution filter weights if a filter modulation-transfer function (MTF) is defined by the user. WTGEN generates symmetrical two-dimensional filters. WTSIN allows the MTF to differ vertically and horizontally. WTGN1 computes a one-dimensional filter only.

Appendix D
ERTS Image Processing Sequence

A. R. Gillespie

The ERTS computer programs described in Appendix C are used in the following sequence:

(1) Data Preparation

TAPE2. Checks for tape errors, missing data.

VMSS. Converts to VICAR format.

ASTRTCH2. Performs linear contrast stretch and picture display.

(2) Geometric Rectification

INSERT. Replaces missing data lines with interpolated data.

PIXJRK. Removes "synthetic" pixels added by Goddard Space Flight Center.

GEOM, LGEOM, GEOMA, EGEOM. Compensate for aspect ratio, roll and pitch of satellite, foreshortening caused by viewing geometry, and nonlinearities in the scan velocity of the multi-spectral scanner (MSS) mirror.

SKEW. Compensates for the Earth's rotation during picture acquisition.

ASPECT. Resamples to set the aspect ratio to unity.

WTGEN, WTSIN. Define convolution filter to restore uniform spatial-frequency response.

FILTER. Applies filter to restore uniform spatial-frequency response.

CROSS, REGISTER. Register images taken at different times, or register images to maps.

(3) Radiometric Rectification

ERTSCAL. Reduces striping using inflight calibration data.

ERTSFIX. Removes striping by matching means and standard deviations in the sensor histograms (probability-distribution or probability-density functions, PDF).

SPREAD6. Reduces striping by forcing the cumulative-distribution function of each sensor to be similar.

STRETCH. Performs nonlinear "table" stretch to cause radiometry to agree with ground observations.

(4) Cosmetics

ERTSFIX. Replaces lines with severe striping by interpolated values.

SAR. Interpolates across large blemishes.

AUTOSAR. Detects and removes bit errors and bad line segments.

FFT2, FFT1. Perform Fourier transformation of an image to identify and remove coherent noise.

(5) Analysis

(a) Extractive routines

LIST. Displays on a line printer pixel listings, histograms, means, and standard deviations of rectangular areas within a picture.

TRNAREA. Computes means and standard deviations of polygonal areas in a multi-channel data set.

STATS. Computes means, standard deviations, and covariance matrices for polygonal training areas in a multi-channel image. Creates data set containing these statistics for use in classification programs.

FFT1, FFT2. Perform one- and two-dimensional Fourier transformations.

POWER. Creates one-dimensional power spectrum.

HISTO. Creates histograms and stores them in a VICAR format data set.

LAVE. Displays mean digital numbers line by line.

LSIGMA. Displays means and standard deviations line by line.

CHROMDIA. Displays chromaticity PDF for three-channel images.

HIST2. Creates two-dimensional PDF and stores it in a VICAR format data set.

(b) Dimension modification: image comparison

NSPACE. Performs dimension rotation and reduction.

COLORSTR. Transforms a three-channel image in radiance coordinates (e.g., blue, green, red) into a three-channel image in color coordinates (e.g., hue, saturation, and intensity, or x-chromaticity, y-chromaticity, and intensity).

REGISTER. Registers automatically two images of the same scene.

CROSS. Prints out correlogram that indicates translation providing best registration for a small region in an image pair.

PICAVE. Averages up to ten images.

DIFFPIC. Differences two images arithmetically.

PIXH. Performs flexible half-word arithmetic involving one or two input pictures.

F. Performs fast, flexible byte arithmetic (using lookup table) for one or two input pictures.

RATIO. Predicts best linear transformations (stretch) to scale ratio or difference pictures into 8-bit output, then fetches F to perform the required operation. Useful for temporal or spectral comparisons.

(c) Creations of new dimensions of an image

PIXSTAT. Creates means, standard deviations, or local variances.

PIXGRAD. Provides local gradient magnitude and direction.

FILTER. Creates local second derivative of digital-number surface (laplacian filter)

FFT2. Enhances specific spatial-frequency bands.

(d) Classification: automated interpretation based on extracted data

HISTLOC. Two-channel classifier.

BAYES. Bayesian classifier that accepts up to 12 channels of image data.

FASTCLAS. Parallelepiped classifier that consults BAYES to resolve ambiguities in up to 12 channels of data. Faster than BAYES.

SAC. Classifier that optimizes operation of FASTCLAS and BAYES by limiting the number of channels examined to those required to achieve separation of classes.

(6) Display

STRETCH. Performs linear and nonlinear contrast modifications.

ASTRTCH2. Performs automatic linear and limited nonlinear contrast modifications.

F, HD, OPTRONIX. Compensate for nonlinearities in film recorder.

MASK. Annotates an image for display.

TEXTAD. Adds annotation within the image.

SCALE. Appends kilometer scales and/or gray scales within an image.

ARROW. Inserts a north-pointing arrow.

SLICE. Performs density slicing for color display of a single-channel image.

FILTER. Emphasizes different spatial spectral features. Enhances local contrast.

CONTOUR. Superimposes contours describing a scalar field (or image) on a picture.

Appendix E
Portable Field Reflectance Spectrometer

A. F. H. Goetz

I. Purpose

At the start of this ERTS investigation and through involvement in other ERTS research in progress, it became obvious that field measurements of surface spectral reflectivity would be necessary to:

(1) Determine the effects of atmospheric absorption and scattering on ERTS spectral image values.

(2) Establish a set of criteria for quantitative image analysis through computer image processing.

(3) Assist in the selection of the best set of spectral bands for geologic mapping in future missions.

(4) Establish the correlation between field-measured surface spectral reflectance and the necessarily small, selected samples measured in laboratory reflectance equipment.

To span the wavelength range of the Skylab S-192 multi-spectral scanner (MSS) in the reflective portion of the spectrum and ERTS MSS bands required a spectral coverage of 0.4 to 2.5 μm. However, no instrument marketed covered the spectral range at the resolution desired or was sufficiently portable for field work in remote areas. In fact, existing specialized systems required a vehicle and generator power to record and analyze data.

The system described here was designed to meet the following criteria:

(1) Backpack, field-portable.

(2) Complete coverage of the spectral region 0.4 to 2.5 μm with moderate resolution ($\Delta\lambda/\lambda$ = 0.02 to 0.04).

(3) Stability over a wide range of temperatures.

(4) Digital data recording.

II. The System

The portable field reflectance spectrometer (PFRS) system consists of a separate optical head and amplifier-recorder assembly (see Fig. E-1). In the field, the electronics pack is worn continuously by the operator. The optical head, mounted on a tripod, is hand-held, but is carried on a pack frame when moving from area to area. A hand-held meter indicates the signal level and is used to set gain levels. In operation, all results are reduced to spectral reflectance values for comparison of areas measured under various lighting conditions.

A. Optical Head

An artist's view of the optical head is shown in Fig. E-2. In sequence, the beam enters the instrument at the left

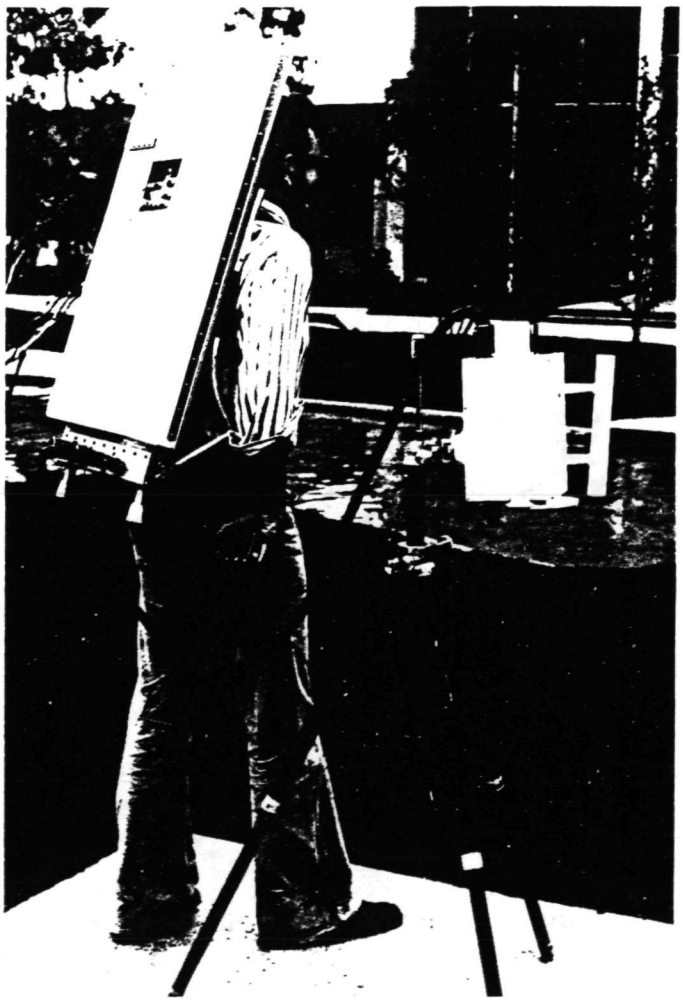

Fig. E-1. Portable field reflectance spectrometer in operating position. Backpack contains the amplifiers, power supply, and digital recording electronics. Optical head contains the chopper, circular variable filter, thermoelectrically cooled detectors, and preamplifiers

and is interrupted by a 280-Hz vibrating reed chopper. A relay lens focuses the incoming light on the slit directly in front of the filter wheel and by way of a beamsplitter onto a total field detector. The circular, variable-filter wedge (see Fig. E-3) defines the wavelength and, in the three opaque sectors, allows for the insertion of engineering information onto the data stream. A second lens focuses the beam on a 1- by 6-mm detector.

The PFRS is capable of operating in a 0° to 50°C environment. Both the total field and the spectral detectors are PbS, thermoelectrically cooled (or heated) to 15° ± 0.02°C. By stabilizing the temperature of the detectors, a major source of signal drift is eliminated.

The total field detector monitors the total irradiance in the field of view as a function of time. By correcting the spectral detector output for irradiance fluctuations over the 30-s scan period, it is possible to operate under high cirrus cloud conditions and to maintain reasonable accuracy in reflectance measurement.

B. Recording Electronics

Figure E-4 is a functional block diagram of the recording electronics in the backpack. Both of the detector channels, spectral and total field, follow parallel amplification and synchronous demodulation paths to the multiplexer. Signal measurement and recording occur at 90-ms intervals. Sample-and-hold circuitry is used for integration within the sampling interval. Analog-to-digital converters follow the multiplexer circuit to ensure compatibility of the signals with digital cassette recording.

During the time that spectral measurements are made, four 12-bit words, consisting of the filter-wheel position, total field detector signal, and spectral detector signal, are recorded along with file number and gain states in each of the detector channels. When the three opaque segments of the filter wheel (see Fig. E-3) are in the field of view, engineering measurements such as battery and power supply voltages as well as optical head and backpack temperature are multiplexed into the signal channels. These diagnostic measurements have proved useful in interpreting anomalies in the field.

Additional digital circuitry formats the signals for recording and controls the filter-wheel rotation. Power is supplied by a 6-V silver zinc battery with a capacity of 80 A-h. In order to conserve power, only the detector coolers and the preamplifiers are energized when the unit is in a standby condition. When a run is initiated, the DC-to-DC converters are energized; filter-wheel rotation and digital recording automatically begin after a 2-s warmup period. At the end of the rotation, the system automatically returns to the standby condition. A file counter that utilizes low-power-drain circuitry remains energized continuously, even after the front panel power switch is turned off, so that no file count error is possible.

III. Operation

When in the field, the optical head is mounted on a tripod about 1.3 m above the surface with the long axis of the slit oriented along the solar azimuth. The surface area covered from this height is approximately 200 cm^2.

Gain settings for both signal channels are made by manually setting the filter to approximately the 0.7-μm position, the point of maximum signal observed on the hand-held meter. The response of the PbS detector is sufficiently flat that only one gain setting is required for the 0.4- to 1.4-μm range. An automatic divide-by-2 gain change is made for the last segment of the filter wheel. A spectrum of the surface is taken, followed immediately by measuring a standard in the same orientation. Fiberfrax, a ceramic wool insulation used as the standard, has a surface that is renewable by peeling the upper layer and pressing the surface flat. This is an important factor, as contamination is inevitable under field conditions.

It is possible to record 100 spectra on the two sides of one digital cassette. With battery power sufficient to record about 700 spectra, an operation of about 2 and 3 days between charges is possible.

A set of interface electronics known as a "playback box," which is capable of displaying the file number and accessing the beginning of any desired file, operates the tape recorder within the backpack unit at a field headquarters. A digital-to-analog converter is included for playback on a strip-chart recorder. This unit acts as a tape controller and interface to the computer for analysis. The spectra are reduced and analyzed with the aid of a PDP 8/e computer and plotter.

IV. Results

Figure E-5a is a typical raw spectrum of a rock surface (andesite). The atmospheric water lines at 0.95 and 1.14 μm are apparent; the 1.4- and 1.9-μm water lines are saturated, and data in those regions are not plotted. Figure E-5b shows a reduced spectrum obtained by taking the ratio of the sample and standard spectra point by point. Residual effects of the 0.95- and 1.14-μm telluric water bands appear because the signal-to-noise ratio is reduced within these bands.

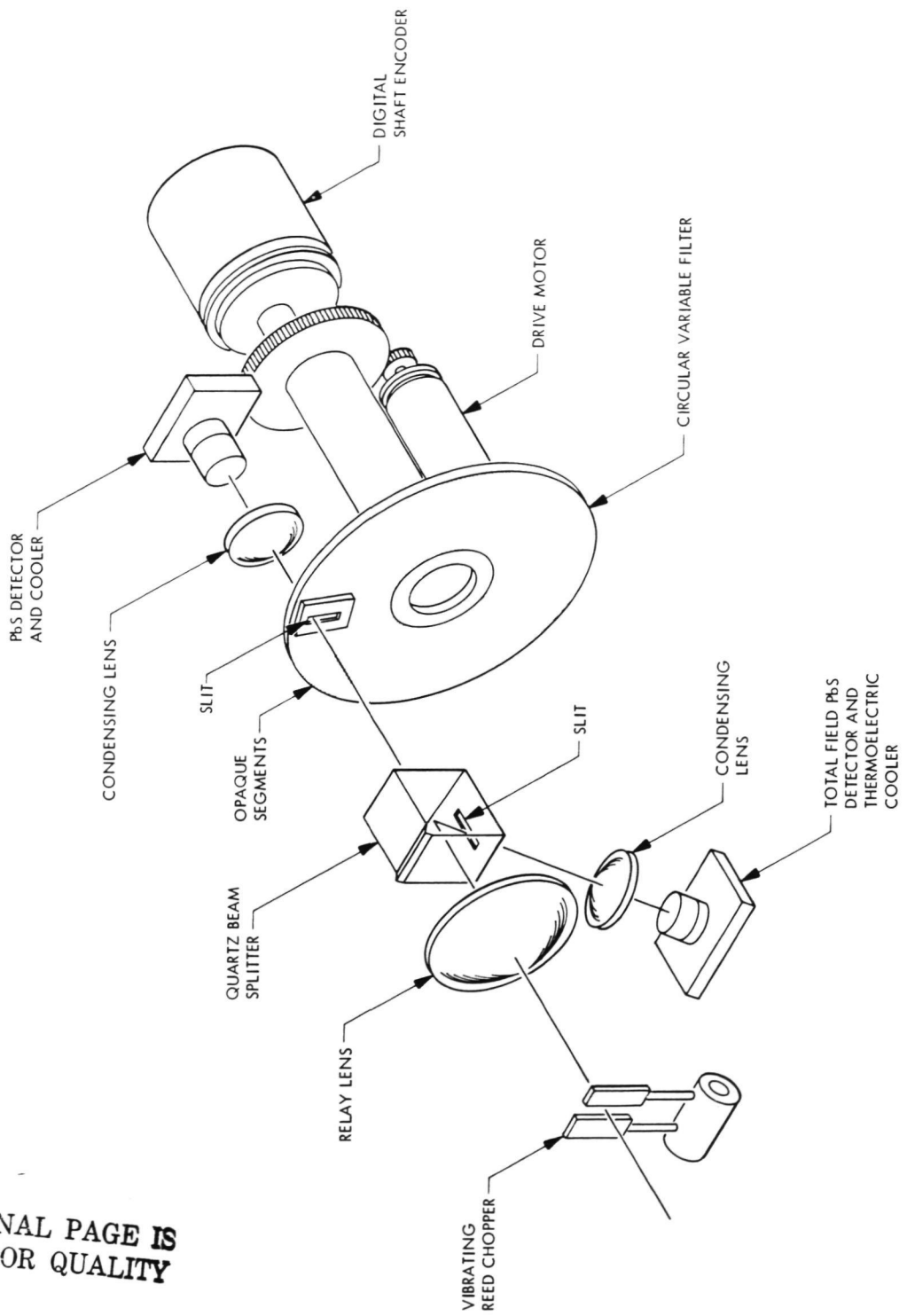

Fig. E-2. Exploded view of optical head. Infrasil lenses are used

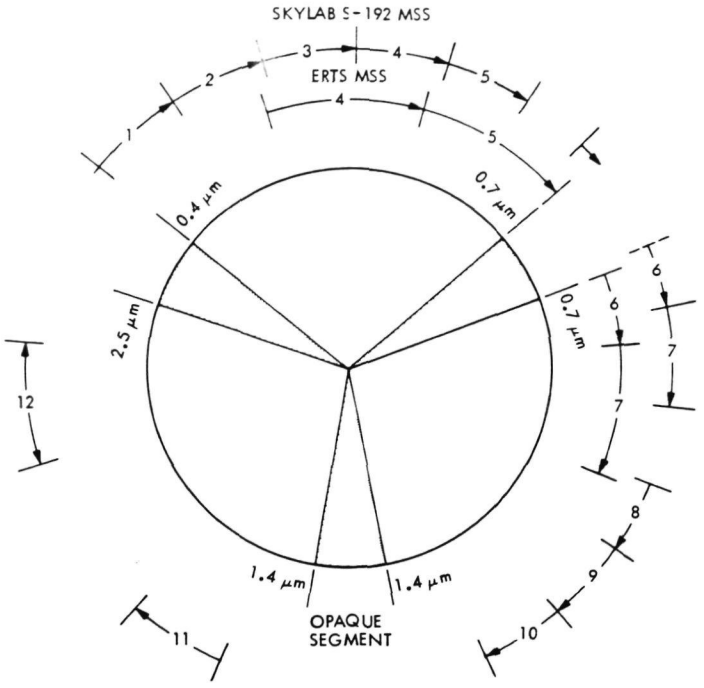

Fig. E-3. Composite circular variable filter wheel with indicated positions of the four ERTS and twelve Skylab S-192 MSS bands

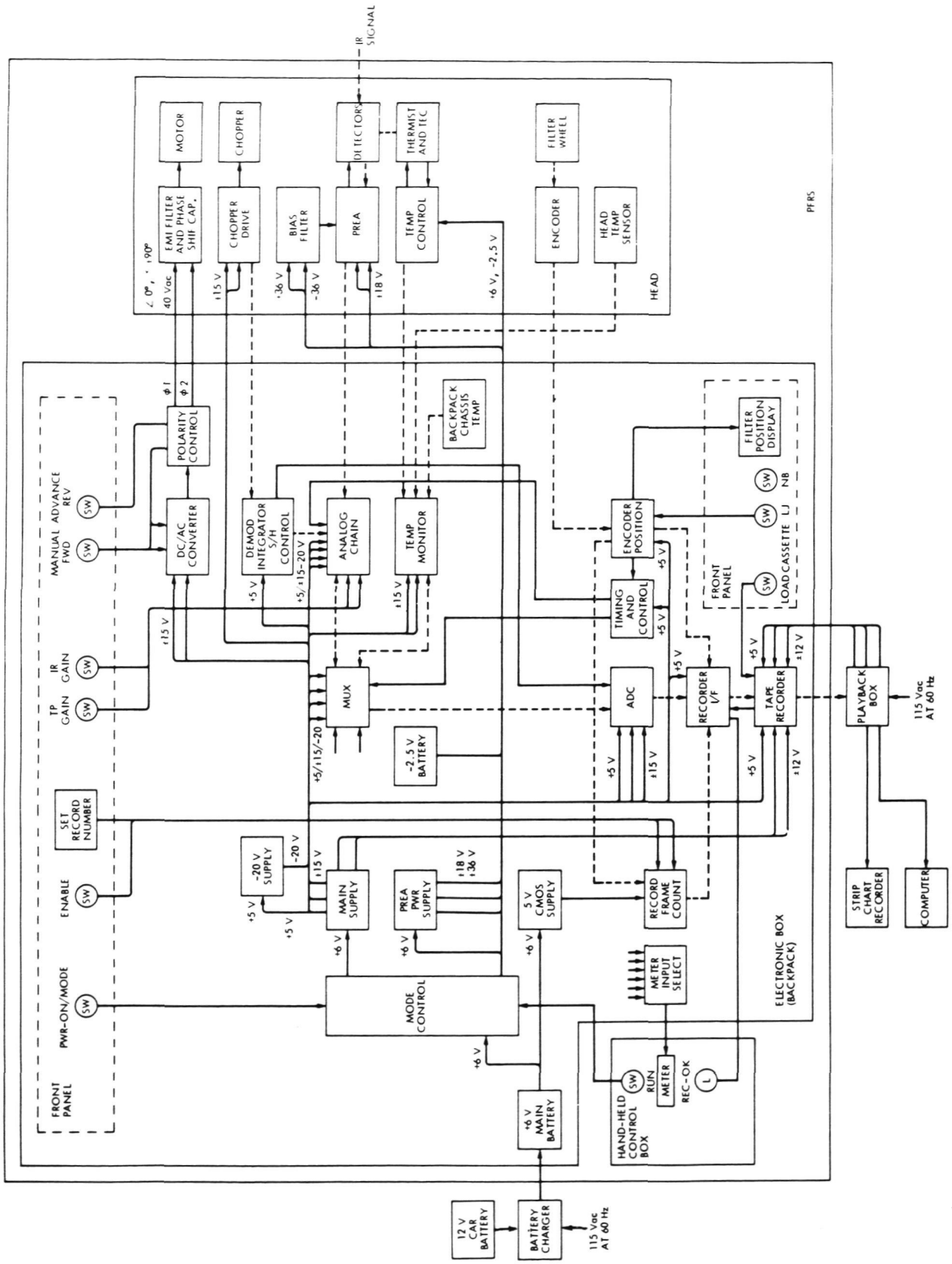

Fig. E-4. Functional block diagram of the portable field reflectance spectrometer

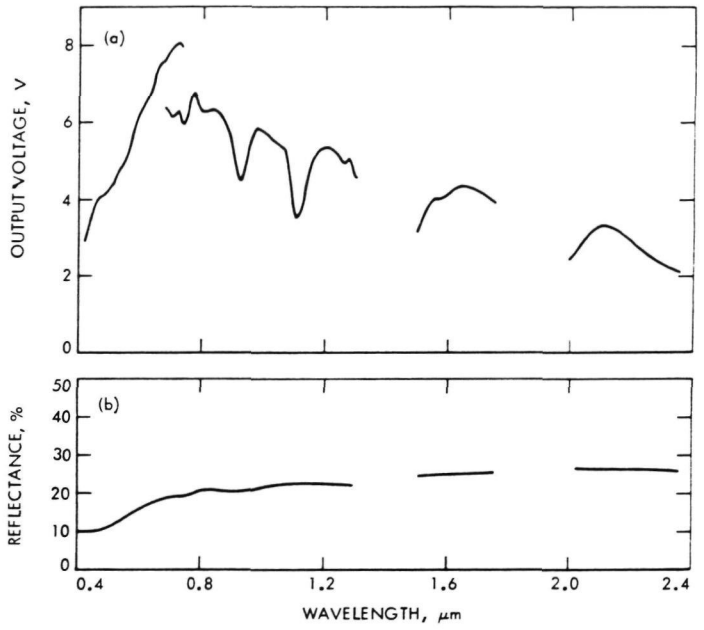

Fig. E-5. (a) Raw spectrum of an andesite sample. (b) Spectral reflectance spectrum of an andesite sample derived from the ratio of Fig. E-5a with a measured spectrum of Fiberfrax

NASA — JPL — Coml., L.A., Calif.